Études par résonance magnétique nucléaire des ordres en compétition dans les cuprates supraconducteurs

Igor Vinograd

Communauté
UNIVERSITÉ Grenoble Alpes

THÈSE

Pour obtenir le grade de

DOCTEUR DE LA COMMUNAUTÉ UNIVERSITÉ GRENOBLE ALPES

Spécialité : Physique de la Matière Condensée et du Rayonnement

Arrêté ministériel : 25 mai 2016

Présentée par

Igor Vinograd

Thèse dirigée par
Dr. Marc-Henri Julien, Directeur de recherche, Laboratoire National des Champs Magnétiques Intenses, CNRS, Grenoble

préparée au sein du **Laboratoire National des Champs Magnétiques Intenses, CNRS, Grenoble**
dans **l'École Doctorale de Physique**

Études par résonance magnétique nucléaire des ordres en compétition dans les cuprates supraconducteurs

Nuclear magnetic resonance studies of competing orders in cuprate superconductors

Thèse soutenue publiquement le **19 décembre 2018**
devant le jury composé de :

Prof. Matthieu Le Tacon
Karlsruher Institut für Technologie, Allemagne, Rapporteur
Prof. Pietro Carretta
Università degli studi di Pavia, Italie, Rapporteur
Dr. Simone Fratini
Institut Néel, CNRS, Grenoble, France, Président
Prof. Antony Carrington
University of Bristol, Royaume-Uni, Examinateur
Dr. Marc-Henri Julien
LNCMI, CNRS, Grenoble, France

Contents

Résumé

Introduction

Trente ans après la découverte de la supraconductivité à haute température critique dans les cuprates, les efforts expérimentaux et théoriques visant à comprendre le mécanisme à son origine se poursuivent. Paradoxalement, il semble que le problème se complexifie avec le temps. En effet, ces dernières années, de nouvelles découvertes incluant un nombre toujours croissant d'anomalies et de phases électroniques, sont venues participer à l'énigme de la supraconductivité dans les cuprates. On peut citer notamment la phase métallique étrange (avec une résistivité linéaire qui ne sature jamais) ou le pseudogap et deux de ces phases électroniques que sont l'ordre de spin et l'ordre de charge plus récemment découvert. L'ordre de charge entre fortement en compétition avec la supraconductivité. Cette compétition peut être étudiée en jouant sur un grand nombre de paramètres comme le dopage, la température, le champ magnétique, la pression hydrostatique ou uniaxiale, le désordre et même la lumière [1]!

Dans cette thèse, l'effet du champ magnétique et de la pression hydrostatique sur l'ordre de charge a été étudié dans $YBa_2Cu_3O_y$ (YBCO). Des mesures par Résonance Magnétique Nucléaire (RMN) de l'ordre de charge et leur analyse détaillée sont présentées au chapitre 3.
Alors que le champ magnétique supprime la supraconductivité et finit par induire une onde de densité de charge à longue portée, il est bien établi que l'application d'une pression hydrostatique augmente T_c. Les travaux du groupe de Louis Taillefer ont suggéré que l'augmentation de T_c pourrait être due à la suppression progressive de l'onde de densité de charge à courte portée [2] et nous présentons au chapitre 4 de cette thèse des mesures par RMN dont l'interprétation est en faveur de ce scénario. Cependant, les interprétations de mesures existantes de transport électrique et de diffusion des rayons X (XRD) vont, elles, à l'encontre de ce scénario. Motivés par cette contradiction apparente, nous avons cherché une description permettant de réconcilier les données de transport, de XRD et de RMN. Nous suggérons de nouvelles mesures de XRD pour confirmer ou infirmer cette description.

Le chapitre 5 présente un phénomène apparemment sans rapport : le gel vitreux des spins dans $La_{2-x}Sr_xCuO_4$ (LSCO). Le contexte de ce travail est le suivant : des mesures récentes de transport dans LSCO sous champ magnétique intense dans le groupe de Louis Taillefer ont été interprétées en

terme de changement abrupt du nombre de porteurs de charge pour un dopage critique $p^* = 0.18$ correspondant au point terminal supposé de la phase pseudogap [3]. Des mesures similaires ont également été effectuées dans YBCO [4]. Un scénario qui pourrait expliquer la perte de porteurs à l'intérieur du pseudogap serait l'existence d'un ordre anti-ferromagnétique. Cependant, aucun ordre magnétique n'a été détecté ni par RMN, ni par μSR, ni par diffusion de neutrons. La diffusion de neutrons constate même l'absence totale de fluctuations de spin à basse énergie : en champ nul, il existe un gap de spin pour $p \gtrsim 0.14$ dans LSCO et pour $p \gtrsim 0.08$ dans YBCO. Nous montrons que, dans LSCO, le taux de relaxation spin-réseau $1/T_1$ pour des champs magnétiques jusqu'à 45 T est augmenté de manière compatible avec un gel vitreux des spins pour des dopages inférieurs à $p = 0.171$ mais pas au delà et en particulier à $p = 0.21$ où plus aucune signature de ce gel n'est observée. Nous avons pu déduire de nos mesures qu'il existe une forme d'ordre anti-ferromagnétique qui apparaît dans une plage de dopage compatible avec l'étendue du pseudogap. Ces mesures suggèrent que la perte de porteurs de charge dans la phase pseudogap pourrait être le résultat d'un ralentissement induit par le champ des fluctuations antiferromagnétiques de spin ou bien que les fluctuations de spin sont déjà en train de ralentir en champ nul et que le champ magnétique ne fait qu'accentuer cette tendance. Un ordre de charge pourrait être pertinent pour expliquer ce phénomène car nous pensons qu'il gèle les fluctuations de spin. Au passage le rôle de cet ordre de charge créerait un lien entre les deux études de cette thèse.

Introduction à la physique des cuprates : du pseudogap à l'ordre de charge

Ce chapitre présente certains aspects des cuprates supraconducteurs utiles à la compréhension de notre étude. On y trouvera les structures cristallines et électroniques du composé parent et le mécanisme de dopage. Le dopage conduit à un grand nombre de phases électroniques qui sont brièvement discutées. L'objet premier de cette introduction est l'ordre de charge et le phénomène de *stripes*, car ce sont les propriétés de ces phases qui ont été étudiées dans cette thèse. Dans la gamme de dopage intermédiaire, on trouve une grande variété de phases électroniques qui peuvent être résumées dans un diagramme de phases p-T, comme indiqué dans la Fig. 1.

Brève introduction à la RMN

La résonance magnétique nucléaire (RMN) est une technique qui peut être utilisée pour étudier aussi bien les liquides que les solides. Les noyaux eux-mêmes ne jouent aucun rôle dans la physique, si bien que le noyau peut être considéré comme faisant partie de la sonde expérimentale. Ce qu'il faut,

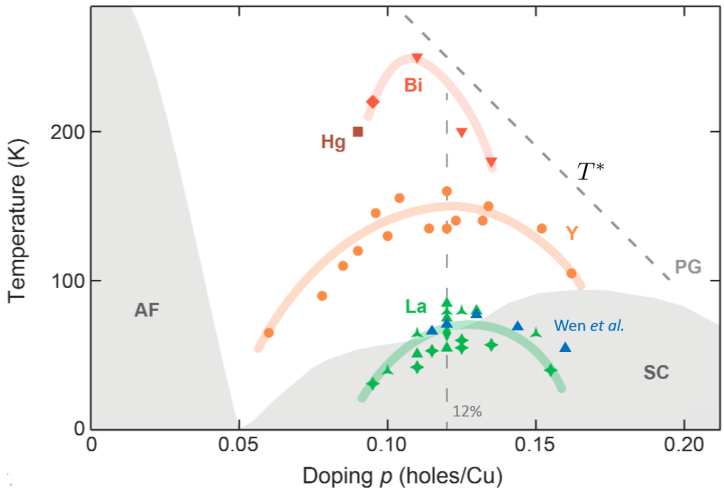

Figure 1: Diagramme de phases $p - T$ schématique des cuprates, basé sur YBCO, comprenant la phase antiferromagnétique à longue portée (AF), la supraconductivité (SC) et le pseudogap (PG) dont la limite supérieure est indiquée par une ligne pointillée. Les données expérimentales pour l'ordre charge à courte portée de différents cuprates dopés par des trous sont indiquées en couleur. Les symboles rouges et bruns désignent respectivement les cuprates à base de bismuth et à base de mercure. Les cercles jaunes (Y) représentent YBCO, les symboles verts correspondent à différents cuprates à base de lanthane (LNSCO, LBCO, LESCO et LSCO). Cette figure est adaptée de la référence [5] de 2016. Les données LSCO récentes de Wen *et al.* [6] ont donc été incluses sous forme de triangles bleus.

c'est une caractérisation de l'interaction entre le noyau et son environnement. Dans les solides, ce sont principalement les interactions hyperfines magnétiques et électriques (quadrupolaires). Grâce aux interactions hyperfines, on peut acquérir des connaissances sur l'état électronique et la structure cristalline : les noyaux agissent en tant que capteurs locaux de champs magnétiques et de gradients de champs électriques. Un spin nucléaire I est décrit par l'opérateur de spin nucléaire $\hat{\boldsymbol{I}}$ qui permet de définir l'opérateur correspondant au moment magnétique nucléaire $\hat{\boldsymbol{\mu}} = \hbar\gamma_N \hat{\boldsymbol{I}}$, où γ_N est le rapport gyromagnétique. Dans un champ magnétique statique $\boldsymbol{B} = B_z\hat{z}$ son hamiltonien est

$$\hat{H}_{Zeeman} = -\hat{\boldsymbol{\mu}}\boldsymbol{B} = -\hbar\gamma_N B_z \hat{I}_z,$$

avec des valeurs propres $E_m = -\hbar\gamma_N B_z m$ appelées *niveaux Zeeman*. Pour un spin nucléaire I, il existe $2I+1$ niveaux Zeeman donnant $2I$ transitions entre les niveaux d'énergie voisins dont la séparation est $E_{m-1} - E_m = \hbar\omega_L$. Les spins nucléaires I minimisent leur énergie en s'alignant avec le champ externe et donnent naissance à une aimantation nucléaire $\boldsymbol{M}_0 = M_z\hat{z}$. En RMN, les transitions entre ces niveaux d'énergie sont induites en appliquant des impulsions radiofréquences résonantes à l'aide d'une bobine d'excitation. Le signal RMN est enregistré avec la même bobine pendant la désexcitation, et est appelé *signal de précession libre* (FID). Classiquement, ce signal correspond à la tension induite sur la bobine par la précession de l'aimantation nucléaire macroscopique. La transformée de Fourier de cette

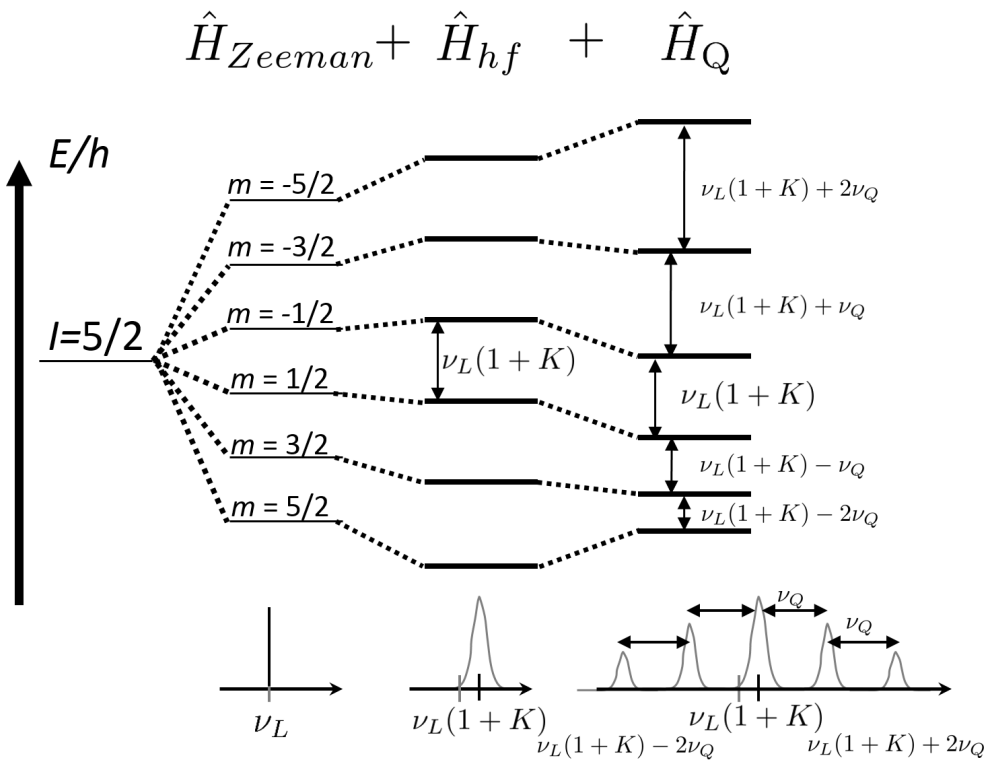

Figure 2: Spectre de RMN schématique pour $I = 5/2$ résultant de l'interaction Zeeman $\hat{H}_{Zeeman}$, de l' interaction hyperfine magnétique entre les noyaux et les électrons $\hat{H}_{hf}$ qui entraîne le décalage de Knight K et de l'interaction quadrupolaire $\hat{H}_Q$ donnant un pic central et des satellites internes et externes décalés de $\pm\nu_Q$ et $\pm 2\nu_Q$, respectivement.

tension donne le spectre RMN. Les interactions avec les électrons modifient les énergies de transition et donc la structure du spectre, comme montré schématiquement pour $I = 5/2$ dans la Fig. 2. Etant donné que les interactions magnétiques se couplent aux degrés de liberté du spin électronique tandis que les interactions quadrupolaires résultent de couplages avec l'environnement de charge, la RMN est en principe capable de distinguer les phénomènes d'ordre de charge et de spin.

Étude de l'ordre de charge dans $YBa_2Cu_3O_y$ par RMN de l'^{17}O

Dans ce chapitre, on présente les spectres RMN de ^{17}O dans YBCO qui révèlent l'ordre de charge. Une analyse détaillée des largeurs de raies et des formes de raies permet de déduire des informations sur cet ordre charge à courte ou longue portée. Dans la phase où l'ordre de charge est à courte portée, les formes de raies sont simples. Les informations essentielles sur l'ordre de charge proviennent donc des largeurs de raies.

Les formes de raies deviennent plus intéressantes dans la phase où l'ordre de charge est à longue portée (i.e. pour des champs élevés). Dans la deuxième partie de ce chapitre, une étude détaillée du splitting de la raie induit par le champ donne un nouvel aperçu de la période de modulation de la densité de

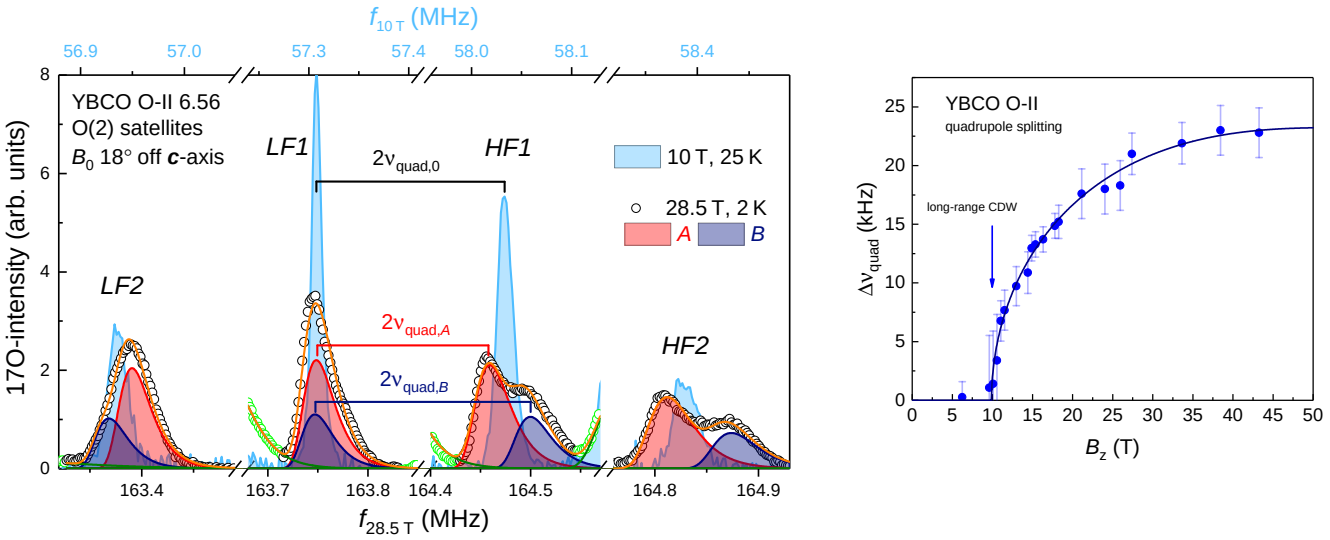

Figure 3: Gauche : les spectres satellites de O(2) mesurés à 10 T & 25 K, pour lesquels il n'y a pas de splitting (couleur bleu clair), et à 28.5 T & 2 K (cercles vides), sont tracés sur la même échelle de fréquence. Les raies centrales (non représentées) sont alignées pour tenir compte des différents Knight shifts moyens.
Le spectre à fort champ est adapté à deux profils EVD (*Extreme Value Distribution*) pour les deux sites A (rouge) et B (bleu foncé). Le rapport de surface A_A/A_B est égal à 2 alors que les largeurs de chaque satellite sont égales. La ligne orange représente l'ajustement complet, y compris les queues des sites O(3) voisins. Les satellites $LF1$ et $HF1$ sont séparés par $2\nu_{\rm quad}$.
Droite : le splitting quadrupolaire $\Delta\nu_{\rm quad} = \nu_{\rm quad,B} - \nu_{\rm quad,A}$ du site O(2) en fonction de B_z d'un echantillon avec $p = 0.109$. Le champ d'onset $B_{\rm onset} = 9.9$ T est déterminé par un ajustement à une tangente hyperbolique.

charge et met en évidence le rôle des discommensurations. Suite à l'analyse des formes de raies pour des modulations commensurables et incommensurables, uni- et bidirectionnelles, nous déterminons que les spectres RMN de l'^{17}O des sites des oxygènes dans les plans CuO_2 peuvent être expliqués par une modulation uniaxiale de période $3a$ ou $3b$.
Sur la base de ce modèle, le champ d'émergence de la phase d'ordre de charge à longue portée, $B_{\rm onset}$, est déterminé pour une plage de dopages $0.088 \leq p \leq 0.136$. Ce champ suit la dépendance en dopage de H_{c2}.

Effet de la pression hydrostatique sur la compétition entre supraconductivité et ordre de charge dans $YBa_2Cu_3O_y$

Dans ce chapitre, nous avons étudié l'effet de la pression hydrostatique sur les ordres de charge à courte et longue portée dans YBCO. Nous constatons que les ordres de charge ne sont que faiblement affectés par l'application de 1.9 GPa. L'amplitude de l'ordre de charge à courte portée, indépendante du champ, diminue de ~ 20 %, comme le montre la figure 4. L'ordre de charge à longue portée qui

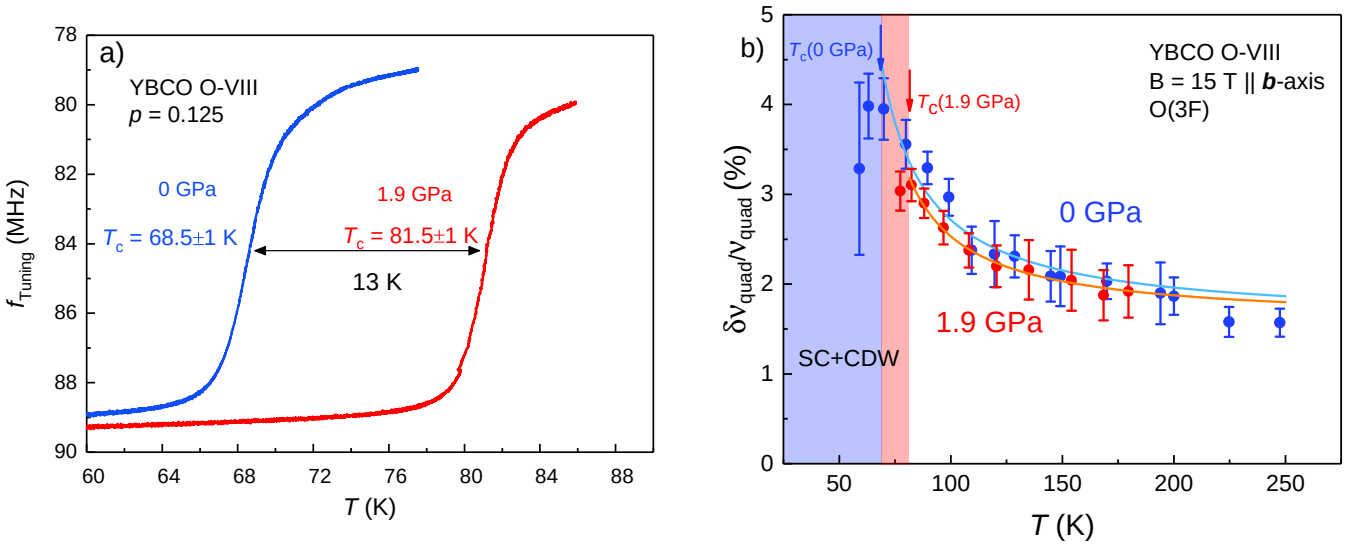

Figure 4: a) : Fréquence d'accord du circuit de résonance RMN de l'échantillon O-VIII (p = 0.125). b) : Dépendance en T de l'élargissement quadrupolaire sans dimension de O(3F) à la pression ambiante (cercles bleus) et à 1.9 GPa (cercles rouges) mesuré avec un champ de 15 T le long de l'axe $\boldsymbol{b}$. Dans cette orientation, les fréquences quadrupolaires sont $\nu_{\rm quad}$ (0 GPa) = 947 kHz et $\nu_{\rm quad}$ (1.9 GPa) = 953 kHz. Les lignes sont des courbes de Curie-Weiss allant jusqu'aux $T_{\rm c}$s respectifs avec un fond indépendant de T, *const.*, fixé à 1.58%

est induit par le champ a un champ d'émergence plus élevé, comme prévu par l'augmentation de $H_{\rm c2}$, mais au-dessus de ce champ, l'amplitude du paramètre d'ordre à 1.9 GPa augmente rapidement pour atteindre une valeur comparable à celle trouvée à pression ambiante.

Nous étudions l'effet de la pression sur le dopage et trouvons qu'il est petit mais pertinent pour comprendre le changement de $T_0(\boldsymbol{P})$ dans les mesures de transport de Putzke *et al.* [7]. Nous trouvons que les mesures de RMN et de transport sont cohérentes avec la proposition de Cyr-Choinière *et al.* selon laquelle la suppression progressive de l'ordre de charge entraîne une augmentation de $T_{\rm c}$ qui sature à $\boldsymbol{P} \sim 15$ GPa [2].

Ces conclusions ne concordent pas avec la suppression complète de l'ordre de charge à $\approx$ 1 GPa, que montrent les mesures de diffraction XRD de Huang *et al.* et Souliou *et al.*. Nous suggérons des expériences XRD supplémentaires qui pourraient aider à tester ces conclusions contradictoires et devraient permettre de mieux comprendre l'ordre de charge dans YBCO.

Ordre magnétique dans $La_{2-x}Sr_xCuO_4$ sous champ magnétique intense

Nos avons effectué des mesures du taux de relaxation spin-réseau $1/T_1$ des noyaux de ^{139}La dans $La_{2-x}Sr_xCuO_4$ (LSCO) pour des dopages $0.148 \leq p \leq 0.21$. Ces mesures démontrent que le champ magnétique est capable d'induire un état magnétique gelé ou presque gelé jusqu'à des niveaux de dopage très élevés, c'est à dire jusqu'à la fontrière de la phase pseudogap à $p^* \simeq 0.18$.

Les données ont été analysées dans l'hypothèse d'un gel continu des spins (temps de corrélation divergeant exponentiellement à $T = 0$), à l'aide du modèle de Bloembergen-Purcell-Pound (BPP) dans lequel une distribution de temps de corrélation a été introduite. Un paramètre important de ce modèle est le champ fluctuant $h_\perp$, qui reflète l'intensité des moments magnétiques que l'on considère comme étant gelés à basse température et à l'échelle de temps de la RMN.

Au dopage $p = 0.148$, nous montrons que $h_\perp$ augmente considérablement en fonction du champ et qu'il finit par atteindre des valeurs comparables à celles mesurées dans LSCO $p = 0.12$ où l'ordre est déjà présent en champ nul (Fig. 1). Cette augmentation de $h_\perp$ se retrouve à plus haut dopage, jusqu'à $p = 0.171$, mais plus le dopage est fort plus le champ nécessaire pour l'observer est grand. Cependant, à $p = 0.21$, aucune preuve d'ordre AFM n'a été trouvée jusqu'à 45 T.

Ce résultat suggère que des fluctuations lentes des spins pourraient conduire à une reconstruction de la surface de Fermi, ce qui a des implications pour les mesures de transport en champ intense qui observent un changement du nombre de porteurs de charge au dopage critique de la phase $p^* = 0.18$. Le champ magnétique pourrait donc affecter le résultat des mesures de transport.

Quant à l'extrapolation de ces résultats en champ nul, qui est un des aspects importants de ce travail, nos mesures ne permettent pas totalement de trancher entre deux scénarios : soit les moments sont déjà gelés en champ nul mais sont difficilement détectables en raison d'une très faible amplitude et d'une inhomogénéité spatiale très forte (auquel cas le champ magnétique, en augmentant l'amplitude des moments, ne fait que révéler l'état fondamental à $B = 0$), soit les moments sont réellement fluctuants et leur moyenne temporelle est nulle à $B = 0$ (auquel cas, le champ induit une transition et les résultats à haut champ ne sont pas directement représentatifs de l'état fondamental à $B = 0$). À partir des données existantes de diffusion des neutrons, *e.g.* Lake *et al.* [8] à $p = 0.163$, il est difficile d'exclure un moment de faible amplitude en champ nul, peut-être à des temperature inférieures à celles étudiées jusqu'à présent. Une des questions soulevées par notre travail est donc de savoir si l'ordre induit par le champ ou même en champ nul est suffisamment puissant pour reconstruire la surface de Fermi.

Conclusion et perspectives

Dans l'étude des cuprates, Il est souvent apparu que l'application du haut champ permettait de découvrir un phénomène qui serait ultérieurement identifié comme une propriété existant déjà en champ nul. Par exemple, les mesures de microscopie par effet tunnel (STM) de Hoffman *et al.* [11] ont révélé une modulation périodique de la densité d'état locale (LDOS) dans $Bi_2Sr_2CaCu_2O_{8+\delta}$, qui a ensuite été découverte en champ nul par d'autres groupes, notamment par Howald *et al.* [12]. De même, la découverte initiale par RMN de l'ordre charge à longue portée induite par le champ dans YBCO par

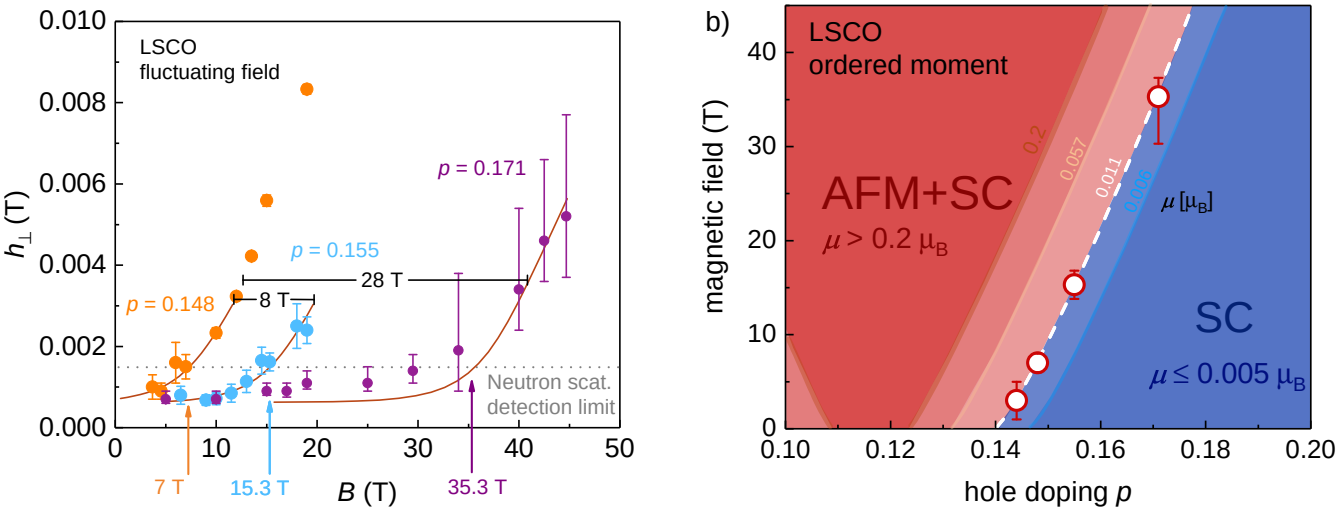

Figure 5: a): Comparaison des champs fluctuants pour LSCO $p = 0.148$, $p = 0.155$ & $p = 0.171$. Les lignes continues sont des guides à l'œil identiques, décalés horizontalement d'environ 8 T et 28 T. À partir de la RMN, il n'y a pas de champ d'onset pour $h_\perp$, mais lors de la diffusion de neutrons par Chang *et al.* dans leur échantillon $p = 0.145$, un moment supérieur à 7 T est détecté [9]. Dans $p = 0.148$, à 7 T, nous trouvons $h_\perp = 0.0015$ T, nous utilisons donc cette valeur pour définir l'échelle du champ correspondant pour $p = 0.155$ et $p = 0.171$. C'est le point, marqué par une flèche, où le guide à l'œil traverse la ligne pointillée horizontale. b): Représentation graphique du moment ordonné μ dans un diagramme de phase en fonction du dopage et du champ externe, basé uniquement sur les données dans LSCO. Les cercles blancs correspondent au champ d'onset à 3 T à $p = 0.144$, selon Khaykovich *et al.* [10], et à la échelle de champ où $h_\perp(B)$ augmente au-dessus de ≈ 1.5 mT dans la figure à gauche (correspondant au moment ordonné $\boldsymbol{\mu} > 0.011\,\mu_B$ en diffusion neutronique). Les points expérimentaux sont reliés par une ligne pointillée blanche. Dans cette plage de dopage, la supraconductivité s'étend jusqu'à environ 50-60 T. La région rouge foncé correspond à $h_\perp(B) > 0.026$ T (correspondant à $\boldsymbol{\mu} > 0.2\,\mu_B$). Les couleurs rouge clair correspondent à des moments plus petits.

Wu *et al.* [13] a précédé la découverte d'un ordre de charge à courte portée en champ nul à l'aide de la diffusion des rayons X [14, 15]. Dans ces exemples, les halos de vortex induits par le champ peuvent être vus comme des loupes qui amplifient les ordres électroniques à courte portée que l'on peut sinon rater facilement. Reste à savoir si cela est également le cas pour l'ordre de spin dans LSCO proche de la limite de la phase pseudogap.

Au niveau des perspectives, notre travail devrait maintenant être étendu dans deux directions opposées mais complémentaires: des études en champ nul (ou bas champ) et des études en champ encore plus élevé. L'extension vers les champs pulsés jusqu'à 100 T est évidente, car les champs pulsés ont été essentiels pour découvrir la reconstruction de la surface de Fermi dans YBCO [16], système modèle (car très peu désordonné) mais qui possèdent des champs critiques supraconducteurs 2 à 3 fois plus élevés que LSCO. Pour ce qui est des expériences de RMN, cette direction est bien entendu extrêmement difficile (mais peut-être possible). Dans la limite opposée des bas champs, on s'attend à des longueurs de corrélation (de spin et/ou de charge) plus courtes et un caractère de plus en plus fluctuant de ces corrélations, rendant les signatures expérimentales plus élusives. Néanmoins, cette limite est tout autant importante puisque l'on sait que les fluctuations AFM, voire de charge, peuvent conduire à un appariement de Cooper.

Dans tous les cas, nos mesures démontrent que la supraconductivité, en réduisant drastiquement l'amplitude des moments fluctuants, a un effet très fort sur le magnétisme à basse énergie dans l'état pseudogap. L'ordre magnétique induit par le champ est intéressant en soi, car son amplitude et (probablement) sa longueur de corrélation étant plus grandes, il est moins impacté par les effets de désordre et donc s'approche de l'ordre "idéal", tel qu'accessible par des modèles théoriques et numériques.

Introduction

Thirty years after the discovery of cuprate high temperature superconductors the experimental and theoretical effort to understand the mechanism behind their superconductivity still continues. Paradoxically, it seems as if this problem is getting harder with time since over the course of the past years cuprates have been found to possess more puzzling properties besides superconductivity that need to be explained: most notably the strange metal phase with a never saturating linear resistivity and the pseudogap, incorporating an ever increasing number of anomalies and electronic phases.
Two of these electronic phases are spin order and the more recently discovered charge order. Charge order strongly competes with superconductivity and the competition can be tuned by a large number of parameters including doping, temperature, magnetic field, hydrostatic and uniaxial pressure, disorder and even light [1]! In this thesis the effect of magnetic field and hydrostatic pressure on charge order has been investigated in $YBa_2Cu_3O_y$ (YBCO). NMR measurements of charge order and detailed analysis thereof are presented in chapter 3. While magnetic field suppresses superconductivity and eventually induces the long-range charge density wave (CDW), hydrostatic pressure increases T_c, both by now well established facts. It has been suggested by the work of Louis Taillefer's group that the increase of T_c might be due to the gradual suppression of the short-range CDW [2] and in this thesis supporting evidence from NMR measurements for this scenario is presented in chapter 4. However, the interpretations of existing electrical transport and X-ray diffraction (XRD) measurements are at odds with this scenario. Motivated by the apparent paradox we looked for an alternative way to describe transport, XRD and NMR data consistently. This could be confirmed or rejected by suggested additional XRD measurements.

Chapter 5 presents a seemingly unrelated phenomenon: Glassy spin freezing in $La_{2-x}Sr_xCuO_4$ (LSCO). The context of this work is the following: Recent high field transport measurements of LSCO in Louis Taillefer's group have been interpreted in terms of a sharp change in the number of carriers across the critical doping $p^* = 0.18$, the putative endpoint of the pseudogap phase [3]. Similar measurements have also been performed in YBCO [4]. A possible scenario that could explain the loss of carriers inside the pseudogap is anti-ferromagnetic order. However, no magnetic order is found in

either NMR, μSR or neutron scattering. Neutron scattering even finds total absence of low-energy spin fluctuations: there is a spin gap for $p \gtrsim 0.14$ in LSCO in zero field and in YBCO there is a spin gap for $p \gtrsim 0.08$. We show that in LSCO the spin-lattice relaxation rate $1/T_1$ in high magnetic fields up to 45 T is enhanced in a way that is consistent with glassy spin freezing for dopings up to $p = 0.171$ but not anymore at $p = 0.21$, so from our measurements we can conclude that there is a form of anti-ferromagnetic order that appears in a doping range that is consistent with the extent of the pseudogap. These measurements suggest that the loss of carriers in the pseudogap phase could either be the result of field-induced slowing down of anti-ferromagnetic spin fluctuations or spin fluctuations are already slowing down in zero field and magnetic field only enhances this tendency. Charge order could be relevant for this phenomenon as it is believed to cause freezing of spin fluctuations, thus creating a potential link between the two studies of this thesis.

Chapter 1

Introduction to the physics of cuprates: From the pseudogap to charge order

This chapter introduces concepts that are relevant to the cuprate superconductors. These involve the crystal and electronic structures of the parent compound and the doping mechanism. Doping leads to a large number of electronic phases which are discussed in short. The focus of this introduction is on charge order and the related phenomenon of stripes, since it is the properties of these phases which have been investigated in this thesis.

1.1 The parent compound

The parent compound of cuprates is an anti-ferromagnetic insulator. This is unexpected from the perspective of a band model. To see why, we can take, for example, La_2CuO_4 (LCO) and count nominal valences of the ions (*i.e.* La^{3+} & O^{2-}) which shows that Cu has the formal value 2+ and is in the $3d^9$-configuration, leading to one hole in the $3d$-orbital. LCO has a tetragonal crystal structure and its principal building block that is common to all cuprates is the CuO_2-plane, with four oxygens surrounding the Cu atom. In LCO, the planar and additional apical oxygens form an elongated octahedron arround the Cu-atom, see Fig. 1.1a. The crystal field lifts the degeneracy of the $3d$ orbitals into e_g & t_{2g}. As can be seen in Fig. 1.1b, the elongated form of the octahedron lowers the energy of the $3z^2 - r^2$ orbital, so a single electron (or hole) is expected to be in the $x^2 - y^2$ orbital. In a tight-binding band model this would lead to half-filled band and metallic behaviour.

It is Coulomb repulsion between holes carrying spin $S = 1/2$ in the $x^2 - y^2$ orbitals that leads to localisation and insulating behaviour. This process is well explained by the Hubbard model at half-filling, according to which holes can move in the CuO_2-plane due to a hopping term t but feel mutual

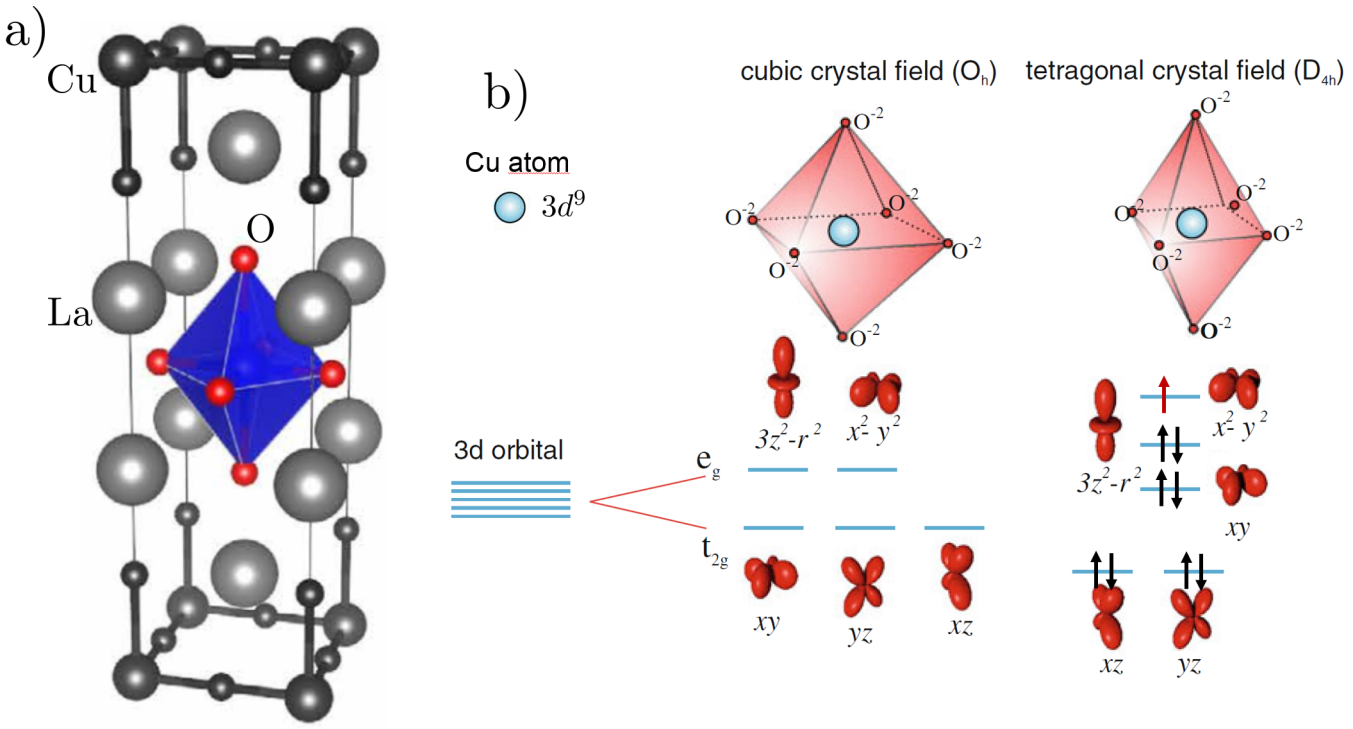

Figure 1.1: a): Crystal structure of La_2CuO_4 with the Cu-atom in the middle of an octahedron of oxygen atoms. b): Energy levels of $3d$ orbitals in a cubic and elongated tetragonal crystal field. Arrows indicate the filling with electrons for a $3d^9$ configuration. Fig. 1.1a is reproduced from ref. [17] and Fig. 1.1b is adapted from ref. [18].

repulsion with cost U when doubly occupying the same lattice site. The model Hamiltonian is

$$\hat{H}_{\text{Hubbard}} = -t \sum_{<j,j+1>,\sigma} (\hat{c}^{\dagger}_{j,\sigma}\hat{c}_{j+1,\sigma} + h.c.) + U \sum_{j} \hat{n}_{j\uparrow}\hat{n}_{j\downarrow} \,. \tag{1.1}$$

In case of half-filling, *i.e.* exactly one hole per site, and large U this leads to insulating behaviour, also called a Mott insulator. As holes stop to move, their kinetic energy becomes large[1]. However, the kinetic energy can be minimised if electrons (or holes) make virtual hops to neighbouring sites, provided that the spins order anti-ferromagnetically. The anti-ferromagnetic ordering is a necessary condition because the Pauli-principle allows doubly occupied sites only if the particles have opposite spin. The energy gain is $\frac{4t^2}{U} = J$ and J effectively becomes the anti-ferromagnetic coupling between neighbouring spins [19]. Hence, anti-ferromagnetism can be understood as a consequence of the Coulomb repulsion. In LCO, the exchange coupling J has been precisely determined from the spin-wave spectrum by neutron scattering [20]. A side-effect of the small spin is that the spin state is not exactly described by the classical Néel state. Quantum corrections consider that spins can be in a superposition of states and fluctuate [21]. Quantum corrections result in an ordered moment $\boldsymbol{\mu} = 0.6\,\mu_B$, *i.e.* smaller than μ_B, the full magnetic moment for $S = 1/2$ with gyromagnetic factor $g = 2$ [22].

The density of states for LCO and the effect of U opening a Hubbard gap on the density of states on Cu is shown in Fig. 1.2b. Experimentally, one finds a more complicated situation than described by the single $3d$ band Hubbard model because $2p$-orbitals of planar oxygen atoms are in the middle of the Hubbard gap so the experimentally measured gap is not U but a charge transfer gap Δ.

1.2 Doping the parent compound

1.2.1 Doping LSCO

LCO can be doped with holes by replacing La with Sr. Sr has a formal valence of 2+, so this replacement introduces holes in the CuO_2-plane[2] with p holes per CuO_2 unit for every Sr-fraction x in the unit cell. Holes can enter both $2p$-orbitals on oxygen as well as $3d$-orbitals on Cu. In fact, the hybridisation between Cu $3d$-orbitals and O $2p$-orbitals leads to a more complicated situation where the resulting density of states has a mixed character. See the left panel of Fig. 1.2 for a comparison between the optical response of LCO from experiment and theoretical bandstructure calculations. Analysis of the doping dependence led Uchida *et al.* [23] to conclude that the density of states of the parent compound is as shown in Fig. 1.2b, while doping leads to the formation of new in-gap states, as represented by Fig. 1.2e.

[1] This is analogous to a free particle with mass m in a 1D box of width L. Its (kinetic) energy is $E(n) = \frac{n^2h^2}{8mL^2}$, where n is the principal quantum number. Decreasing L increases the energy.

[2] Some parent compounds like Nd_2CuO_4 can be doped with electrons by substituting Nd^{2+} with Ce^{3+}.

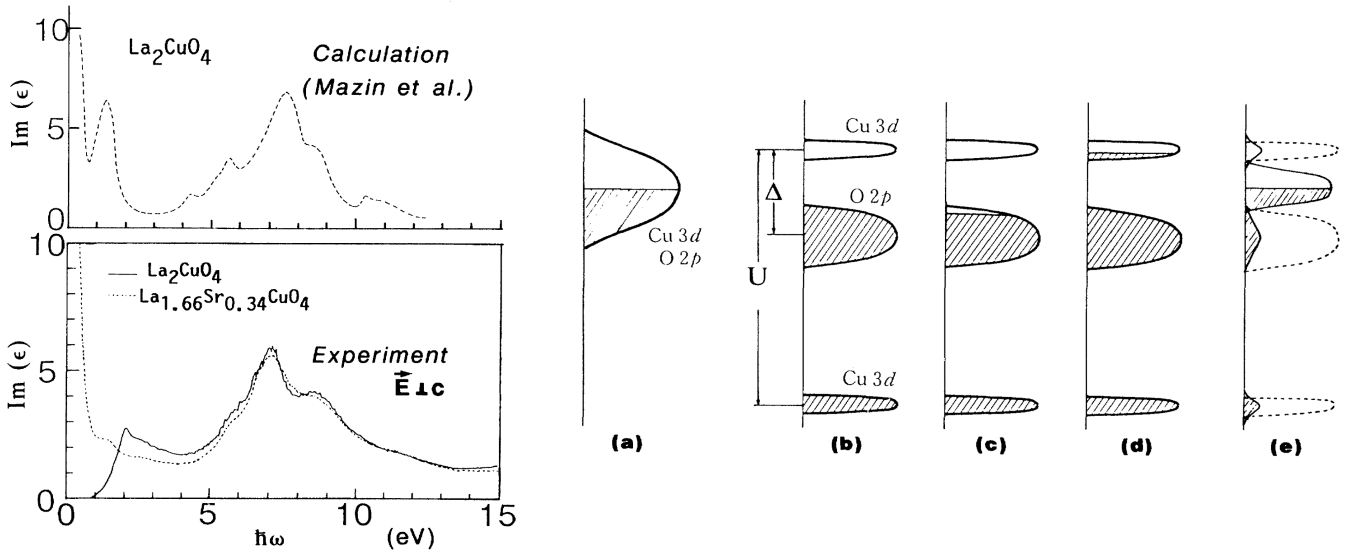

Figure 1.2: Left panel: Comparison of experimental and theoretical optical response (Im(ϵ) is the imaginary part of the dielectric function) for LCO where experimentally there is a gap of width 2 eV while band calculations predict metallic behaviour. Right panel: Different scenarios for the density of states: a) Metal (no gap). b) LCO with Hubbard gap U between the half-filled $3d^9$ band and a charge transfer gap between $2p$ band and unoccupied upper Hubbard gap. c) & d) show the effects of hole and electron doping, respectively, provided the form of the band is unaffected by doping. e) More realistic scenario where doping leads to in-gap states of mixed character between Cu and oxygen orbitals. Figures are reproduced from ref. [23].

1.2.2 Doping YBCO

$YBa_2Cu_3O_y$ (YBCO) is a related cuprate that can be doped with holes by increasing the oxygen content from $y = 6$ to $y = 7$ [3]. The crystal structure is shown in Fig. 1.3.

The oxygen concentration can be varied continuously while oxygen atoms in the chain layers can form periodic chain structures for x $\leq$ 0.35 that are named O-I, O-II, O-III, O-V, O-VIII etc., indicating the period of the chain ordering along the ***a***-axis [24], see Fig. 3.9 for examples of O-II and O-VIII orderings. Highly ordered O-II samples have very little disorder leading to very sharp lines in NMR spectra, an essential requirement for the analysis performed in chapter 3 of this manuscript.

However, the chain layer leads also to a number of problems: Increasing oxygen concentration translates in a non-linear fashion into effective hole doping p since additional oxygen will draw charge both from Cu-atoms in the chain layer itself as well as from the CuO_2-bi-layer [25]. This leads to uncertainty about the actual carrier density and results in different groups using different calibrations to determine the hole doping of their samples. Another problem that results from the mixed valence of Cu in the chain-layer is that it can develop metallic behaviour on its own: This makes it difficult to interpret in-plane resistivity measurements [26] and can lead to peculiar charge modulation phenomena

[3] Additional hole doping can be achieved by replacing Y^{3+} by Ca^{2+}.

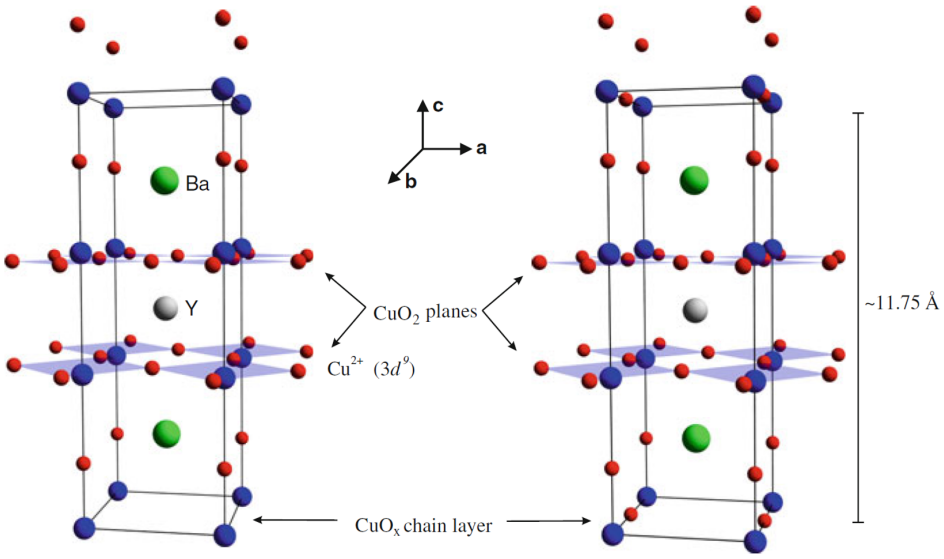

Figure 1.3: The crystal structure of $YBa_2Cu_3O_y$ for $y = 6$ and $y = 7$. YBCO has a double CuO_2-layer with apical oxygen above the planar Cu(2). The difference between left and right is that the basal CuO_x-layer contains no oxygen (x=0) for $y = 6$ and one oxygen (x=1) for $y = 6 + x = 7$ leading to full CuO-chains running along the ***b***-axis.

for which STM and NMR find evidence [27, 28], so the CuO_x-layer can potentially affect phenomena that originate in the CuO_2-planes [29].

These aspects show that the real physical system is more complicated than the simple Hubbard model. However, the doped Hubbard model, away from half-filling, is, within its limitations, able to capture a substantial part of the cuprate physics.

1.3 Phase diagram of cuprates

What follows is a brief discussion of different phases that appear in hole doped cuprates. The case of electron doping is not explicitly discussed, although many aspects of hole and electron doping are analogous. For a review of electron doped cuprates see ref. [30].

1.3.1 Fermi liquid at large p

On an intuitive level it is clear that increasing the number of holes will eventually lead to a metallic state because doping of holes reduces the number of spins. Naively speaking, after the replacement of a large fraction of the spins only few particles will remain that should be able to move rather freely. In fact, in the high doping limit, cuprates are Fermi liquids, as can be seen from a large hole-like Fermi surface inferred from ARPES and transport measurements in $Tl_2Ba_2CuO_{6+\delta}$ (Tl2201) [31, 32], including a large frequency in quantum oscillations that translates into a carrier density $n = 1 + p$ holes per CuO_2 unit [33], see Fig. 1.4. However, in the doping range where samples are still supercon-

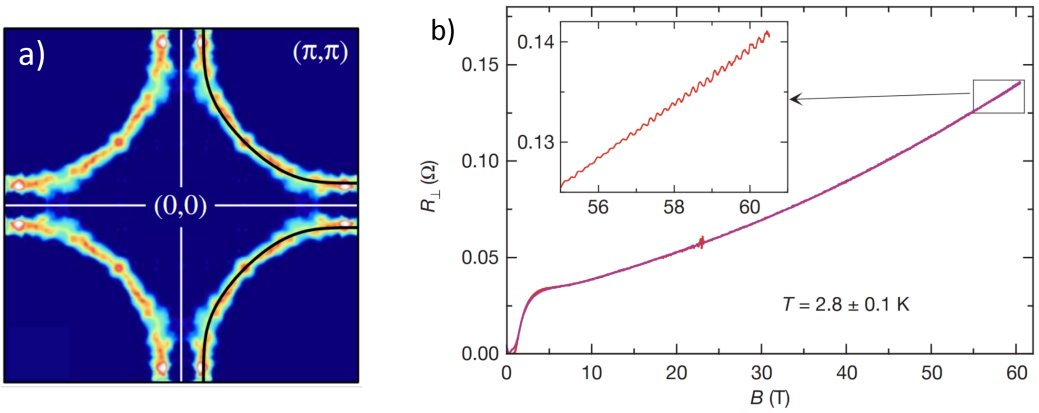

Figure 1.4: a): Fermi-surface of Tl2201 ($T_c = 30$ K & $p \approx 0.26$) measured by ARPES at $T = 10$ K, reproduced from ref. [34]. b): Quantum oscillations of $\boldsymbol{c}$-axis resistivity of Tl2201 ($T_c = 10$ K & $p = 0.30$) at $T = 2.8$ K, reproduced from ref. [34].

ductors, the properties are not those of a simple metal, since measured effective masses are enhanced ($m^* = 4.1 \pm 1.0\ m_e$ in Tl2201 at $p = 0.3$ [33]) which signals the effect of remaining electronic correlations.

In the intermediate doping range a rich variety of electronic phases is realised that can be summarised in a p-T phase diagram, as shown in Fig. 1.5.

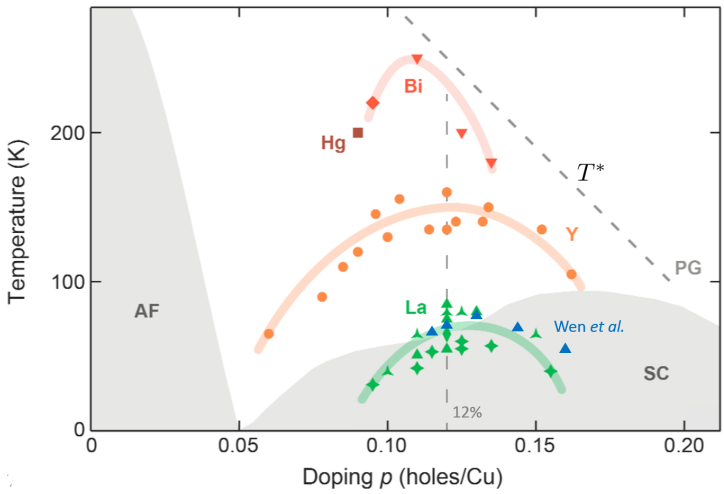

Figure 1.5: Schematic phase diagram of cuprates, based on YBCO, including the long-range antiferromagnetic phase (AF), superconductivity (SC) and the pseudogap (PG), whose upper boundary is indicated by a tilted dashed line. Experimental data for the short-range CDW of different hole doped cuprates is shown in colour. Red and brown symbols stand for Bi-based and Hg-based cuprates, respectively. Yellow circles (Y) stand for YBCO, green symbols belong to different La-based cuprates (LNSCO, LBCO, LESCO and LSCO). This figure is adapted from ref. [5] from 2016, so the recent LSCO data of Wen *et al.* [6] has been included as blue triangles.

1.3.2 AFM insulator

At low doping, cuprates remain insulating and anti-ferromagnetic (AFM) as the parent compound. The AFM long-range order is rapidly destroyed but an anti-ferromagnetically correlated spin-glass can extend into the superconducting phase at low T. A detailed discussion can be found in the beginning of chapter 5.

1.3.3 Superconductivity

Cuprates become superconductors upon doping. The superconducting T_c has a similar, approximately parabolic dependence, peaked near $p = 0.16$ in all cuprates[4], as has been characterised by Tallon *et al.* [35]:

$$T_\mathrm{c}(p)/T_{\mathrm{c,\,max}} = 1 - 82.6\,(p - 0.16)^2 \qquad \textit{Tallon's law} \tag{1.2}$$

The dome-shaped superconducting phase is generic to all cuprate families but $T_{\mathrm{c,\,max}}$ varies a lot: For $Bi_2Sr_{2-x}La_xCuO_6$ (La-Bi2201) $T_{\mathrm{c,\,max}} = 32$ K while Tl2201 has $T_{\mathrm{c,\,max}} = 90$ K, both having a single CuO_2-layer[5]. Actually, T_c can deviate more or less strongly from the parabolic dependence around $p = 0.12$. From Fig. 1.5 one can see that this doping coincides with the maximum of the short-range CDW phase which is discussed after the pseudogap.

Superconductors are characterised by two characteristic length scales: The London penetration depth λ_L, which is a measure of the length scale over which external fields are screened by superconducting currents and the coherence length ξ, which gives the order of magnitude for the size of Cooper pairs. When λ_L/ξ is large, then one speaks of type-II superconductors that remain superconducting even when subjected to high magnetic fields by allowing magnetic flux to enter through vortices. From mean-field BCS theory one expects SC to survive up to the critical field

$$\mu_0 H_{c2} = \frac{\Phi_0}{2\pi\xi^2}, \qquad \text{where } \Phi_0 = h/2e \text{ is the Flux quantum.} \tag{1.3}$$

Cuprates are extreme type-II superconductors: The $\boldsymbol{c}$-axis coherence length, ξ_c, can be smaller than the lattice spacing ($\xi_c \approx 1$ Å [37]), so the critical field can be enormous when the external field is applied parallel to the CuO_2-plane. $\xi_{ab} \sim 20$ Åis larger, still leading to very large H_{c2} for fields perpendicular to the plane [37, 38]. However, due to the small coherence length, the superconducting state is not well described by standard mean-field BCS theory. Experimentally, it is found that the superconducting order parameter $\Delta(\boldsymbol{k})$ (the gap) has predominantly d-wave orbital symmetry which implies that the pairing interaction is not isotropic [39]. d-wave pairing can result directly from electronic interactions (see, *e.g.*, refs. [40] or [41]).

[4] Conventionally, the doping range is divided into *underdoped* ($0 < p \lesssim 0.16$) and *overdoped* ($0.16 \lesssim p$) while $p \sim 0.16$ is called *optimally doped*.

[5] Generally, $T_{\mathrm{c,\,max}}$ increases within the same family if the unit cell contains multiple CuO_2-layers [36].

1.3.4 Pseudogap

NMR has played an important role in identifying the anomalous electronic properties in the pseudogap phase: After initial indications for gapped spin-excitations above the superconducting T_c from relaxation rate ($1/T_1$) measurements of Imai *et al.* [42] and Warren *et al.* [43], the doping dependence of the pseudogap was properly characterised using ^{89}Y-Knight shift measurements by Alloul *et al.* [44]. It was found that the spin susceptibility decreases gradually (see Fig. 1.6a), so from the NMR perspective T^*, the temperature indicated by the tilted dashed line in Fig. 1.5, appears to mark a crossover, not a phase transition.

The pseudogap phase has two principal characteristics: Firstly, for $T < T^*$, the density of states and the spectral weight is found to decrease gradually [45, 46, 47, 48] and secondly, rotational and/or time-reversal symmetries appear to be broken [49, 50, 51, 52, 53, 54]. Above T^* the electrical resistivity is linear in T, so an important characteristic of the pseudogap is the departure from linear resistivity [55].

Understanding the mechanism behind the pseudogap is made difficult through the mixed character of the electronic (spin and charge) excitations: The pseudogap inherits the strong interactions that lead to insulating behaviour in the parent compound but doping introduces an increasing amount of carriers that can neither be gapped in the same way as in the case of half-filling nor be regarded as free charge carriers. The nature of the resulting electronic excitations and the degree to which these contribute to the Knight shift and the relaxation rate is currently not understood. According to Lee *et al.*, the decrease of the spin susceptibility, as found in Knight shift measurements of Alloul *et al.* or magnetisation measurements of Nakano *et al.* in LSCO [56] could come from singlet correlations that are similar in nature to the quantum corrections that lead to a reduced ordered moment of the parent compound, as previously discussed [19]. In the superconducting state, the spin state of Cooper pairs is a singlet, so from the Knight shift it is difficult to distinguish the pseudogap and the superconducting gap below T_c. Hence, high magnetic fields are helpful to suppress superconductivity to see the effect of the pseudogap down to low T.

1.4 Various forms of charge order

Within the pseudogap, spin and charge modulations have been discovered at $T < T^*$. While in La-based cuprates spin and charge modualtions appear to be coupled, most other cuprate families seem to be less susceptible to spin ordering whereas charge order has become a universal of cuprates, as is shown in the following.

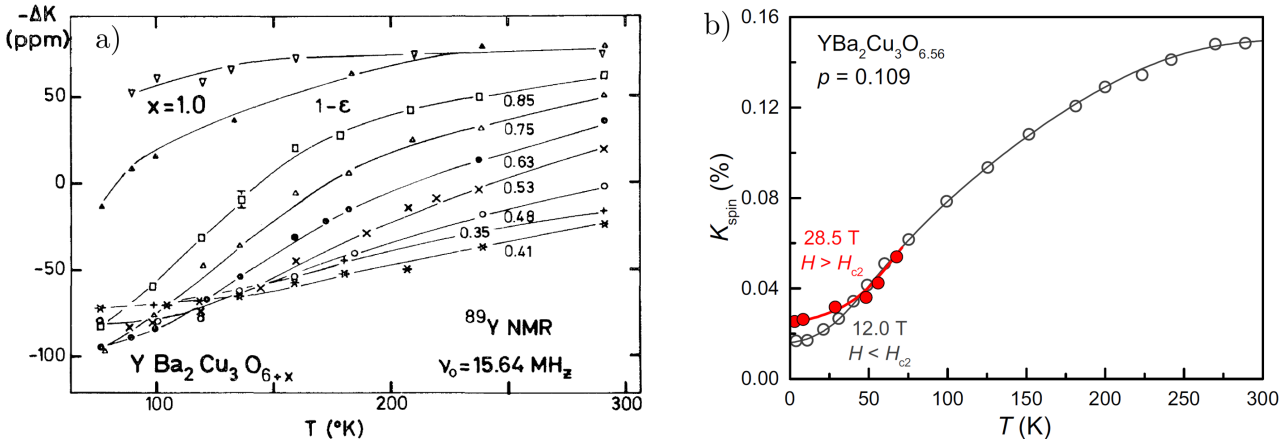

Figure 1.6: a): T-dependence of ^{89}Y-Knight shift in YBCO, showing the gradual decrease of the spin susceptibility. The shift is negative because of the sign of the hyperfine coupling constant. The figure is reproduced from ref. [44]. b): T-dependence of ^{17}O-Knight shift in YBCO $p = 0.109$ at 12 T $< \mu_0 H_{c2}$ and 28.5 T $> \mu_0 H_{c2}$. The figure is part of ref. [57].

1.4.1 Stripe phase in La-based cuprates

Stripes are joint modulations of spin and charge density with collinear wave vectors. Stripes were first predicted for a doped Hubbard model in a mean-field treatment by Zaanen and Gunnarson [58][6]. Their calculations predicted a smooth modulation of charge, see Fig. 1.7a. The experimental confirmation of stripes came first in nickelates ($La_{2-x}NiO_{4+\delta}$), an isostructural compound to cuprates, which remains insulating when doped. Stripes were discovered by transmission electron microscopy (TEM) [60] and subsequently characterised by neutron scattering [61]. Using neutron scattering, stripes were also found in Nd-codoped LSCO, $La_{2-x-y}Nd_ySr_xCuO_{4+\delta}$ (LNSCO) [62]. Tranquada *et al.* showed that the wave vector of the charge super-lattice peaks $\pm\delta_{\text{charge}}$ is twice as large as the corresponding wave vector $\pm\delta_{\text{spin}}$, giving $\delta_{\text{charge}} = 2\delta_{\text{spin}}$, see Fig. 1.7c. In neutron scattering the charge modulation cannot be measured directly and was inferred from the displacements of the lattice Bragg spots. Subsequent XRD measurements of $La_{1.6-x}Nd_{0.4}Sr_xCuO_4$ with x = 0.12 confirmed the slightly incommensurate $\pm\delta_{\text{charge}} = \pm 0.236$ [63]. AFM correlations were also discovered in LSCO at finite energy in a large doping range[7] early on [64, 65] but the discovery of a charge density modulation followed only much later by XRD measurements of Croft *et al.* [66] and very recently by Wen *et al.* [6], see Fig. 1.5.

When comparing LSCO with LNSCO one should be careful because co-doping of Nd leads to a slightly different structure at low T, the *low temperature tetragonal* (*LTT*) phase which appears to favour stripes. At low T, $La_{2-x}Ba_xCuO_4$ (LBCO) for x close to x = 0.12 is also in the *LTT* phase and develops stripes as can be seen in Fig. 1.8a. One can see that superconductivity is strongly suppressed around

[6] Similar work by Poilblanc and Rice based on the doped $t-J$ model was reported shortly thereafter [59] and showed the condition $\delta_{\text{charge}} = 2\delta_{\text{spin}}$ more clearly.

[7] Long-range magnetic order at low T is only seen in a reduced doping range $p \lesssim 0.14$.

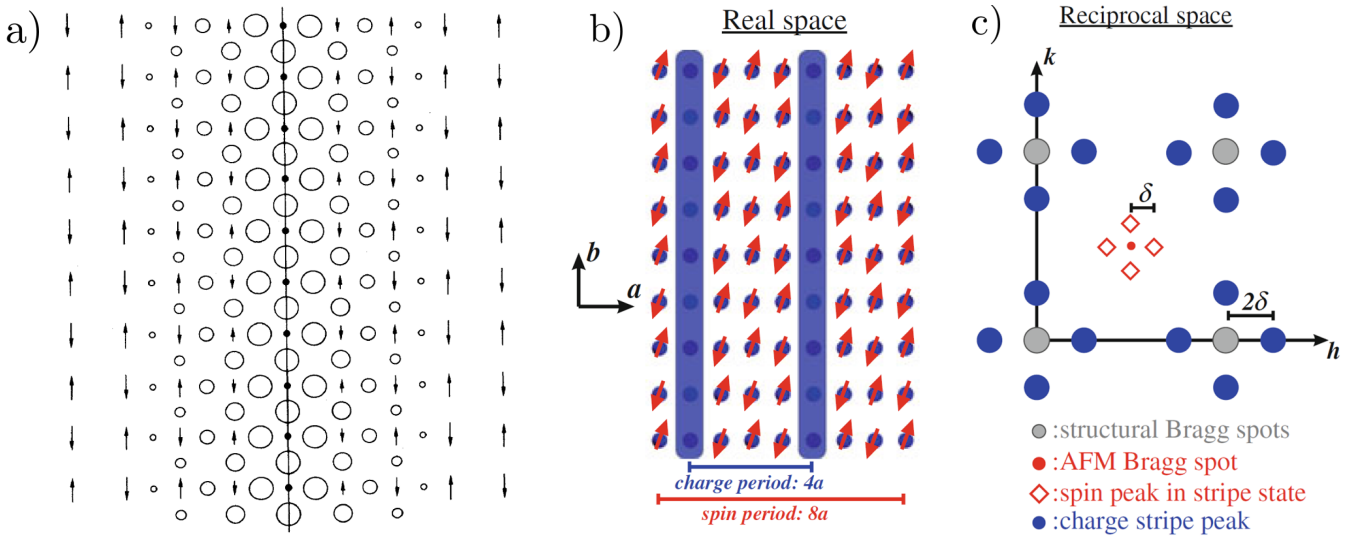

Figure 1.7: a): The uniaxial stripe which results from mean-field calculations of Zaanen and Gunnarson [58]. The figure is reproduced from ref. [58]. b): Schematic real space image of the charge and spin pattern found by Tranquada *et al.* in $La_{1.6-x}Nd_{0.4}Sr_xCuO_4$ with x = 0.12. Holes form periodic boundaries between AFM domains. (Idealised picture for $x = 1/8$.) Note that in this picture the holes do not extend into the AFM domains. c): Schematic diffraction pattern found by neutron scattering. Stripes exists along h and k, leading to four peaks shifted by $\pm\delta_{\text{charge}}$ and $\pm\delta_{\text{spin}}$ because stripes are rotated by 90° between neighbouring planes [63]. Figures b) & c) are reproduced from ref. [18].

x = 0.12, much stronger than in LSCO. From Fig. 1.8a it appears that the charge modulation found below T_{CO} is a direct consequence of the *LTT* structure. However, by applying hydrostatic pressure the *LTT* distortion can be suppressed by 1.85 GPa while the stripe order remains, see Fig. 1.8b. Interestingly, the suppressed T_c is partially, but not yet completely recovered with the application of 15 GPa. This behaviour appears to be similar to the increased T_c of YBCO under hydrostatic pressure, where at $p \approx 0.117$, T_c increases from 64 K to 105 K upon application of an equal pressure of 15 GPa [70]. This is the topic of chapter 4.

Magnetic field effects

Neutron scattering measurements by Lake *et al.* in LSCO have shown that magnetic order can be enhanced using magnetic fields at dopings where it exists in zero field [71]. At higher dopings a spin gap prevents magnetic order but magnetic field enhances slow fluctuations inside the gap [8]. In an intermediate doping range $p \sim 0.145$ it has even been shown by others that quasi-static order can be induced with field [10, 9]. In the early measurements by Lake *et al.* the field-induced magnetic signal has been interpreted to originate from regions surrounding vortex cores, in which SC is suppressed. Since the anti-ferromagnetic correlation length deduced from the AFM peaks is larger than the vortex cores, halos of AFM correlations are thought to surround the cores. This picture of halos that are nucleated

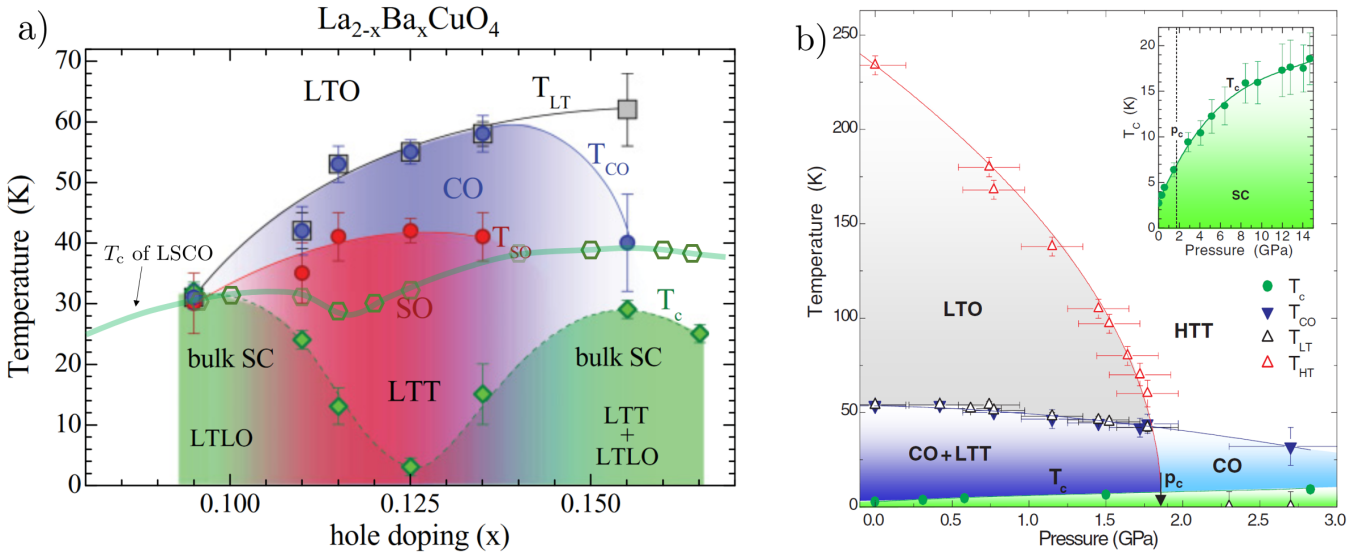

Figure 1.8: a): T-doping phase diagram of LBCO at ambient pressure. Close to x = 0.12 charge order appears below T_{CO} which coincides with T_{LTT}. At lower T stripe order SO (red phase) sets in while SC is strongly suppressed. For comparison the T_c of LSCO [67] is shown as empty green hexagons. The figure is adapted from ref. [68]. b): T-pressure phase diagram of LBCO at x = 0.12 showing the suppression of the LTO and LTT phases at $p_c = 1.85$ GPa. Charge order survives above p_c. Inset: Pressure dependence of T_c. Figure is reproduced from ref. [69].

inside vortex cores is supported by NMR measurements of Mitrovic *et al.* in nearly optimally doped YBCO [72] and has been very influential in the interpretation of field-induced order in the SC state of cuprates found by STM [11] and more recently by NMR [73].

1.4.2 Charge density waves by STM

In 2002, scanning tunneling microscopy (STM) in magnetic field by Hoffman *et al.* [11] showed evidence of periodic modulations of the local density of states LDOS=LDOS($\boldsymbol{r}, E$) in $Bi_2Sr_2CaCu_2O_{8+\delta}$ close to optimal doping. To reveal the LDOS modulation Hoffman *et al.* subtracted the STM data at 0 T data from data at 5 T. Round halos of the modulation appeared around SC vortices, see Fig. 1.9. Subsequent STM measurements of Howald *et al.* [12, 74] and Vershininet al. [75] confirmed the existence of the LDOS modulation in zero field.

To determine the wave vector of the modulation, the real-space STM topograph can be Fourier transformed, as shown in Fig. 1.10b from the study of Howald *et al.* [74]. In the raw data (see Fig. 1.10a) the modulation is not visible, however, after filtering away spurious contributions due to quenched disorder and the incommensurate supermodulation of the BiO surface, a 2D pattern of uniaxial character in the LDOS becomes evident. If integrated over energy E (or voltage V), the LDOS corresponds to the electronic charge density at position $\boldsymbol{r}$. Thus, as long as the modulation of the LDOS is energy-

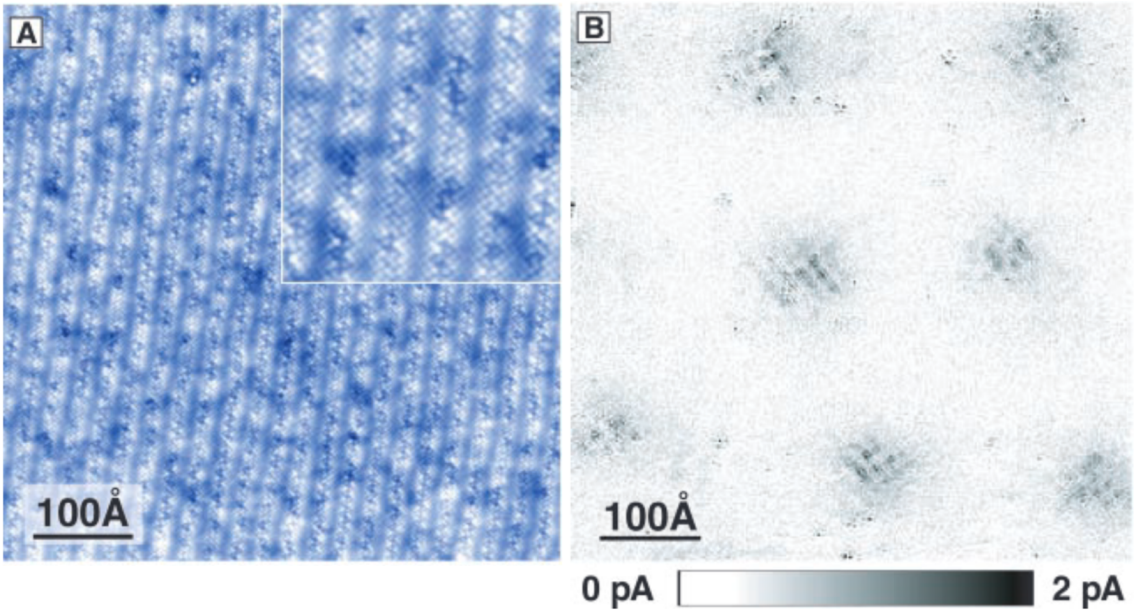

Figure 1.9: a): Raw STM topograph of Bi2212 ($T_c = 89$ K) with atomic resolution at low T. b): STM data at B =5 T with 0 T data having been subtracted reveals halos with an approximately $4a_0$-modulated checkerboard pattern in the (V-integrated) LDOS. The halos are centered around vortices. This figure is reproduced from ref. [11].

independent (non-dispersive[8]), it is likely to result from a modulation of the charge density [78]. As can be seen from Fig. 1.10d, Howald *et al.* have confirmed that the modulation close to $q = 0.25\,2\pi/a_0$ (corresponding to a commensurate period of $4a_0$) is only weakly energy dependent and concluded that the LDOS modulation is due to stripes, similar to those found in La-based cuprates discussed in the previous section [12].

In the following years, similar modulations were found in Bi2212 at lower dopings [79] as well as in Bi2201 [80] and Na-doped $Ca_2CuO_2Cl_2$ [81], indicating that this phenomenon might be universal. STM studies in Bi2212 suggested that the LDOS modulation might be related to the pseudogap, since the signature of fluctuating stripes diappeared above T^* [82]. STM measurements have been influential for studies of other cuprate families. Especially the very first experiment of Hoffman *et al.* [11] has been a motivation for subsequent high field studies.

1.4.3 Charge order in YBCO

Transport measurements in high fields of Louis Tallefer's group have played a vital role in the discovery of charge order in YBCO. In high fields up to 62 T the Hall number R_H or equivalently R_{xy} of a YBCO sample with $p \approx 0.10$ develops a negative sign and slow quantum oscillations [16], as shown

[8] Dispersive modulations of the LDOS can result from quasiparticle interference (QPI) due to impurities. Studies of the dispersion of the interference patterns give information about the Fermi-surface. [76, 77]

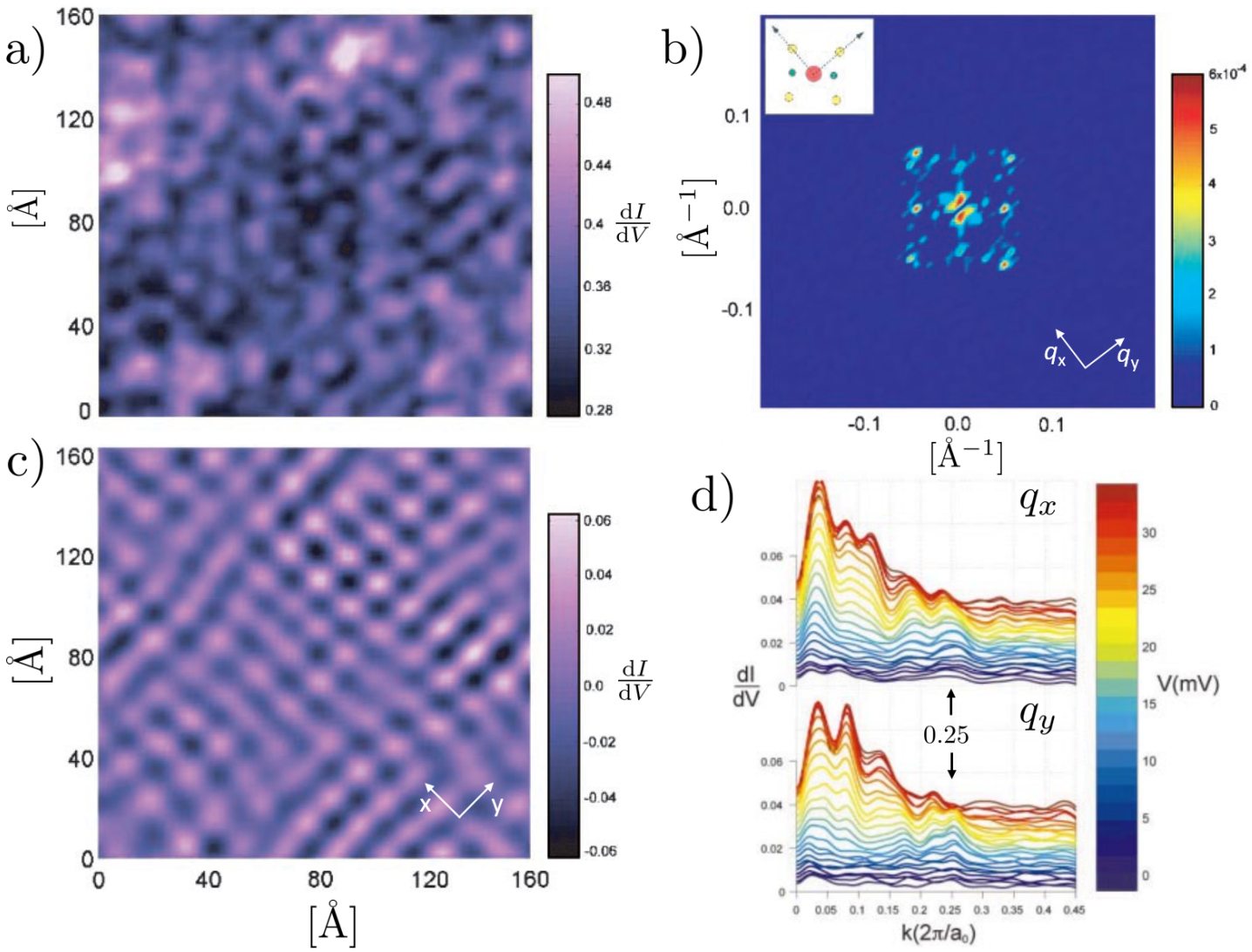

Figure 1.10: a): Raw STM topograph of Bi2212 ($T_c = 90$ K) for $V = 15$ mV at $T = 8$ K. $\frac{dI}{dV}$ is proportional to the LDOS. b): Fourier transform of a), giving three contributions (as sketched in the inset): intensity in the center is due to quenched disorder (red circle), horizontal dots (green circles) result from the incommensurate supermodulation of the BiO surface and four peaks at $(\pm\pi, 0)$ and $(0, \pm\pi)$ are due to the LDOS modulation. c): STM topograph from a) after filtering out the disorder at small q and the supermodulation. The LDOS modulation with period of $4a_0$ becomes evident. Fig. a)-c) are adapted from ref. [74]. d): Line cuts along q_x and q_y show only weakly dispersive peak close to $q = 0.25\, 2\pi/a_0$. This figure is adapted from ref. [12].

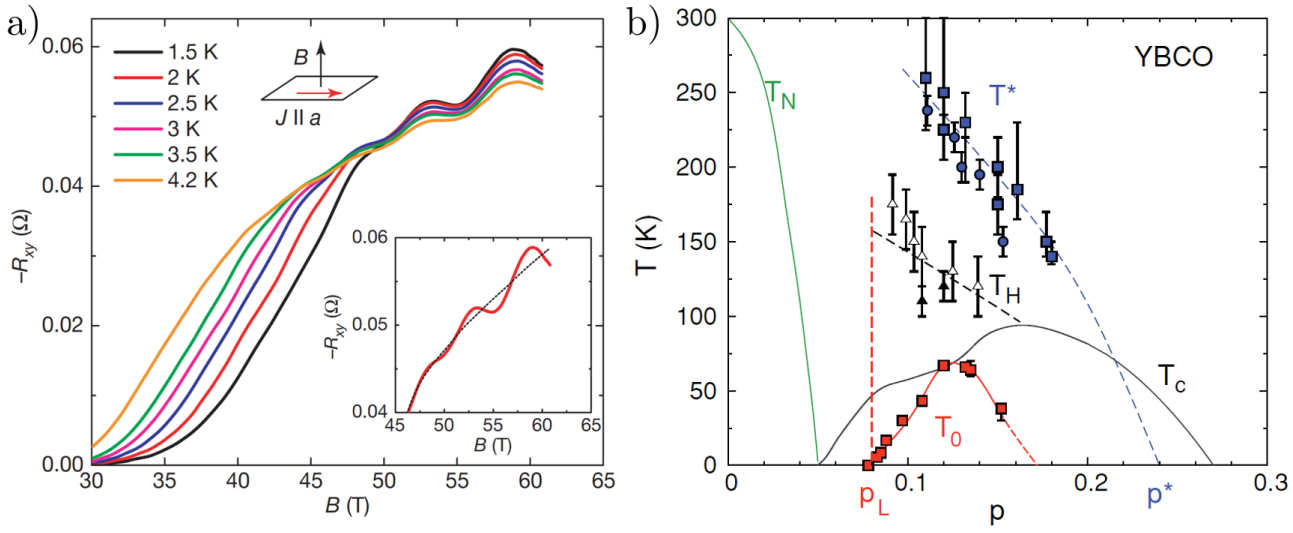

Figure 1.11: a): Slow quantum oscillations in the Hall number $R_{xy} = R_H$ for YBCO with $p \approx 0.10$. The figure is reproduced from ref. [16]. b): T-doping phase diagram of YBCO showing the pseudogap temperature T^*, as determined from resistivity and the in-plane anisotropy of the Nernst effect [53], T_H, below which R_H starts to decrease and T_0, below which R_H becomes negative.

in Fig. 1.11a. This is evidence for an electron pocket of small size, very unexpected for a hole-doped cuprate with a hole-like Fermi-surface. Subsequent Hall effect measurements by LeBoeuf *et al.* over a large doping range showed that R_H starts to decrease already at a rather high temperature T_H and becomes negative at a temperature T_0, that forms a dome that is centered at $p \approx 0.12$ [83]. The doping range in which R_H is negative in high fields is coincident with the doping range where T_c has an anomalous plateau and deviates from the parabolic form expected from eq. 1.2.

It is the small electron pocket which implies a Fermi-surface reconstruction, that forms the context in which NMR set out to search for signatures of stripe order in high fields. Wu *et al.* did indeed find charge stripes, as evidenced by a field-induced splitting in the ^{63}Cu-NMR quadrupole satellite spectrum (see Fig. 1.12a)& c)), however, there was no sign of magnetic order down to low T (see Fig. 1.12d), in fields that completely suppress superconductivity of the studied YBCO samples ($p = 0.104$ & $p = 0.12$) [13].

This discovery was followed by a large number of XRD studies in zero magnetic field, the first being by Ghiringhelli *et al.* [14], which have found that a short-ranged, incommensurate CDW modulation already exists along both $\boldsymbol{a}$ and $\boldsymbol{b}$-axes, appearing already at $T_{CDW} \sim 150$ K, see Fig. 1.13. The peak at T_c in the T-dependence of the XRD signal intensity shows that the CDW and SC are competing. This has been confirmed by XRD measurements in magnetic field by Chang *et al.* [15], also shown in chapter 3, Fig. 3.13b. The wave vector, reproduced in Fig. 1.13d) shows that the wave vector is found to lie close to q =0.31, rather different from LBCO and Eu-codoped LSCO in the stripe phase. The doping dependence of the wave vector in YBCO has been interpreted as evidence that CDW

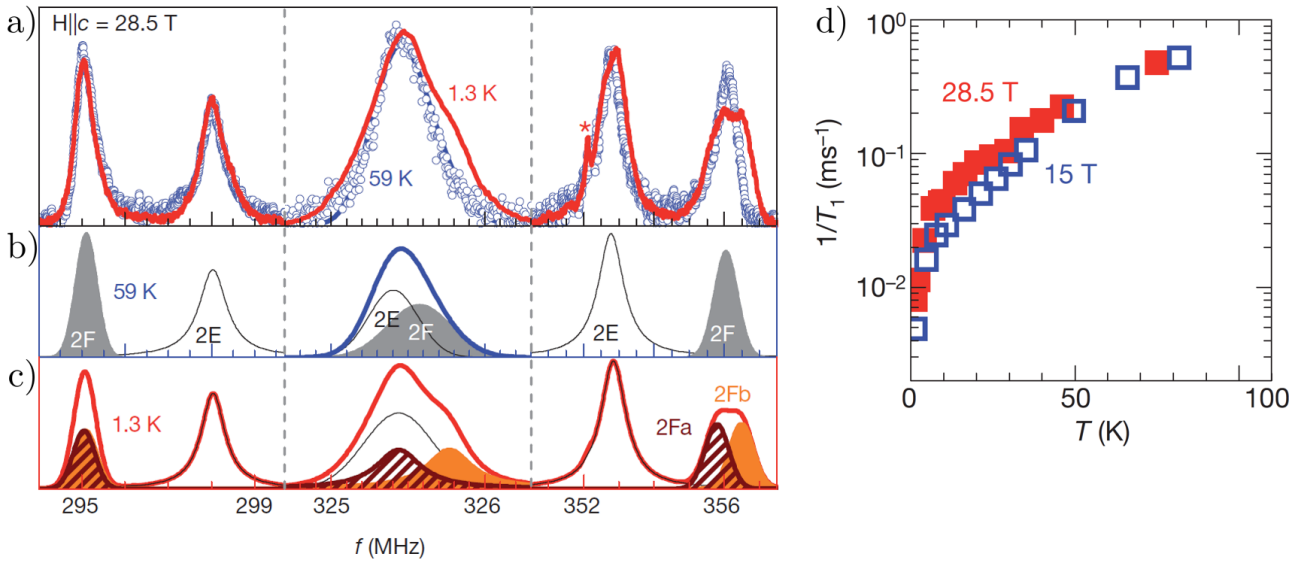

Figure 1.12: a)-c): High field ^{63}Cu-NMR spectra of YBCO with $p = 0.108$. The data at 59 K ($T > T_{\text{onset}}$) and at 1.3 K ($T > T_{\text{onset}}$) is shown in a) with fits of the 59 K spectrum in b) and fits of the low T spectrum in c). The Cu(2F) high frequency satellite belonging to in-plane Cu below filled CuO-chains visibly splits while Cu(2E) shows no splitting. This has been interpreted as a uniaxial commensurate modulation with period $4a$ along the $\boldsymbol{a}$-axis. d): Spin-lattice relaxation rate $1/T_1$ measured on Cu(2) of the $p = 0.104$ sample decreases down to low T even after SC is suppressed by 28.5 T, showing no sign of long-range magnetic order. All figures are reproduced from ref. [13]

formation is related to the Fermi-surface, particularly, the wave vector connecting 'hot spots' [85]. A similar doping dependence has been measured by Hücker *et al.* [86]. Importantly, the short-range CDW can also be measured by NMR as it broadens the NMR lines [87]. Since the T-dependence of the quadrupolar broadening and the XRD intensity are very similar, both showing an onset T close to 150 K at $p \sim 0.11 - 0.12$, it implies that the short-range CDW is static.

Inelastic XRD measurements in zero-field have revealed a strong phonon anomaly at the CDW vector that appears below T_c which underlined the complex relation between the CDW and SC [88, 89, 90]. These measurements are discussed in the context of hydrostatic pressure in chapter 4. Subsequent XRD measurements in high fields up to 28 T by Gerber *et al.* [91] and a detailed study up to 17 T by Chang *et al.* [92] have helped to make the link between the short-range CDW in low fields (including zero field) and the field-induced long-range CDW phase, discovered by NMR: While the short-range CDW exists along both the $\boldsymbol{a}$ and $\boldsymbol{b}$-axes and shares a broad peak at half-integer values for the anti-phase correlation along the $\boldsymbol{c}$-axis ($l = 0.5, 1.5$, etc.), Gerber *et al.* and Chang *et al.* found that the field-induced CDW is uniaxial and runs uniquely along the $\boldsymbol{b}$-axis [92]. The uniaxial modulation develops coherence in all spatial direction, including the $\boldsymbol{c}$-axis where its correlation from one unit cell to the next is in-phase, leading to peaks at integer values ($l = 1$, etc.). A typical $B - T$ phase diagram

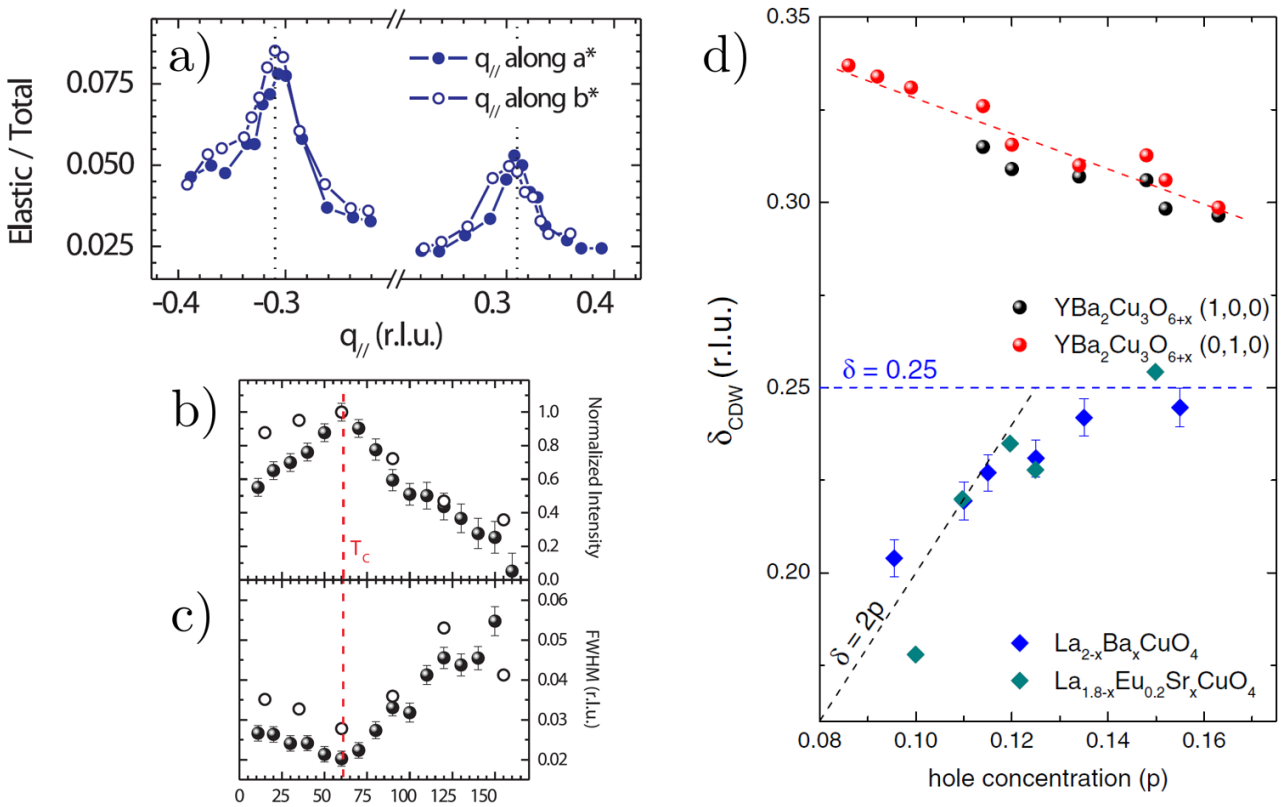

Figure 1.13: a): Incommensurate CDW peaks along the ***a***-axis (filled circles) and the ***b***-axis (empty symbols) in YBCO6.6 at $T = 15$ K. b) shows the T dependence of the XRD intensity of YBCO6.6 at $q = (0, -0.31)$ which shows a decrease below T_c, signaling competition of CDW and SC. c) shows the T-dependence of the peak width. The minimal peak width at T_c shows that there the correlation length is maximal. In b) and c) empty symbols correspond to the elastic signal (REXS) while filled symbols are energy-integrated (RXS). The figures are reproduced from ref. [14]. d): The doping dependence of the CDW wave vector δ_{CDW} in YBCO along the ***a***-axis (black circles) and the ***b***-axis (red circles) is very different as compared with the wave vectors found in LBCO (blue diamonds) and Eu-codoped LSCO (emerald diamonds). This figure is reproduced from ref. [84].

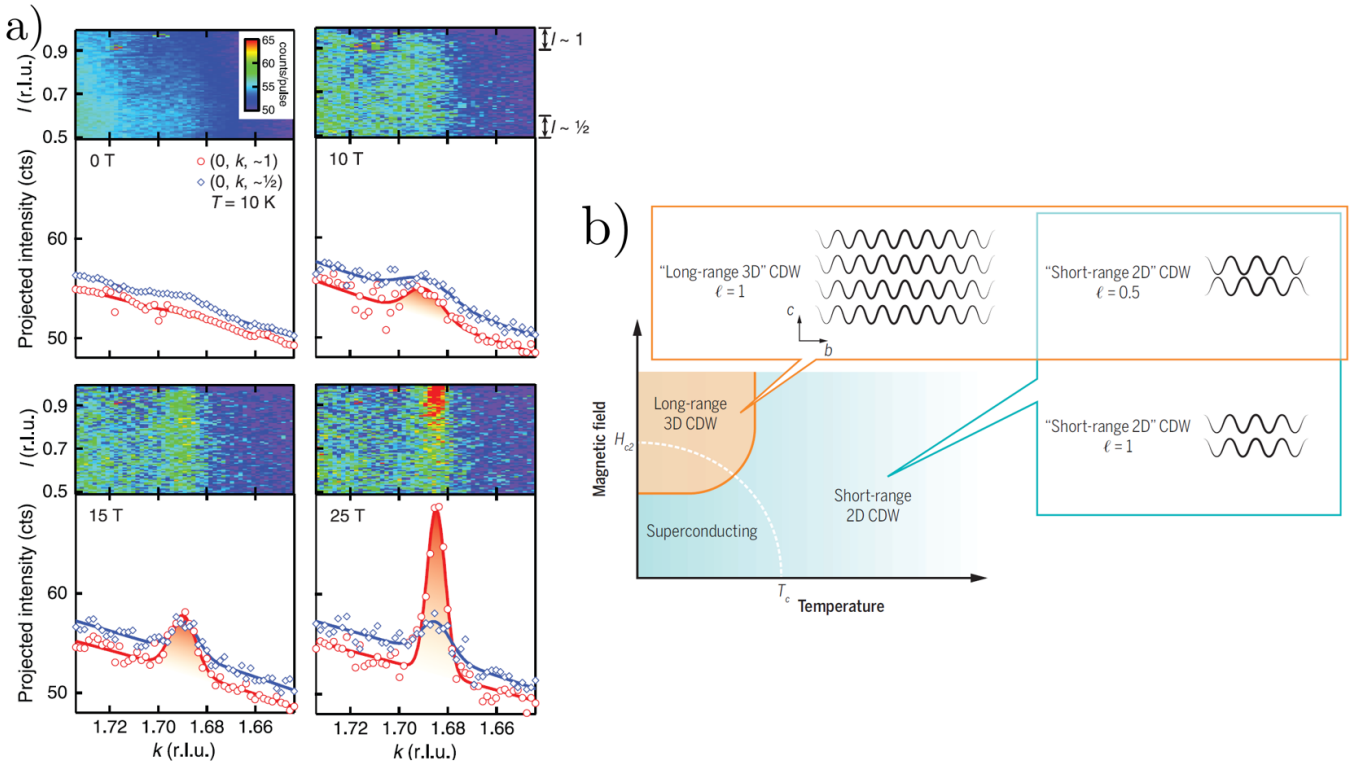

Figure 1.14: a): Field evolution of the XRD intensity with integer l in-phase correlations (red symbols) and half-integer l anti-phase correlations (blue symbols) in YBCO6.67 at $T = 10$ K. This figure is adapted from ref. [91]. b): Typical $B-T$ phase diagram of charge ordered YBCO based on XRD [91, 14, 15], NMR [13, 73, 87] and sound velocity [93] visualising the long ranged in-phase correlations in the field-induced CDW phase. In NMR, the NMR lines are broadened in the short-range phase while there is an additional splitting in the field-induced long-range CDW phase. This figure is reproduced from ref. [94].

of a charge ordered YBCO sample is shown in Fig. 1.14b. One of the principal results of the high field XRD measurements is that the amplitude of the CDW modulation increases with field while the period of the modulation remains unchanged.

Which CDW reconstructs the Fermi-surface?

Since slow quantum oscillations [16, 95] are measured in high fields at which the long-range CDW is induced, one could infer that it is the long-range CDW - not the short-range CDW - which is responsible for the Fermi-surface reconstruction. However, there is a number of arguments that point to the contrary. The main argument is that the decrease of the Hall number R_H starts below $T_H > T_c$ where there is only the short-range CDW and no field-dependence [15]. In case of samples close to $p = 0.12$ the Hall number actually becomes negative at $T_0 > T_c$, so there is no need to apply high fields that would induce long-range order to measure negative R_H [83]. Secondly, it has been shown that without making additional assumptions about the Fermi-surface [96], a reconstruction that leads to an electron pocket of the right size can only be achieved by a bi-axial order [97]. The third argument

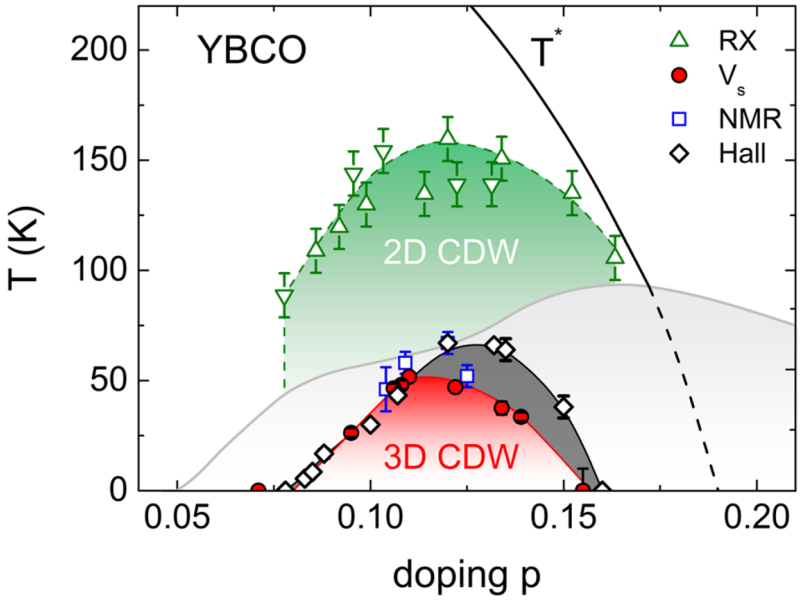

Figure 1.15: T-doping phase diagram of YBCO showing that T_0, as inferred from Hall effect measurements (empty diamonds) and T_{CO}, as inferred from the ultrasound velocity, v_s (red circles), are two distinct temperatures. The onset T of short-range CDW from resonant XRD (green triangles) and the onset T of long-range CDW inferred from the splitting of the NMR line (blue squares) are also shown. Onset T from NMR and ultrasound differ since NMR is sensitive to 2D long-range precursor correlations above T_{CO}. See section 3.3.4 for a complete discussion. This figure is reproduced from ref. [98].

is that T_0 and T_{CO}, the temperature at which ultrasound measurements detect long-range order are distinct. The phase diagram inferred from ultrasound measurements is shown in Fig. 1.15.

1.4.4 Universality of charge order in cuprates

So far, charge order in La-based cuprates, in Bi2201 & Bi2212, Na-doped $Ca_2CuO_2Cl_2$ and YBCO has been discussed. Over the past years, XRD measurements have confirmed charge order in the Bi-based compound previously studied by STM [85, 99] as well as in $HgBa_2Cu_{4+\delta}$ (Hg1201) [100], where quantum oscillation similar to those found in YBCO have been reported [101]. All these measurements are summarised in the phase diagram shown in Fig 1.5.

With $Nd_{2-x}Ce_xCuO_{4+\delta}$ charge order has also been confirmed in an electron-doped cuprate, once again by resonant XRD [102]. However, the details of the charge ordering process differs from one family of cuprates to the other. For example, long-range charge order has not been reported in high fields besides YBCO and La-Bi2201 [103] and even there differences in the $B-T$ phase diagrams are rather striking, since in La-Bi2201 charge order remains field induced even at $T > T_c$. See section 3.3.5 for details.

Another important difference between cuprate families concerns magnetic order. As noted by Comin and Damascelli [5], with the exception of La-based cuprates, charge order and magnetic order appear to

be mutually exclusive in zero field. Wu *et al.* have demonstrated this clearly in the case of YBCO [13]. How magnetic field can induce magnetic order in LSCO is the topic of chapter 5. Potential implications for the relation between anti-ferromagnetic correlations, the pseudogap and charge order are discussed in section 5.10.

Chapter 2

Short introduction to NMR

Nuclear magnetic resonance (NMR) is a technique that can be used to study both liquids and solids. The nuclei themselves play no role in the physics, so effectively the nucleus can be seen as part of the experimental probe. What is needed is a characterisation of the interaction between the nucleus and its environment. In solids, these are principally the magnetic and electric (quadrupolar) hyperfine interactions. Due to the hyperfine interactions one can gain knowledge of the electronic state and the crystal structure: the nuclei act as local sensors of magnetic fields and electric field gradients.
This introduction is brief and covers only those aspects that are of direct relevance for the manuscript. It is based on the books of Abragam and Slichter [104, 105] as well as a selection of Ph.D. theses [106, 107, 108, 109]. Some specialised aspects of NMR are included in the chapters discussing experimental results. The reader can refer to more extensive reviews of NMR in cuprates by Rigamonti *et al.* [110] and Walstedt [111].

A nuclear spin I is described by the nuclear spin operator $\hat{\boldsymbol{I}}$ which is used to define the operator corresponding to the nuclear magnetic moment $\hat{\boldsymbol{\mu}} = \hbar\gamma_N \hat{\boldsymbol{I}}$, where γ_N is the gyromagnetic ratio. In a static magnetic field $\boldsymbol{B} = B_z\hat{z}$ its Hamiltonian is

$$\hat{H}_{Zeeman} = -\hat{\boldsymbol{\mu}}\boldsymbol{B} = -\hbar\gamma_N B_z \hat{I}_z,$$

with eigenvalues $E_m = -\hbar\gamma_N B_z m$, called *Zeeman levels*. For a nuclear spin I there are $2I+1$ Zeeman levels giving $2I$ transitions between neighbouring energy levels whose separation is $E_{m-1} - E_m = \hbar\omega_L$. Nuclear spins I minimise their energy by aligning with the external field and build up a nuclear magnetisation $\boldsymbol{M}_0 = M_z\hat{z}$. N_m nuclear spins out of N_0 total spins are in a state with eigenvalue E_m according to the Boltzmann weights, following

$$N_m = N_0 \frac{e^{-\frac{E_m}{k_B T}}}{\sum_{m=-I}^{I} e^{-\frac{E_m}{k_B T}}}, \tag{2.1}$$

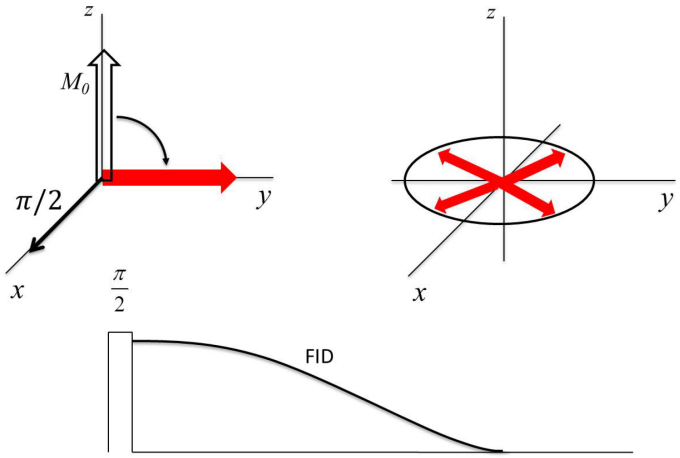

Figure 2.1: A $\frac{\pi}{2}$-pulse is applied to the nuclear magnetisation $\boldsymbol{M}_0$, initially polarised along the z-axis, and rotates it into the x-y-plane. The individual nuclei will eventually de-phase such that the macroscopic magnetisation will be lost (T_2-process) and the NMR signal will decay. This figure is reproduced from ref. [109].

such that the nuclear magnetisation is

$$M_z = \sum_m N_m \mu_{m,z} = N_0 \gamma_N \hbar \frac{\sum_{m=-I}^{I} m e^{-\frac{E_m}{k_B T}}}{\sum_{m=-I}^{I} e^{-\frac{E_m}{k_B T}}} \approx \frac{I(I+1)}{3 k_B T} (\gamma_N^2 \hbar^2) B_z. \tag{2.2}$$

In NMR, transitions between these energy levels are induced by applying resonant radio-frequency pulses using an excitation coil. The NMR signal is recorded with the same coil during the de-excitation, called *Free Induction Decay* (FID). The quantum mechanical description of the FID is complicated [112]. Classically, the FID is understood as the voltage in the coil which is induced by the precessing macroscopic nuclear magnetisation. To generate the FID a $90° = \frac{\pi}{2}$-pulse is applied along the x-axis which rotates the magnetisation in the x-y-plane, see Fig. 2.1. Since individual nuclei experience slightly different local magnetic fields their precession rates will differ and the macroscopic magnetisation will de-phase over the *spin-spin relaxation time* T_2. they will return into equilibrium after a characteristic time, called T_1, through interactions with the environment, meaning principally the electronic system and structural degrees of freedom, usually called the *lattice*, thus the name *spin-lattice relaxation time*[1]. These two processes are captured by the *Bloch-equations*:

$$\frac{\mathrm{d}M_{x,y}}{\mathrm{d}t} = \gamma_N (\boldsymbol{M} \times \boldsymbol{B})_{x,y} - \frac{M_{x,y}}{T_2} \tag{2.3a}$$

$$\frac{\mathrm{d}M_z}{\mathrm{d}t} = \gamma_N (\boldsymbol{M} \times \boldsymbol{B})_z - \frac{M_0 - M_z}{T_1} \tag{2.3b}$$

The induced voltage during the FID is Fourier-transformed and gives the spectrum of precession frequencies. Interactions with electrons modify the transition energies and the structure of the spectrum.

[1] The nuclear spin system on its own reaches an equilibrium state after a usually much shorter T_2, through nuclear spin-spin interactions [106].

2.1 Magnetic interactions

Magnetic interactions exist with other nuclear spins and the electrons with spin $\hat{\boldsymbol{S}}$ and orbital momentum $\hat{\boldsymbol{L}}$ that are not necessarily on the same site. This leads to the hyperfine Hamiltonian

$$\hat{H}_{hf} = \gamma_N \gamma_e \hbar^2 \hat{\boldsymbol{I}} \cdot \left(\frac{3\boldsymbol{r}(\hat{\boldsymbol{S}} \cdot \boldsymbol{r})}{r^5} - \frac{\hat{\boldsymbol{S}}}{r^3} \right) + \frac{8\pi}{3} \hat{\boldsymbol{S}} \delta(\boldsymbol{r}) - \frac{\hat{\boldsymbol{L}}}{r^3} \,. \tag{2.4}$$

Here, γ_e is the electron's gyromagnetic ratio. The on-site interaction with p & d-electrons, whose probability density vanishes at the nuclear site ($\boldsymbol{r} = 0$), is described by the dipolar term in the brackets. Interactions with spins on neighbouring sites are also described by this term. On-site s-electrons have non-zero probability at $\boldsymbol{r} = 0$. This is taken into account by the contact interaction in the second term. Since I and S can fluctuate, the nucleus experiences a fluctuating field $\delta H(t)$ which is the dominant mechanism for magnetic relaxation processes. The time-averaged fluctuating field $\delta H =< \delta H(t) >$ can be non-zero and leads to the Knight shift.

The third term leads to an orbital magnetic moment induced by the applied field. The orbital magnetic moment is not proportional to the density of states and is usually only weakly T dependent [113].

2.1.1 Knight shift K

The Knight shift has two principal contributions, K^{orb} and K^{spin}. Since K^{orb} comes from the nearly T-independent orbital magnetic moment it contributes to the residual shift. To express K^{spin}, the hyperfine interaction is usually written in matrix form as $-\gamma_N \hbar \boldsymbol{I} \bar{A} \boldsymbol{S}$ using the hyperfine coupling tensor $\bar{A}$. Then the spin part of the Knight shift is given by

$$\bar{K}^{\text{spin}} = \frac{\bar{A}}{|g|\mu_B} \chi_0 \,, \tag{2.5}$$

where $|g|$ is the Landé g-factor and $\chi_0 = \chi(q = 0, \omega = 0)$ is the spin susceptibility which is assumed to be uniform. The Knight shift derives its name from its effect to shift the resonance frequency $\omega_L = (1 + K)\gamma_N B$ (isotropic K for simplicity). Written through the time-averaged fluctuating field this gives $\omega_L = \gamma_N \mu_0 (H_0 + \delta H)$.

2.1.2 Spin-lattice relaxation T_1

Moriya has derived an expression for the spin-lattice relaxation rate based on the magnetic hyperfine interaction [114]:

$$\frac{1}{T_1} = \frac{\gamma_N^2}{2} \int_0^\infty e^{i\omega_L t} < \{\delta H_+(t) \delta H_-(0)\} > \, \mathrm{d}t \tag{2.6}$$

Here $\delta H_{\pm}(t)$ are fluctuating fields derived from a fluctuating spin that interacts with the nucleus through the hyperfine coupling[2]:

$$\frac{1}{T_1} = \frac{\gamma_N^2}{2} A_\perp^2 \int_0^\infty e^{i\omega_L t} < \{S_+(t)S_-(0)\} > \mathrm{d}t \tag{2.7}$$

where $A_\perp$ is the hyperfine coupling constant perpendicular to the applied magnetic field. Using the fluctuation-dissipation theorem the spin fluctuations are related to the imaginary part of the spin susceptibility $\chi_\perp^{''}(\omega)$,

$$\chi_\perp^{''}(\omega) = \frac{(g\mu_B)^2}{2k_BT} \int_0^\infty e^{i\omega_L t} < \{S_+(t)S_-(0)\} > \mathrm{d}t \tag{2.8}$$

one obtains

$$\frac{1}{T_1} = \frac{\gamma_N^2}{(g\mu_B)^2} k_B T \, A_\perp^2 \frac{\chi_\perp^{''}(\omega_L)}{\omega_L} \,. \tag{2.9}$$

Up to now the periodic lattice of electronic spins has not been taken into account for the sake of simplicity. By summing over the periodic lattice of electronic spins and Fourier-transforming Moriya's final result is

$$\frac{1}{T_1} = \frac{\gamma_N^2}{(g\mu_B)^2} k_B T \sum_{\boldsymbol{q}} |A_\perp(\boldsymbol{q})|^2 \frac{\chi_\perp^{''}(\omega_L, \boldsymbol{q})}{\omega_L} \,. \tag{2.10}$$

$|A_\perp(\boldsymbol{q})| = |\sum_j A_{\alpha\alpha}(\boldsymbol{r}_j) \exp(-i\boldsymbol{q}\cdot\boldsymbol{r}_j)|$ is called the *form factor*. It depends on the relative position of the nucleus with respect to the electronic spins. For this reason in cuprates, $^{17}T_1^{-1}$, the relaxation rate measured at the ^{17}O nuclear site in the CuO_2-plane is less sensitive to anti-ferromagnetic spin-fluctuations than $^{63}T_1^{-1}$ at the neighbouring Cu-site because for oxygen the form factor vanishes at $\boldsymbol{q} = (\pi, \pi)$ [115, 116].

The functional form by which the return into equilibrium occurs , depends on the nuclear spin. Here we discuss only the case of magnetic relaxation. For $I = 1/2$, as for ^{1}H (protons) the relaxation curve is a single exponential:

$$\frac{^1M_0 - {}^1M_z(t)}{^1M_0} = e^{-\frac{t}{T_1}} \tag{2.11}$$

For $I > 1/2$ there are multiple transitions and the relaxation depends on which transition is excited. For the central transition ($1/2 \leftrightarrow -1/2$) of $I = 7/2$, as in the relevant case of ^{139}La, the relaxation curve is described by

$$\frac{^{139}M_0 - {}^{139}M_z(t)}{^{139}M_0} = \frac{1225}{1716} e^{-(\frac{28t}{T_1})^\beta} + \frac{75}{364} e^{-(\frac{15t}{T_1})^\beta} + \frac{3}{44} e^{-(\frac{6t}{T_1})^\beta} + \frac{1}{84} e^{-(\frac{t}{T_1})^\beta} \,, \tag{2.12}$$

with $\beta = 1$, see refs. [117] or [118] for a derivation. A stretching exponent $\beta < 1$ phenomenologically accounts for a stretched relaxation curve which can result from a distribution of relaxation times. The properties of the stretched relaxation curve are discussed in ref. [119] and in chapter 5. Examples for

[2] Moriya defined $\{AB\} = \frac{1}{2}(AB + BA)$ and for spin operators, $\{S_+S_-\} = (S_xS_x + S_yS_y)$. We assume that $\bar{A}$ is diagonal.

saturation curves measured by saturation recovery ($M_z(t=0)=0$) can be found in Fig. 5.7.
There can also be relaxation mechanisms in which the quadrupole moment couples to a fluctuating electric field gradient [118]. This leads to a different functional form than the purely magnetic and homogeneous relaxation curve with $\beta = 1$. If one continues to fit with eq. 2.12, quadrupolar relaxation can lead to $\beta \neq 1$. This is what is found in LSCO at the structural transition, see Fig. 5.3.

2.2 Quadrupole interactions

The quadrupole interaction is the result of the electrostatic energy of a nuclear quadrupole moment[3] eQ in the electric field gradient $\nabla\mathbf{E}$ (EFG) due to surrounding charges, mostly the electronic orbitals around the nucleus. Quite generally, the electrostatic energy U_{el} can be expanded in multipole moments by Taylor expansion of the electric potential of the surrounding charges:

$$\begin{aligned} U_{el} &= \int \mathrm{d}\mathbf{r}\ \rho_{nuc}(\mathbf{r})V(\mathbf{r}) \\ &= \int \mathrm{d}\mathbf{r}\ \rho_{nuc}(\mathbf{r})\left[V(0)+\sum_\alpha x_\alpha \left(\frac{\partial V}{\partial x_\alpha}\right)_{\mathbf{r}=0} + \frac{1}{2}\sum_{\alpha,\ \beta} x_\alpha x_\beta \left(\frac{\partial^2 V}{\partial x_\alpha \partial x_\beta}\right)_{\mathbf{r}=0} + ...\right] \\ &= \quad Z\,V(0) \quad + \mathbf{d}\cdot\mathbf{E}(0) \quad + \frac{1}{2}\sum_{\alpha,\ \beta}\int \mathrm{d}\mathbf{r}\ \rho_{nuc}(\mathbf{r}) x_\alpha x_\beta \left(\frac{\partial^2 V}{\partial x_\alpha \partial x_\beta}\right)_{\mathbf{r}=0} + ... \end{aligned}$$

The first term is just a constant (Z is the nuclear charge), the second term, where $\mathbf{d}$ is the nuclear dipole moment, is effectively zero because the nucleus rests at a position $\mathbf{r} = 0$ where the electric field is zero. However, components of the electric field gradient tensor are generally non-zero. To get a contribution to the nuclear Hamiltonian one has to canonically quantise the classical electrostatic interaction by changing x_α into operators $\hat{x}_\alpha$ that satisfy the commutation relations $[\hat{x}_\alpha, \hat{p}_\beta] = i\hbar\delta_{\alpha\beta}$. This leads to the quadrupole Hamiltonian

$$\hat{H}_Q = \frac{e}{6}\sum_{\alpha,\ \beta}\sum_{\text{protons }k}\left(3\hat{x}_{\alpha k}\hat{x}_{\beta k} - \delta_{\alpha\beta}\hat{r}_k^2\right)\left(\frac{\partial^2 V}{\partial x_\alpha \partial x_\beta}\right)_{\mathbf{r}=0}$$

In this form $\hat{H}_Q$ is not very useful to evaluate its contribution to the Zeeman states. Interestingly, it is possible to express $\hat{H}_Q$ and its matrix elements through nuclear spin operators $\hat{I}_\alpha = \hat{l}_\alpha + \hat{s}_\alpha$ instead of position operators $\hat{x}_{\alpha k}$ [105]. This is a result of the *Wigner-Eckart Theorem* and is possible because components of *orbital* angular momentum of the protons $\hat{l}_\alpha$ have similar commutation relations among themselves as well as with position operators:

$$[\hat{I}_\alpha, \hat{I}_\beta] = i\hat{I}_\gamma$$
$$[\hat{I}_\alpha, \hat{x}_\beta] = [\hat{l}_\alpha + \hat{s}_\alpha, \hat{x}_\beta] = [\hat{l}_\alpha, \hat{x}_\beta] = i\hat{x}_\gamma$$

[3] e is the elementary charge. Q is the proportionality factor of quadrupole moment to e.

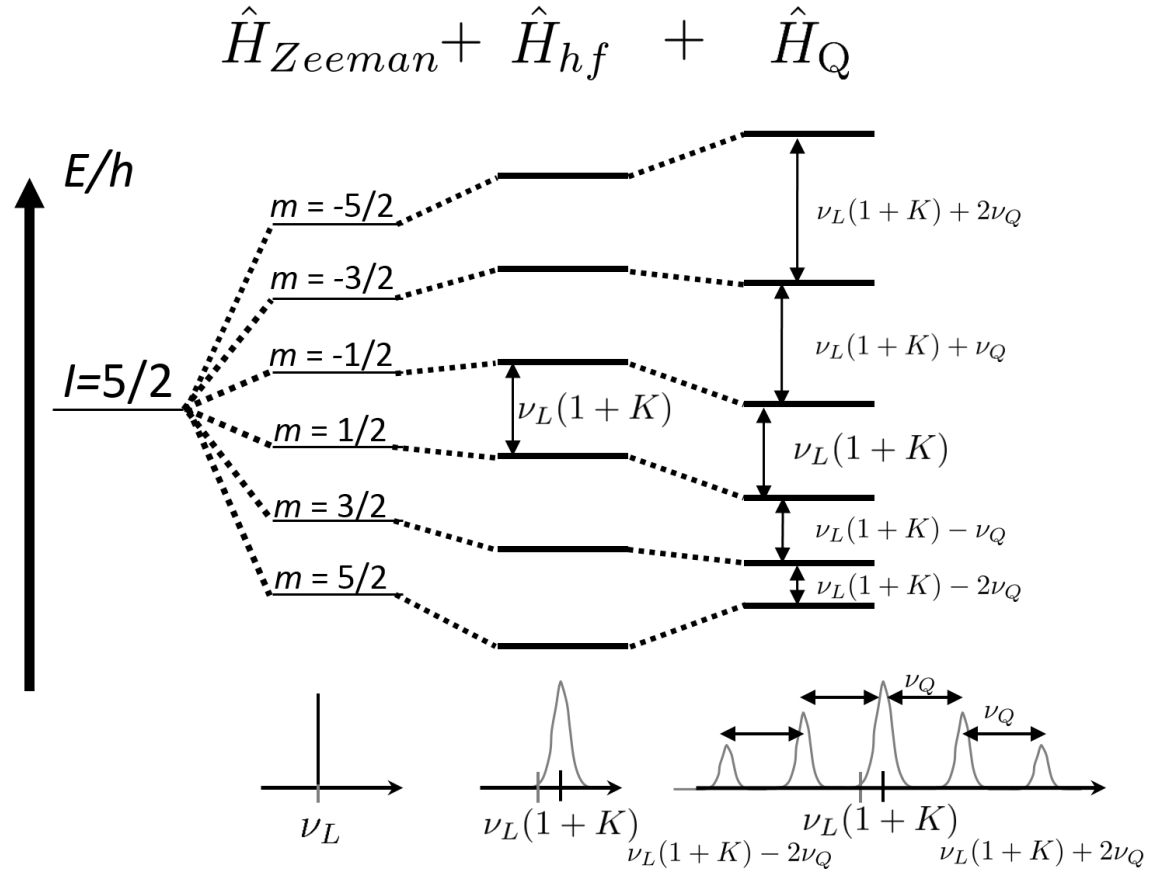

Figure 2.2: Schematic NMR spectrum for $I = 5/2$ as a result of the Zeeman interaction $\hat{H}_{Zeeman}$, the magnetic hyperfine interaction between nuclei and electrons $\hat{H}_{hf}$, which results in the Knight shift K, and the quadrupole interaction $\hat{H}_Q$, giving a central peak and inner and outer satellites that are shifted by $\pm\nu_Q$ and $\pm 2\nu_Q$, respectively.

If $\hat{I}_\alpha$ were pure spin angular momentum, that is $\hat{I}_\alpha = \hat{s}_\alpha$, these commutation relations would not hold and an expression of $\hat{H}_Q$ through nuclear spin operators would be impossible. Since the minimal non-zero value of orbital angular momentum is $l = 1$, it is clear that spin-1/2 nuclei ($s = 1/2$, $l = 0$) cannot have quadrupole interactions. Their nuclear density is spherical and has no quadrupole moment. On the other hand, nuclei with $I > 1/2$ can possess a quadrupole moment that couples to the EFG. This property makes NMR sensitive to the charge distribution. The quadrupole interaction lifts the degeneracy of transitions between the Zeeman levels which results in complex spectra with $2I$ peaks per local site, as shown schematically for $I = 5/2$ in Fig. 2.2. If expressed through nuclear spin operators, $\hat{H}_Q$ becomes

$$\hat{H}_Q = \frac{h\nu_Q}{2}\left(\hat{I}_Z^2 - \frac{I(I+1)}{3} + \frac{\eta}{6}(\hat{I}_+^2 + \hat{I}_-^2)\right). \tag{2.13}$$

For this we define $\nu_Q = \frac{3eQV_{ZZ}}{2I(2I-1)h}$, where Z is the direction of the principal axis of the EFG tensor[4]. In the principal axis frame the EFG tensor is diagonal and using Laplace's equation $V_{XX}+V_{YY}+V_{ZZ} = 0$,

[4] X, Y, Z are the principal axes. We write $\frac{\partial^2 V}{\partial Z^2} = V_{ZZ}$, $\frac{\partial^2 V}{\partial X^2} = V_{XX}$, etc. for brevity.

we define the asymmetry parameter

$$\eta = \frac{V_{XX} - V_{YY}}{V_{ZZ}}, \quad \text{where} \quad 0 \leq \eta \leq 1. \tag{2.14}$$

If the Larmor frequency $\frac{\omega_L}{2\pi} = \nu_L$ is much larger than ν_Q, $\hat{H}_Q$ can be treated as a perturbation. Then, following ref. [113], to 2$^{\text{nd}}$ order the transition frequencies $(E_{m-1} - E_m)/h$ are given by

$$\begin{aligned}\nu(m \leftrightarrow m-1) = & \overbrace{\nu_L}^{0^{\text{th}}\text{ order}} + \overbrace{\frac{1}{2}\nu_Q(m-\frac{1}{2})[3\cos^2\theta - 1 - \eta\sin^2\theta\cos 2\phi]}^{1^{\text{st}}\text{ order}} \\ & \overbrace{+(\nu_Q^2/32\nu_L)\sin^2\theta \quad \Big[\{102m(m-1) - 18I(I+1) + 39\}\cos^2\theta\left(1 + \frac{2}{3}\eta\cos 2\phi\right)}^{2^{\text{nd}}\text{ order}} \\ & \qquad - \{6m(m-1) - 2I(I+1) + 3\}\left(1 - \frac{2}{3}\eta\cos 2\phi\right)\Big] \\ & + \frac{\eta^2}{72}\frac{\nu_Q^2}{\nu_L}\Big[24m(m-1) - 4I(I+1) + 9 - \{30m(m-1) - 2I(I+1) + 12\}\cos^2\theta] \\ & \qquad - \{\frac{51}{2}m(m-1) - \frac{9}{4}I(I+1) + \frac{39}{4}\}\cos^2 2\phi\,\sin^4\theta\Big].\end{aligned} \tag{2.15}$$

Here, θ and ϕ are Euler angles that define the field direction with respect to the principal axes: When $\boldsymbol{B}$ is parallel to Z then $\theta = 0°$, and if $\boldsymbol{B}$ is parallel to Y then $\theta = 90° \,\&\, \phi = 0°$.
The directions of principal axes X, Y, Z can differ from one local environment to the next, so the angles θ & ϕ are not necessarily the same for all local environments. An example is shown in Fig. 2.3a: The CuO_2-plane of YBCO is sketched where nuclei at O(2) and O(3)-sites experience different EFGs due to the p-orbitals along the CuO-bonds. As expected from the symmetry of the p-orbital, the principal axis Z is directed along the bond. O(2) and O(3) sites have rather different angle dependencies as the field is tiled progressively from the $\boldsymbol{c}$-axis towards the $\boldsymbol{b}$-axis, see Fig. 2.3b.

Constraints for 8-peak fitting

In case of $I = 5/2$, the spectrum consists of a central line and two pairs of satellites. The 2$^{\text{nd}}$-order quadrupole interaction affects inner and outer satellites differently, so the separation between neigbouring satellites is not the same on the low-frequency side and on the high-frequency side. When all four satellites of two different ^{17}O-sites are fitted (8-peak fitting), a constraint that remains true is

$$(f_{HF2} - f_{LF2})/(f_{HF1} - f_{LF1}) = 2$$

If the two sites have very similar environments, then their 2$^{\text{nd}}$-order quadrupole shifts can be assumed to be equal. This has been used as a constraint to fit low-field spectra of partially overlapping O(3E) & O(3F) (Fig. 3.7), as well as high field spectra where O(2) satellites split into O(2A) & O(2B), see Fig. 3.29.

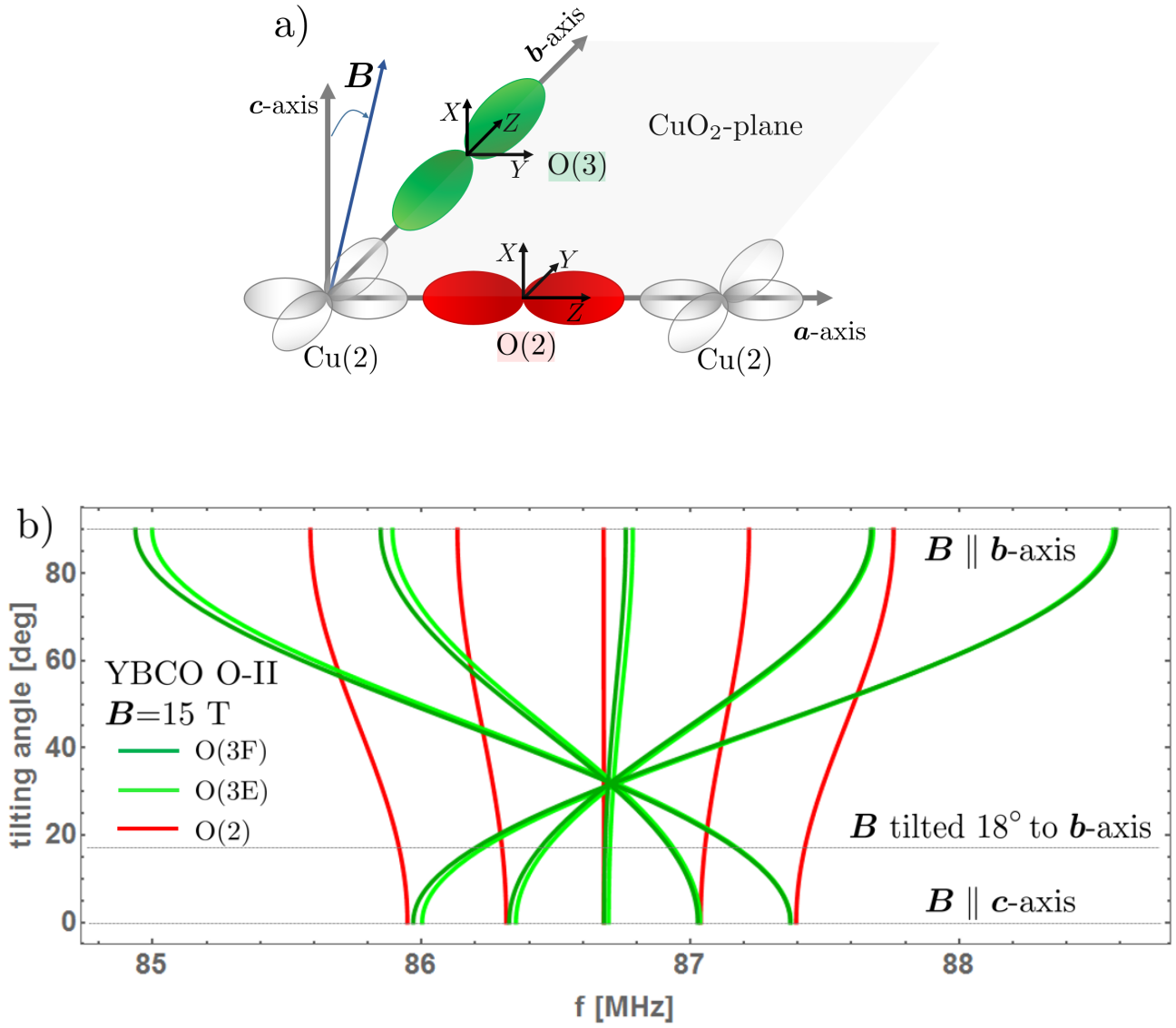

Figure 2.3: a): Sketch of the CuO_2-plane with the local environments of Cu(2) and O(2) & O(3). p-orbitals along the CuO-bonds determine the direction of the principal axes (X, Y, Z) of the O-sites. Z is along the bond for both sites. b): Angle dependence of the ^{17}O-NMR spectrum of the O(2) & O(3) sites of the CuO_2-plane of YBCO at $\boldsymbol{B}$=15 T progressively tilted from $\boldsymbol{c}$ to $\boldsymbol{b}$, calculated from eq. 2.15 for $I = 5/2$ with experimentally determined parameters (ν_Q, η and K) from YBCO6.56. Spectra overlap for $\boldsymbol{B} \parallel \boldsymbol{c}$ since the $\boldsymbol{c}$-axis corresponds to X for both O(2) & O(3). When $\boldsymbol{B} \parallel \boldsymbol{b}$, the field is along Z for the O(3) sites (maximal separation of satellites $= \nu_Q$) and along Y for O(2).

Key message

Since magnetic interactions couple to electronic spin degrees of freedom while quadrupole interactions results from couplings to the charge environment, NMR is in principle able to distinguish between charge and spin ordering phenomena.

Chapter 3

^{17}O-NMR of charge ordered $YBa_2Cu_3O_y$

After the initial discovery of the long-ranged 3D CDW phase in high magnetic fields using ^{63}Cu-NMR, the attention has shifted progressively from ^{63}Cu to ^{17}O. Two reasons can be given: Firstly, the spin-spin relaxation time T_2 is an order of magnitude longer on O than on Cu in the CuO_2-plane, so ^{17}O-NMR suffers much less from the wipe-out effect. Secondly, the quadrupole frequencies ν_Q of the respective O and Cu-sites in the CuO_2-planes are approximately 1 MHz and 30 MHz, so recording ^{17}O-spectra is more efficient, since the frequency range is smaller.

In this chapter ^{17}O-spectra of charge ordered YBCO are presented. Detailed analysis of the linewidths and lineshapes allows to deduce information about short-range and long-range CDW phases. In the short-range CDW phase the lineshapes are simple, so the essential information about the CDW comes from the linewidths. This is the first part.

Lineshapes become more interesting in the long-ranged CDW phase in high fields. In the second part of this chapter, a detailed study of the field-induced line-splitting gives new insight into the period of the charge density modulation and highlights the role of discommensurations.

3.1 NMR linewidth and the short-range 2D CDW

3.1.1 The ^{17}O-NMR spectrum of the O-II sample

Since every local O-site will contribute five peaks to the NMR spectrum the first task is to identify which peaks belong to the same local site. As the analysis of ^{17}O-spectra is a substantial part of this manuscript, it is helpful to see how quadrupolar and magnetic (Knight shift) interactions affect the spectra of a particularly clean sample with O-II chain ordering. To 1stst order, the quadrupolar interaction leads to a symmetric spectrum. However, as the Knight shifts differ, the center of gravity is not the same for all sets of peaks belonging to different sites. As a consequence, peaks that are well resolved on one side of the spectrum can overlap on the opposite. This is exactly what happens for

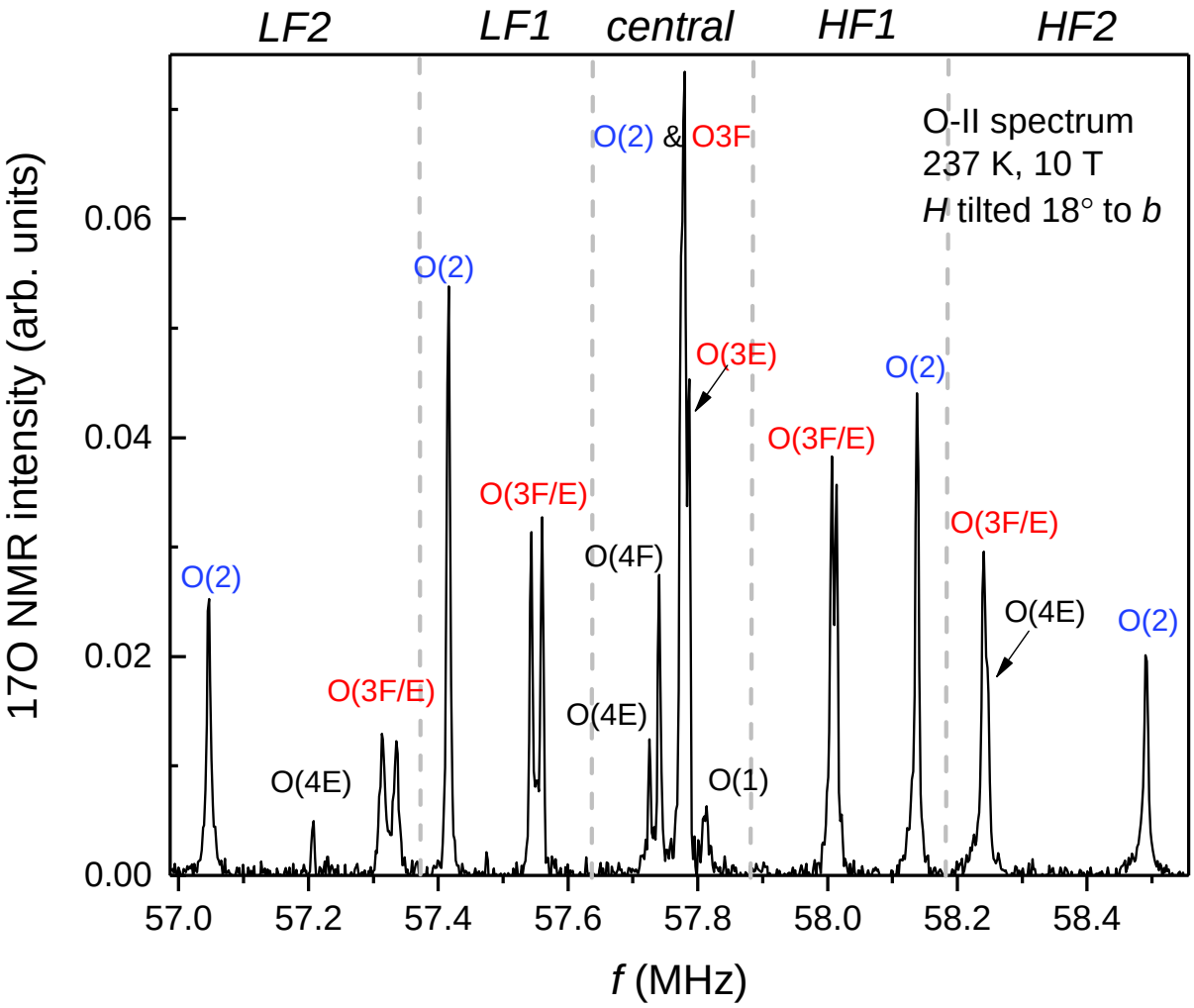

Figure 3.1: High T ^{17}O spectrum distinguishing O(2) sites(bonds along a-axis) and O(3E/F) sites (bonds along b-axis). O(2) sites appear as single symmetric peaks, O(3E/F) form two sites O(3E) and O(3F) that are well resolved on the low frequency side of the spectrum but partially overlap on the high frequency side. To 1^{st} order, the central peaks for O(2), O(3E/F) and O(1) (chain oxygen) and O4(E/F) (apical oxygens) are separated due to differences in the respective Knight shifts.

the O(3E) and O(3F) sites in the spectrum in Fig. 3.1.

The outermost low-frequency satellites (LF2) of O(3F) and O(3E) are well separated and two peaks are easily visible, but on the opposite, high-frequency side of the spectrum (HF2) there is only one peak visible for O(3F/E). The origin lies in the differences in Knight shifts and effective quadrupole frequencies for O(3E) and O(3F). As O(3E) and O(3F) experience different electric field gradients due to either oxygen-full or oxygen-depeleted CuO chains running above the CuO_2-plane, their effective (angle-dependent) quadrupole frequencies $\nu_{\rm quad}(\phi)$ differ. At this particular orientation with respect to the magnetic field one finds experimentally that $\nu_{\rm quad,O(3F)} > \nu_{\rm quad,O(3E)}$. In addition, the central peak of O(3F) has a lower frequency than O(3E), which implies that O(3F) has a smaller Knight shift, $K_{\rm O(3E)} < K_{\rm O(3E)}$(see Fig. 3.1). Due to the Knight shift all O(3E) peaks are slightly shifted to higher

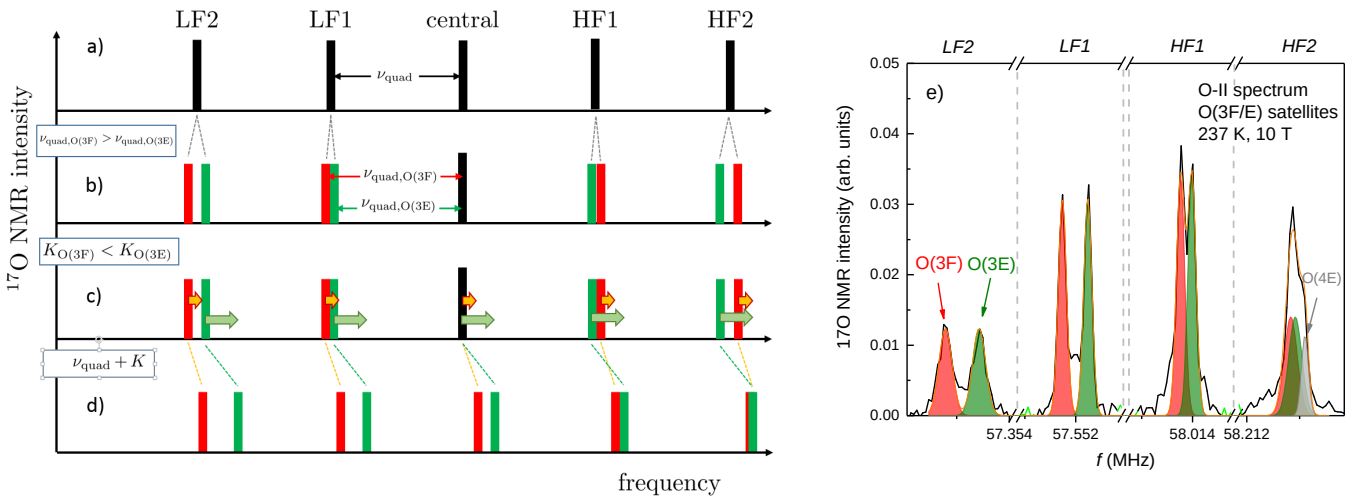

Figure 3.2: a-e): Sketches to explain why O(3E) and O(3F) overlap on the high frequency side (HF1 & HF2) but not on the low frequency side (LF2 & LF1) as found in e). a): Sketch of NMR spectrum for $I = \frac{5}{2}$ as in the case on ^{17}O for a single site with transitions separated by quadrupole frequency ν_{quad}. b): If there are two distinct sites, more specifically, O(3F) in red and O(3E) in green with $\nu_{quad,O(3F)} > \nu_{quad,O(3E)}$, then satellites of O(3F) will lie further outward than satellites of O(3E). Notice that the central line does not distinguish quadrupolar environments to 1st order. Also, the difference between two sites is twice as visible on outer satellites (LF2 & HF2) compared to inner satellites (LF1 & HF1). c): Considering differences in the Knight shifts, $K_{O(3E)} > K_{O(3F)}$ (indicated by a longer green and a shorter red arrow, respectively), leads to positive shift of all O(3E) peaks, with respect to O(3F). d): Taken together quadrupolar and Knight shifts lead to the final spectrum: The central line splits due to different Knight shifts and HF2 satellites of O(3E) and O(3F) nearly fully overlap on the high frequency side, but are well separated on the low frequency side. e): O(3E) & O(3F) satellite peaks from Fig. 3.1, including Gaussian fits for all O(3) satellites. HF2 of O(3E/F) overlap partially with HF1 of the apical oxygen site O(4E), coloured in grey.

frequencies with respect to O(3F). Fig. 3.2 visualises step by step how these differences in quadrupole frequencies and Knight shifts lead to overlap on the high-frequency side of the spectrum, but not on the other.

The peak widths of the O(2) site of the O-II sample

So far, the position of NMR peaks have been discussed but their individual widths have been neglected. However, similar mechanisms of coupled quadrupolar shifts and Knight shifts are also responsible for the widths of the respective peaks. Since each peak results from the summed NMR intensity of a macroscopic number of nuclei, the peak's width can be understood as the width of the histogram or distribution of individual nuclei. Each nucleus possesses its own quadrupole frequency ν_{quad} and Knight shift K.

In the following, the focus will be on the widths of O(2) satellites, *i.e.* satellites belonging to the oxygen

on bonds along the $\boldsymbol{a}$-axis because in an idealised O-II crystal all O(2) are identical. Experimentally, one finds that satellites have Lorentzian lineshapes and similarly small widths at room temperature, but develop Gaussian broadening upon cooling. To fit the entire continuous lineshape evolution from Lorentzians to Gaussians, we utilise the Voigt lineshape. The Voigt lineshape is a convolution of Lorentz and Gauss and by increasing the Gaussian *full width at half maximum* (FWHM), w_G, the initial Lorentzian becomes a Gaussian.

$$f_{\text{Voigt}}(x) = (f_{\text{Lorentz}} \star f_{\text{Gauss}})(x) = A\frac{2\ln 2}{\pi^{\frac{3}{2}}}\frac{w_L}{w_G}\int_{-\infty}^{\infty}\frac{e^{-t^2}}{(\sqrt{\ln 2}\frac{w_L}{w_G})^2 + (\sqrt{4\ln 2}\frac{x-x_c}{w_G} - t)^2}\mathrm{d}t \tag{3.1}$$

using

$$f_{\text{Lorentz}}(x) = \frac{2A}{\pi}\frac{w_L}{4(x-x_c)^2 + w_L^2} \tag{3.1a}$$

$$f_{\text{Gauss}}(x) = \sqrt{\frac{4\ln 2}{\pi}}\frac{e^{-\frac{4\ln 2}{w_G^2}x^2}}{w_G}\,. \tag{3.1b}$$

There is no analytical expression for the FWHM of the Voigt lineshape but there is a simple approximate expression[120]:

$$w_{\text{Voigt}} = 0.5346\,w_L + \sqrt{0.2166\,w_L^2 + w_G^2}\,. \tag{3.2}$$

As the convolution in 3.1 is computationally more demanding, an alternative to the Voigt lineshape is the Pseudo-Voigt lineshape, which simply sums a Lorentzian and a Gaussian with weights m and $1-m$, respectively:

$$f_{\text{Pseudo-Voigt}}(x) = A\Big[m\cdot\frac{2}{\pi}\frac{w}{4(x-x_c)^2 + w^2} + (1-m)\cdot\sqrt{\frac{4\ln 2}{\pi w}}e^{-\frac{4\ln 2}{w^2}(x-x_c)^2}\Big] \tag{3.3}$$

The advantage of Eq. 3.3 is that there is only one width parameter w that corresponds the FWHM. Interestingly, the Pseudo-Voigt is able to fit Voigt lineshapes very well, so both the Voigt as well as the Pseudo-Voigt lineshapes fit the O(2) satellites very well. Their T-dependence is reproduced in Fig. 3.3. The widths of this O-II sample (y=6.56, p=0.109) have already been measured and analysed by Wu *et al.*[87]. However, the O-II data that has been acquired at 10 T is recent and was taken after the measurements of O-II under hydrostatic pressure, to allow for the comparison of spectra with and without pressure in the same conditions. To have higher signal-to-noise ratios measurement times have been longer and additionally the T-range has been extend below T_{c} where the line broadening had not been studied extensively.

This abstract serves on the one hand to summarise previous results, as they build the basis of the understanding, and on the other hand, to refine the analysis in certain aspects.

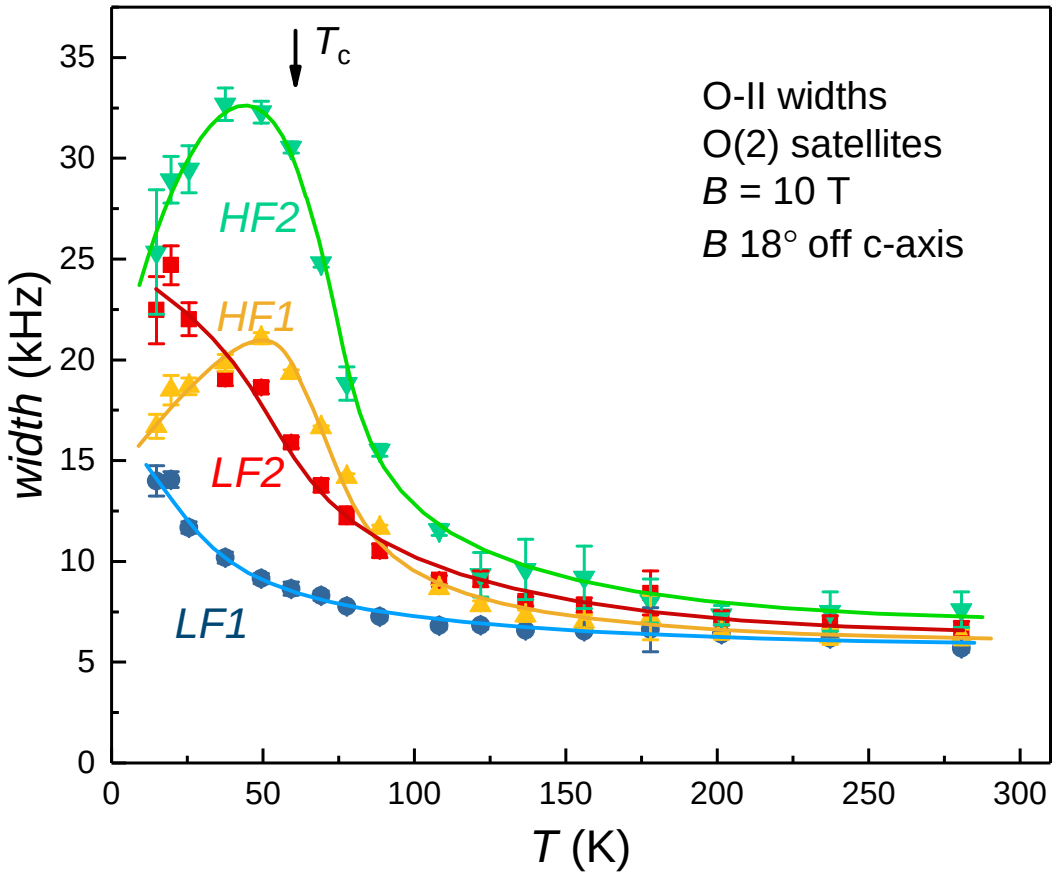

Figure 3.3: T-dependence of O(2)(bonds along a-axis) satellites' FWHM for B=10 T tilted by 18° off the c-axis towards b. FWHM is determined by fitting to Voigt lineshapes. Lines are guides to the eye.

Remarkably, the high T linewidths are small and very similar for all satellites which indicates that the main contribution to the high T width is of magnetic origin, meaning that it comes from a distribution of Knight shifts. The distribution is small with respect to the average Knight shift ($\delta\nu_{\mathrm{mag},0}/K(280\ \mathrm{K}\ ) \approx 7\%$). If there had been a substantial quadrupolar broadening then the outer satellites, $LF2$ & $HF2$, should be up to twice as broad as the inner satellites, $LF1$ & $HF1$. The absence of quadrupolar broadening signals the high quality of the sample since any structural or chemical inhomogeneity would have led to broader outer satellites. This reasoning is also confirmed by an equally narrow central line, but in this field orientation the central lines of different local O-sites overlap, so the width of the central line could not be determined with the same precision as for the well-resolved satellites.

Below $T \approx 200$ K the satellites start to broaden in a complicated way. The broadening is neither of purely magnetic origin, since purely magnetic broadening increases all satellites' widths equally, nor of purely quadrupolar origin, since $HF2$ and $LF2$ (as well as $HF1$ and $LF1$) do not broaden symmetrically. Wu *et al.* have proposed a simple model for the widths which includes both quadrupolar $\delta\nu_{\mathrm{quad}}$

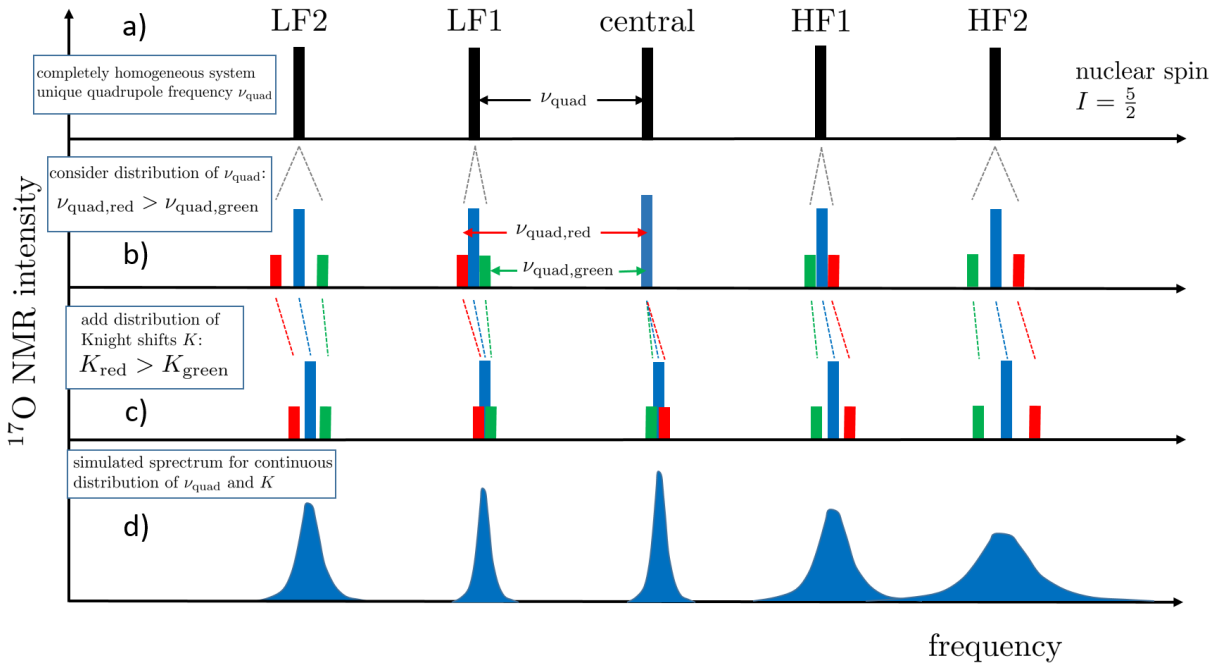

Figure 3.4: Sketch of the behaviour of the ^{17}O spectrum for a single local site subject to quadrupole and correlated magnetic broadening. a): Idealised spectrum with five transitions separated by a unique effective quadrupole frequency ν_{quad}. b): Considering a discrete distribution of three effective quadrupole frequencies $\nu_{\text{quad,red}} > \nu_{\text{quad}} > \nu_{\text{quad,green}}$ does not affect the central transition to 1$^{\text{st}}$ order but broadens outer and inner satellites symmetrically. c): Allowing for a distribution of Knight shifts, $K_{\text{red}} > K_{\text{average}} > K_{\text{green}}$, where larger K is correlated with larger ν_{quad}, leads to asymmetric broadening of the spectrum: $w_{HF2} > w_{LF2}$, as well as $w_{HF1} > w_{LF1}$. Larger Knight shift shifts stronger to higher frequencies, as indicated by the coloured dashed lines. d): If the distribution of effective quadrupole frequencies is continuous then the resulting spectrum is smooth, but it still shows the same asymmetry as c).

and magnetic broadening $\delta\nu_{\text{mag}}$ and in addition distinguishes two types of magnetic contributions: An *uncorrelated* magnetic contribution $\delta\nu_{\text{mag,0}}$ that is responsible for the finite width at high temperature but is otherwise weakly T-dependent and a second magnetic contribution, $\delta\nu_{\text{mag,c}}$, which is *correlated* with $\delta\nu_{\text{quad}}$ [87]. Fig. 3.4 serves to visualise how these three ingredients manage to broaden the O(2) peaks in an asymmetric way.

In this figure one can see in which way $\delta\nu_{\text{mag,c}}$ is correlated to $\delta\nu_{\text{quad}}$: The red contribution to the NMR intensity, which has the larger effective quadrupole frequency $\nu_{\text{quad,red}}$, also has the larger Knight shift K_{red}. Simultaneously, the smaller effective quadrupole frequency $\nu_{\text{quad,green}}$ correlates with the smaller Knight shift K_{green} and as a result satellite peaks on the high frequency side of the spectrum are broader than their counterparts on the low frequency side. Had the correlation between ν_{quad} and K been reversed, then the resulting spectrum would be equally asymmetric, with the sole difference that the low frequency side would be broader than the high frequency side, *i.e.* $w_{LF2} > w_{HF2}$, as well as $w_{LF1} > w_{HF1}$. The fact that the experimental spectrum of O(2) is asymmetric and that the high

frequency satellites are broader, necessarily implies that the larger ν_{quad} correlates with larger K.

Modeling of the peak broadening

To formulate this mechanism mathematically, an additional consideration is necessary. From Fig. 3.4 one can see that, for example in $HF1$, $\delta\nu_{\text{quad}}$ and $\delta\nu_{\text{mag,c}}$ both increase the width. However, it is not clear how these two broadening contributions add up to the resulting total width. One might sum linearly, or sum the squares, or imagine more complicated mechanisms. Experimentally, the peaks are well described by the Voigt lineshape. At high T one finds $w_L \gg w_G$ and with cooling the Gaussian width w_G increases strongly until the opposite limit $w_L \ll w_G$ is reached. Thus the additional broadening due to $\delta\nu_{\text{quad}}$ and $\delta\nu_{\text{mag,c}}$ is mainly of Gaussian character and as Gaussian widths are summed in squares, the resulting formulae to calculate the total widths are the following:

$$w_{HF2} = \sqrt{(2\delta\nu_{\text{quad}} + \delta\nu_{\text{mag,c}})^2 + \delta\nu_{\text{mag,0}}^2} \tag{3.4a}$$

$$w_{HF1} = \sqrt{(\delta\nu_{\text{quad}} + \delta\nu_{\text{mag,c}})^2 + \delta\nu_{\text{mag,0}}^2} \tag{3.4b}$$

$$w_{central} = \sqrt{\delta\nu_{\text{mag,c}}^2 + \delta\nu_{\text{mag,0}}^2} \tag{3.4c}$$

$$w_{LF1} = \sqrt{(\delta\nu_{\text{quad}} - \delta\nu_{\text{mag,c}})^2 + \delta\nu_{\text{mag,0}}^2} \tag{3.4d}$$

$$w_{LF2} = \sqrt{(2\delta\nu_{\text{quad}} - \delta\nu_{\text{mag,c}})^2 + \delta\nu_{\text{mag,0}}^2} \tag{3.4e}$$

Summing (or subtracting) $\delta\nu_{\text{quad}}$ and $\delta\nu_{\text{mag,c}}$ before taking the square of the sum (difference) is essential to capture the effect of the correlation between quadrupole and magnetic effects.

Here the simplification is made that the uncorrelated magnetic broadening $\delta\nu_{\text{mag,0}}$ also has Gaussian character, which is not correct since high T line shapes are Lorentzians. At lower T where most of the broadening comes from $\delta\nu_{\text{quad}}$ and $\delta\nu_{\text{mag,c}}$ this is not an issue, but especially at high T this model is not very adequate to determine small contributions from $\delta\nu_{\text{quad}}$, so error bars tend to be relatively large at high T as can be seen in Fig. 3.6a. This set of five equations with only three parameters $\delta\nu_{\text{quad}}$, $\delta\nu_{\text{mag,c}}$ and $\delta\nu_{\text{mag,0}}$ is over-determined and does not necessarily have a solution. Even if two equations are discarded there still does not need to be a solution because the equations are non-linear. Simple algebra allows to verify that if a solution exists, the following dimensionless equation must be true:

$$\frac{w_{HF2}^2 - w_{LF2}^2}{w_{HF1}^2 - w_{LF1}^2} = 2 \tag{3.5}$$

The left side of this equation can be calculated from the data and compared with the expected value of 2, as shown in Fig. 3.5. Evidently, eq. 3.5 is never exactly fulfilled, so the set of equations cannot be numerically solved for the measured widths. However, within error bar this equation is mostly verified. It is very sensitive to the satellite widths when the widths become small, so error bars are

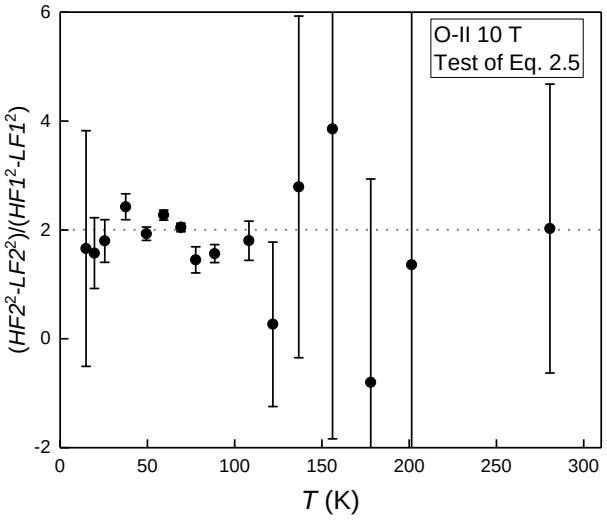

Figure 3.5: T-dependence left side of Eq. 3.5 evaluated for O(2) widths that are shown in Fig. 3.3. Error bars are large where the differences of widths are small. The dotted grey line marks the value 2. When Eq. 3.5 is valid broadening parameters can be determined reliably.

very large at high T, although the uncertainty in the widths themselves never surpasses 1 kHz in the fits.

Although there is no unique way to find an approximate solution, an elegant way to determine the broadening parameters is to combine the eqs. 3.4a to 3.4d in symmetric ways to find analytic expressions for $\delta\nu_{\mathrm{quad}}$ and $\delta\nu_{\mathrm{mag,c}}$[1].

$$\delta\nu_{\mathrm{quad}} = \sqrt{\frac{w_{HF2}^2 + w_{LF2}^2 - w_{HF1}^2 - w_{LF1}^2}{6}} \tag{3.6a}$$

$$\delta\nu_{\mathrm{mag,c}} = \frac{w_{HF1}^2 - w_{LF1}^2}{4\delta\nu_{\mathrm{quad}}} \tag{3.6b}$$

$$\delta\nu_{\mathrm{mag,0}} = \sqrt{\frac{w_{HF2}^2 + w_{LF2}^2 + w_{HF1}^2 + w_{LF1}^2 - 10\delta\nu_{\mathrm{quad}}^2 - 4\delta\nu_{\mathrm{mag,c}}^2}{4}} \tag{3.6c}$$

As soon as $\delta\nu_{\mathrm{quad}}$ and $\delta\nu_{\mathrm{mag,c}}$ have been determined, the remaining parameter is the uncorrelated magnetic broadening $\delta\nu_{\mathrm{mag,0}}$. Using any of eqs. 3.4a to 3.4d allows to determine $\delta\nu_{\mathrm{mag,0}}$ from a single width, but as $\delta\nu_{\mathrm{mag,0}}$ can vary somewhat from one width to the other, it is best to calculate the average $\delta\nu_{\mathrm{mag,0}}$ using all available widths, as done in eqs. 3.6c. It should be repeated that there is no unique way to determine the broadening parameters but, independently of the particular chosen procedure, the resulting broadening parameters are expected to be consistent within error bars resulting from the experimental uncertainty of the measured widths. Fig. 3.6 shows the quadrupole and magnetic broadenings.

[1] The correlated magnetic broadening can also be determined for the outer satellites by $\delta\nu_{\mathrm{mag,c}} = \frac{w_{HF2}^2 - w_{LF2}^2}{8\delta\nu_{\mathrm{quad}}}$ and as long as the left-hand side of eq. 3.5 is close to 2 the result will be close to equal for inner and outer satellites. However, as inner satellites have stronger intensity, using eq. 3.6b is more reliable.

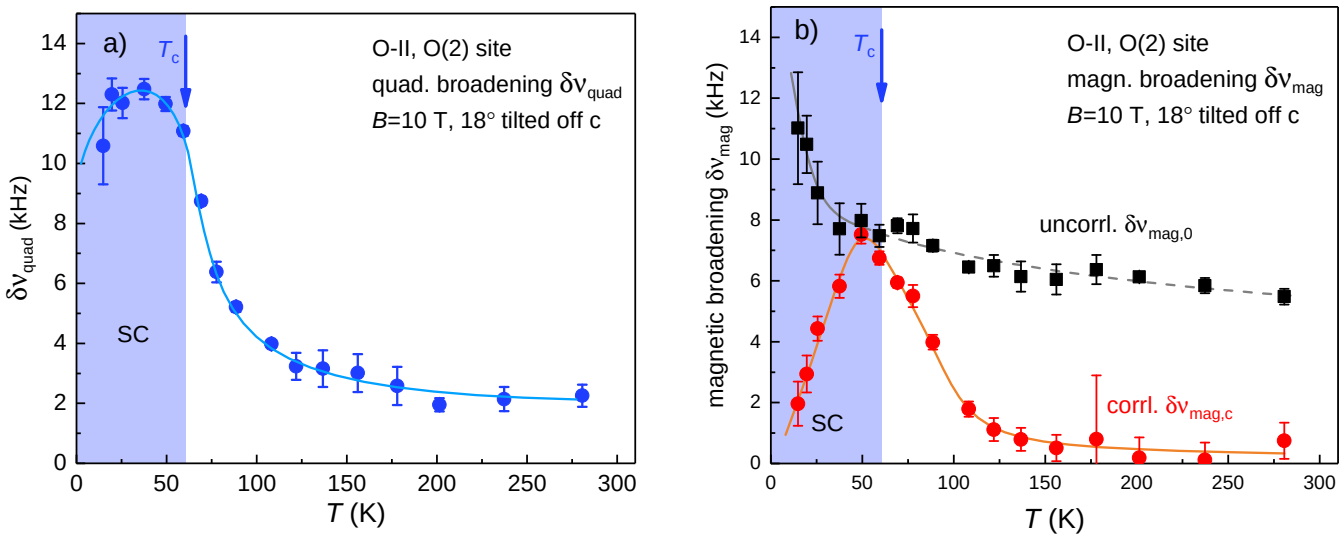

Figure 3.6: a):Quadrupole broadening $\delta\nu_{\mathrm{quad}}$ of O(2) calculated using Eq. 3.6a. The blue line is a guide to the eye. b) Uncorrelated magnetic broadening($\delta\nu_{\mathrm{mag,0}}$) (black squares) and correlated magnetic broadening $\delta\nu_{\mathrm{mag,c}}$ (red circles) calculated by Eq. 3.6c and Eq. 3.6b, respectively. Lines are guides to the eye. Blue shaded region in a) and b) indicates the superconducting phase at B =0 T.

Discussion of broadening contributions

Quadrupole broadening $\delta\nu_{\mathrm{quad}}$

The quadrupole broadening has been discussed in depth by Wu *et al.* [87]. For the sake of completeness three aspects should be highlighted that established the quadrupole broadening as a direct probe of the short-ranged 2D CDW: Firstly, since the broadening is quadrupolar it must come from some sort of inhomogeneity that can modify the electric field gradient (EFG). The EFG is sensitive to anything that affects the local charge environment of the nuclei, either structural variations like variations of ionic positions or chemical inhomogeneity like variations of the local hole doping. Both make unit cells inequivalent and structural and chemical inhomogeneities can, of course, be coupled. In principle, the inhomogeneity can be ordered and periodic or disordered and random. Disorder is T-independent, since if there are for example impurities, then these will be there at any T, unless there is atomic motion like in ionic conductors, which is not the case in YBCO below ambient T [121, 122]. In fact - this is the second point - the quadrupole broadening is very small at high T, so structural and chemical inhomogeneities are small. With cooling towards T_c the quadrupole broadening increases strongly. The fact that the quadrupole broadening sets in and grows upon cooling signals an electronic instability. Thirdly, the growing quadrupole broadening perfectly correlates with the T-dependence of XRD intensity above T_c (see ref. [87] Fig. 4a for O-II and Fig. 3.13a of this manuscript for O-VIII) and below T_c the XRD intensity and $\delta\nu_{\mathrm{quad}}$ show the same T- and magnetic field B-dependence due to the competition with superconductivity (SC), suggesting that the quadrupole broadening is simply

another way to probe the short-ranged 2D CDW modulation extensively studied by X-ray diffraction techniques. A very important contribution from NMR is that the underlying charge order must be static on the NMR-timescale which is as low as 10 kHz as given by the typical line width in this case. If faster fluctuations were present, then these would be averaged out in the NMR experiment but could contribute to the XRD intensity. The XRD intensity would have a higher onset temperature, which is not the case.

The quadrupole broadening depicted in Fig. 3.6a has been measured with finite field and since B =10 T is sufficient to partially suppress SC, the quadrupole broadening grows below the zero-field $T_{\rm c}$. However, the growth of the quadrupole broadening below $T_{\rm c}$ is slowed and stagnates before decreasing at very low T.

Uncorrelated magnetic broadening $\delta\nu_{\rm mag,0}$

The response to SC is more dramatic in the magnetic broadenings, $\delta\nu_{\rm mag,0}$ and $\delta\nu_{\rm mag,c}$, shown in Fig. 3.6b . $\delta\nu_{\rm mag,0}$, which dominates the width at high T, shows only a very weak increase with cooling in the entire normal state, but a rapid increase appears below 25 K. This rapid increase is likely not due to a growing distribution of Knight shifts but rather due to vortex broadening below the vortex melting temperature $T_{\rm vs}$ at which the vortex lattice freezes [57, 93]. Vortex broadening is identical on all satellites and is not coupled to the quadrupole broadening, so it has to appear as a contribution of the uncoupled magnetic broadening $\delta\nu_{\rm mag,0}$. In YBCO7, using ^{17}O-NMR, the vortex broadening has been found to give an additive contribution to the broadening of the in-plane oxygen sites [123]. In YBCO7 the vortex broadening is of the order of 50 kHz, much larger than the rapidly growing contribution to $\delta\nu_{\rm mag,0}$ in Fig. 3.6b. As vortex broadening is roughly proportional to H_{c2} [124] and given the large difference in to H_{c2} values for the YBCO6.56 and the YBCO7 (H_{c2}(y = 7)/H$_{\rm c2}$(y = 6.56) $\approx$ 6) samples[38] a vortex broadening of around 5-10 kHz appears reasonable. The weak increase of $\delta\nu_{\rm mag,0}$ already visible far above $T_{\rm c}$ is possibly due to weak magnetic correlations that exist at all dopings in YBCO. Anti-ferromagnetic correlations exist both in the SC state and in the normal state and can be brought to evidence by only small concentrations of Zn-doping [123, 125].

Correlated magnetic broadening $\delta\nu_{\rm mag,c}$

$\delta\nu_{\rm mag,c}$ has a very interesting behaviour. It starts to grow simultaneously with the quadrupole broadening but it does not scale simply with $\delta\nu_{\rm quad}$ for $T > T_{\rm c}$, since the slope of $\delta\nu_{\rm quad}$ tends to diverge towards $T_{\rm c}$ whereas $\delta\nu_{\rm mag,c}$ increases just linearly. The contrast becomes much more dramatic below $T_{\rm c}$. $\delta\nu_{\rm mag,c}$ is very sensitive to SC and starts to drop very rapidly even before reaching $T_{\rm vs}$. This rapid drop has not been reported by Wu *et al.*, since the broadening had not been studied below $T_{\rm c}$. However,

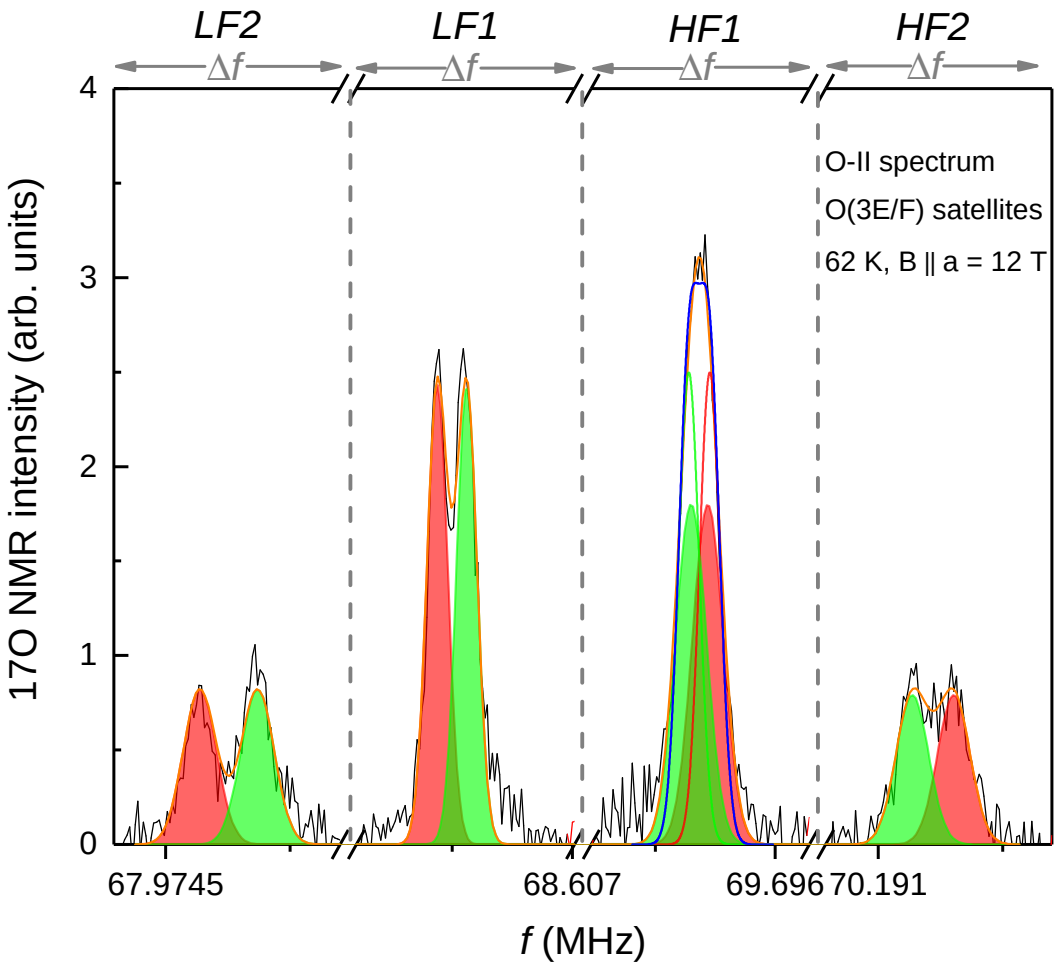

Figure 3.7: O-II samples O(3) satellites at 62 K with 12 T applied parallel to a-axis. Widths and areas for same satellites of O(3E) & O(3F) are constrained to be equal ($w_{\mathrm{O(3E),LF2}} = w_{\mathrm{O(3F),LF2}}$ etc.) and are plotted on the same scale Δf. The free fit (filled areas) leads to $w_{\mathrm{HF1}} > w_{\mathrm{LF1}}$ but enforcing $w_{\mathrm{HF1}} = w_{\mathrm{LF1}}$ leads to an equally good fit. This is shown by the narrower empty peaks on $HF1$ that add up to the blue envelope.

a simple explanation for the origin of $\delta\nu_{\mathrm{mag,c}}$ in the normal state has been given and can naturally be extended to the SC state. Naively one would assume that if there is a CDW that modulates the charge density and consequently the hole doping, then nuclei close to maxima of the modulation would not only experience a higher EFG[2] but also a higher Knight shift, since both EFG and Knight shift increase with doping. While $\delta\nu_{\mathrm{quad}}$ still grows below the zero-field T_{c} and develops something like a plateau, $\delta\nu_{\mathrm{mag,c}}$ must decrease since the ground state at T=0 is a condensate of Cooper pairs with total S=0 and thus $K_{\mathrm{spin}}(T = 0)$=0. So if there had been no SC then $\delta\nu_{\mathrm{mag,c}}$ would have followed the T-dependence of $\delta\nu_{\mathrm{quad}}$.

[2]In principle, if the nucleus is surrounded by completely filled shells its EFG is zero. With increasing hole doping the filling of the shells decreases, so the EFG increases.

The peak widths of the O(3) site of the O-II sample

The discussion has so far focused on the O(2) site and shall now be extended to the O(3) sites on bonds along the ***b***-axis. In Figs. 3.1 & 3.2 is has been shown that for O(3E) and O(3F) sites the high frequency satellites ($HF1$ and $HF2$) overlap, so it is not possible to determine all satellite widths as precisely as for O(2). Applying the field parallel to the ***a***-axis, as presented in Fig. 3.7, could permit Tao Wu to at least additionally resolve $HF2$ for O(3E) and O(3F). In this orientation it is quite evident that the widths of $LF2$ and $HF2$ are very similar. In Fig. 3.7 two fits are made for the overlapping $HF1$ satellites: An unconstrained fit gives w_{HF1}=15 kHz > 10 kHz=w_{LF1} but if constraining $w_{\mathrm{HF1}} = w_{\mathrm{LF1}}$ it also describes the data well. The symmetric widths for high and low satellites have the implication that $\delta\nu_{\mathrm{mag,c}} \approx 0$ at T=62 K, a temperature for which O(2) widths are most asymmetric due to large $\delta\nu_{\mathrm{mag,c}}$. This is very surprising since one would expect that the CDW modulation affects O(2) and O(3) sites in the same way. The absence of correlated magnetic broadening does not imply that there is no quadrupole broadening as the outer satellites are broader than the inner satellites. Assuming that $\delta\nu_{\mathrm{mag,c}} \approx 0$ is a general property of O(3) sites, spectra of O(3) sites have been fit using the constraints $w_{\mathrm{HF1}} = w_{\mathrm{LF1}}$ & $w_{\mathrm{HF2}} = w_{\mathrm{LF2}}$ to reduce the uncertainty of the fitting. In Fig. 3.8 results of this fitting are presented which show that O(2) and O(3) sites broaden in similar ways, with the peculiar exception that $\delta\nu_{\mathrm{mag,c}} \approx 0$ for O(3).

The origin of the absence of $\delta\nu_{\mathrm{mag,c}}$ in case of O(3) could, so far, not be determined experimentally but a recent numerical simulation by Atkinson *et al.* based on a multiorbital model with a Fermi surface that has been reconstructed by staggered (anti-ferromagnetic) moments on the Cu sites has reproduced magnetic and quadrupolar broadenings on O(2) and O(3) by calculating the local density of states (LDOS) and the charge densities [126]. Within their model, the authors correctly deduced a long-ranged uniaxial CDW along the ***b***-axis and also predict that magnetic broadening deduced from the LDOS is site-dependent. However, in the simulation O(3) sites are found to have a stronger magnetic broadening, not O(2) sites, as has been determined experimentally from NMR. In the simulation the underlying lattice is tetragonal and orthorhombicity, making O(2) and O(3) inequivalent, is included through stronger hopping along the ***b***-axis. Disorder, which is relevant to pin CDW fluctuations at high T enters isotropically. One could speculate that the additional use of anisotropic disorder potentials, better mimicking the effect of disorder coming from the CuO chains, could affect which site, O(2) or O(3), has more magnetic broadening without changing the direction of the uniaxial modulation along the ***b***-axis.

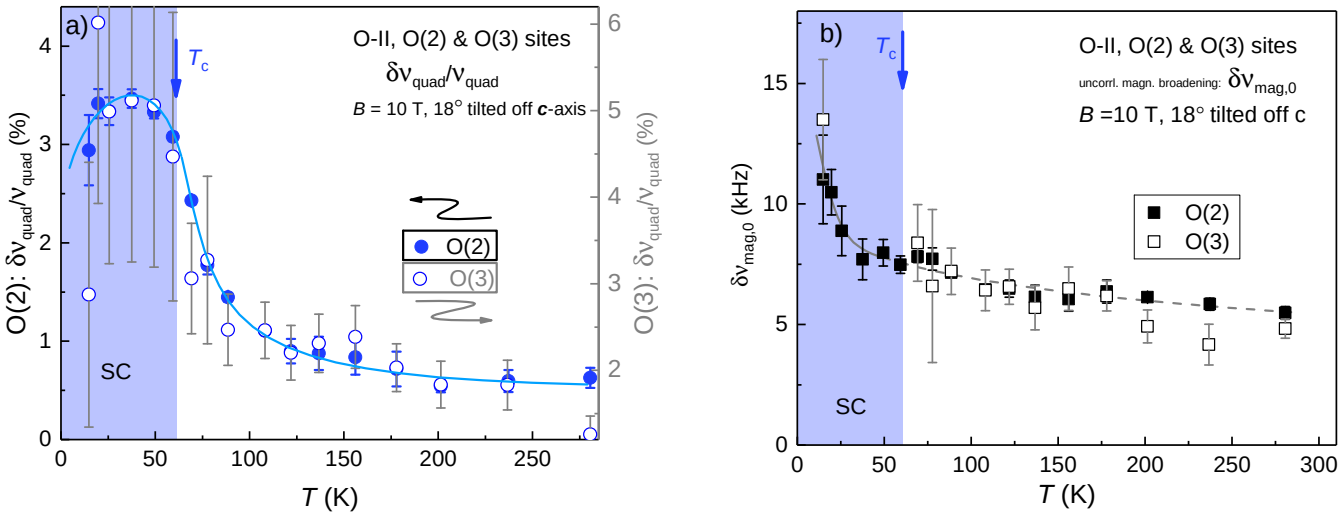

Figure 3.8: a):Dimensionless quadrupole broadening $\frac{\delta\nu_{\rm quad}}{\nu_{\rm quad}}$ of O(2) (filled circles) & O(3) sites (empty circles). To compare the quadrupole broadening for both sites it has to be rescaled by the effective quadrupole frequency $\nu_{\rm quad}$ to account to 1$^{\rm st}$ order for the angle dependence of $\delta\nu_{\rm quad}$. Considering that $\frac{\delta\nu_{\rm quad}}{\nu_{\rm quad}}$ of O(3) has a larger offset at high T than O(2) the quadrupole broadening can be scaled for O(2) and O(3) sites. The blue line is a universal guide to the eye. b) Uncorrelated magnetic broadening $\delta\nu_{\rm mag,0}$ of O(2) (filled squares) & O(3) sites (empty squares). Within experimental uncertainty, above $T_{\rm c}$ O(2) and O(3) have the same $\delta\nu_{\rm mag,0}$. Due to excessive uncertainty in the widths of O(3) for most $T < T_{\rm c}$, $\nu_{\rm mag,0}$ cannot be reliably determined for O(3) and is only shown for the lowest T of 15 K. Its high value shows that $\delta\nu_{\rm mag,0}$ of O(3) sites increases, presumably, due to vortex broadening at low T, as has been found for O(2).

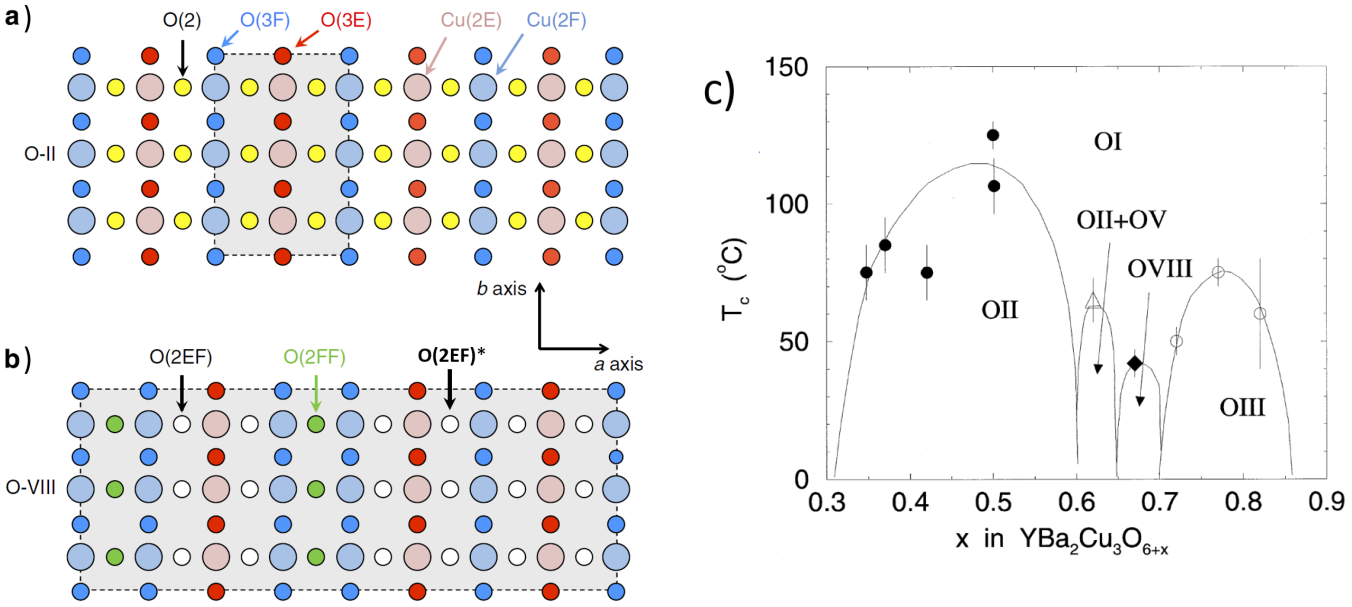

Figure 3.9: a,b): Inequivalent O and Cu in-plane sites for idealised O-II and O-VIII chain ordering where oxygen-filled and oxygen-deficient chains run along the b-axis. Grey rectangles indicate the unit cell of the chain ordered superstructure. Blue sites (Cu(2F) & O(3F)) are situated below oxygen-filled chains, red sites (Cu(2E) & O(3E)) reside below oxygen-deficient chains. For O-II, all O(2) sites are equivalent, in between a filled and an empty chain. In O-VIII, there are more types of O(2): O(2FF), marked in green, situated in between two filled chains and O(2EF), in white, between an empty and a filled chain. More precisely one can distinguish two O(2EF) sites by considering not only neighbouring but also next-neighbouring chains: O(2EF) has two filled next-neighbouring chains, O(2EF)* one filled and one empty next-neighbouring chain. O(2FF) always has empty next-neighbouring chains. If we consider neighbouring and next-neighbouring chains environments, there are also multiple inequivalent O(3E) and O(3F) sites. Figs. 3.9(a,b) are reproduced from ref. [87]. c): Phase diagram of chain ordering superstructures as a function of chain-oxygen concentration x (reproduced from ref. [24]). T_c is the temperature above which there are no chain superstructures, measured in °C.

3.1.2 Quadrupole broadening of the O-VIII sample

Structure and spectrum

The more complicated chain structure of O-VIII leads to a larger number of inequivalent local sites than in case of O-II. The analysis of the spectra is complicated because these sites overlap partially. A full spectrum at high T is shown in Fig. 3.10. Four different in-plane sites can be distinguished but the focus will be on O(3F) only, because other peaks are either less intense (O(2FF)) or contain multiple local environments (O(2EF) & O(3E)) which makes the determination of the quadrupole broadening unfeasible.

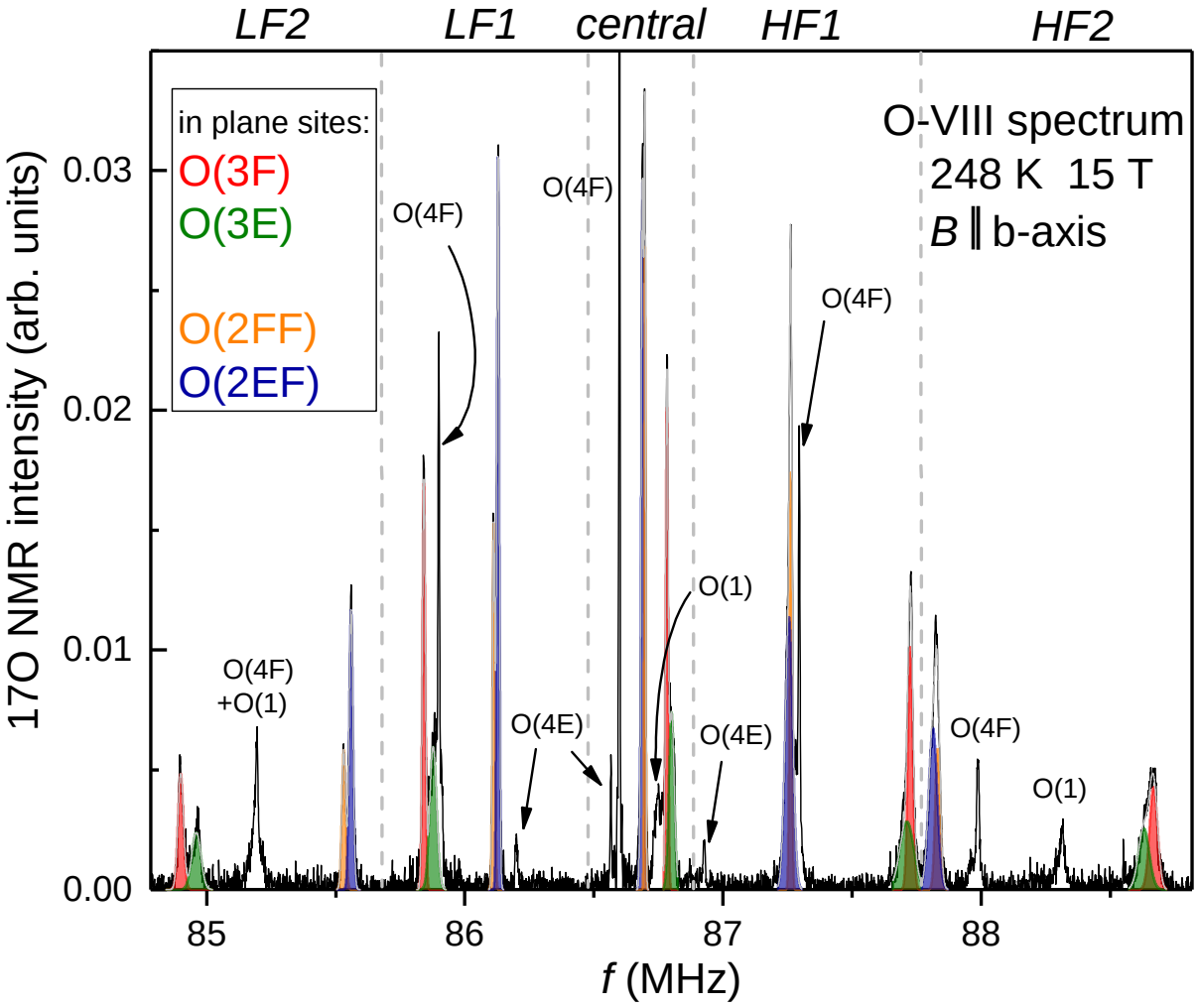

Figure 3.10: High T ^{17}O spectrum of a O-VIII sample. Only fits of in-plane peaks are coloured. O(3F) & O(3E) have area ratio 1.25 : 1, O(2EF) & O(2FF) have area ratio 2 : 1. Apical peaks O(4F) are situated below oxygen-filled chains, O(4E) sit below empty chains. Due to fast repetition O(4E) sites are not relaxed and have weak intensities. O(1) belongs to in-chain oxygen sites.

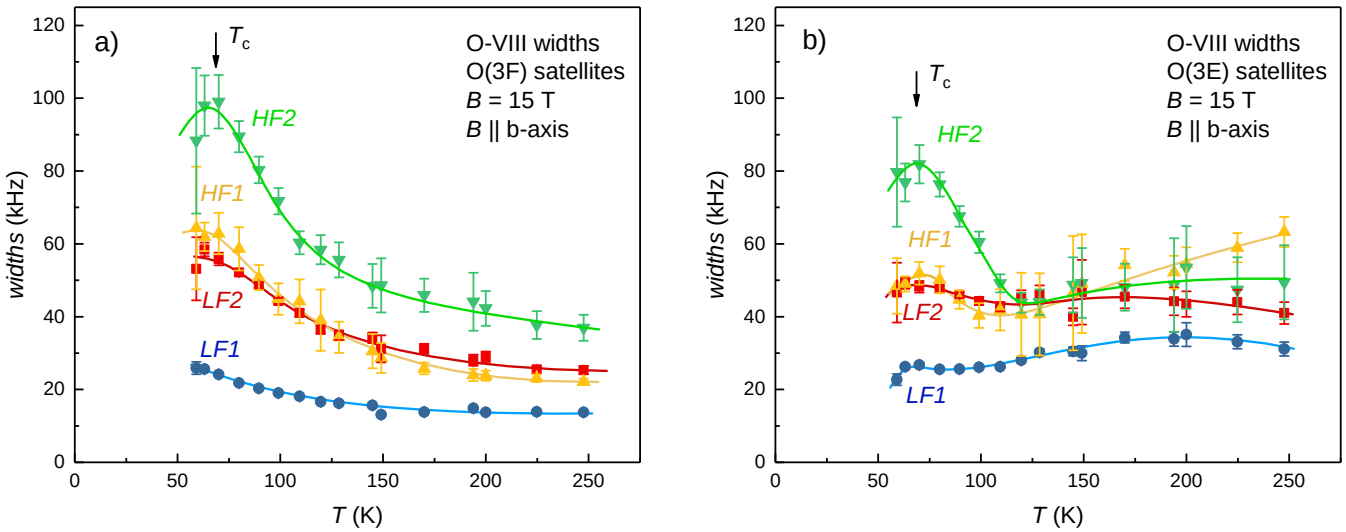

Figure 3.11: a): T-dependence of O(3F) satellites' FWHM. b): T-dependence of O(3E) satellites' FWHM. Spectra were measured at B=15 T along the b-axis. FWHM is determined by fitting to Gaussian lineshapes. Lines are guides to the eye. Below T_c the NMR-signal is rapidly lost in this field-orientation.

Peak widths of O(3) sites of the O-VIII sample

In the determination of the quadrupole broadening it is essential that the satellite peaks' widths for a particular in-plane site can be fit reliably. It is essential that the peak belongs to only one particular local site, as is the case for O(2) in the previously discussed O-II sample. However, if disorder broadens the peaks it is possible that what appears to be one peak actually belongs to two inequivalent sites, with different effective quadrupole frequencies ($\nu_{\mathrm{quad},1} \neq \nu_{\mathrm{quad},2}$) and different Knight shifts ($K_1 \neq K_2$). Consequently, the associated peak widths can vary with T due to T-dependent differences in quadrupole frequencies and Knight shift. Quadrupole frequencies are only weakly T-dependent, so the main effect comes from the strongly T-dependent Knight shift [44]. As the pseudogap causes each site's Knight shift to decrease with cooling, all differences in Knight shifts tend to decrease, making peaks sharper and more symmetric [127]. In fact, peaks that narrow upon coolingare likely to incorporate two (or more) inequivalent local sites.

Fig. 3.11 shows the T-dependence of the satellites' FWHM for O(3F) and O(3E). Although O(3E) and O(3F) are expected to have similar widths, O(3E) satellite widths have a non-monotonic T-dependence, while in case of O(3F) all satellites broaden with cooling, as has been found for O(2) sites in O-II. The T-dependence of O(3E)'s widths is complicated but can be explained by two or more inequivalent sites inside each O(3E) satellite. Oppositely to the situation described by Fig. 3.2 inequivalent sites overlap more for $LF2$ & $LF1$ than $HF2$ & $HF1$ at high T. With cooling, the Knight shift difference decreases and all peaks narrow before they begin to broaden strongly below 100-120 K due to the intrinsic broadening coming from the short-ranged CDW. Given the absence of an particular feature

in the lineshape (shoulder or splitting), determining the individual widths of the inequivalent sites of O(3E) is not possible. Understanding the behaviour of widths of peaks that incorporate multiple inequivalent sites is important in the broader context of ^{17}O-NMR in cuprates. In Hg1201 similar T-dependence of the broad satellite widths occurs but instead of associating it with inequivalent local sites due to disorder, Lee *et al.* interpreted it as a combination of spin and charge modulations [128]. However, we note that these modulations are B-independent up to 30 T and T-independent up to 400 K. Consequently, the broadening is likely to be the result of structural disorder.

Modeling the peak widths of the O(3F) site

O(3F) widths do not show any narrowing at high T, so the set of satellite peaks associated with O(3F) belongs to a much cleaner local environment. However,there remains some width difference between high and low frequency satellites at high T, unlike in O-II, so there must still be some significant disorder associated with this site. Visibly, at high T the outer satellites $LF2$ & $HF2$ are the broadest. This indicates that there is some finite quadrupole broadening $\delta\nu_{\mathrm{quad,0}}$ that was negligible in O-II. If the disorder is due to structural or chemical (doping) inhomogeneity, then $\delta\nu_{\mathrm{quad,0}}$ should be largely T-independent. To be distinguished from $\delta\nu_{\mathrm{quad,0}}$ the T-dependent quadrupole broadening due to the short-ranged CDW will be called $\delta\nu_{\mathrm{quad,c}}$. Assuming that the T-independent contribution $\delta\nu_{\mathrm{quad,0}}$ has Gaussian character, the equations 3.4a to 3.4e for the satellite widths are thus modified to the following set of equations:

$$w_{HF2} = \sqrt{(2\delta\nu_{\mathrm{quad,c}} + \delta\nu_{\mathrm{mag,c}})^2 + \delta\nu_{\mathrm{mag,0}}^2 + (2\delta\nu_{\mathrm{quad,0}})^2} \tag{3.7a}$$

$$w_{HF1} = \sqrt{(\delta\nu_{\mathrm{quad,c}} + \delta\nu_{\mathrm{mag,c}})^2 + \delta\nu_{\mathrm{mag,0}}^2 + \delta\nu_{\mathrm{quad,0}}^2} \tag{3.7b}$$

$$w_{central} = \sqrt{\delta\nu_{\mathrm{mag,c}}^2 + \delta\nu_{\mathrm{mag,0}}^2} \tag{3.7c}$$

$$w_{LF1} = \sqrt{(\delta\nu_{\mathrm{quad,c}} - \delta\nu_{\mathrm{mag,c}})^2 + \delta\nu_{\mathrm{mag,0}}^2 + \delta\nu_{\mathrm{quad,0}}^2} \tag{3.7d}$$

$$w_{LF2} = \sqrt{(2\delta\nu_{\mathrm{quad,c}} - \delta\nu_{\mathrm{mag,c}})^2 + \delta\nu_{\mathrm{mag,0}}^2 + (2\delta\nu_{\mathrm{quad,0}})^2} \tag{3.7e}$$

Determining the magnetic broadening contributions becomes increasingly difficult but eq. 3.6a used to determine the quadrupole broadening changes only slightly:

$$\delta\nu_{\mathrm{quad,tot}}(T) = \sqrt{\delta\nu_{\mathrm{quad,c}}(T)^2 + \delta\nu_{\mathrm{quad,0}}^2} = \sqrt{\frac{w_{HF2}^2 + w_{LF2}^2 - w_{HF1}^2 - w_{LF1}^2}{6}} \tag{3.8}$$

In eq. 3.8 the T-dependence of $\delta\nu_{\mathrm{quad,c}}$ has been explicitly added, since it is expected to be responsible for entire T-dependence of the *total* quadrupole broadening. Fig. 3.12a shows the total quadrupole broadening of O(3F), as determined by eq. 3.8. The effect of $\delta\nu_{\mathrm{quad,0}}$ is not additive, so if $\delta\nu_{\mathrm{quad,0}}$ increases it does not simply shift a T-independent baseline upwards. The functional form of the total quadrupole broadening appears to change as $\delta\nu_{\mathrm{quad,0}}$ increases. This is shown in Fig. 3.12b. For

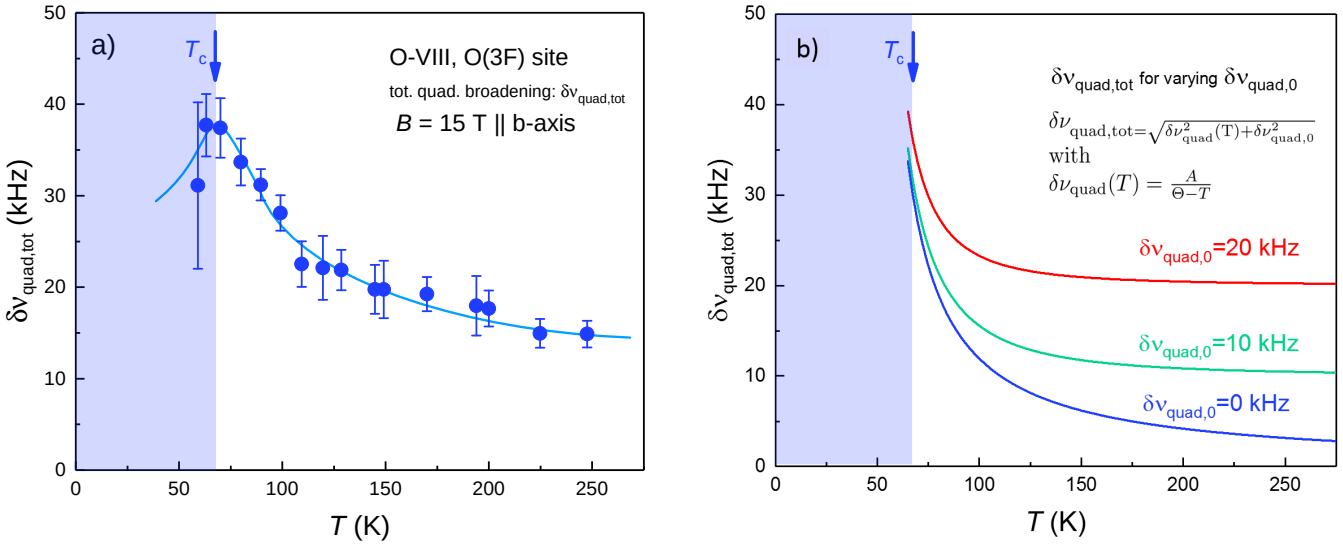

Figure 3.12: a): T-dependence total quadrupole broadening of the O(3F) site. b): Visualisation of how the total quadrupole broadening $\delta\nu_{\mathrm{quad,tot}}$ is affected by different values for the T-independent $\delta\nu_{\mathrm{quad},0}$, assuming that the T-dependent $\delta\nu_{\mathrm{quad,c}}$ follows a Curie-Weiss behaviour. Increasing $\delta\nu_{\mathrm{quad},0}$ leads to the impression that there is a decreasing onset temperature for the quadrupole broadening, although in principle Curie-Weiss behaviour has no onset.

illustrational purposes one can assume $\delta\nu_{\mathrm{quad,c}}(T)$ to follow a Curie-Weiss behaviour (which thus has no onset temperature), but as $\delta\nu_{\mathrm{quad},0}$ increases, the resulting total quadrupole broadening loses the appearance of Curie-Weiss behaviour but appears to be rather flat at high T, giving the impression of an onset T. The larger $\delta\nu_{\mathrm{quad},0}$ gets, the lower the onset temperature of CDW correlations appears to be. As a result, the larger the T-independent quadrupole broadening resulting from disorder is, the more difficult it becomes to determine the T-dependent quadrupole broadening due to the CDW correlations.

Comparison with XRD

At this point it is interesting to compare the total quadrupole broadening determined for the O(3F) site with the XRD intensity measured in a O-VIII sample of very similar doping by Chang *et al.* [15]. In XRD, intensity due to the CDW grows upon cooling on top of a weakly T-dependent background coming from the chain superstructure that is subtracted. It is reasonable to subtract the background since XRD intensities are additive. Wu *et al.* have shown that the XRD intensity scales very well with total quadrupole broadening of the O(2) site in the O-II sample, which is only very weakly affected by a small $\delta\nu_{\mathrm{quad},0}$.

For O-VIII, this scaling is shown in Fig. 3.13a using $\delta\nu_{\mathrm{quad,tot}}$ of O(3F) and the XRD intensity at wave vector Q=(1.695,0,0.5) at B=0 T. The comparison is made with the zero-field XRD intensity

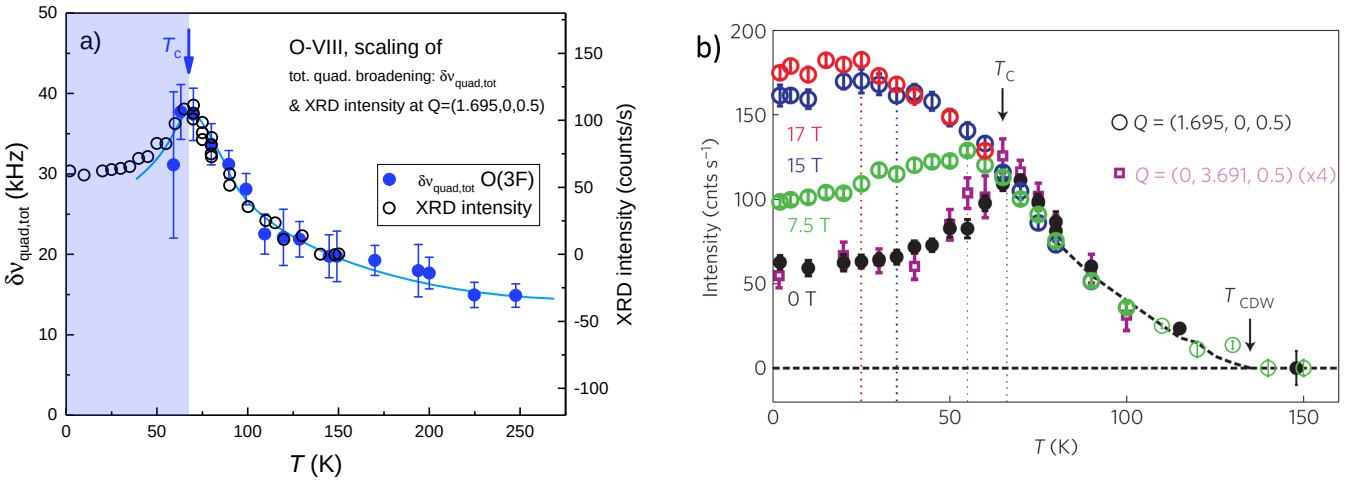

Figure 3.13: a): T-dependence total of the quadrupole broadening of the O(3F) site scaled to the XRD zero-field intensity of the CDW modulation with Q=(1.695,0,0.5) for a similar O-VIII sample. XRD intensity is reproduced from ref. [15] and is shown in panel b). Here different fields are applied along the c-axis.

since the quadrupole broadening has been measured with an in-plane field of 15 T which suppresses superconductivity only very weakly. This is confirmed by the peak in $\delta\nu_{\mathrm{quad,tot}}$ close to T_c and the rapid loss of NMR intensity below T_c due to entrance into the vortex solid phase. Above T_c XRD intensity is field-independent, so intensities at finite field are also used for the scaling. Fig. 3.13a shows that this scaling appears to work for the O-VIII sample although larger $\delta\nu_{\mathrm{quad,0}}$ could have affected the T-dependence of the total quadrupole broadening. However, due to substantial experimental uncertainty in the quadrupole broadening it is difficult to determine whether $\delta\nu_{\mathrm{quad,c}}(T)$ would have scaled better or worse to the XRD intensity after correcting for $\delta\nu_{\mathrm{quad,0}}$. In any case, there is no doubt that short-ranged CDW correlations induce T-dependent quadrupole broadening in the ^{17}O-spectra of the O-VIII sample although overlap of peaks belonging to different sites makes the determination of the quadrupole broadening less precise than for the O-II sample.

Comparison of the O-II & O-VIII samples

It would be desirable to compare the strength of the quadrupole broadening in the O-II and the O-VIII sample. This is difficult, since, as reported by Wu *et al.* [87], O(2) and O(3) sites do not have the same quadrupole broadening. In addition, the quadrupole broadening varies with the angle between the magnetic field and the EFG tensors principal axes, even after having been scaled by ν_{quad}. However, the quadrupole broadening measured for different direction and different sites can be scaled linearly and shares the same T-dependence. Together these two aspects show why the quadrupole broadening on O(2) and O(3) sites has to be plotted on different scales in Fig. 3.8a.

So in Fig. 3.14 the quadrupole broadening is compared for the O(3) site with the field applied along

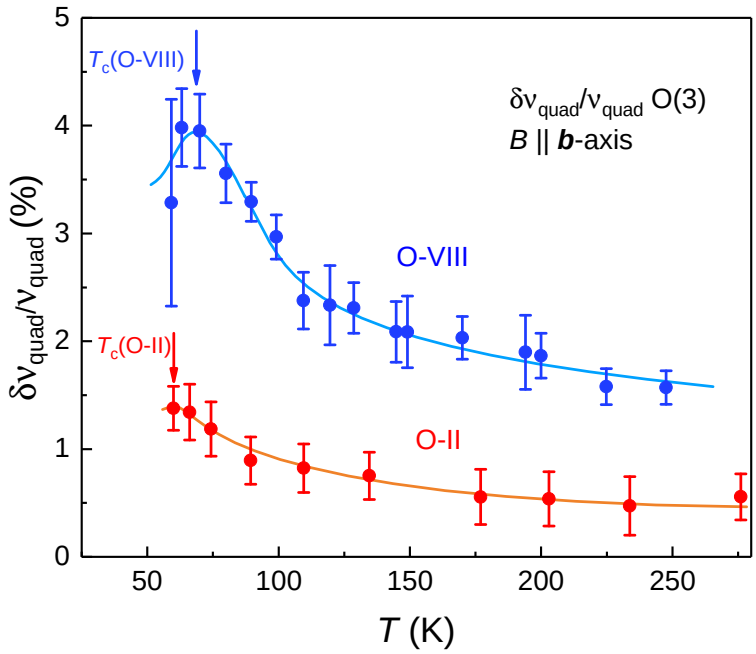

Figure 3.14: T dependence of the dimensionless quadrupole broadening $\frac{\delta\nu_{\rm quad}}{\nu_{\rm quad}}$ of the O(3E/F) sites of O-II sample (red circles) and the O(3F) site of the O-VIII sample (blue circles) measured in the same orientation B along the ***b***-axis at fields of 12 T and 15 T, respectively. Lines are guides to the eye. The O-II data has been reproduced from ref. [87].

the ***b***-axis for both samples. Evidently, the quadrupole broadening is about two to three times larger in the O-VIII sample. This is true both at high T, where the quadrupole broadening is dominated by $\delta\nu_{\rm quad,0}$, as well as at low T, where the T-dependent contribution $\delta\nu_{\rm quad,c}$ is largest. Increasing quadrupole broadening when going from O-II with hole dopings $p \approx 0.10$-0.11 to O-VIII samples ($p \approx 0.12$-0.125) is consistent with the XRD intensity being largest for $p \approx 0.12$-0.125 [86, 84]. At high T. the fact that $\delta\nu_{\rm quad,0}/\nu_{\rm quad}$ is larger for the O-VIII sample than for O-II is a sign of increased disorder.

As discussed before, it is not clear how to determine precisely $\delta\nu_{\rm quad,c}$ when $\delta\nu_{\rm quad,0}$ is not negligible, so we can only compare samples on a qualitative level.

3.2 Simulation of the lineshapes and linewidths for uniaxial & bi-axial CDWs

To see which difficulties exist in determining the structure of the CDW from the NMR lineshapes, it is helpful to consider the inverse problem first: Given a particular well characterised charge modulation - that implies knowing its dimensionality (uniaxial $1q$, bi-axial $2q$, etc.), its profile (sinusoid, box-shape,

etc.), its form factor (s, s'+d, etc.)[3], its amplitude and its wave vector - how should the NMR-spectrum look like? Already for the simple case of a uniaxial $1q$ commensurate sinusoidal charge modulation it is not evident how to answer this question because the NMR spectrum is measured as a function of nuclear resonance frequency and not directly as a function of charge amplitude. For ^{63}Cu & ^{17}O-NMR in cuprates, the information about the charge amplitude is encoded in the corresponding distribution of the quadrupole frequency ν_Q and the Knight shift K. Decoding these distributions is not easy, because ν_Q is proportional to the gradient of the electric field (EFG) resulting from the charge modulation. In principle, the EFG can have a non-linear dependence on the local charge amplitude, so in special cases the EFG might decrease although the local charge amplitude increases.

When NMR spectra of CDW systems are analysed, a standard assumption is that the EFG and thus also ν_Q are linearly proportional to the local amplitude of the charge density. Then it is simple to simulate spectra by plotting histograms of the CDW amplitudes, sampled at the nuclear positions. It is of interest to see how the EFG behaves with doping in case of cuprates, because this can allow to see to which extent the assumption of linear proportionality between ν_Q and doping is appropriate. On average, linear increase of ν_Q with hole doping seems to be equally correct for electron doped [129][4] and hole doped cuprates, both for in-plane Cu(2) and O(2) & O(3) sites [130, 131, 132]. However, especially in the case of YBCO, one should keep in mind that ordered chain superstructures create different local sites like O(3E) & O(3F) and Cu(2E) & Cu(2F) whose relative differences in ν_Q are not negligible in comparison with the total effect due to doping. Still, for each individual site the assumption of linear proportionality should be correct [133].
First, we model spectra assuming linear proportionality of the charge amplitude and ν_Q. The effect of an additional quadratic term is discussed later.

3.2.1 Basic principles of the lineshape simulation

We can now present how simulated NMR spectra look like for sinusoidal uniaxial $1q$ and bi-axial $2q$ modulations. What is presented in the following is partly based on work of Michihiro Hirata during his Post-doc in Grenoble.

To discuss commensurate and incommensurate modulations one needs to define the wave vector of a modulation. XRD studies in YBCO find biaxial incommensurate CDW modulations along the $\boldsymbol{a}$ and

[3]The form factor determines how charge density is distributed on Cu-atoms and the four surrounding O-atoms. s: charge on Cu only, s': isotropic charge on O only, d: π-phase shift between charge modulations on adjacent O-atoms. Mixtures like s'+d are possible.

[4]For increasing electron doping ν_Q decreases in electron doped cuprates.

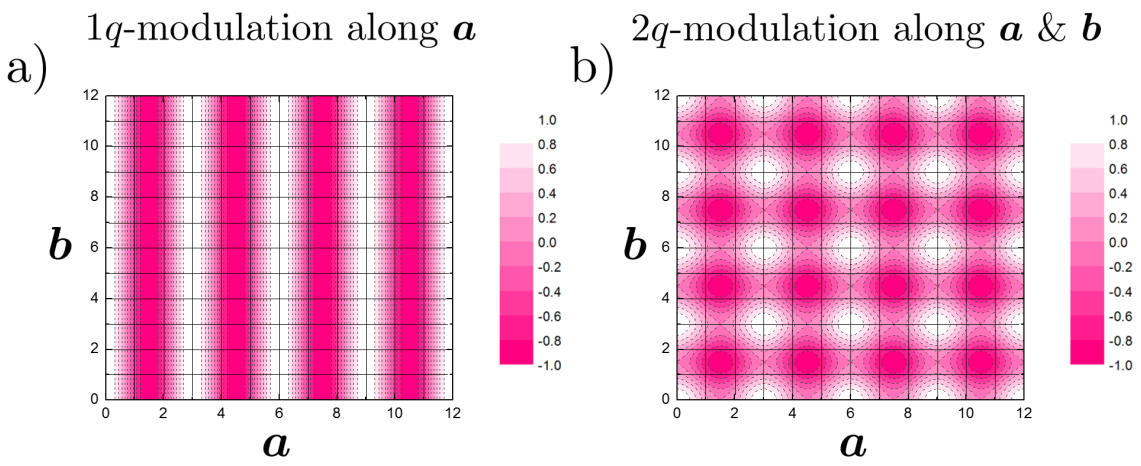

Figure 3.15: a): Charge pattern for a uniaxial $1q$ modulation along the $\boldsymbol{a}$-axis with wave vector $\boldsymbol{q}_a = (H, 0)$ with $H = 0.31$. b): Bi-axial $2q$ modulation which results from the sum of two uniaxial modulations along $\boldsymbol{q}_a = (H, 0)$ and $\boldsymbol{q}_b = (0, K)$. Continuous lines separate unit cells and define the underlying lattice. The figures were made by Michihiro Hirata.

$\boldsymbol{b}$-axes with wave vectors ≈ 0.31 r.l.u., which is close to, but distinct from the commensurate value of $1/3$ r.l.u.[5]. It is thus interesting to see which type of NMR spectrum is expected for incommensurate modulations.

We discuss uniaxial and bi-axial modulations and formulate them in a way that is general for both commensurate and incommensurate modulations. We start with the spatial modulation of ν_{Q} and generalise thereafter to the case of correlated modulations of ν_{Q} and K.

Starting with a $1q$ modulation and excluding any $\boldsymbol{c}$-axis component, an exemplary in-plane wave vector $\boldsymbol{q} = (H, 0)$ would lead to a charge modulation $\rho(\boldsymbol{r})$ of amplitude $\Delta\rho$ around an average charge density ρ_0 at a particular lattice site, as shown in Fig. 3.15a. For commensurate modulations the phase ϕ relates the shift of the maxima of the modulation with respect to the closest lattice position. Since each maximum of an incommensurate modulation is shifted differently with respect to the closest lattice position, the phase ϕ has no meaning for the incommensurate modulation and can be set to 0. For a $1q$ CDW with wave vector $\boldsymbol{q} = (H, 0)$ one gets[6]:

$$\begin{aligned}\rho(\boldsymbol{r}) &= \rho_0 + \Delta\rho\cos(\boldsymbol{q}\cdot\boldsymbol{r} + \phi) \\ &= \rho_0 + \Delta\rho\cos(H\frac{2\pi}{a}\cdot xa + \phi) \\ &= \rho_0 + \Delta\rho\cos(2\pi H\cdot x + \phi)\end{aligned}$$

[5]Wave vector coordinates in reciprocal space are usually given in *relative length units* (r.l.u.) with (H,K,L) meaning $(H\frac{2\pi}{a}, K\frac{2\pi}{b}, L\frac{2\pi}{c})$. In the following real-space coordinates $\boldsymbol{r}$ will be given in units of the unit cell parameters $\boldsymbol{r}=(xa, yb, zc)$.

[6]In reality, it is possible that the actual modulation deviates from a sinusoidal form the level of resolution of the CDW in cuprates does currently not allow to address this question in general.

Assuming that the EFG is proportional to the charge density, we can write

$$\nu_{\mathrm{Q}}(x) = \nu_{\mathrm{Q},0} + \Delta\nu_{\mathrm{Q}} \cos(2\pi H \cdot x + \phi) \tag{3.9}$$

This equation says that if the charge density ρ is modulated in the range of $\pm\Delta\rho$, then the quadrupole frequencies $\nu_{\mathrm{Q}}(x)$ will be modulated proportionally in the range of $\pm\Delta\nu_{\mathrm{Q}}$. $\nu_{\mathrm{Q}}(x)$ varies in space, but NMR does not resolve it spatially. Each nucleus samples the amplitude of the modulation at its atomic position. Thus, the NMR spectrum gives a histogram of the sampled amplitudes. More precisely, since every nucleus of a particular lattice site contributes to a set of peaks (the central peak and the satellite peaks), the histogram of the sampled amplitudes will in principle be visible in the lineshape of each of these peaks. Satellite peaks will, of course, have a higher sensitivity to a spatial modulation of $\nu_{\mathrm{Q}}(x)$ than the central peak.

This histogram is sensitive to the dimensionality of the modulation and can distinguish incommensurate and commensurate wave vectors, as will be shown in the following. It is easy to extend from a uniaxial to a bi-axial modulation, *i.e.* joint modulations along $\boldsymbol{q}_a = (H, 0)$ and $\boldsymbol{q}_b = (0, K)$[7] which have the following density:

$$\begin{aligned}\rho(\boldsymbol{r}) &= \rho_0 + \frac{\Delta\rho}{2}\cos(\boldsymbol{q}_a \cdot \boldsymbol{r} + \phi_a) + \frac{\Delta\rho}{2}\cos(\boldsymbol{q}_b \cdot \boldsymbol{r} + \phi_b) \\ &= \rho_0 + \frac{\Delta\rho}{2}\cos(2\pi H \cdot x + \phi_a) + \frac{\Delta\rho}{2}\cos(2\pi K \cdot y + \phi_b)\end{aligned}$$

To have a maximal and minimal charge amplitude of $\pm\Delta\rho$, as for the uniaxial modulation, we choose to divide each component by 2, See Fig. 3.15b. Here the amplitudes of the modulations along $\boldsymbol{q}_a = (H, 0)$ and $\boldsymbol{q}_b = (0, K)$ are chosen to be equal, but it is also possible to introduce anisotropy. As in the case of a uniaxial modulation one finds a spatial modulation of ν_{Q}:

$$\nu_{\mathrm{Q}}(x, y) = \nu_{\mathrm{Q},0} + \frac{\Delta\nu_{\mathrm{Q}}}{2}\cos(2\pi H \cdot x + \phi_a) + \frac{\Delta\nu_{\mathrm{Q}}}{2}\cos(2\pi K \cdot y + \phi_b) \tag{3.10}$$

These equations are valid for both commensurate and incommensurate wave vectors.

Lineshapes for $1q$ & $2q$ incommensurate modulations

In Fig. 3.16 histograms of a uniaxial and a bi-axial incommensurate CDW are shown. They are constructed numerically from eq. 3.9 and eq. 3.10 by counting how frequently each particular ν_{Q} value is realised. Singularities in the $1q$ case come from the extrema which are sampled most frequently [134, 135]. The histogram of the $2q$ modulation has only one peak, centered at zero shift. These singularities are very sharp in the limit of infinite correlation length but, due to other broadening

[7] XRD studies have not found checker-board CDWs with wave vectors $(\pm H, \pm K)$, so we restrict ourselves to wave vectors along the CuO bonds.

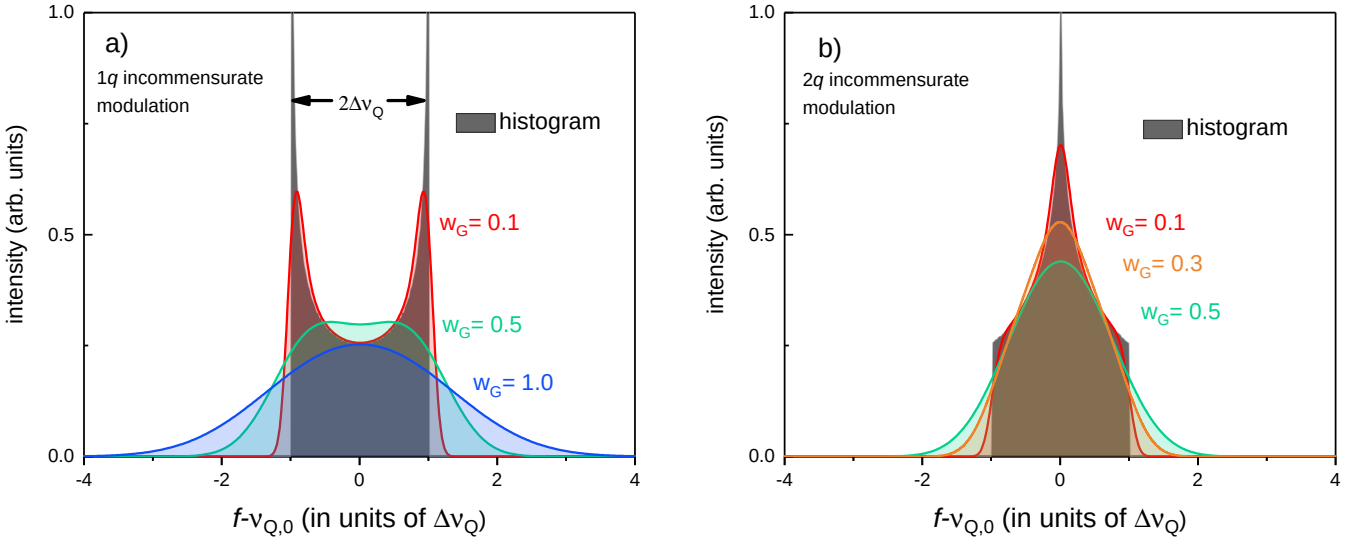

Figure 3.16: a): Here the histogram (grey colour) of a uniaxial incommensurate modulation is determined from eq. 3.9. The histogram is centered at $\nu_{\mathrm{Q},0}$ and the two singularities are separated by the maximum possible value $2\Delta\nu_{\mathrm{Q}}$, as defined by eq. 3.9. To simulate the effect of other broadening contributions (uncorrelated magnetic broadening $\delta\nu_{\mathrm{mag},0}$, disorder, etc.) the histogram is convoluted with Gaussians of different widths w_{G}. w_{G} is measured in units of $\Delta\nu_{\mathrm{Q}}$. The integrated area of the broadened shapes is identical to the area of the histogram b): Histogram of a bi-axial incommensurate modulation as determined from eq. 3.10. Since this histogram's singularity is in the center it is more easily smoothed than in the $1q$ case.

contributions, the singularities will be smoothed. These shapes are independent of the value for the phases ϕ and are also independent of the particular values of the wave vectors as long as they are both incommensurate, so from NMR it is not possible to determine if an incommensurate wave vector q=0.3101 is closer to the value 1/3 or 1/4. But evidently, the dimensionality of the modulation can be determined from the number of peaks, as long as the peaks are resolved.

Adding the Knight shift modulation

What is shown so far for the quadrupole frequencies $\nu_{\mathrm{Q}}(x)$ & $\nu_{\mathrm{Q}}(x,y)$ also applies to the Knight shifts $K(x)$ & $K(x,y)$ for $1q$ and $2q$ charge modulations, respectively. As discussed previously, the correlated magnetic broadening $\delta\nu_{\mathrm{mag,c}}$ of O(2) should be correlated with the quadrupole broadening $\delta\nu_{\mathrm{q}}$, because the modulated charge density $\rho(\boldsymbol{r})$ does not only modulate $\nu_{\mathrm{Q}}(\boldsymbol{r})$ but also the Knight shift $K(\boldsymbol{r})$. As both ν_{Q} as well as K are increasing with doping [44] the Knight shift $K(\boldsymbol{r})$ should follow the modulation of $\rho(\boldsymbol{r})$ in a similar way as $\nu_{\mathrm{Q}}(\boldsymbol{r})$. If the Knight shift $K(\boldsymbol{r})$ were not correlated with the quadrupole frequencies $\nu_{\mathrm{Q}}(\boldsymbol{r})$ then it would just broaden the quadrupolar lineshapes as uncorrelated magnetic broadening $\delta\nu_{\mathrm{mag},0}$.

So, by analogy, for uniaxial modulations one finds:

$$K(x) = K_0 + \Delta K \cos(2\pi H \cdot x + \phi) \tag{3.11}$$

For bi-axial modulations, one should be careful not to confuse the Knight shift K with the wave vector $(0, K)$ which appears in the argument of the second cosine.

$$K(x,y) = K_0 + \frac{\Delta K}{2}\cos(2\pi H \cdot x + \phi_a) + \frac{\Delta K}{2}\cos(2\pi K \cdot y + \phi_b) \tag{3.12}$$

For the case of $1q$ and $2q$ incommensurate modulations of the charge density, the Knight shift K should give the same incommensurate histograms as in Fig. 3.16. The only difference is that $\Delta\nu_{\mathrm{Q}}$ should be replaced by $\gamma B\Delta K$. The factor γB is necessary to get the frequency shift, since the NMR spectrum is recorded as a function of frequency.

Under the assumption that quadrupole frequencies and Knight shifts are perfectly correlated, the lineshapes of the NMR peaks will remain unchanged. Only the width of the histograms will change as it will be determined by the combination of $\Delta\nu_{\mathrm{Q}}$ and $\gamma B\Delta K$. In close analogy to the discussion of the correlation of $\delta\nu_{\mathrm{mag,c}}$ with $\delta\nu_{\mathrm{q}}$, $\Delta\nu_{\mathrm{Q}}$ and $\gamma B\Delta K$ are additive for $HF1$ and $HF2$ whilst being subtracted on the low frequency satellites $LF1$ and $LF2$. The total frequency shifts, which are valid for correlated quadrupole and Knight shifts for both commensurate and incommensurate uniaxial and bi-axial modulations are summarised in the following set of equations:

$$\Delta f_{\mathrm{tot,HF2}} = 2\Delta\nu_{\mathrm{Q}} + \gamma B\Delta K \tag{3.13a}$$

$$\Delta f_{\mathrm{tot,HF1}} = \Delta\nu_{\mathrm{Q}} + \gamma B\Delta K \tag{3.13b}$$

$$\Delta f_{\mathrm{tot,central}} = \gamma B\Delta K \tag{3.13c}$$

$$\Delta f_{\mathrm{tot,LF1}} = \Delta\nu_{\mathrm{Q}} - \gamma B\Delta K \tag{3.13d}$$

$$\Delta f_{\mathrm{tot,LF2}} = \Delta\nu_{\mathrm{Q}} - \gamma B\Delta K \tag{3.13e}$$

For incommensurate modulations $2\Delta f_{\mathrm{tot}}$ is equal to the total width of the incommensurate lineshape, as visible from Fig. 3.16. For commensurate modulations with a finite number of peaks in the histogram (see e.g. Figs. 3.20 & 3.21) the maximal separation of the peaks can depend on the phase ϕ and is not necessarily equal to $2\Delta f_{\mathrm{tot}}$, but this quantity is proportional to the separation of the resolved peaks. Since $\Delta f_{\mathrm{tot,HF2}}$ is largest, any singularity or splitting in the NMR spectrum is expected to first become visible on the $HF2$ satellite.

3.2.2 Lineshape analysis in the short-ranged 2D CDW phase

One can try to use this model to determine which type of modulation could account for the observed line broadenings in the short-ranged CDW phase. Since XRD studies find a bi-axial modulation with incommensurate wave vectors, we would expect to see the incommensurate lineshape shown in Fig. 3.16b. However, if the short-ranged CDW consists of domains of incommensurate uniaxial modulations, then NMR, being a local probe, would see the corresponding lineshape, shown in Fig. 3.16a.

These lineshapes can be resolved in the limit of low disorder and small magnetic field because then magnetic broadening becomes small and the remaining contribution to lineshape is of quadrupolar origin. In ^{17}O-NMR the low field limit is out of reach: fields of at least 10 T must be applied in order to have good signal. For the well-ordered O-II sample, even close to T_c where the quadrupole and the correlated magnetic broadenings become maximal, no measured satellite peak deviates remarkably from Voigt or Gaussian lineshapes and no singularities characteristic of uniaxial or bi-axial incommensurate lineshapes could be resolved. Is this consistent with the presented model? To test this, we estimate whether the determined uncorrelated magnetic broadening shown in Fig. 3.6 and effects of disorder are sufficiently large to mask any singularity of the CDW.

From Fig. 3.16 one can see that when Gaussian broadening becomes large and $w_G \gtrsim 0.5\Delta\nu_Q$ is satisfied, then the singularities of the uniaxial incommensurate lineshape are effectively washed out. For the bi-axial incommensurate modulation $w_G \gtrsim 0.3\Delta\nu_Q$ would already mask any singularity. Including the correlated modulation of the Knight shift this inequality becomes $w_G \gtrsim 0.5\Delta f_{tot}$ & $w_G \gtrsim 0.3\Delta f_{tot}$. We estimate w_G and Δf_{tot} from the broadening contributions of O(2): $\delta\nu_{mag,0}$ contributes to w_G and $\delta\nu_q$ & $\delta\nu_{mag,c}$ contribute to Δf_{tot}.

Assuming $\Delta\nu_Q \approx \delta\nu_q$ and $\gamma B\Delta K \approx \delta\nu_{mag,c}$[8], for the $HF2$ satellite we find that if the approximate expression

$$\delta\nu_{mag,0} \gtrsim 0.5\Delta f_{tot,HF2} \approx 0.5(2\delta\nu_q + \delta\nu_{mag,c}) \qquad 1q\text{-detection limit}$$

is true, then even on the $HF2$ satellite any singularity from a uniaxial incommensurate modulation should be smoothed. For the bi-axial modulation the corresponding inequality is

$$\delta\nu_{mag,0} \gtrsim 0.3(2\delta\nu_q + \delta\nu_{mag,c}). \qquad 2q\text{-detection limit}$$

The comparison of $\Delta f_{tot,HF2}$ and w_G is shown in Fig. 3.17a. $\Delta f_{tot,HF2}$ lies above the $1q$-detection limit but below the $2q$-detection limit. In Fig. 3.17b, a few $HF2$ satellites in the relevant T range are shown. The spectrum at 59.3 K allows to exclude that the quadrupole broadening is due to a purely uniaxial incommensurate modulation. At lower T, small deviations from the symmetric Voigt lineshape appear and the peak develops a small asymmetry which is not expected for an incommensurate modulation, but the signal-to-noise ratio decreases strongly approaching the temperature of vortex melting and thus does not allow to determine the form of the charge modulation.

In conclusion, the origin of the quadrupole broadening in the short-ranged CDW phase is likely to be bi-axial. However, it is not necessarily incommensurate, since commensurate 2D modulations can, depending on the phases ϕ_a and ϕ_b, have many overlapping peaks that result in a nearly symmetric lineshape, as shown in Fig. 3.18b. They would also remain unresolved.

[8] The total width of the histogram on the $HF2$ satellite is $2\Delta f_{tot,HF2}$, but since $\delta\nu_q$ and $\delta\nu_{mag,c}$ correspond to the FWHM of Gaussian broadening contributions, the FWHM of the histogram is approximated as half of its total width.

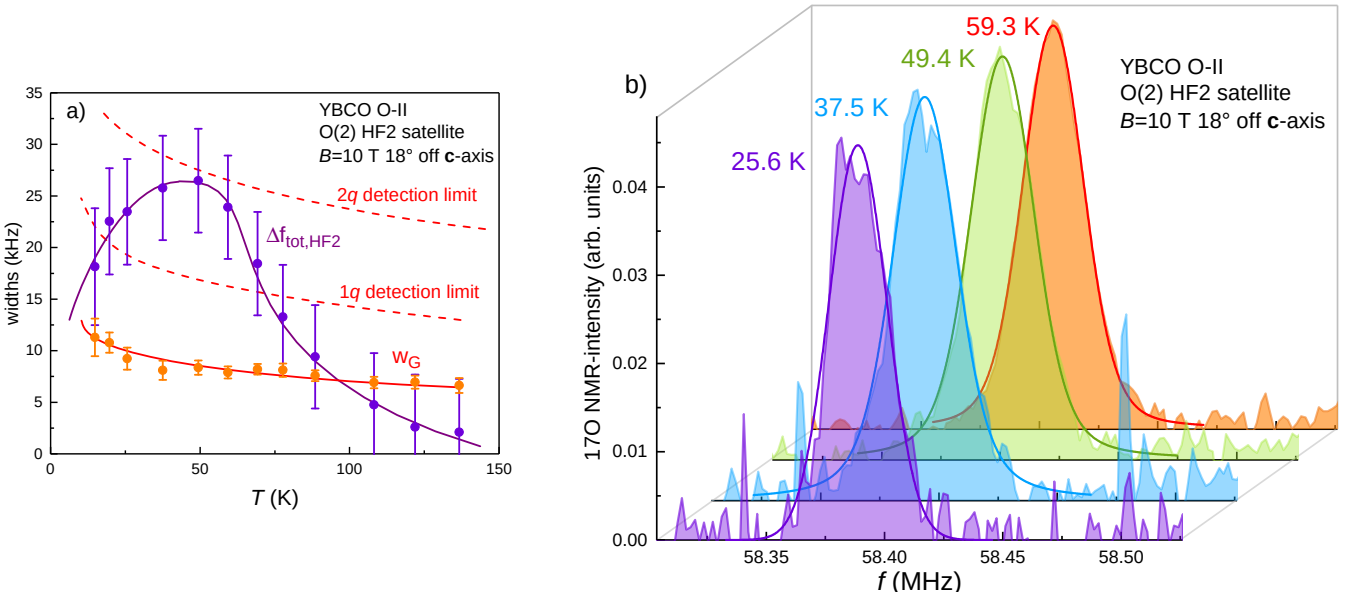

Figure 3.17: a): T-dependence of the estimated width of a lineshape due to a CDW modulation given by $\approx \Delta f_{\mathrm{tot,HF2}}$ (purple circles) and the corresponding T-dependence of the effects of disorder and uncorrelated magnetic broadening, w_{G} (orange circles). Detection limits for $1q$ and $2q$ incommensurate modulations are estimated by $2w_{\mathrm{G}}$ and $3.3w_{\mathrm{G}}$, respectively. Lines are guides to the eye. b): $HF2$ satellite spectra for a few temperatures for $T < T_{\mathrm{c}}$ where lineshapes could be affected by a $1q$ incommensurate modulation. Lines are fits to the symmetric Voigt lineshape.

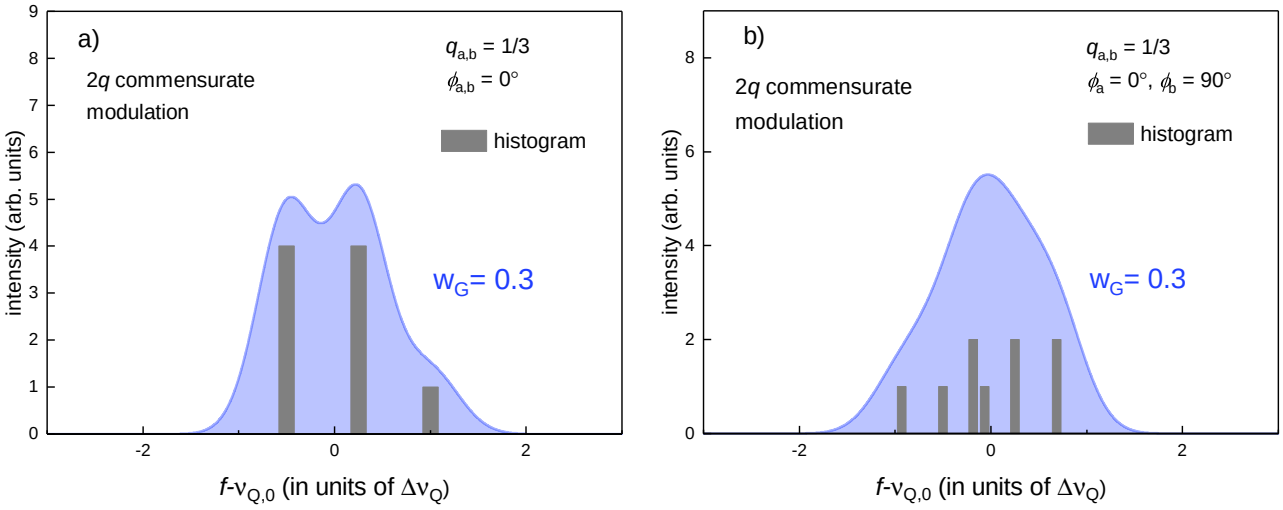

Figure 3.18: a): Expected NMR-spectrum for a $2q$ commensurate modulation with wave vector q=1/3 along the $\boldsymbol{a}$ and $\boldsymbol{b}$ axes and equal phases $\phi_a = \phi_b = 0$. The corresponding histogram has been broadened by a Gaussian of width w_{G}=0.3 (in units of $\Delta\nu_{\mathrm{Q}}$). b): Analogous NMR-spectrum as in a) with the difference that the phases are unequal $\phi_a = 0$, $\phi_b = 0$. Evidently, a bi-axial modulation can lead to a large number of peaks that will overlap.

Low field NMR ($B \lesssim 3$ T) of the $HF2$ satellite close to T_c is predicted to be able to resolve the lineshape of a 2D incommensurate modulation, since in the limit of low fields the uncorrelated magnetic broadening becomes small in the O-II sample, where $\delta\nu_{\mathrm{quad},0} \approx 0$.

3.2.3 Beyond the linear model

Up to this point it has been assumed that the EFG is linearly proportional to the charge density. In the spirit of a Taylor expansion, we can introduce a quadratic term to improve this model. We do this for uniaxial modulations only, but equivalent treatment in bi-axial modulations is also possible. Eq. 3.9 is then extended by a quadratic term:

$$\nu_{\mathrm{Q}}(x) = \nu_{\mathrm{Q},0} + \quad a_1\Delta\rho(\boldsymbol{r}) \quad + \frac{a_2}{2}\Delta\rho(\boldsymbol{r})^2 \tag{3.14}$$

$$\nu_{\mathrm{Q}}(x) = \nu_{\mathrm{Q},0} + \Delta\nu_{\mathrm{Q},1}\cos(2\pi H\cdot x+\phi) + \frac{\Delta\nu_{\mathrm{Q},2}}{2}\cos^2(2\pi H\cdot x+\phi) \tag{3.15}$$

Here $\Delta\nu_{\mathrm{Q},1}$ is linearly proportional to the amplitude of the modulation $\Delta\rho(\boldsymbol{r})$ through a_1 and $\Delta\nu_{\mathrm{Q},2}$ is proportional to the square of the modulation. $\Delta\nu_{\mathrm{Q},1}$ and $\Delta\nu_{\mathrm{Q},2}$ have units of frequency.
If this quadratic model is used for an incommensurate $1q$ modulation then the histogram is not symmetric and the right singularity is decreased for $\Delta\nu_{\mathrm{Q},2}>0$. An example is shown in Fig. 3.19.
We expect that $\Delta\nu_{\mathrm{Q},2}$ is small with respect to $\Delta\nu_{\mathrm{Q},1}$. Otherwise ν_Q would not increase linearly with doping, as inferred from NMR and NQR measurements in hole and electron doped cuprates [129, 130, 131, 132].

3.2.4 Simulation of the line splitting

In principle, simulations of line splitting do not differ conceptually from simulations of lineshapes. Line splittings are found when the amplitudes of the charge modulations become large compared to other width contributions, like disorder or uncorrelated magnetic broadening. An example of this has been shown in Fig. 3.16a and in Fig. 3.19 for the $1q$ incommensurate modulation.
The focus will now be on commensurate $1q$ modulations since NMR-spectra from O(2) sites in the high field 3D CDW phase are well described by a commensurate $1q$ modulation of period $3a$ or $3b$ (where a and b are the unit cell parameters). From NMR-spectra of O(2) alone, it is not possible to determine whether the modulation is along the $\boldsymbol{a}$-axis or $\boldsymbol{b}$-axis.
To be precise, a commensurate modulation has a wave vector $\boldsymbol{q}$=(H,K), where H & K can be written as ratios, e. g. $H = \frac{m}{n}$, where m and n are integers. Simulations of NMR spectra are made, as shown previously for incommensurate modulations, by sampling the spatially modulated quadrupole frequencies $\nu_{\mathrm{Q}}(x)$ for $1q$ and $\nu_{\mathrm{Q}}(x,y)$ for $2q$ (analogously for Knight shift $K(x)$ & $K(x,y)$) at the atomic positions of the nuclei and the construction of corresponding histograms. Even in the limit of

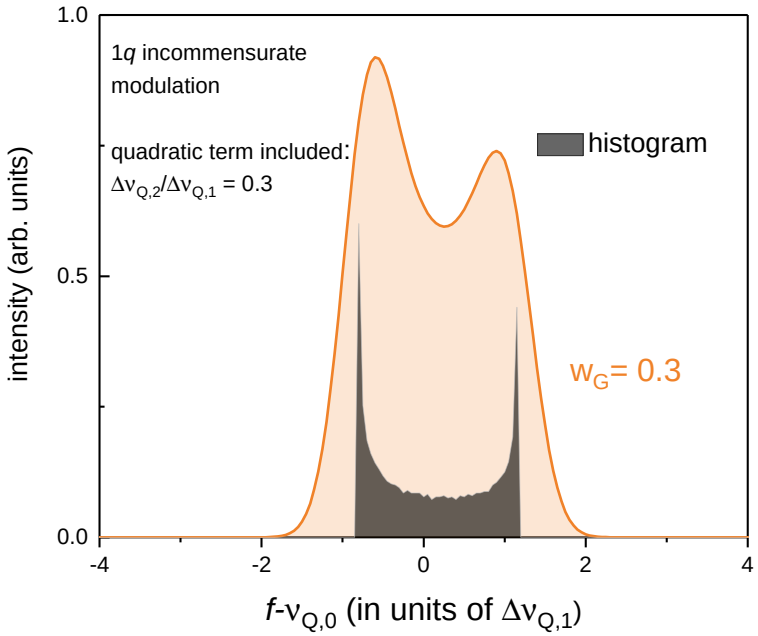

Figure 3.19: Expected NMR-spectrum for a uniaxial incommensurate modulation within the quadratic model, as defined by eq. 3.14. Here, $\Delta\nu_{Q,2}/\Delta\nu_{Q,1} = 0.3$, so the quadratic term is smaller than the linear term. Gaussian broadening of 0.3 in units of $\Delta\nu_{Q,1}$ has been added.

infinite correlation length, the histograms of commensurate modulations are discrete. Since a wave vector $H = \frac{m}{n}$ belongs to a modulation that repeats its m oscillations every n unit cell parameters, there are at most n distinct quadrupole frequencies for $1q$. Simultaneously, this means that NMR can distinguish different commensurate wave vectors. The phase ϕ is important for commensurate modulations, since the choice of a particular ϕ can lead to different overlap of contributions to the histogram. In the limit of large n, peaks in the histogram will overlap and one recovers effectively the same histogram as for an incommensurate modulation.

$1q$ commensurate modulations, $q = 1/3$ & $q = 1/4$

Repeated discommensurations (phase slips of $k\times 2\pi/n$) can allow a modulation with an incommensurate wave vector to become commensurate with the lattice in between two phase slips [136], as will be discussed in depth in the following. In this context the commensurate wave vector $q = 1/3$ is relevant to the discussion of charge order in YBCO, since it is close to the incommensurate wave vector found by XRD. Blackburn *et al.* are the first to have suggested $q = 1/3$ for ^{63}Cu-NMR data in the long-range CDW phase although their idea was not linked to discommensurations but rather that the CDW undergoes a lock-in transition from an incommensurate to a commensurate wave vector [137].
Fig. 3.20 visualises how histograms of the uniaxial commensurate $q = 1/3$ modulation depend on the phase ϕ. Since the number of atoms per period is an odd integer ($n/m = 3$), it is possible to have asymmetric histograms, as can be seen in panels k) and m) for $\phi = 0°$ and $\phi = 60°$, respectively. With

the exception of particular phases, like $\phi = 30°$ and $\phi = 60°$ (panels l & n), the NMR spectrum is generally expected to be asymmetric for $q = 1/3$.

If n is an even number, this is no longer the case, irrespective of ϕ. That even n leads to symmetric spectra can be visualised by a polar plot for $q = 1/4$. The phase is chosen to be irrational $\phi = \pi/e$, where e is Euler's constant, and the resulting spectrum is symmetric, as shown in Fig. 3.21.

3.2.5 Discommensurations

Discommensurations have been introduced by McMillan to describe CDW phases in the layered transition metal dichalcogenide $2H$-$TaSe_2$ [138]. In $2H$-$TaSe_2$ there are three wave vectors corresponding to three propagation directions at 120° to each other. The CDW was found to undergo a sequence of transitions: Upon cooling down, at 120 K an incommensurate CDW appears in which the wave vectors are of length $Q = 1/3 - \delta$, *i.e.* incommensurate with the lattice. The incommensurability δ is T-dependent and upon further cooling it decreases until it disappears at 90 K. Below 90 K the CDW wave vectors lock in with the lattice to the commensurate value $Q_0 = 1/3$ [139, 140].

In the framework proposed by McMillan, the CDW is actually commensurate even above 90 K: While the period of the modulation is locally always $3a$, repeated phase slips of $2\pi/3$ occur, called discommensuration, where the phase jumps. Since the phase is not constant, it can affect the wave vector measured in diffraction experiments. In $2H$-$TaSe_2$ repetitive discommensurations make the wave length of the modulation appear to be different from $3a$ on a larger scale and decreasing incommensurability δ is a measure of the density of the discommensurations. NMR measurements by Suits *et al.* in $2H$-$TaSe_2$ are consistent with the framework proposed by McMillan [141]. Since NMR is a local probe it can be used to test whether the modulation is commensurate with the lattice on the local scale.

Discommensurations do not always lead to incommensurate wave vectors. Soumyanarayanan *et al.* from Jennifer Hoffman's group have studied $2H$-$NbSe_2$ with STM and found a $1q$ commensurate modulation with wave vector $Q = 2/7$, but whose local period is $3a$ [142]. Repeated phase slips of $2\pi/3$ increase the apparent wave vector to $Q = 2/7$ while the local modulation has $Q_0 = 1/3$, as shown in Fig. 3.22.

Study of discommensurations by Mesaros' *et al.*

Recently Mesaros *et al.* have shown that the charge density modulations in STM images of underdoped $Bi_2Sr_2CaCu_2O_{8+x}$ (Bi-2212) are best fit by a commensurate period of $4a$. They have explained how discommensurations can shift the position of the CDW peaks in the Fourier transforms of the STM images away from the wave vector $Q_0 = 1/4$ that corresponds to the commensurate modulations of

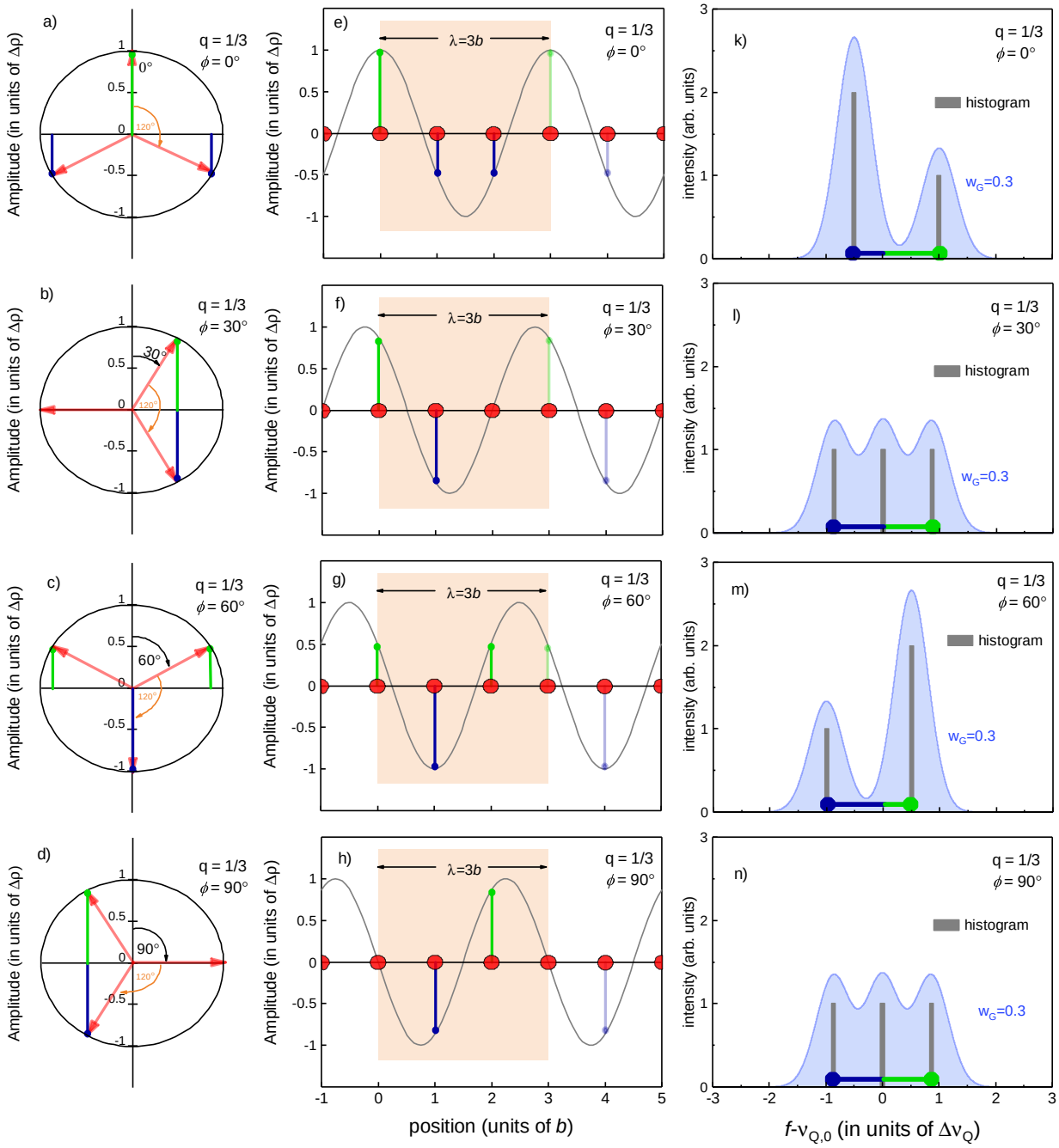

Figure 3.20: Panels k)-n) show the phase (ϕ) dependence of the NMR spectra for a commensurate modulation with wave length $\lambda = 3b$ that are based on histograms that are by convoluted with a Gaussian of width $w_G = 0.3$. The histograms are determined by sampling the modulation (grey line) at the atomic positions (red circles), as shown in panels e)-h). Atoms that experience a large positive amplitude (vertical axis) have a large positive quadrupole shift $f - \nu_{Q,0}$ in the NMR spectra (horizontal axis). Positive (negative) shifts are green (blue), atoms situated at nodes of the modulations have a zero shift.

Polar plots in a)-d) serve to visualise how the amplitude of the modulation at each atom changes with increasing phase ϕ. Each atom is represented by a red arrow of unit length and the angle between two arrows is $360°/3 = 120°$. The arrows projections on the vertical axis directly give the modulation's amplitude at the atomic position. From the polar plot it is easily seen when the resulting NMR spectrum is symmetric.

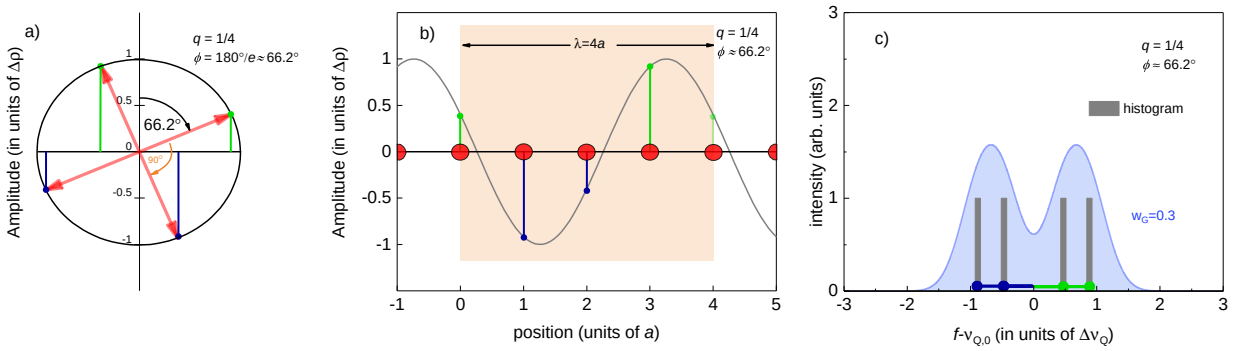

Figure 3.21: Panels a)-c) show the expected NMR spectrum for a commensurate modulation with wave length $\lambda = 4a$ and an irrational phase ($\phi = \pi/e \approx 66.2°$), based on the histogram that was convoluted with a Gaussian of width $w_G = 0.3$. Panel c) shows that it can be difficult to resolve all four peaks due to finite widths, however the spectrum remains symmetric.

Panel a) visualises that for modulations with even n every atom (represented by a red arrow) experiencing a positive amplitude there exists a complementary atom (arrow rotated by 180°) experiencing a negative amplitude of the same magnitude, so resulting histograms are always symmetric.

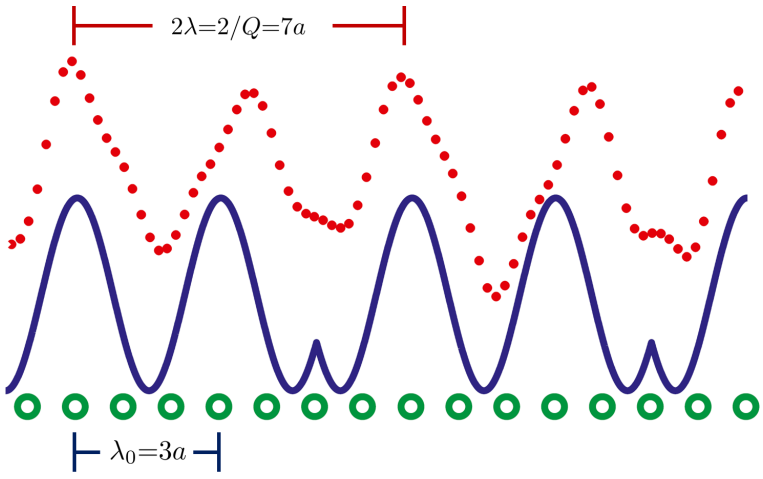

Figure 3.22: Q=2/7 1q modulation with discommensurations in 2H-$NbSe_2$. The blue line is a modulation with local period $\lambda_0 = 3a$ and repeated phase slips of $2\pi/3$. Green circles mark the atomic lattice positions. The red dotted line is a line-cut of the experimental STM image along the direction of the uniaxial modulation, which has two apparent periods per $7a$. The figure is reproduced from ref. [142].

period $4a$. Their simulations were made for $Q_0 = 1/4$ ($n = 4$) but their explanations are equally valid for other commensurate charge modulations and in particular for $Q_0 = 1/3$ ($n = 3$), the wave vector relevant to the discussion of YBCO.

Mesaros *et al.* discuss the case of uniaxial modulations in detail, where the modulation is given by

$$\Psi(x) = A\exp[i\Phi(x)] = A\exp[i(Q_0 x + \varphi)] \tag{3.16}$$

It is a plane wave with amplitude A and a position-dependent phase argument $\Phi(x)$. The slope with which $\Phi(x)$ increases is entirely determined by the wave vector Q_0 if the phase φ is constant. However, if discommensurations occur, where the phase changes in steps of $2\pi/n$, the phase φ becomes position-dependent and is given by $\varphi(x)$. The slope of the phase argument $\Phi(x)$ and consequently the apparent wave vector of the modulation can change if discommensurations of the same sign occur repeatedly. The new wave vector is given by the average slope $\overline{Q}$, defined by the following equation:

$$\Phi(x) = Q_0 x + \varphi(x) = \overline{Q}x + \widetilde{\varphi}(x) \tag{3.17}$$

$\widetilde{\varphi}(x)$ contains the residual phase fluctuations which remain after $\overline{Q}x$ is subtracted from the phase argument $\Phi(x)$. They will average to zero ($\overline{\widetilde{\varphi}(x)} = 0$), but can lead to additional structure in the Fourier transform. Fig. 3.23 serves to visualise how repeated discommensurations of $+\pi$ increase the average slope of the phase argument $\Phi(x)$ which is reflected in a positive shift of the main peak in the Fourier transform of the modulation $|\Psi(q)|$. If the discommensurations are ordered then satellite peaks appear but their size is strongly dependent on the disorder of the discommensuration pattern and on the amount of discommensurations.

An intuitive approach to the effect of discommensurations is to comare the number of maxima that appear in a given window of the modulation with the number of periods that the undistorted modulation (*i.e.* without discommensurations) would have in the same window. In panel Ai of Fig. 3.23, in a window with length $8 \times 4a$, the undistorted modulation with $Q_0 = 1/4$ would make 8 periods equivalent to 8 maxima, whereas discommensurations allow to increase the number of maxima up to 10. Thus the average wave vector becomes $\overline{Q} \approx 10/32 = 0.31$. The positive phase slips of $+\pi$ increased the phase argument $\Phi(x)$ as if the underlying modulation had a wave vector of $\overline{Q} \approx 0.31$. The more numerous discommensurations are, the faster the phase argument will grow and the larger the incommensurability $\delta = \overline{Q} - Q_0$ will be.

Coming back to the example of discommensurations in the uniaxial modulation in $2H$-$NbSe_2$ this means that if the Fourier transform of the STM image has a dominant wave vector $Q = 2/7$, it can be the result of a modulation that has a wave vector $Q_0 = 1/3$ if a periodic discommensuration is included: Over the length $L = 7a$ a modulation with $Q = 2/7\frac{2\pi}{a}$ increases its phase argument by $QL = 2/7\frac{2\pi}{a} \times 7a = 4\pi$. Over the same length of $7a$, the modulation with $Q_0 = 1/3\frac{2\pi}{a}$ acquires a

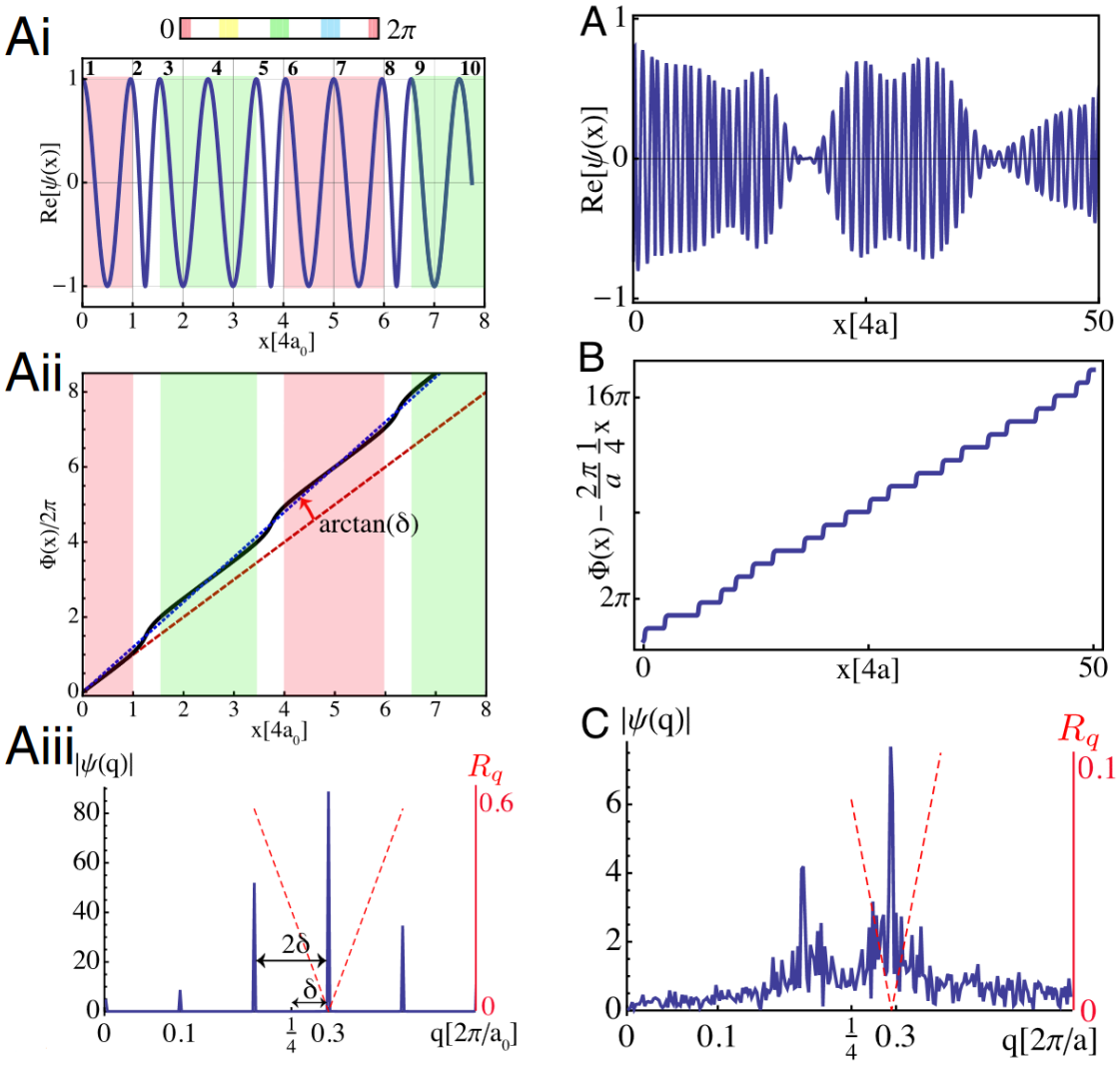

Figure 3.23: Visualisation of the effect of discommensurations on the Fourier transform of uniaxial charge modulations with $Q_0 = 1/4$. Ai): The blue line is the real part of the complex wave $\Psi(x)$ (eq. 3.16) for $Q_0 = 1/4$ with discommensurations that separate coloured regions of constant phase φ. Maxima of the modulations are counted from 1 to 10. The background colours indicate the value of the phase, given by the bar above the panel. Aii): The phase argument $\Phi(x)$ (black line) corresponding to the modulation in the panel Ai grows due to $Q_0 x$ (dashed red line) and phase slips of $+\pi$ at the positions of the discommensurations. Together with the discommensurations $\Phi(x)$ grows faster. The linear approximation (dashed red line) gives $\overline{Q}x$ and the difference in slope between Q_0 and $\overline{Q}$ is arctan(δ). Aiii): $|\Psi(q)|$ is the Fourier transform of the modulation in Ai. It has a main peak at $q = \overline{Q} \approx 0.31$ that was shifted by δ from the commensurate value $Q_0 = 1/4$. Additional satellite peaks shifted by 2δ relative to $\overline{Q}$ appear due to the periodic lattice formed by repeated discommensurations. R_q and the red dashed lines are linked to the fitting procedure to determine the average slope $\overline{Q} \approx 0.31$ and are explained in [136].

A): The panel shows a modulation similar to Ai, with the difference that the scale is larger and disorder in the amplitude as well as in the positions of discommensurations was added. B): Here $Q_0 x$ was subtracted from the phase argument $\Phi(x)$, leaving only $\varphi(x)$. $\varphi(x)$ is the acquired phase due to discommensurations between 0 and x C): The Fourier transform of the disordered modulation in A shows a peak close to $q = 0.3$ and a remaining satellite from the disordered lattice of the discommensurations. Both peaks have finite widths due to disorder and the satellite peaks are strongly reduced in intensity. The satellite peak at $+2\delta$ diappeared.

All figures have been reproduced from ref. [136].

larger phase argument $Q_0 L = 1/3\frac{2\pi}{a} \times 7a = \frac{14}{3}\pi$ which is $2\pi/3$ too much, so a negative discommensuration of -$2\pi/3$ has to occur.

The necessary amount of discommensurations is thus determined by the difference in phase arguments acquired over some length x, which basically reformulates eq. 3.17:

$$\delta \cdot L = QL - Q_0 L = \varphi(L) \qquad \Rightarrow \qquad \delta = \frac{\varphi(L)}{L} \tag{3.18}$$

Here we see that $\varphi(L)$ has the meaning of the acquired phase due to discommensuration between 0 and L, and δ becomes proportional to the density of necessary discommensurations. However, it should be noted that this model is for uniaxial modulations. The incommensurabilities of wave vectors of a bi-axial modulation should also be related to the density of discommensurations, but as the topology of the discommensurations is more complicated and discommensurations that lie in planes normal to their respective wave vectors can merge [138]. Then the linear relation between the incommensurability and the density of discommensurations might be different.

Relevance of discommensurations for YBCO

Eq.3.18 is very useful to make clear that the amount of discommensurations that would be necessary to make an incommensurate modulation with $Q = 0.323$ locally commensurate with $Q_0 = 1/3 = 0.\overline{3}$ is small. This consideration is particularly interesting for the 3D CDW phase where XRD finds a predominantly uniaxial modulation [92, 143].

For the O-II sample studied by NMR ($p = 0.109$, $y = 6.56$) we estimate $Q = 0.323 \pm 0.005$ from XRD studies of YBCO samples with similar hole doping [144, 84, 86]. High field XRD studies did not observe a change of the wave vector as a function of field [92, 143]. The incommensurability $\delta = Q - Q_0 = 0.323 - 0.\overline{3} \approx -0.01 \pm 0.005$ implies that after $L = 100a$ the acquired phase due to phase slips is only $\delta \cdot L = -0.01\frac{2\pi}{a} \times 100a = -2\pi$. For $n = 3$ possible phase slips are either $\pm 2\pi/3$ or $\pm 4\pi/3$. This means that at most three phase slips per $100a$ are necessary to make a modulation locally commensurate with the lattice, if all phase slips are negative. Such a small number of discommensurations is difficult to resolve in XRD measurements, because the intensity of satellite peaks, as seen in the Fourier transforms in Fig. 3.23 in panels Aiii & C, is expected to be small. Discommensurations themselves are also not expected to be visible in the NMR-spectrum: If each discommensuration is small and affects the phase of the modulation in the vicinity of only one or two atoms, then no more than 5% of the NMR spectral intensity should be directly affected. However, discommensurations are essential to justify the fitting procedure which is consistent with a uniaxial modulation of period $3a$ or $3b$.

3.3 NMR line splitting and the long-range 3D CDW in high fields

3.3.1 Line splitting in ^{63}Cu-NMR

In YBCO charge density waves have been discovered using ^{63}Cu-NMR of the high frequency satellites (HFS) of Cu(2E) & Cu(2F) [13]. The principal discovery was that underdoped YBCO with dopings close to $p \approx 1/8$ undergoes a field-induced transition into a charge ordered phase that leads to a splitting of the Cu2F line. Since only the HFS of Cu(2F) experienced a splitting, while the HFS of Cu(2E) remained unsplit, a $\lambda = 4a$ modulation was invoked, with the phase of the modulation chosen such that Cu(2E) is situated at the nodes of the modulation, experiencing no variation of the charge density. In this scenario Cu(2F) should be split into two peaks (Cu(2Fa) & Cu(2Fb)) of equal amplitude. Verifying this is difficult since the HFS of Cu(2F) already has an asymmetric lineshape at $T > T_{\mathrm{CO}}$ Cu(2Fa) & Cu(2Fb) partially overlap. In addition, the spin-spin relaxation times T_2 of Cu(2Fa)& Cu(2Fb) are becoming short at low T. If the two peaks experience different relaxation rates, which actually happens to be the case, the area ratio can change for increasing delay τ. Because of the asymmetric lineshape and the short T_2 there is some uncertainty in what the T_2-relaxation-corrected area ratio is, so Wu *et al.* could not easily draw information about the period of the modulation from the splitting itself. Fig. 3.24 shows the T-dependence of the splitting HFS of Cu(2F).

^{17}O-NMR is advantageous to ^{63}Cu-NMR in that the relaxation time of the in-plane O(2) and O(3) sites is an order of magnitude longer than on the adjacent Cu(2F), so spectra do not need to be corrected for T_2, if short delays are used ($\tau \sim 20\mu s$). Wu *et al.* have consequently focused on ^{17}O-NMR and found similar splittings as on the Cu2F site and characterised the field and T-dependence of the 3D CDW phase for differently doped samples [73]. Although O(2) & O(3) are expected to be affected by charge order in the same way, the splittings on the O(2) site appeared more clearly than in the spectra of O(3) sites, because O(3) sites do not experience a magnetic splitting. This is reminiscent of the absence of a correlated quadrupole broadening $\delta\nu_{\mathrm{mag,c}}$ on the O(3) sites and has found no explication so far.

3.3.2 Asymmetric lineshapes in ^{17}O-NMR

In ^{17}O-NMR of YBCO, besides the peak splitting, there is a second phenomenon that manifests itself in the spectra of both O(2) & O(3). When entering the long range 3D CDW phase, all O(2) and O(3) peaks develop a pronounced asymmetry in the lineshapes of the individual peaks. Rui Zhou has been able to quantify this effect and could show that the peak asymmetry is a result of an asymmetric distribution of Knight shifts [145]. The evolution of the peak asymmetry with B and T is shown in Fig. 3.25. The asymmetric distribution of Knight shift has found a natural explanation in the enhanced local density

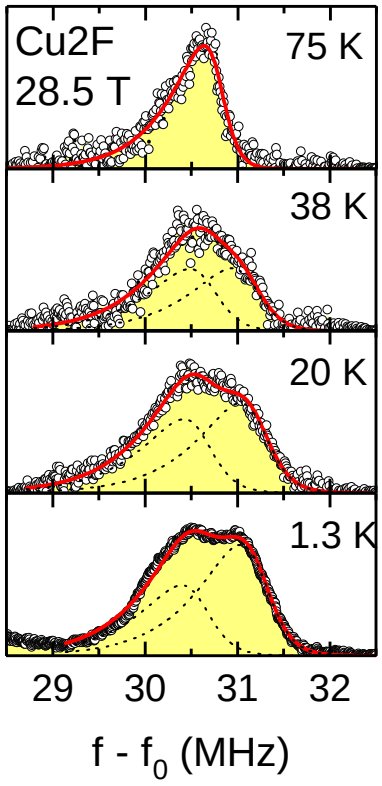

Figure 3.24: T-dependence of Cu2F HFS for an O-II sample with $p = 0.104$ at 28.5 T at $T = 75$ K$> T_{\mathrm{CO}}$ and a few temperatures below T_{CO}. At $T = 75$ K HFS has an asymmetric lineshape. Below T_{CO} the area ratio of the splitting peaks is close to 1-to-1, but with decreasing T the area ratio deviates from 1-to-1. T_2 becomes very short at low T, so the area ratio changes at least partly because the left peak has shorter T_2. The figure is reproduced from ref. [13].

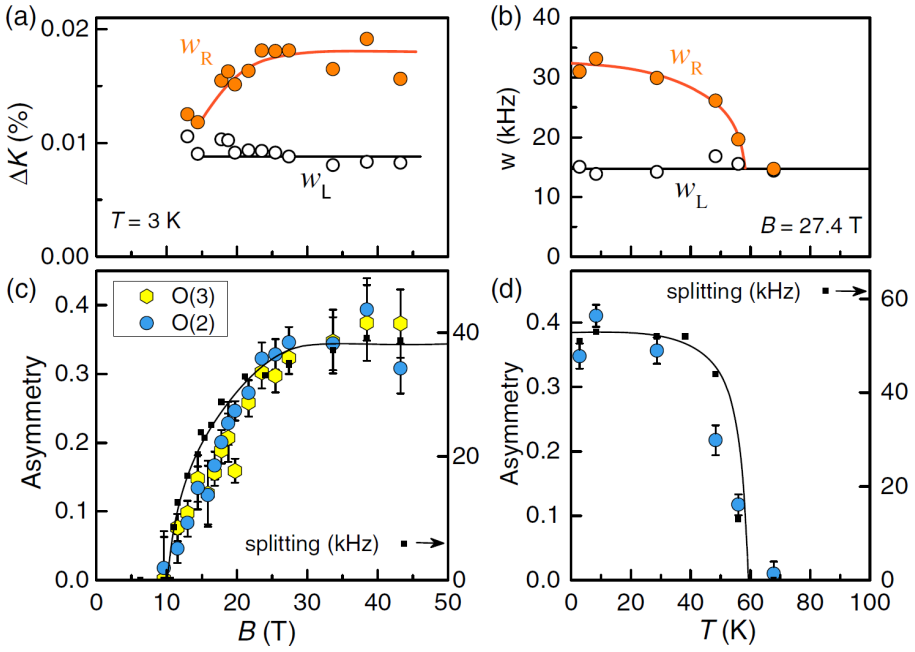

Figure 3.25: B- and T-dependencies the peak asymmetry found in the O-II sample ($p = 0.109$). a): B-dependence of the asymmetric left (w_L) and right (w_R) peak widths determined from bi-Gaussian fits of O(2)$LF1$. Since the widths are predominantly of magnetic origin, w_L & w_R are scaled by the magnetic field, showing that the growing asymmetry is a result of growing skewed ($K > 0$) Knight shift distribution. b): T-dependence of w_L & w_R in high field. c): B-dependence of the asymmetry$=(w_R - w_L)/(w_R + w_L)$) calculated for O(2) and O(3). The asymmetry has the same onset field as the splitting (small black squares) and saturates above ≈25 T. d): T-dependence of the asymmetry at high field, calculated from widths in panel b). This figure is part of ref. [145].

of states (LDOS) due to electronic quasiparticle boundstates that are "scattering resonances" formed at defects. Similarly asymmetric peak shapes, that can be fit with bi-Gaussians, have been found in Zn-doped YBCO where the asymmetry is independent of the amount of disorder [123]. There, the LDOS is enhanced around the Zn-impurity, but the in case of the scattering resonances found by Zhou *et al.* the question is which kind of defect or impurity is strong enough to create the quasiparticle bound states in the CuO_2-planes. As the asymmetry follows the B- and T-dependence it is possible that the underlying scattering mechanism originates in the CDW itself. Discommensurations of the CDW modulation are a natural candidate, since they appear together with the CDW modulation and are situated in the CuO_2-plane[9].

Disentangling the effect of the splitting and the asymmetric broadening on the satellites of O(2) and O(3) is a very difficult task that has been mastered by Rui Zhou by finding a suitable way to account for the asymmetric shape of the split peaks. It turned out that in high fields the asymmetry of the peaks saturates at a value close to 0.35, a value at which the bi-Gaussian peak shape it very similar to the profile of an *Extreme value distribution* (EVD). The EVD profile is described by the following function:

$$f_{\mathrm{EVD}}(x) = b\exp[-\exp(-z) - z + 1] \qquad \text{with} \quad z = \frac{(x - x_c)}{w} \tag{3.19}$$

Here b is the amplitude. Due to the simple functional form and only three free parameters the EVD profile is a robust function in fitting routines.[10]

The asymmetry has been determined for the lineshape of LF1 on O(2) and O(3). Although these are two different sites, their asymmetry is remarkably similar, as shown in Fig. 3.25c. However, the asymmetry is not necessarily identical on all satellites of the same site. The asymmetric lineshape results from the convolution of the intrinsic width of each satellite with the skewed distribution of Knight shifts. The distribution of Knight shifts results from the enhanced LDOS around impurities (see inset of Fig. 3.26) and is identical on all satellites. On the other hand, the intrinsic widths differ from one satellite to the other satellite, as the quadrupole broadening $\delta\nu_{\mathrm{quad}}$ and the magnetic broadening $\delta\nu_{\mathrm{mag,c}}$ combine differently, given by eqs. 3.4a to 3.4e. Thus, the $HF2$ satellite will have a smaller asymmetry than the narrow $LF1$ satellite.

[9] In ref. [126], Atkinson *et al.* propose a different origin of the enhanced LDOS: In their model the asymmetry results from the curvature of the Fermi surface (FS) at the hot spot, *i.e.* parts of the FS between which enhanced scattering occurs.

[10] The advantage of the EVD profile over the bi-Gaussian is that the asymmetry is fixed without a constraint. We use Origin 2017 for fitting and have remarked that fitting with an EVD works better than using bi-Gaussians with constrained asymmetry, although the number of free parameters is the same.

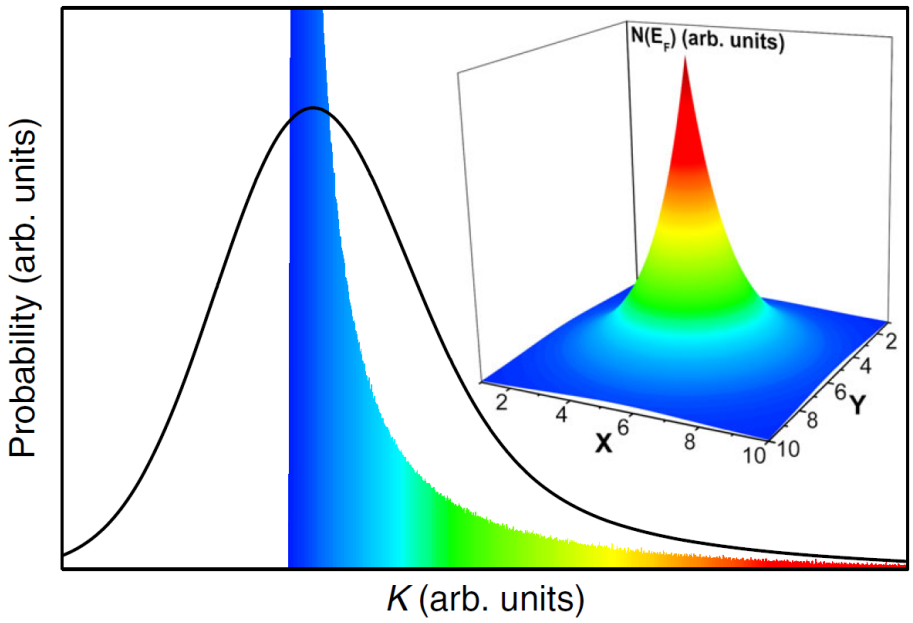

Figure 3.26: The main figure shows the probability distribution of the Knight shifts, which result from the enhanced LDOS at the Fermi energy E_{F} ($K \propto N(E_{\mathrm{F}})$). The inset shows the enhanced LDOS that falls off exponentially away from the impurity. The Knight shift distribution is a histogram of the LDOS depicted in the inset and is convoluted by a Gaussian to give the asymmetric lineshape (black line). This figure is part of ref. [145].

3.3.3 Line splitting in ^{17}O-NMR

A second major improvement in the data analysis by Rui Zhou is the use of 8-peak-fitting: Since ^{17}O has a nuclear spin $I = 5/2$, there are five peaks for each site. A central peak and four satellite peaks whose separations are determined by the quadrupole interaction. For two sites, A and B there are 10 peaks in total, but as central lines of A and B overlap, the focus is on the satellites. To 1$^{\mathrm{st}}$ order in the quadrupole interaction, (a good approximation at $B \gtrsim 20$ T) the resonance frequencies of the four satellite peaks have the relation $(f_{HF2} - f_{HF1}) : (f_{HF1} - f_{LF1}) : (f_{LF1} - f_{LF2}) = 1 : 2 : 1$. Using this as a constraint for each set of satellites allows to fit the four satellites of the two inequivalent sites simultaneously. This is very useful to see to which extent the coupled Knight shift splitting and quadrupole splitting compensate each other on the low frequency satellites, as expected from eqs. 3.13d & 3.13e. Indeed, applying this constraint to 8-peak-fits of the full satellite spectra allows to discriminate the quality of Gaussian fits as compared to the EVD fitting. Fits with Gaussian and EVD lineshapes of the spectra at two different fields are shown in Fig. 3.27. The 8-peak-fit with EVD profiles has the highest quality and produces consistent results for both fields. In both cases the total splitting on the $LF1$ satellite is nearly zero which legitimises the determination of the lineshape asymmetry from $LF1$ and shows that it is not due to an unresolved splitting. It should be noted that fitting all peaks with EVD profile implies that all satellites have the asymmetry of the EVD. As discussed,

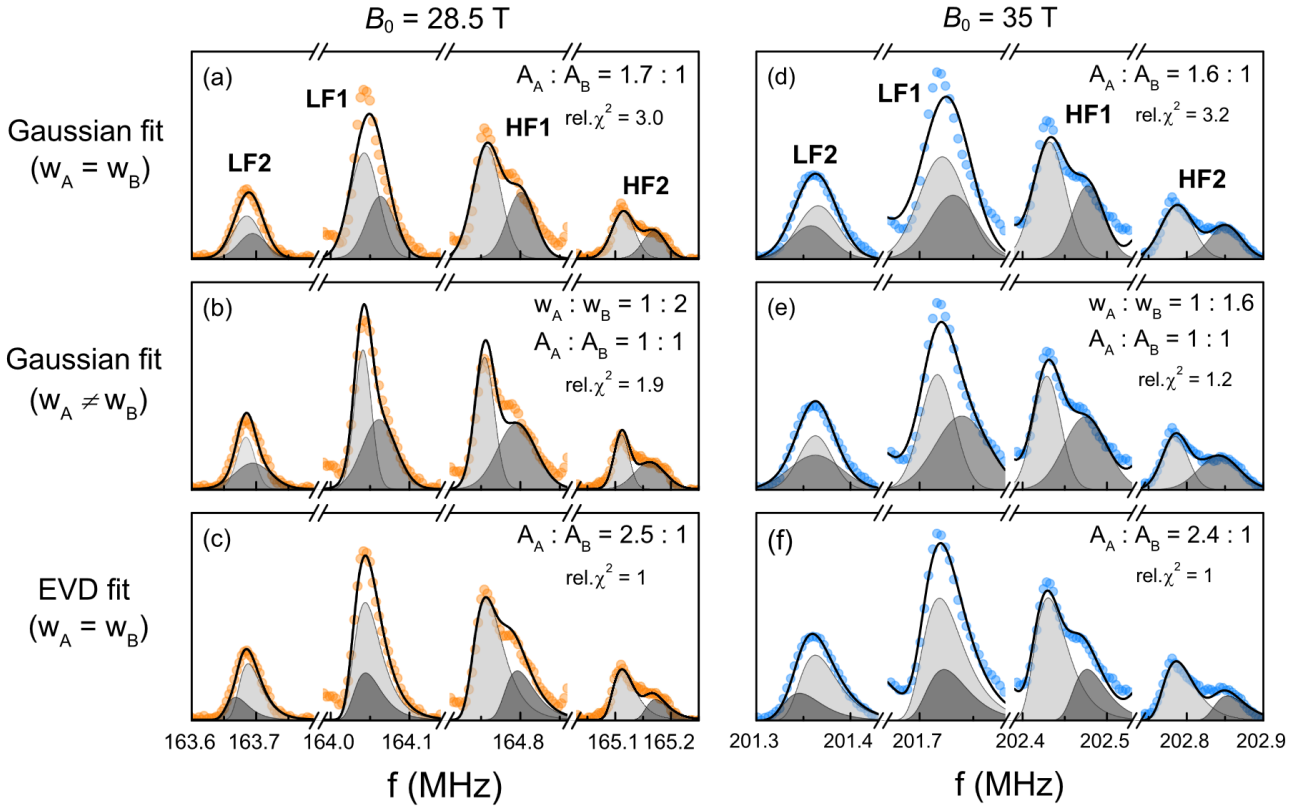

Figure 3.27: Low T (2 K) satellite spectra of the split O(2) site at B=28.5 T & B=35 T within three scenarios: (a, d): The splitting is described by two Gaussians of equal width and unequal areas; (b,e): two Gaussians of equal areas but unequal widths; or (c,f): two EVDs with equal widths. The quality of the fits is best for the EVD fits. Gaussian fits have higher relative χ^2. In addition the splitting on $LF1$ is nearly perfectly compensated which legitimises the determination of the asymmetry by bi-Gaussian fitting from $LF1$. The near absence of a splitting on $LF1$ is not enforced manually but is a stable result due to the constraint for the resonance frequencies of the quadrupole satellites. This figure is part of ref. [145].

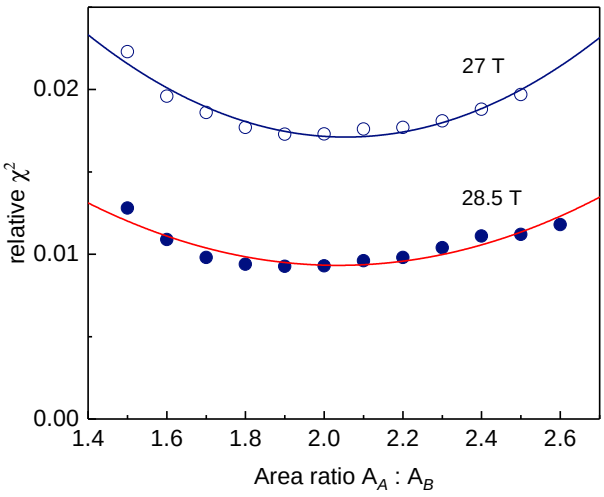

Figure 3.28: Determination of the area ratio $A_A : A_B$ of the split peaks for YBCO6.56. The quality of 8-peak -fits of O(2) satellites with EVD profiles is determined at 28.5 T and 27 T as a function of the area ratio of site A and B from the relative χ^2 of the fit. For both fields an area ratio close to 2-to-1 is optimal.

this is not the case, but the good quality of the fit implies that the asymmetry of all satellites is similar.

An interesting result from the 8-peak-fitting with EVDs is that the area ratio of the two splitting peaks, is closer to 2-to-1 than 1-to-1. The area ratio 1:1 would be expected if the splitting was coming from a broadened lineshape of an incommensurate $1q$ modulation within a linear model, see Fig. 3.16a. The area ratio itself is not a free parameter of the fit, since keeping the area ratio as a free parameter for all satellites is a nonlinear constraint. Nonlinear constraints are not possible in linear fitting algorithms implemented in Origin. Nevertheless, the quality of the fit, the relative χ^2, can be estimated as a function of the area ratio. From Fig. 3.28 one can see that an area ratio close to 2-to-1 is optimal. The area ratio of the two sites A & B being close to 2-to-1 is reminiscent of the histogram of a commensurate $1q$ modulation with wave vector $q = 1/3$ with phase $\phi = 0°$, as shown in panel k) of Fig. 3.20. According to panel k), the shift of the positions of the two peaks from the average value $\nu_{Q,0}$ is -1 : 2 for the two peaks. It means that the quadrupole frequency $\nu_{\mathrm{quad,A}}$, of the left peak with higher intensity, decreases half as much as the quadrupole frequency $\nu_{\mathrm{quad,B}}$ of the right peak increases, both relative to $\nu_{\mathrm{quad},0}$, the quadrupole frequency of the unsplit spectrum.
Unsplit and split spectra at 10 T and 28.5 T, respectively, are shown in Fig. 3.29. The spectra are plotted on the same frequency scale and have been aligned on the central peaks (not shown). The splitting of the two peaks is different on each satellite as it results from differences in the quadrupole

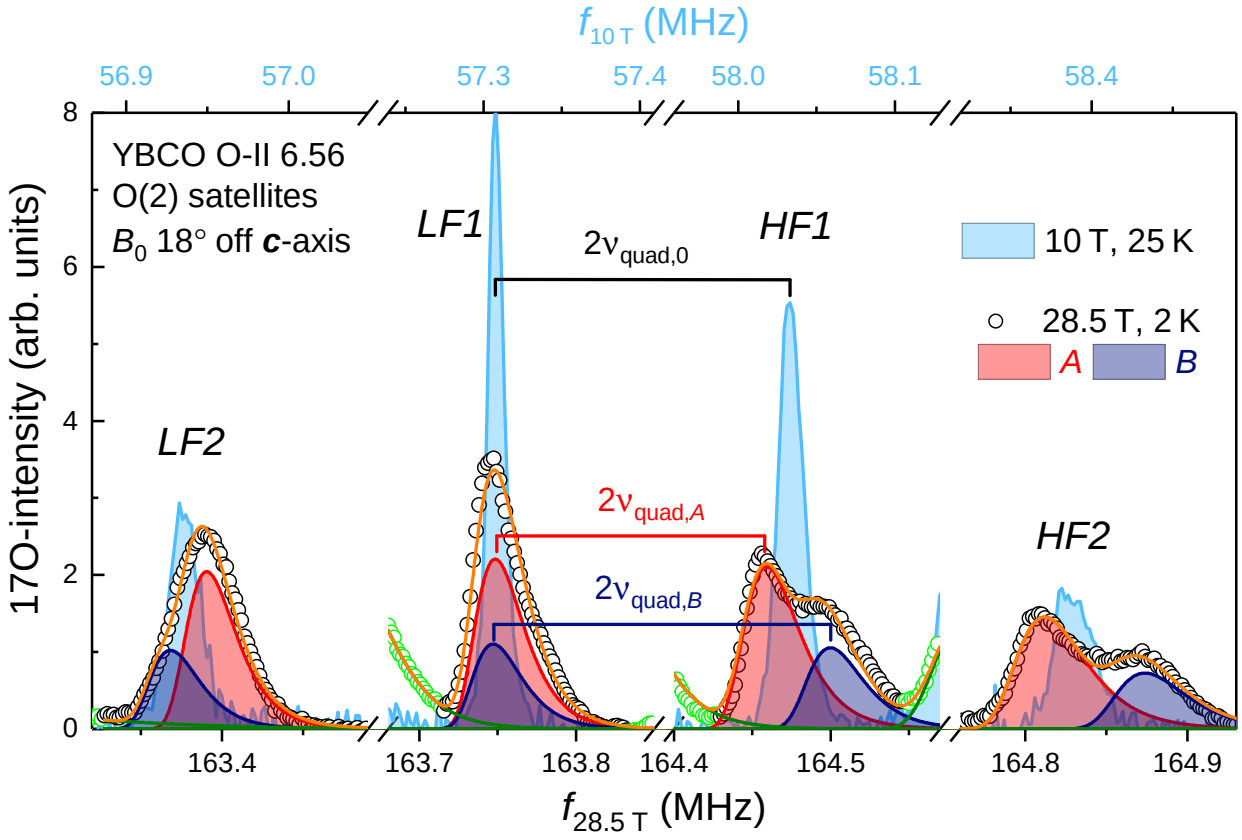

Figure 3.29: O(2) satellite spectra measured at 10 T & 25 K, where there is no splitting (light blue colour), and 28.5 T & 2 K (empty circles), are plotted on the same frequency scale. The central peaks (not shown) are aligned to account for different average Knight shifts.

The high field spectrum is fit with two EVD profiles for the two sites A (red) and B (dark blue). The area ratio $A_A : A_B$ is 2-to-1 while widths on each satellite are equal. The orange line is the envelope of the full fit including the tails of neighbouring O(3) sites. $LF1$ and $HF1$ are separated by $2\nu_{\rm quad}$.

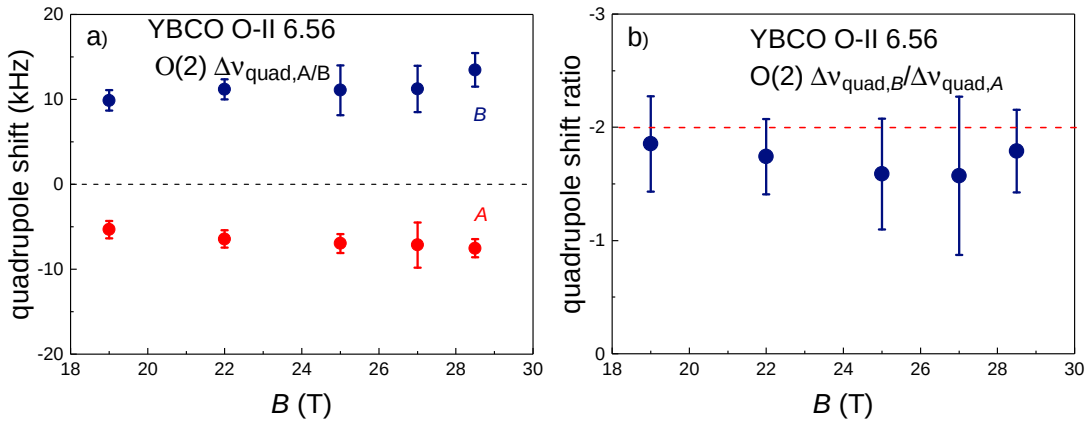

Figure 3.30: a): The quadrupole shifts of the A (red) and B (dark blue) sites of O(2) are caluculated following eq. 3.20 and are determined from 8-peak-fits of O(2) satellite spectra at 2 K using EVD profiles of equal width with area ratio $A_A : A_B = 2 : 1$, as explained in Fig. 3.29.
b): The quadrupole shift ratio is based on the shifts in panel a). The ratios are consistent with -2, as expected for a commensurate $1q$ modulation with wave vector $q = 1/3$ and phase $\phi = 0°$.

frequencies and Knight shifts of the sites A and B. To extract the quadrupole shifts we calculate

$$\begin{aligned} \Delta\nu_{\mathrm{quad,A}} &= \nu_{\mathrm{quad,A}} - \nu_{\mathrm{quad,0}} \quad \text{and} \\ \Delta\nu_{\mathrm{quad,B}} &= \nu_{\mathrm{quad,B}} - \nu_{\mathrm{quad,0}} \\ \text{and expect} \qquad \Delta\nu_{\mathrm{quad,A}} &: \Delta\nu_{\mathrm{quad,B}} = -1 : 2. \end{aligned} \tag{3.20}$$

Fig. 3.30 shows the quadrupole shifts of sites A and B in a range of fields where the quadrupole splitting can be determined reliably. The quadrupole shift of site B is larger, as expected. The average ratio is -1.75 and lies reasonably close to -2.

Discussion of line splitting in ^{17}O-NMR

In summary, we have discussed that in the long-ranged 3D CDW phase the ^{17}O-NMR spectra of in-plane sites O(2) and O(3) of the YBCO O-II sample ($p = 0.109$) undergo profound changes: All in-plane peaks become strongly asymmetric and develop a line splitting. Both phenomena have the same B and T dependence. The splitting of the O(2) site is well resolved in high fields and is well described by two peaks with area ratio $A_A : A_B = 2 : 1$. The splitting originates in a joint Knight shift and quadrupole splitting. The quadrupole splitting of the two peak is found to have a shift ratio $\Delta\nu_{\mathrm{quad,A}} : \Delta\nu_{\mathrm{quad,B}} \approx -1 : 2$. The area ratio and quadrupole shift ratio are both consistent with a commensurate uniaxial modulation with wave vector $q = 1/3$ and phase $\phi = 0°$. Other phases would lead to a qualitatively different spectrum.

The commensurate wave vector $q = 1/3$ is close to the incommensurate wave vector $q \approx 0.323$ found by XRD for samples of similar doping. We explain the incommensurate wave vector found by XRD with a small density of discommensurations that allows the uniaxial CDW modulation to become locally commensurate with the lattice. The small density of discommensurations is not directly resolvable by NMR, since any change in the spectra would redistribute a fraction of the intensity that is proportionate to the density of discommensurations. In XRD discommensurations should lead to satellite peaks of the main CDW peak, but their intensity is also proportional to the amount of discommensurations and can in addition be reduced by disorder.
However, the asymmetric lineshape of the in-plane oxygen peaks is likely the result of enhanced LDOS from in-plane impurity resonances which appear together with the long-range CDW. Discommensurations of the long-range CDW itself could be a source of quasiparticle scattering and thus provide a unified framework to explain the main phenomena encountered by NMR in the long-range 3D CDW phase: The asymmetry of the line shapes and splitting with 2-to-1 area ratio.

We have explored the $1q$ incommensurate modulation with the quadratic model, defined by eq. 3.14. Including $\Delta\nu_{\mathrm{Q},2}$, which is proportional to the square of the charge modulation. We found that $\Delta\nu_{\mathrm{Q},2}$ has to be of the same size as the linear term $\Delta\nu_{\mathrm{Q},1}$ to reproduce the lineshape of the $HF2$ satellite of O(2), see Fig. 3.31. Such a large quadratic term seems to be unreasonable.

3.3.4 Determination of the onset field of long range CDW

Having established that the splitting results from two asymmetric peaks of equal width and an area ratio of 2-to-1, we can try to determine the B and T-dependence of the splitting. Ideally, full satellite spectra of the O(2) satellites should be used to perform 8-peak-fitting. However, always measuring full spectra with sufficiently high signal-to-noise ratio using resistive magnets of LNCMI in Grenoble, or the NHMFL's hybrid magnet in Tallahassee, is time-consuming. Frequently, only the $HF2$ satellite of O(2) is recorded, since its splitting is largest. Fitting $HF2$ allows to determine the total splitting

$$\Delta\nu_{\mathrm{tot,HF2}} = \Delta\nu_{\mathrm{mag}} + 2\Delta\nu_{\mathrm{quad}}. \tag{3.21}$$

The field at which $HF2$ starts to split is defined as the onset field B_{onset}. B_{onset} for four underdoped YBCO samples has been reported by Wu *et al.* in 2013 [73]. Surprisingly, for samples of the same doping, B_{onset} was found to lie below B_{CO}, as defined by the thermodynamic transition found by ultrasound measurements of LeBoeuf *et al.* [93]. For $p = 0.109$ $B_{\mathrm{onset}} \sim 10$ T was found, while the sample with $p = 0.108$ studied by ultrasound had $B_{\mathrm{CO}}(T)$ that extrapolated to ∼17 T at low T, recently confirmed by measurements in another ultrasonic mode at low T [98]. This discrepancy was explained by detailed XRD measurements in high field by Chang *et al.* [92]. They found that the

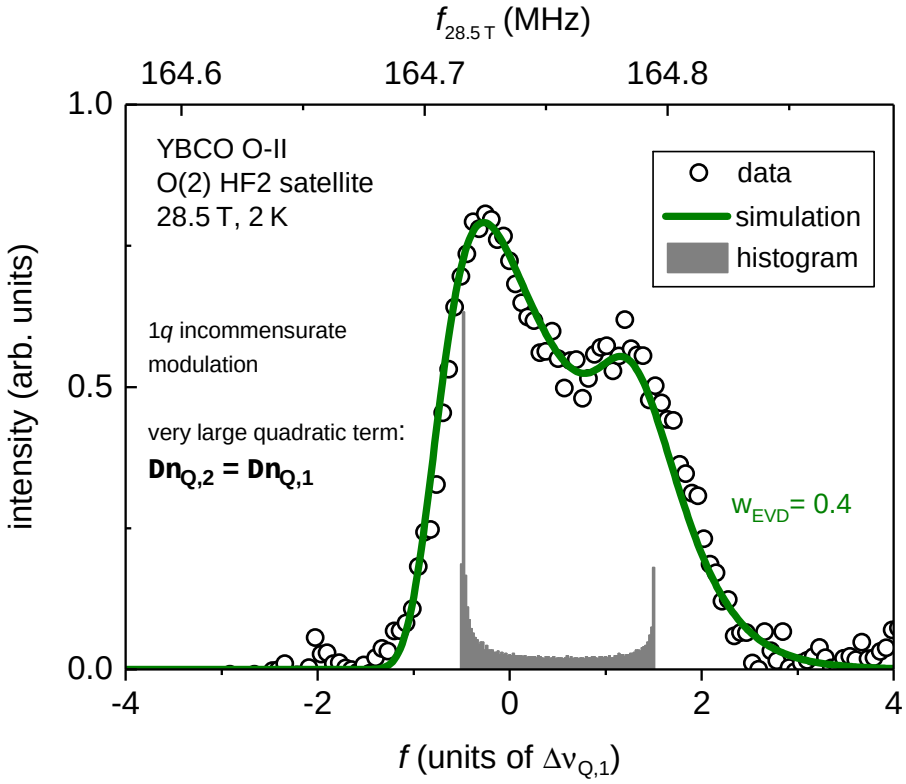

Figure 3.31: Simulation of the spectrum of the $HF2$ satellite of O(2) at 28.5 T, 2 K with a $1q$ incommensurate modulation within the quadratic model. The histogram is determined for $\Delta\nu_{Q,2} = \Delta\nu_{Q,1}$ and is broadened by convolution with an EVD profile with width $w_{EVD} = 0.4$. The simulated lineshape describes the data well, but the quadratic term necessary to simulate the lineshape of the data is of the same size as the linear contribution.

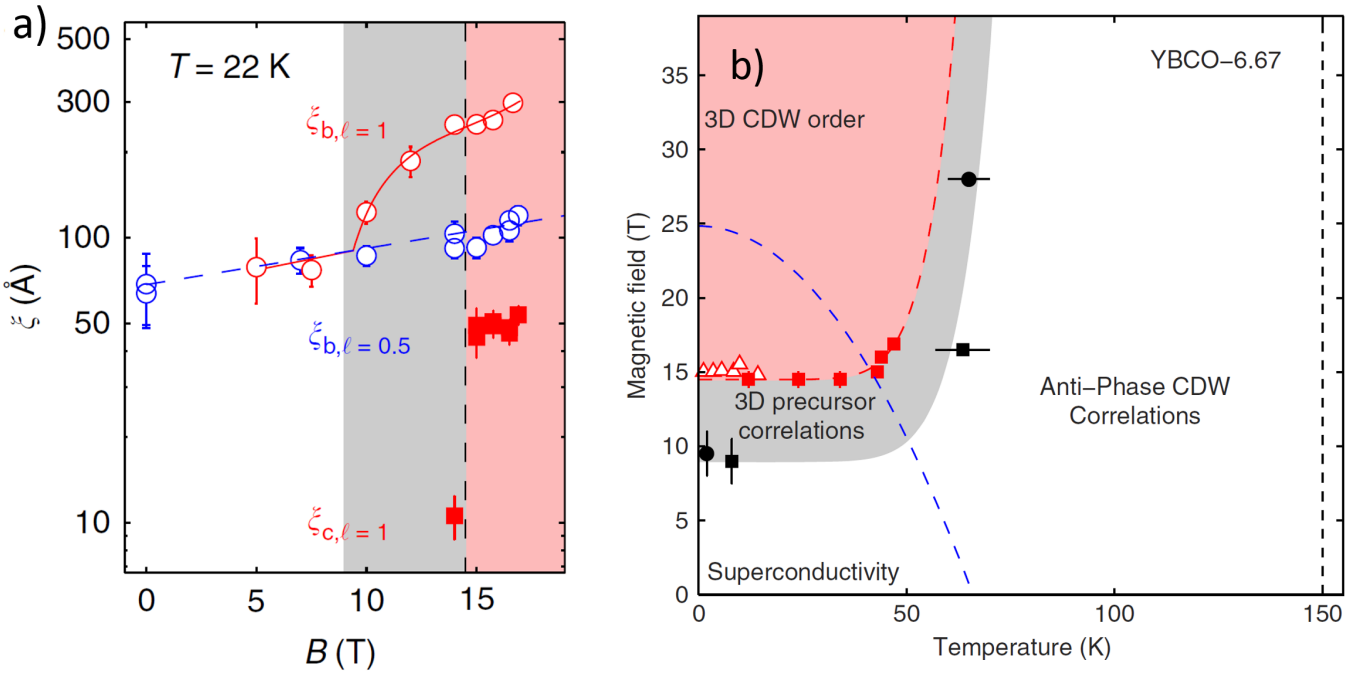

Figure 3.32: a): Field dependence of correlation legths in YBCO 6.67 as found by XRD. Measured wave vectors are (0,3.687,l), where l is 0.5 (anti-phase correlations) or 1. While the in-plane correlation length $\xi_{b,l=1}$ increases rapidly close to 10 T, the $\boldsymbol{c}$-axis correlation length $\xi_{c,l=1}$ increase abruptly around 15 T. In-plane anti-phase correlations $\xi_{b,l=0.5}$ (blue) show no discontinuity. b): B-T phase diagram for the long range 3D CDW. The red region corresponds to the phase where correlation lengths in 3D become large, as expected for a thermodynamic transition, based on thermal Hall (empty triangles) and XRD measurements (red squares). The grey region corresponds to the phase where the in-plane correlation length of the uniaxial modulation with q=(0,3.687,1) is large, but $\boldsymbol{c}$-axis correlation are weak, as measured by XRD (black squares) and NMR (black circles) The blue dashed line is a sketch of a putative mean field H_{c2}, the black dashed line indicates the onset of 2D short range charge order (anti-phase correlations). The figures are reproduced from ref. [92].

in-plane correlation length $\xi_{b,l=1}$ of the uniaxial wave vector along $\boldsymbol{b}$ starts to grow rapidly at a field $\sim B_{\rm onset}$ while the $\boldsymbol{c}$-axis correlation length $\xi_{c,l=1}$ of the same wave vector increase abruptly at a higher field, close to $B_{\rm CO}$, see Fig. 3.32.

As NMR is a local probe, it will find a splitting as soon as the in-plane correlation length of charge order becomes long enough that a large fraction of the sample experiences CDW modulations of sufficiently large amplitude. Whether these CDW modulations are correlated along the $\boldsymbol{c}$-axis, will not affect the splitting. On the other hand, a thermodynamic probe like ultrasound will experience a phase transition when the inter-plane coupling becomes sufficiently strong that correlations in all spatial directions become large, as expected by the Mermin-Wagner theorem, which states that in 2D, continuous symmetries cannot be broken at non-zero T [146].

Fitting of the splitting on $HF2$

To fit $HF2$ satellite spectra as a function of field, the splitting peaks have to be fit by a function that has variable asymmetry, since the asymmetry is zero for $B < B_{\text{onset}}$ and grows for $B > B_{\text{onset}}$. When fitting the splitting as a function of T, the same applies for T above and below T_{onset}, but the focus here is on the onset field at low T of approximately 2 K. The bi-Gaussian could be used for this, but the bi-Gaussian does not describe the data well around its maximum. A better function to fit asymmetric peaks is the *Asymmetric Pseudo-Voigt profile*. It is defined in the same way as the Pseudo-Voigt profile in eq. 3.3, with the difference that the width evolves smoothly as a function of the parameter x. Stancik and Brauns have proposed a form that is analogous the Fermi-Dirac function [147]:

$$w(x) = \frac{2w_0}{1 + \exp a(x - x_c)} \tag{3.22}$$

Here w_0 is the width parameter that is equal to the FWHM for $a = 0$ and x_c is the peak center. For $a > 0$ the FWHM and the position of the peak maximum have to be determined numerically.
We model the splitting with two asymmetric Pseudo-Voigt lineshapes with 2-to-1 area ratio, the width w_0 and asymmetry parameter a are identical for the two peaks. For simplicity the weight of the Lorentzian contribution to the lineshape m is set to zero. This function is able to fit NMR data very accurately, but due to the large amount of parameters, fits of the split $HF2$ satellite are necessarily unstable close to B_{onset}: When two peaks with unequal areas merge, the resulting lineshape is broad and asymmetric and can thus be fit equally well by either one or two peaks. The cross-correlation of parameters in this nonlinear model makes the determination of error bars difficult.
We have written an iterative least squares routine in MATLAB to find the optimal set of parameters to simulate the splitting. This brute force routine iterates though the entire parameter space that can reproduce the experimental data and calculates the total difference between the data and the simulated lineshape. This procedure finds the optimal splitting, but it gives no direct access to the uncertainties of the parameters. At this point a comment about the determination of uncertainties might be appropriate.

Uncertainties

Ideally, a fitting procedure determines two things: The set of parameters that corresponds to the global maximum of the quality of the fit (χ^2, R^2, etc.) and the error bars (standard deviations) of each fitting parameter. The error bars are estimated locally from the curvature of χ^2 in the parameter space at the global maximum. If the curvature is small, then it can result in very large standard deviations that surpass the physically admissible range. For example, the calculated error bar of the position of a peak can become 200 kHz although the total width of the fitted lineshape is only 20 kHz. Fixing

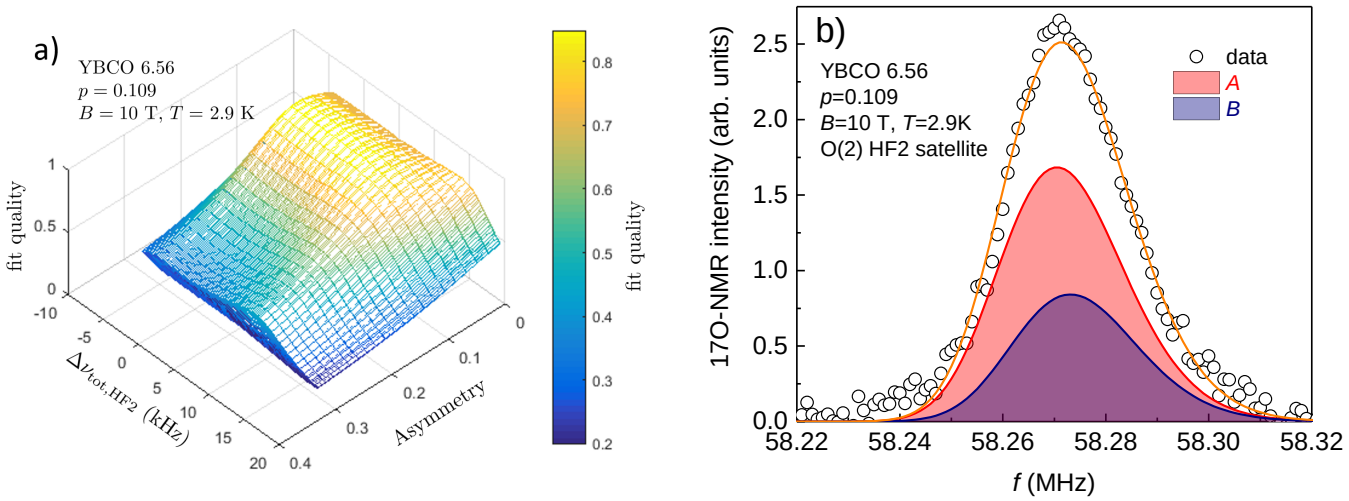

Figure 3.33: a): Flat global maximum of the quality of the fit for the O-II sample ($p = 0.109$) at 10 T & 2.9 K, as calculated within the MATLAB routine. The fit quality is 1 if the difference between fit and data goes to zero. Since the maximum of the fit quality is very broad, we find that the uncertainty of the splitting $\Delta\nu_{\rm tot}$ is ~ 10 kHz. This surface plot contains many layers, because a particular value of the splitting $\Delta\nu_{\rm tot} = x_{c,B} - x_{c,A}$ can be realised by different pairs of peak positions $x_{c,B}$ & $x_{c,A}$. b): Best fit of O(2) HF2 satellite at 10 T. The broad peak can be fit by a large range of parameters, as can be seen from panel a). Red and dark blue lines are Asymmetric Pseudo-Voigt lineshapes with Lorentzian contribution $m = 0$ and area ratio 2-to-1.

the error bars by hand to ± 10 kHz would be a legitimate procedure, because the peak position lies with certainty within the fitted lineshape. Nonetheless, this is likely to be a strong overestimation as conventional error bars are defined by the standard deviation σ, which corresponds to a confidence level of 68%.

Typically, flat global maxima of the fit quality in parameter space exist when two or more parameters are cross-correlated and indicate that the fitting model is inadequate (see Fig. 3.33a). If, as in our case, the splitting is correlated with the asymmetry, then ideally, the model should be reformulated in such a way that the asymmetry is parametrised by the splitting $\Delta\nu_{\rm tot}$. In our model the splitting, the width and the asymmetry are correlated parameters, because they all depend on the order parameter of 3D charge order, $\Delta_{\rm 3D\,CDW}$. The problem that we face is that *a priori* we do not know the functional dependence $\Delta\nu_{\rm tot}(\Delta_{\rm 3D\,CDW})$, etc. Thus, we cannot, for example, express the asymmetry directly through the splitting to reduce the amount of free parameters. Consequently, close to $B_{\rm onset}$ we are necessarily in a situation where error bars from standard fitting procedures are ill-defined.

For the accuracy of the MATLAB routine there are two risks when $B \sim B_{\rm onset}$: If the spectrum is a single broad peak, then the routine will become sensitive to the noise of the data. Hence, it is desirable to increase the statistics of the raw data and to measure many spectra. The resulting scattering will be a measure of the uncertainty. A second danger that remains, is that the global maximum of the quality of the fit might to some extent be model dependent. To cope with this problem we repeat the analysis

doping p [holes]	T_c [K]	oxygen content y	chain ordering
0.088	52.3 ± 2	6.49	O-II
0.0109	60.0 ± 1	6.56	O-II
0.125	68.5 ± 1	6.68	O-VIII
0.136	78.3 ± 1	6.77	O-III

Table 3.1: Information on ^{17}O-enriched YBCO samples, grown by Ruixing Liang at UBC. The oxygen content of the O-II ordered sample with $p = 0.088$ was determined by ^{63}Cu-NMR in ref. [148].

with slightly varying models for which we release the constraints on the area ratio or the Lorentzian contribution to the peak shape, m. For $B \sim B_{\text{onset}}$ we determine the error bar for the splittings from the range in which splittings of different models fall. This procedure is somewhat arbitrary, but it is reasonable to account for this systematic error. However, this error becomes small above B_{onset} and an ad-hoc error has to be added. It can be estimated by plots of the fit quality like Fig. 3.33a, but we have no objective criterion that says how much the fit quality has to decrease at one standard deviation σ, so it is possible that our error bars are overestimated with respect to the standard-deviation.

To reduce the parameter space we can constrain the width w_0. A lower bound for the single peak widths can be determined by extrapolating their field dependence from low field data, as if the 2D short-range CDW correlations extended without change into the high field phase. This is motivated by the fact that in XRD anti-phase correlations ($l = 0.5$) do not decrease inside the high field phase (see Fig. 3.32a), which in NMR is reflected in a constant left width w_L (see Fig. 3.25a). A width calculated from low field data is a lower bound to the correct total with, because $w_{\text{calc}}(B) = 2w_L < w_L + w_R = w_{\text{tot}}$. So, if the widths of all satellites are available at a field $B < B_{\text{onset}}$, then the broadening contributions $\delta\nu_{\text{quad}}$, $\delta\nu_{\text{mag,c}}$ and $\delta\nu_{\text{mag,0}}$ can be calculated from the equations 3.6a to 3.6c. As the quadrupole broadening $\delta\nu_{\text{quad}}$ is field independent in the short-range 2D CDW phase and magnetic broadenings $\delta\nu_{\text{mag,c}}$ & $\delta\nu_{\text{mag,0}}$ are linearly proportional to the field, the field dependence of the width of each satellite can be calculated for arbitrary field using equations 3.4a to 3.4a. For $HF2$ this gives

$$2w_{L,HF2} = \sqrt{(2\delta\nu_{\text{quad}} + \frac{\mathrm{d}\delta\nu_{\text{mag,c}}}{\mathrm{d}B}B)^2 + (\frac{\mathrm{d}\delta\nu_{\text{mag,0}}}{\mathrm{d}B}B)^2} \tag{3.23}$$

We make use of this equation to constrain the width of the O-III sample ($p = 0.136$) and the weakly doped O-II sample (p=0.088). Sample information is summarised in table 3.1.

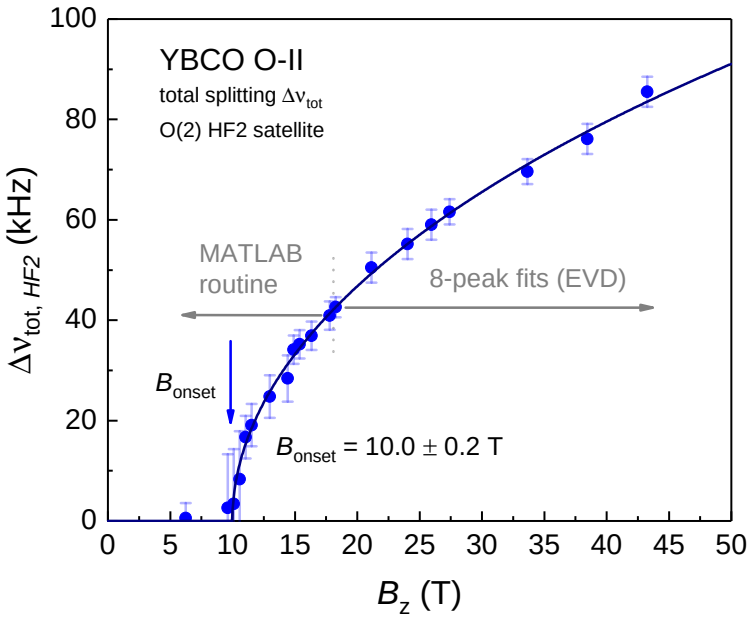

Figure 3.34: Total splitting $\Delta\nu_{\mathrm{tot,HF2}}$ of the O(2) $HF2$ satellite of the O-II sample ($p = 0.109$) at $T \approx 2$ K, with the sample tilted by 16-18° off the $\boldsymbol{c}$-axis. $\Delta\nu_{\mathrm{tot,HF2}}$ is plotted against B_z, the projection of the field along the $\boldsymbol{c}$-axis. The splitting has been determined by a least squares routine in MATLAB for $B_z \leq 17.6$ T and by 8-peak fits of full spectra with EVD profiles. The line is a fit with the tanh-fit, defined in eq. 3.25b and gives $B_{\mathrm{onset}} = 10.0 \pm 0.2$ T.

Splitting of O-II sample $p = 0.109$

For the O-II sample with hole doping $p = 0.109$ the splitting of the $HF2$ satellite has been determined using the MATLAB routine for fields up to 18.5 T. For $B_0 \geq 19$ T the splitting has been determined using 8-peak fits with EVD profiles. Fig. 3.34 shows the results.

For the fields where 8-peak fits have been done the full quadrupole splitting is obtained easily using eqs. 3.20. It would be interesting to separate the contributions from the quadrupole and the magnetic splittings to $\Delta\nu_{\mathrm{tot,HF2}} = 2\Delta\nu_{\mathrm{quad}} + \Delta\nu_{\mathrm{mag}}$. To determine $\Delta\nu_{\mathrm{quad}}$ it is necessary to know $\Delta\nu_{\mathrm{mag}}$ and vice-versa. However, both splittings originate from the CDW modulation, so they are expected to be proportional to each other. If this is the case and if the proportionality constant is B independent, then both splittings can be determined from $HF2$ only. As $\Delta\nu_{\mathrm{mag}}$ is proportional to the field ($\Delta\nu_{\mathrm{mag}} = \gamma B \Delta K$), we expect $\Delta\nu_{\mathrm{quad}} B/\Delta\nu_{\mathrm{mag}}$ to be constant. From Fig. 3.35 one can see that this is indeed the case.

We can thus express $\nu_{\mathrm{tot,HF2}}(B)$ through $\Delta\nu_{\mathrm{quad}}(B)$ alone by

$$\nu_{\mathrm{tot,HF2}}(B) = 2\Delta\nu_{\mathrm{quad}}(B) + \Delta\nu_{\mathrm{mag}}(B) = (2 + \frac{B}{24.6})\Delta\nu_{\mathrm{quad}}(B) \tag{3.24}$$

and calculate $\Delta\nu_{\mathrm{quad}}(B)$ for the fields $B_0 \leq 18.5$, as shown in Fig. 3.36.

To fit the splitting one can use a function that is inspired by an interpolation formula to the T-

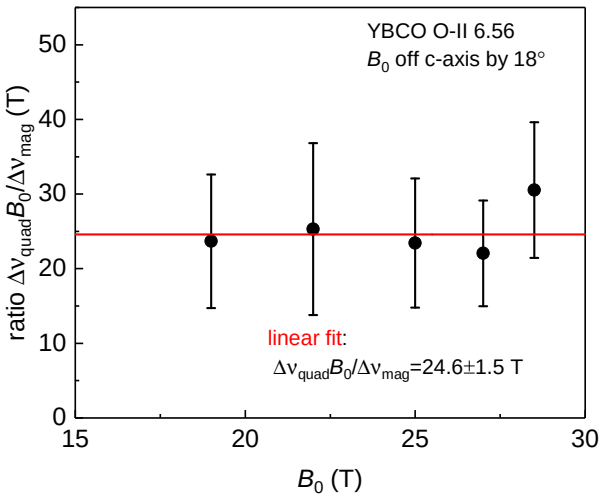

Figure 3.35: Quadrupole and magnetic splittings are determined from the 8-peak-fitting with EVD profiles for the O-II sample. The ratio of the quadrupole and magnetic splitting is multiplied by the applied field B_0 to compensate the linear field dependence of $\Delta\nu_{\mathrm{mag}}$. This ratio is found to be field independent in the range between 19 T and 28.5 T.

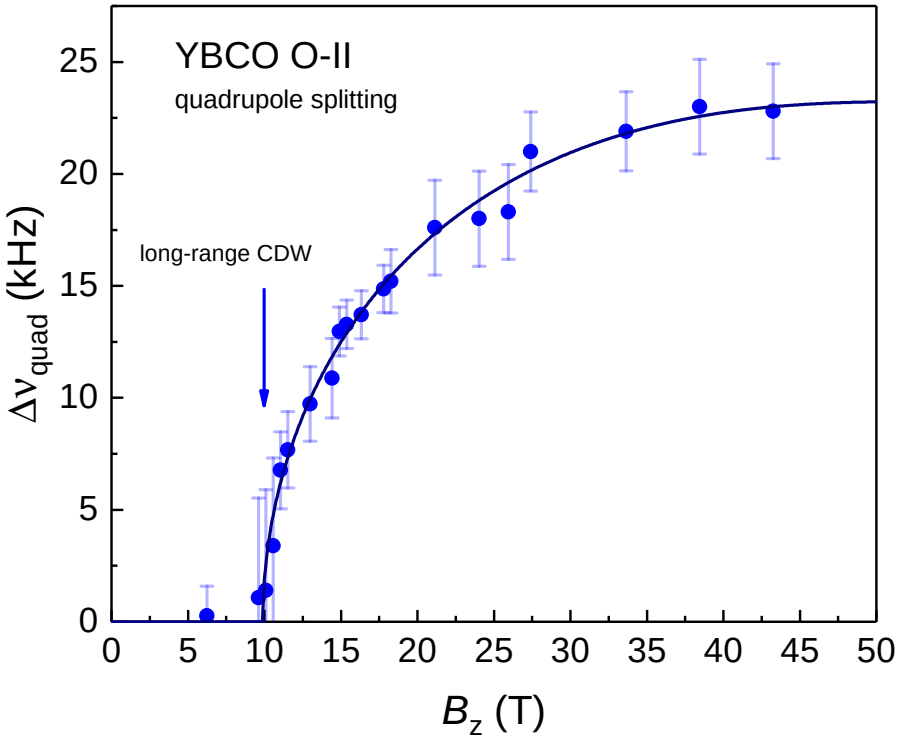

Figure 3.36: Quadrupole splittings $\Delta\nu_{\mathrm{quad}}$ of the O(2) site as a function of B_z. For $B_z \leq 17.6$ T the quadrupole splitting is calculated from $\nu_{\mathrm{tot,HF2}}$ of Fig. 3.34 using eq. 3.24. For fields above 17.6 T, $\Delta\nu_{\mathrm{quad}}$ is directly determined from 8-peak fits. The line is a tanh-fit, defined in eq. 3.25.

dependence of the BCS-gap, $\Delta_{BCS}(T)$ [149]:

$$\Delta_{BCS}(T) = \Delta_0 \tanh\left(1.74\sqrt{\frac{T_\mathrm{c}}{T}-1}\right)$$

By analogy, for $\Delta\nu_\mathrm{quad}(B)$ this gives

$$\Delta\nu_\mathrm{quad}(B) = \Delta\nu_{\mathrm{quad,\,max}} \tanh\left(1.74\sqrt{\frac{B_\mathrm{sat}-B_\mathrm{onset}}{B_\mathrm{sat}-B}-1}\right), \tag{3.25a}$$

where B_sat is the field above which $\Delta\nu_\mathrm{quad}(B)$ saturates at $\Delta\nu_{\mathrm{quad,\,max}}$. And as $\Delta\nu_\mathrm{mag}$ is found to be proportional to $\Delta\nu_\mathrm{quad}$ it follows the same B-dependence and finally for the total splitting we find

$$\begin{aligned}\nu_\mathrm{tot,HF2}(B) &= 2\Delta\nu_\mathrm{quad}(B) + \Delta\nu_\mathrm{mag}(B) \\ &= (2\Delta\nu_{\mathrm{quad,\,max}} + \gamma B \Delta K_\mathrm{max}) \tanh\left(1.74\sqrt{\frac{B_\mathrm{sat}-B_\mathrm{onset}}{B_\mathrm{sat}-B}-1}\right)\end{aligned} \tag{3.25b}$$

Here ΔK_max is the value at which the Knight shift splitting saturates.

This analysis confirms the earlier results obtained by Wu *et al.* [73]. The only difference is that based on the new analysis with 8-peak fits $\Delta\nu_{\mathrm{quad,max}}$ is smaller by about 10 kHz, compared to ref. [73]. As the B-dependence of the quadrupole splitting is analogous to the T-dependence of the BCS gap $\Delta_{BCS}(T)$, it suggests that $\Delta\nu_\mathrm{quad}$ can be interpreted as an order parameter of the long-range CDW phase. It is, however, not the order parameter of the thermodynamic long-range 3D CDW phase as probed by ultrasound [93, 98], but the order parameter of long-ranged in-plane (2D) CDW correlations that precede the true thermodynamic phase transition when long-ranged order in all spatial directions is achieved.

The tanh-fit finds a saturation field B_sat of 58 T. Such a high saturation field is not expected for this sample because no field dependence is expected beyond $H_{c2} \approx 24$ T. However, $\Delta\nu_\mathrm{quad}$ is constant within the measurement precision above ≈ 25 T. $B_\mathrm{sat} \gg H_{c2}$ can thus be seen as an artifact of the very gradual saturation of eq. 3.25.

Splitting of O-VIII sample $p = 0.125$

Determining the splitting is more difficult in the O-VIII sample, since the O(2) satellites contain two distinct sites, O(2EF) & O(2FF), as discussed in section 3.1.2. The two sites can be distinguished at high T, because their Knight shifts are different, but with decreasing T all Knight shifts become smaller and so does the Knight shift difference. Consequently, at low T O(2EF) & O(2FF) overlap more, but they do not coincide due to the remaining difference in quadrupole frequencies ν_quad. The unequal area ratio of O(2EF) & O(2FF) results in a slightly asymmetric lineshape of O(2), even below B_onset. Hence it is more difficult to resolve a splitting and error bars are larger.

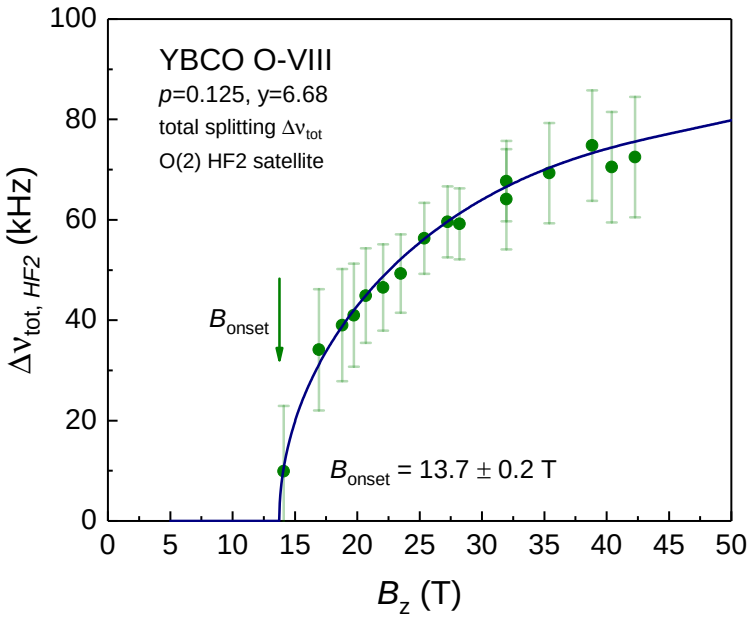

Figure 3.37: Total splitting $\Delta\nu_{\mathrm{tot,HF2}}$ of the O(2) $HF2$ satellite of the O-VIII sample ($p = 0.125$) at $T \approx 2$ K, with the sample tilted by $\approx 20°$ off the $\boldsymbol{c}$-axis. $\Delta\nu_{\mathrm{tot,HF2}}$ is plotted against B_z, the projection of the field along the $\boldsymbol{c}$-axis. The splitting has been determined by a least squares routine in MATLAB. The analysis by 8-peak fits of a full spectrum with EVD profiles at $B_z = 28.4$ T leads to a consistent total splitting. The line is a fit with the tanh-fit, defined in eq. 3.25b and gives $B_{\mathrm{onset}} = 13.7 \pm 0.2$ T.

All the data has been acquired and pre-analysed by Michihiro Hirata and Rui Zhou. In the context of this thesis the analysis has been refined together with Rui Zhou.

The MATLAB routine was used to determine the splitting of the O(2) $HF2$ satellite. The area ratio was fixed to 2-to-1. The single peak width w_0 was not constrained, because no full spectrum was measured below B_{onset}. We found that w_0 scatters less as a function of field if the Lorentzian contribution, m, is not constrained. m decreases with increasing field.

The resulting splitting is shown in Fig. 3.37. The fitting error bar of the onset field is small, because the scattering of the data points is small, but the true uncertainty is likely to be significantly larger. An uncertainty of ± 2 T is reasonable.

Splitting of O-III sample $p = 0.136$

This O-III ordered sample has broad and slightly asymmetric O(2) satellites, for the same reason as the O-VIII sample. The analysis of this sample is different in that the single peak width w_0 could be constrained by the width as given by eq. 3.23.

For this, the broadening contributions were determined from a full spectrum at $B_0 = 22$ T. This field lies just below B_{onset}. By constraining the single peak widths in the MATLAB routine to the

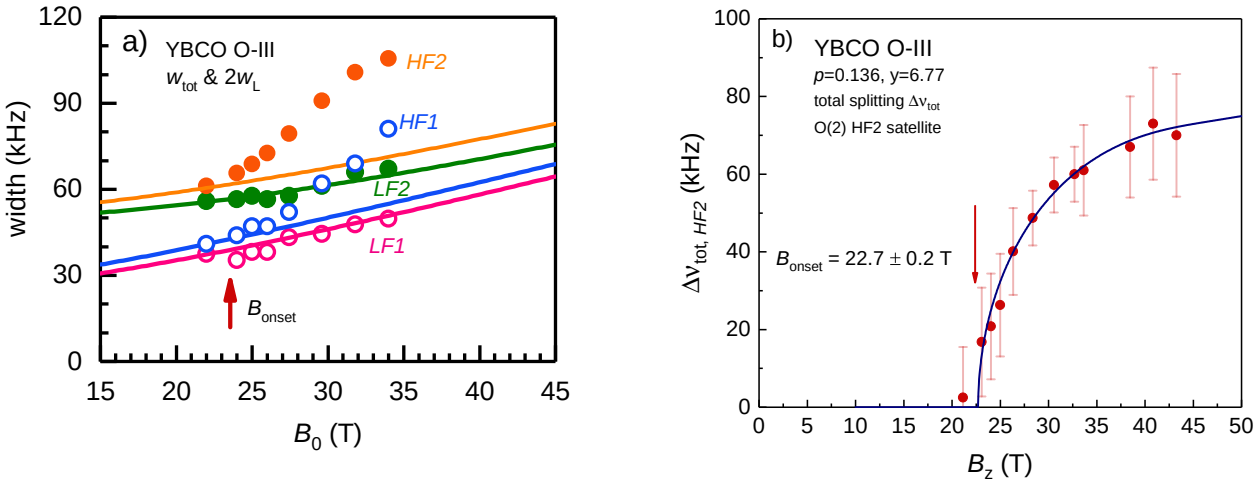

Figure 3.38: a): Comparison of experimental widths $w_{\rm tot}$ of O(2) satellites of the O-III sample at low $T \sim$2 K with the calculated widths, $2w_L$, as a function of the applied field B_0. $2w_L(B)$ is calculated from equations analogous to eq. 3.23 from broadening contributions at $B_0 = 22$ T, below the onset field: $\delta\nu_{\rm quad} = 24.8$ kHz, $\delta\nu_{\rm mag,c} = 2.9$ kHz and $\delta\nu_{\rm mag,0} = 30.3$ kHz. Since the total splitting on $LF1$ is small, its total width is dominated by the single peak width w_0. The total width of $HF1$ and $HF2$ increases rapidly because of the growing splitting. b): Total splitting $\Delta\nu_{\rm tot,HF2}$ of the O(2) $HF2$ satellite of the O-III sample ($p = 0.136$) at $T \approx 2$ K, with the sample tilted by $\approx 16°$ off the $\boldsymbol{c}$-axis. $\Delta\nu_{\rm tot,HF2}$ is plotted against B_z, the projection of the field along the $\boldsymbol{c}$-axis. The splitting has been determined by a least squares routine in MATLAB. The analysis by 8-peak fits of a full spectrum with EVD profiles at $B_z = 32.7$ T leads to a consistent total splitting. The line is a fit with the tanh-fit, defined in eq. 3.25b and gives $B_{\rm onset} = 22.7 \pm 0.2$ T.

calculated width $2w_L$, as given by eq. 3.23 from the broadening contributions, one should underestimate the single peak width. However, when comparing the measured widths $w_{\rm tot}$ of each satellite with the corresponding calculated width $2w_L$ one finds that the measured $w_{\rm tot}$ of low frequency satellites $LF1$ and $LF2$ are not growing faster than the calculated field dependence of $2w_L$, see Fig. 3.38a. This does not mean that these satellites show no asymmetric broadening. O(2) $LF1$ is markedly asymmetric at high field [145]. However, it could mean that the broadening contributions used in calculating $2w_L$ were overestimated. As a result, we can expect $2w_{L,HF2}(B)$ to be a reasonable single peak width w_0 for the MATLAB routine.

The resulting splitting is shown in Fig. 3.38b. Again, the fitting error bar of the onset field is small, but the true uncertainty is likely to be significantly larger, because of uncertainties concerning the constrained single peak width. An error bar of ± 2 T is reasonable.

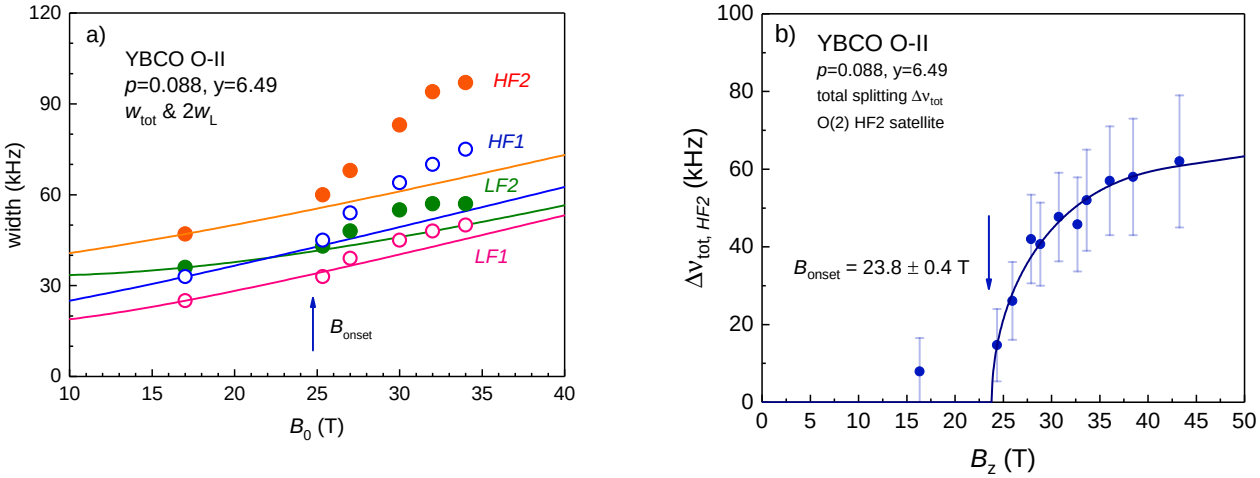

Figure 3.39: a): Comparison of experimental widths $w_{\rm tot}$ of O(2) satellites of the O-II sample with $p = 0.088$ at low T ∼2 K with the calculated widths $2w_L$ as a function of the applied field B_0. $2w_L(B)$ is calculated from equations analogous to eq. 3.23 from broadening contributions at $B_0 = 17$ T, below the onset field: $\delta\nu_{\rm quad} = 17.3$ kHz, $\delta\nu_{\rm mag,c} = 6.6$ kHz and $\delta\nu_{\rm mag,0} = 22.6$ kHz. Since the total splitting on $LF1$ is small, its total width is dominated by the single peak width w_0. The total width of $HF1$ and $HF2$ increases rapidly because of the growing splitting above the onset field. b): Total splitting $\Delta\nu_{\rm tot,HF2}$ of the O(2) $HF2$ satellite of the O-II sample with $p = 0.088$ at $T \approx 2$ K, with the sample tilted by $\approx 16°$ off the $\boldsymbol{c}$-axis. $\Delta\nu_{\rm tot,HF2}$ is plotted against B_z, the projection of the field along the $\boldsymbol{c}$-axis. The splitting has been determined by a least squares routine in MATLAB. The analysis by 8-peak fits of a full spectrum with EVD profiles at $B_z = 32.7$ T leads to a consistent total splitting. The line is a fit with the tanh-fit, defined in eq. 3.25b and gives $B_{\rm onset} = 23.8 \pm 0.4$ T.

Splitting of O-II sample $p = 0.088$

The O-II sample with a low doping of $p = 0.088$ has the broadest lines at high T of all samples dicussed so far [148, 145]. The lines are so broad that a splitting of O(2) $HF2$ into two peaks is not resolvable at low T and high fields. Still, by constraining the widths, as done for the O-III sample a reliable onset field can be determined from the splitting values given by the fit.

The broadening contributions have been determined from a full spectrum at $B_0 = 17$ T. The measured widths $w_{\rm tot}$ of each satellite are compared with the calculated width $2w_L$ in Fig. 3.39a. As the calculated $2w_{\rm L,LF1}(B)$ grows slower than the measured width $w_{\rm tot,LF1}$ the broadening contribution appear not to be overestimated for this sample. Thus, we expect that by constraining the single peak width w_0 of the $HF2$ satellite to the caluculated $2w_{L,HF2}(B)$, w_0 is underestimated and consequently the splitting could be overestimated. However, as the asymmetry of the single peak profile is expected to be weaker on $HF2$ than on $LF1$, this error is not significant. The resulting splitting is shown in Fig. 3.39b. As before, the fitting error bar of the onset field is smaller than the true uncertainty. Assigning an error bar of ±2.5 T is reasonable.

Fig. 3.40 shows high field spectra for each doping $p = 0.125$, $p = 0.136$ and $p = 0.088$ all measured at 34 T, corresponding to $B_z \approx 32.3$ T. Visibly, the splitting is not well resolved for $p = 0.136$, even less for $p = 0.088$, so it is essential to constrain the single peak widths for these samples.

Doping dependence of B_{onset}

The principal field scale for a superconductor is H_{c2}. Phenomena that compete with superconductivity (SC) become field dependent by feeding off the weakening SC at high fields. It is thus natural that $B_{\mathrm{onset}}(p)$, determined by NMR [73] and $B_{\mathrm{CO}}(p)$ from ultrasound [98], follow the doping dependence of H_{c2}, reported by Grissonnanche *et al.* [38], as shown in Fig. 3.41a.

The remarkable aspect about these field scales is that they share an equivalent doping dependence around $p = 0.12$. They differ only by an additive constant and B_{CO} lies exactly in the middle between B_{onset} and $\mu_0 H_{\mathrm{c2}}$:

$$\mu_0 H_{\mathrm{c2}} = B_{\mathrm{CO}} + 7\,\mathrm{T} = B_{\mathrm{onset}} + 14\,\mathrm{T} \tag{3.26}$$

The relation works better than multiplicative scalings of these field scales, as suggested by Jang *et al.* [143] or Laliberté *et al.*[98]. It is consistent with the observation of Jang *et al.* that the XRD intensity of the 3D peak saturates at $\mu_0 H_{\mathrm{c2}}$, ≈ 14 T above the onset field $\mu_0 H_{\mathrm{3D}}$, which is equivalent to B_{CO}. Account should be taken that Laliberté et al. have reproduced erroneous NMR data from Chang *et al.* [92], instead of the original publication of Wu *et al.* [73].

Eq. 3.26 is useful to extract information about the doping dependence of the saturated quadrupole splitting $\Delta\nu_{\mathrm{quad,\,max}}(p)$. According to it $\Delta\nu_{\mathrm{quad}}(p)$ is expected to be saturated 14 T above B_{onset}, which has been precisely determined from fits of the total splitting. If we assume that eq. 3.24 is valid in the full doping range, then we can calculate the average $\Delta\nu_{\mathrm{quad,\,max}}(p)$ from all fields above H_{c2} using identical criteria. As seen previously, the tanh-fit itself has a very gradual saturation. This is a useful property when determining the onset field, but the parameters B_{sat}, $\Delta\nu_{\mathrm{quad,\,max}}$ and the slope of the magnetic splitting $\gamma\Delta K$ cannot be determined reliably from the fit, because of cross-correlation of the fitting parameters. The validity of eq. 3.24 for other dopings than $p = 0.109$ could not be verified, but as the ^{17}O-NMR spectra have been acquired in the same field orientation and as the analysis is equivalent, it is a reasonable assumption.

As shown in Fig. 3.42, $\Delta\nu_{\mathrm{quad,\,max}}(p)$ does not vary strongly with doping in the investigated range. This could appear to be at odds with recent work by Jang *et al.* [150]. There, the XRD intensity of the 3D CDW peak was measured in fields of 30 T at 10 K for a range of dopings and the intensity decreases rapidly with underdoping. At $p = 0.09$ the intensity is only 25% of the intensity at $p = 0.12$. As the onset temperature of 3D charge order T_{CO} decreases rapidly with underdoping [98], the XRD

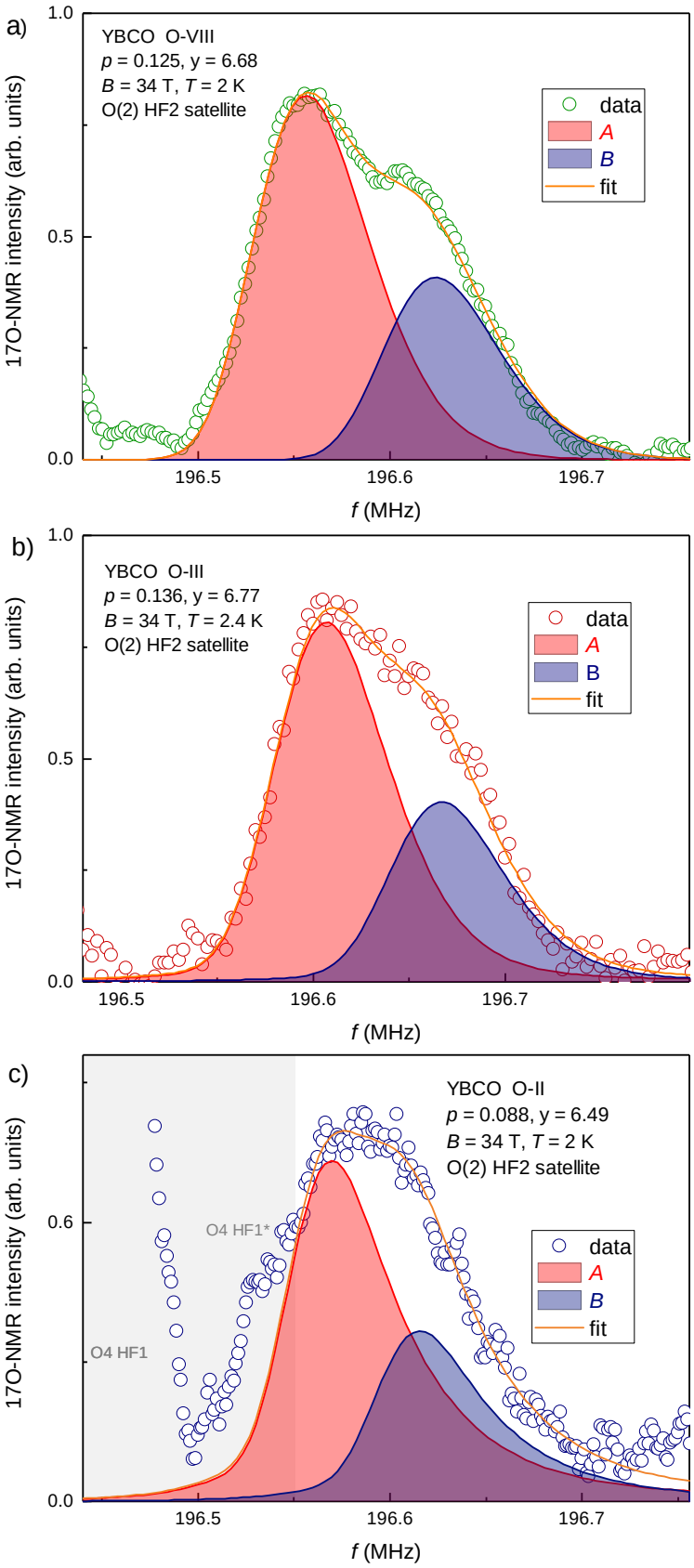

Figure 3.40: O(2) HF2 satellites at 34 T for a): O-VIII, $p = 0.125$ with a well resolved splitting, b): O-III, $p = 0.136$ with a visible shoulder and c): O-II, p=0.088 with no clear splitting. Due to overlap at low frequency with the O(4) HF1 satellite and some additional peak, here called O(4) HF1*, the frequency range that is shaded in grey was excluded from the fit. Evidently, the resulting error bars increase from a) to c).

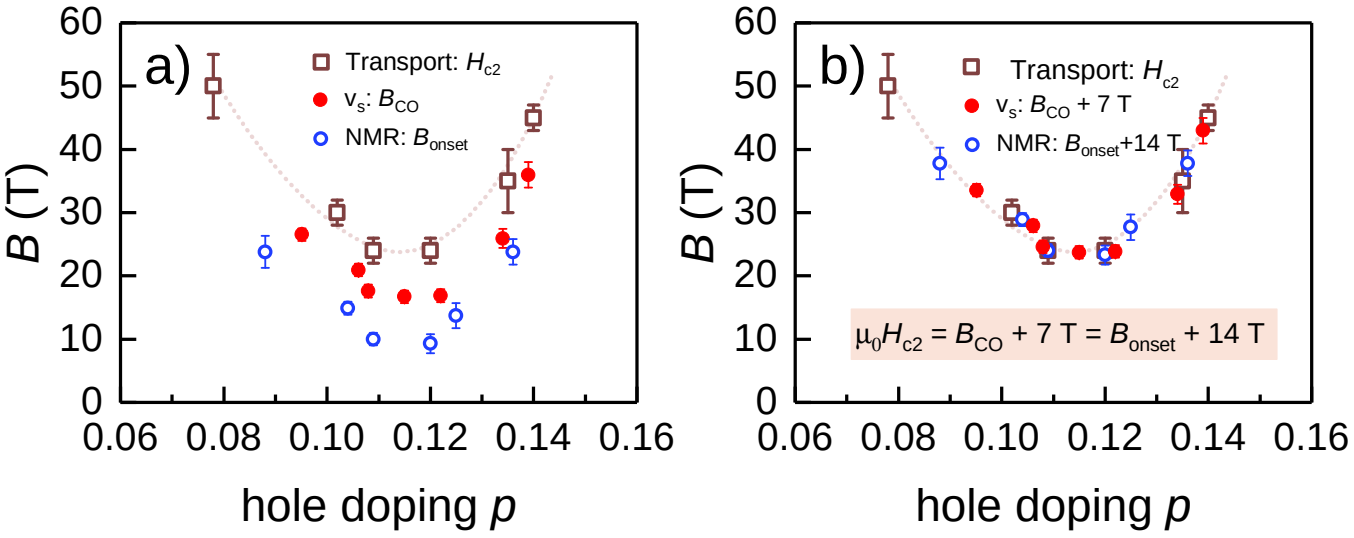

Figure 3.41: Doping dependence of field scales in YBCO. a): Comparison of H_{c2} (brown squares), determined by transport [38], B_{CO} from sound velocity v_s [98] and B_{onset} from NMR. The NMR data at $p = 0.104$ & $p = 0.12$ is from ^{63}Cu-NMR [73]. Other NMR data is from ^{17}O-NMR. b): Perfect scaling of all field scales by addition of doping-independent constant field, as given by eq. 3.26.

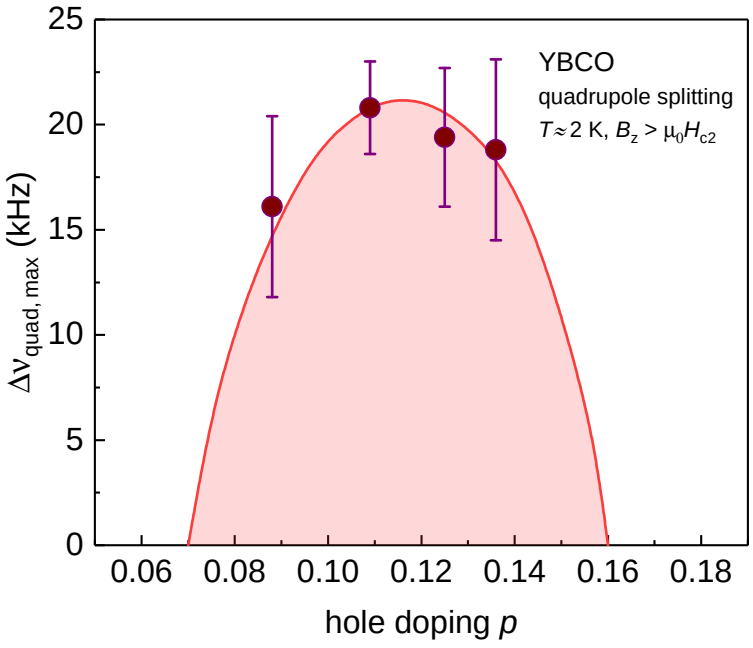

Figure 3.42: Doping dependence of the maximal quadrupole splitting $\Delta\nu_{\mathrm{quad,\,max}}$ in YBCO. It is determined at each given doping from the average of all quadrupole splittings measured at $B_z > \mu_0 H_{c2}$. The red line is a parabolic guide to the eye. By constraint, it goes to zero at $p = 0.07$ and $p = 0.16$, so its center is at $p = 0.115$.

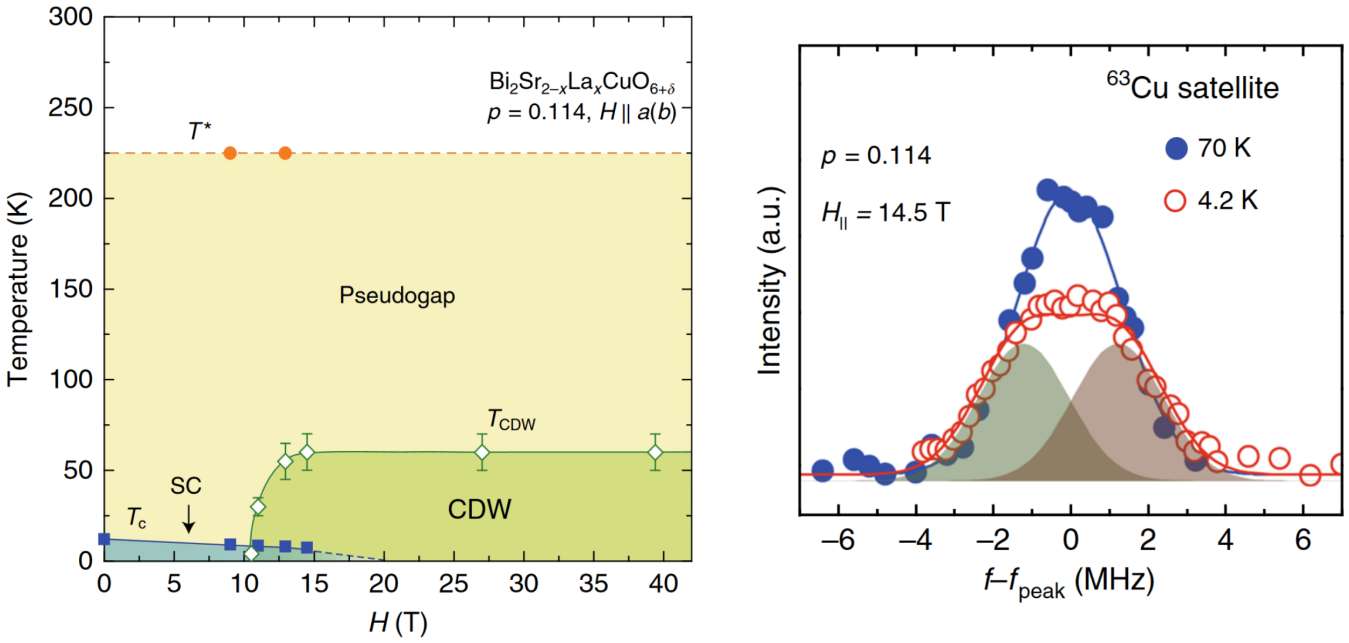

Figure 3.43: Left panel: T-H phase diagram of $Bi_2Sr_{1.25}La_{0.75}CuO_{6+\delta}$ ($p = 0.114$). A CDW phase is induced above $H_{CDW} = 10.4$ T and persists up to $T_{CDW} = 60$ K, way above $T_c = 12$ K. The pseudogap below T^* is field-independent.
right panel: ^{63}Cu NMR satellite spectrum at 70 K and 4.2 K at 14.5 T. The low T spectrum shows indications of a splitting with symmetric area ratio. Figures are reproduced from ref. [103].

intensity at $p = 0.09$ and 10 K may not saturated ($T_{CO}(p = 0.09) \approx 20$ K), although SC has been completely suppressed. On the other hand, the NMR measurements are performed in the low T and high field limits simultaneously.

To which extent the quadrupole splitting or the XRD intensity of the 3D peak are equivalent, is a matter of debate. The quadrupole splitting is a quantity that is sensitive to the local amplitude of the charge modulation. In principle, the integrated intensity in XRD should be proportional to the amplitude, but it also depends on the correlation volume. Consequently, the integrated intensity could remain constant, if a decreasing CDW amplitude is compensated by a growing correlation volume.

3.3.5 Comparison of YBCO and Bi-2201

Recently, field-induced charge order has been reported in underdoped $Bi_2Sr_{2-x}La_xCuO_{6+\delta}$ by Kawasaki *et al.* using ^{63}Cu-NMR [103]. The results are similar to YBCO in terms of no concomitant spin order being found, but differences exist in many respects: The field is applied parallel to the CuO_2-planes and at $p = 0.114$ charge order remains field-dependent at $T < T_{CDW} = 60$ K, temperatures that are much higher than the superconducting $T_c = 12$ K, see Fig. 3.43. Since T_c and $\mu_0 H_{c2,in-plane} = 29$ T are very low, it is not so surprising that an in-plane field of 10.4 T can induce a CDW, but the fact that the CDW is field-dependent for $T > T_c$ defies understanding.

The lineshape of the ^{63}Cu satellite, shown in Fig. 3.43, indicates that the satellite splits into two equal peaks. Kawasaki *et al.* discuss the line splitting as the result of a uniaxial incommensurate charge modulation, whose characteristic two-horn spectrum is strongly broadened by disorder. This is consistent with the incommensurate wave vector $q = 0.26$ found by resonant XRD by Comin *et al.* in zero field [85]. In the same study, Comin *et al.* have also done STM and ARPES on the same sample ($p = 0.12$). With STM they found a commensurate $4a$ modulation.

Like STM, NMR is a local probe, so the $4a$ modulation should also be reflected in the NMR spectrum. As discussed and shown in Fig. 3.21, depending on the phase, a splitting with 1-to-1 area ratio can also be consistent with a $1q$ commensurate modulation with period $4a$. As $q = 0.26$ is close to the commensurate $q = 1/4$, diffraction experiments and local probes become consistent if the mechanism of discommensurations is invoked which makes the modulation locally commensurate with period $4a$ [136].

The situation in Bi2201 is thus very analogous to underdoped YBCO, with the difference that the incommensurate wave vectors found in YBCO are close to $q = 1/3$ and the NMR spectrum in high fields can distinguish commensurate and incommensurate periods.

Interestingly, the ARPES measurements in Bi2201 by Comin *et al.* showed that the incommensurate wave vector $q = 0.26$ connects the endpoints of Fermi arcs and concluded that the origin of the incommensurate wave vectors lies in "nesting" between hot spots.

In the framework of McMillan, Coulomb interactions make the incommensurate modulation energetically unfavourable and discommensurations appear to minimise the Coulomb interaction locally, without changing the incommensurate period on a larger length scale [138]. From this perspective, both the Fermi surface, as well as local Coulomb interaction are important to understand the CDW.

3.4 Summary

This chapter focused on two aspects of the ^{17}O-NMR spectra of underdoped YBCO that give direct information about charge order: The width and the lineshapes of peaks that correspond to the oxygen sites in the CuO_2-planes. It summarises a part of the work of the NMR group over the past ten years or so.

2D short-range CDW & quadrupole broadening $\delta\nu_{\mathrm{quad}}$

In the 2D short-range CDW phase the satellite peaks of O(2) & O(3) sites broaden with lowering temperature. Following the evolution of all satellite peaks widths allows to extract magnetic and quadrupolar broadening contributions.

The quadrupole broadening $\delta\nu_{\mathrm{quad}}$ measures the width of the distribution of quadrupole frequencies ν_{Q} and is proportional to the strength of the CDW in the 2D short-range CDW phase. Consequently, $\delta\nu_{\mathrm{quad}}$ scales with the intensity of the CDW superstructure peaks in XRD.

$\delta\nu_{\mathrm{quad}}$ is extracted for an O-II sample ($p = 0.109$) with well ordered chains, for which the analysis is extended to $T < T_{\mathrm{c}}$.

The analysis is applied to an O-VIII sample ($p = 0.125$) where the correlation length of chain ordering is lower. The determination of $\delta\nu_{\mathrm{quad}}$ becomes more complicated, because it comprises the effect of the CDW modulation and structural disorder.

3D long-range CDW & quadrupole splitting $\Delta\nu_{\mathrm{quad}}$

When high magnetic fields are applied, the in-plane CDW correlations develop long-ranged character and the amplitude of the CDW modulation becomes sufficiently large to split the satellite peaks. To determine the amplitude of the CDW modulation, magnetic and quadrupolar contributions to the splitting have to be separated.

Following a lineshape analysis for $1q$ and $2q$ commensurate and incommensurate modulations we determine that the full ^{17}O-NMR spectrum of O(2) & O(3) sites in high fields can be explained by a uniaxial commensurate modulation with period $3a$ or $3b$.

Based on this model, the onset field of the long-range CDW phase, B_{onset}, is determined for a range of dopings $0.088 \leq p \leq 0.136$. This field follows the doping dependence of H_{c2}.

Chapter 4

Tuning the competition between superconductivity and charge order with hydrostatic pressure in $YBa_2Cu_3O_y$

4.1 Overview of the effect of hydrostatic pressure in YBCO

With the discovery of superconductivity in cuprates, initially in LBCO, it was quickly realised that the T_c of this compound can be increased by applying hydrostatic pressure [151]. This led to the realisation that the substitution of La to a smaller cation could lead to the same effect through chemical pressure. The replacement of La by the smaller Y led to the discovery of YBCO and proved to be a great success as its maximal T_c increased beyond the boiling temperature of liquid nitrogen.[1] However, the further application of hydrostatic pressure on fully oxygenated $YBa_2Cu_3O_7$ shows no significant increase of T_c [152]. In fact, recent measurements by Alireza *et al.* have shown that T_c continuously decreases down to below 10 K [153], see Fig. 4.1. This effect can be understood rather easily knowing the doping dependence of T_c of related compounds like Ca-doped YBCO or LSCO that can be heavily overdoped. For them, T_c decreases beyond some optimal doping value following a parabolic dependence, also known as *Tallon's law* [35]. The mechanism by which hydrostatic pressure increases doping is understood from YBCO's crystal structure being most compressible along the $\boldsymbol{c}$-axis [154]: Reduced distance from CuO-chains to CuO_2-planes leads to improved charge transfer and consequently to higher hole doping. This is the principal effect of pressure on optimally or overdoped YBCO: As the hole doping is increased, T_c continuously decreases. Work by Alireza *et al.* confirms that the application of hydrostatic pressure

[1] The fact that the substitution of La by Y increased T_c cannot be regarded as the effect of chemical pressure since LBCO (mono-layer) and YBCO (bi-layer) have different crystal structures in which Y does not simply replace La. Chu *et al.* were just lucky.

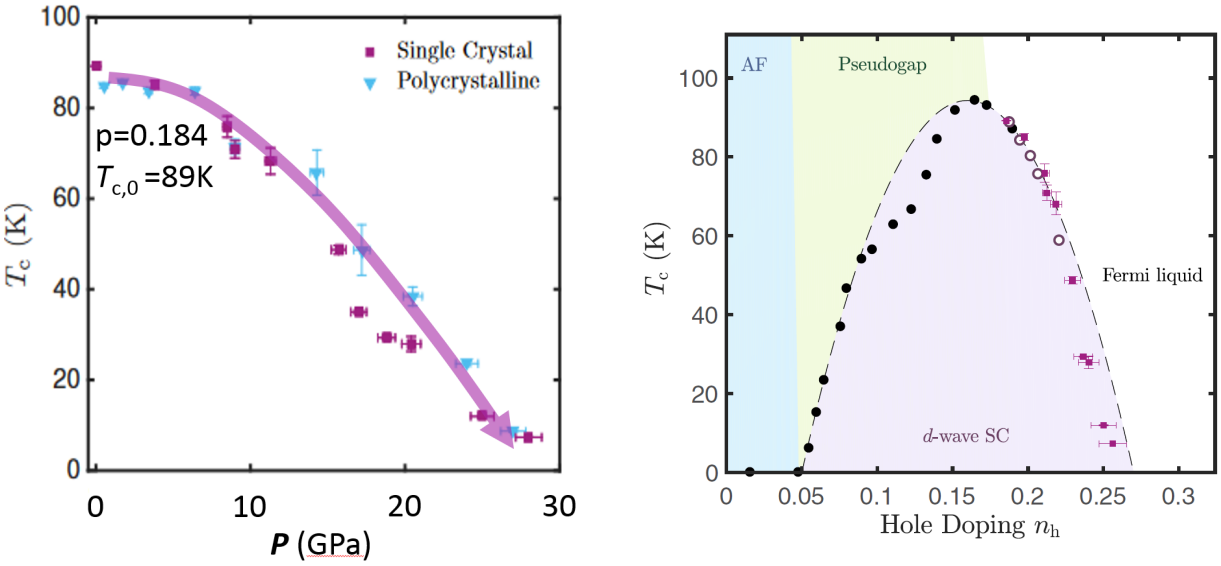

Figure 4.1: a): T_c as a function of hydrostatic pressure up to 28 GPa for overdoped single crystals and polycrystals of YBCO. b): Hole doping ($n_h = p$) dependence of T_c. Filled circles denote ambient pressure T_c of YBCO, empty circles denote ambient pressure T_c of Ca-doped YBCO. Purple squares show evolution of T_c of the overdoped single crystal in a) whose pressure dependence has been converted into pressure induced doping dependence. Both graphs are reproduced from Alireza *et al.* [153].

of nearly 30 GPa is sufficient to decrease T_c from 89 K to less than 10 K, implying an increase of hole doping from $p(\boldsymbol{P}$=0 GPa)≈ 0.184 to $p(\boldsymbol{P}$=28 GPa)≈ 0.26. This type of effect is expected to occur at any hole doping and can be called the „pressure-induced doping effect". In contrast, „intrinsic" pressure effects are dependent on properties at a particular doping and can lead to qualitatively different effects than the increase of the doping. An example for an intrinsic effect of pressure was found in underdoped YBCO samples. A YBCO6.6 sample studied by Sadewasser *et al.* has revealed a T_c of 105 K at 15 GPa, significantly higher than the maximal T_c of 94 K that is achieved by optimising the doping at ambient pressure [70]. To reach a T_c beyond 94 K some other effect of pressure has to boost T_c. Cyr-Choinière *et al.* have remarked that T_c is most sensitive to pressure for samples which also show charge order [2], see Fig. 4.2. They have suggested that it is the suppression of the CDW phase that competes with superconductivity which leads to the increased maximal T_c under hydrostatic pressure.

This hypothesis has been tested by transport and XRD measurements. In two XRD studies it was found that charge order is absent at just 1 GPa [90, 155]. From this very rapid suppression it follows that the suppression of charge order cannot be the dominant mechanism behind the sustained increase of T_c up to at least 15 GPa as found by Sadewasser *et al.*. On the other hand, various transport measurements (slow quantum oscillations and a negative Hall number R_H) still show the signatures of charge order close to or beyond the moderate pressure of 1 GPa [156, 7, 2]. Since transport measurements are performed in high magnetic field, while XRD measurements are in zero field, and as magnetic field

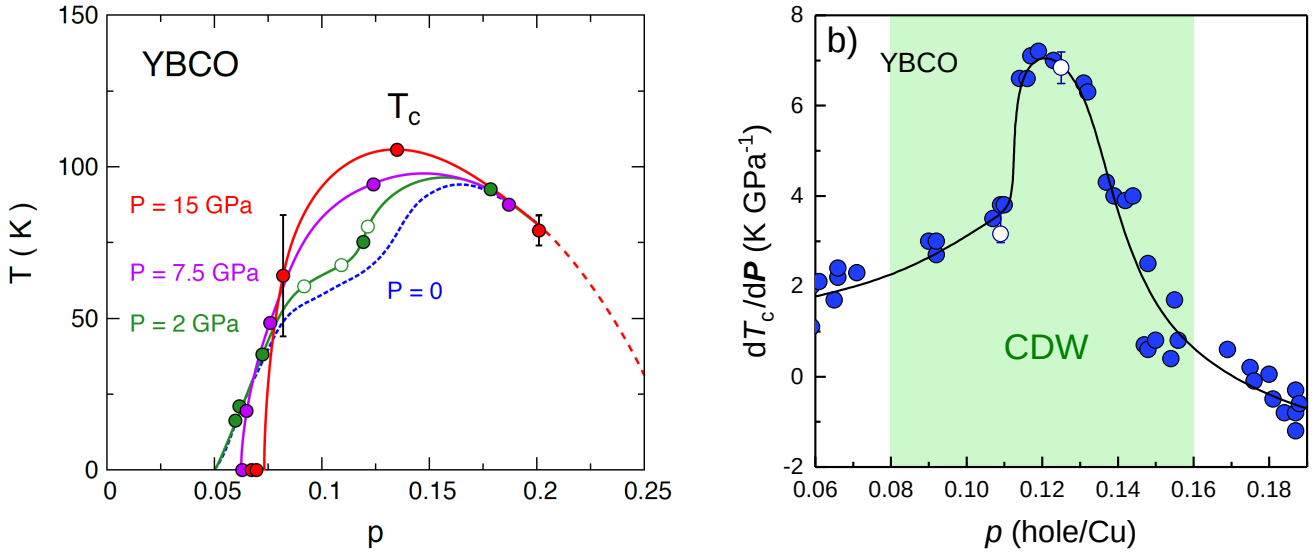

Figure 4.2: a): T_c dome vs hole doping p at different pressures. b): Slope of the hydrostatic pressure dependence $\frac{dT_c}{dP}$(blue) of T_c vs hole doping p. Empty circles are our measurements. The line is a guide to the eye. The left panel and data in right panel are reproduced from Cyr-Choinière *et al.* [2].

is known to strengthen charge order, parts of the community were led to believe that there is not necessarily a contradiction between the XRD and transport measurements. It is thus interesting to study charge order under pressure by NMR since both field-induced & field-independent CDWs can be studied. The aim of the following sections is to present the NMR results and compare them in detail with results from other probes.

4.2 Experimental NMR setup & the pressure cell

To perform NMR measurements under hydrostatic pressure we have utilised a commercial Beryllium-copper (BeCu) clamp pressure cell (version CTF-HHPC50) that was acquired in 2015 from C & T Factory Co. Ltd. in Tokyo, Japan. The pressure medium of choice was Daphne oil 7373 [157], as suggested by Michihiro Hirata. He has been a Post-Doc in the NMR group from 2013 until early 2016 and had experience with this pressure medium and the cell from his PhD in Professor Kanoda's NMR group at the University of Tokyo. The same combination of pressure cell and pressure medium has been used to study both organic and iron-based superconductors with NMR [158, 159]. This type of pressure cell is very simple: A hydraulic press is used to compress the soft Teflon capsule containing the Daphne oil in which the sample is immersed. After the desired pressure is achieved, the top BeCu locknut is screwed tightly to hold the top piston and the top piston backup in place once the external pressure of the press is released.

In principle, an ideal pressure medium is soft to minimise non-hydrostatic shear stress at the samples

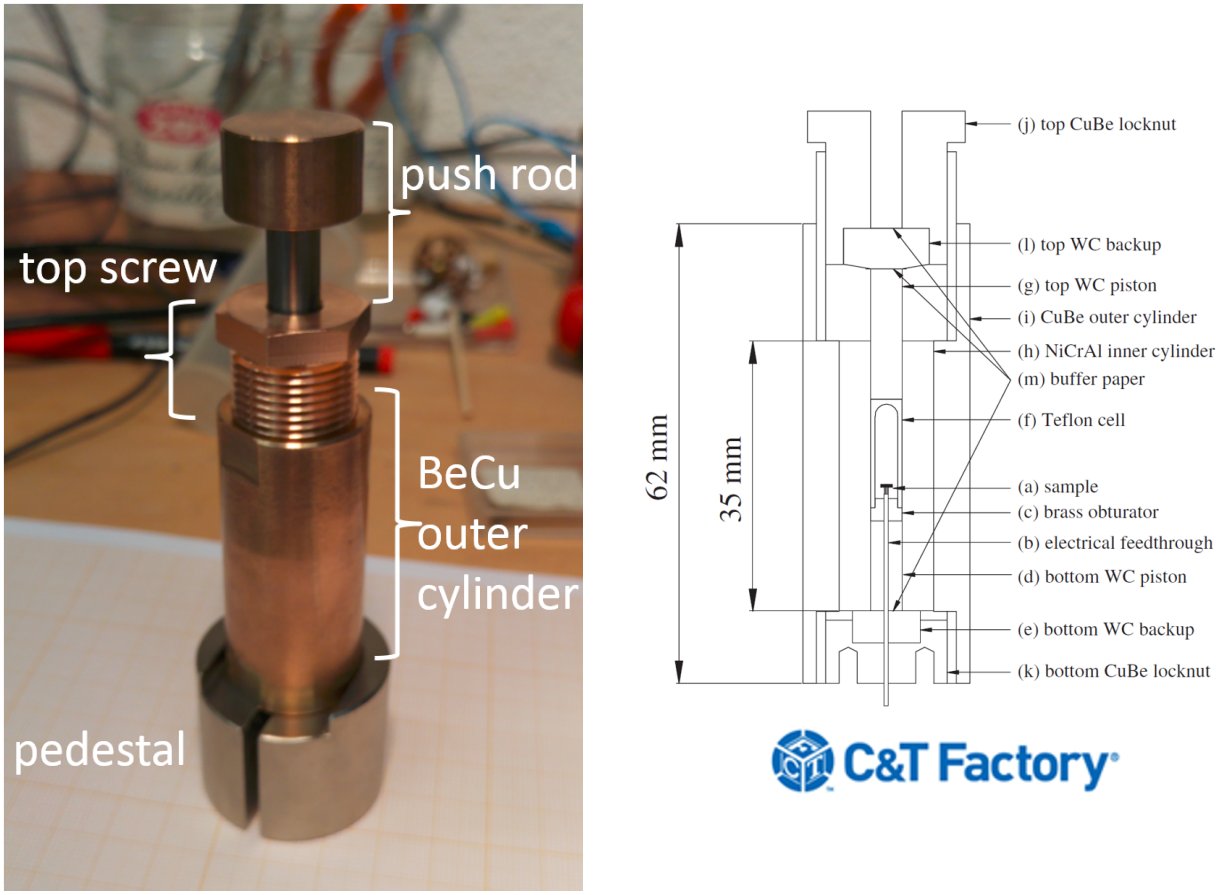

Figure 4.3: a): Photo of the C&T Factory BeCu pressure cell. b): Scheme of the BeCu pressure cell reproduced from Yokogawa *et al.* [157].

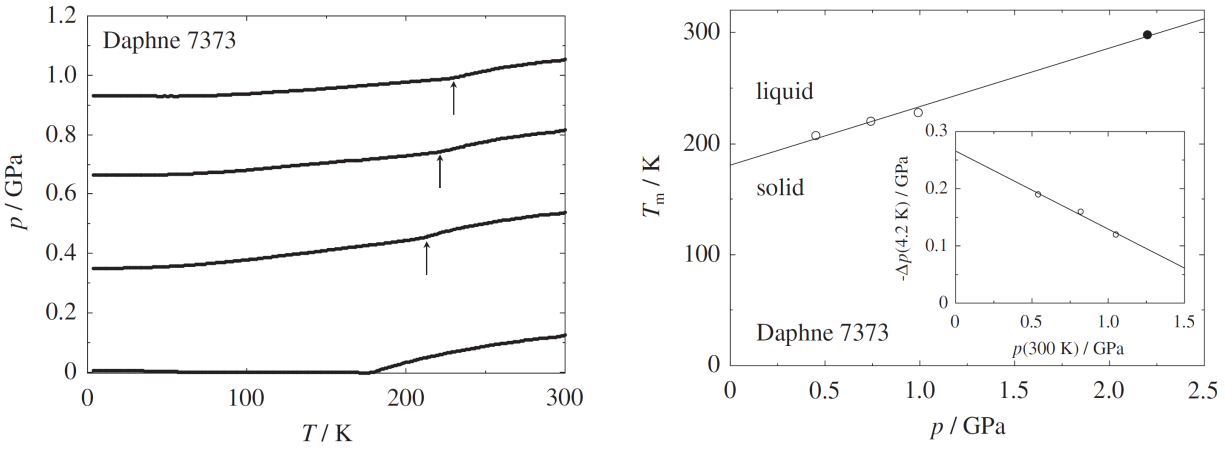

Figure 4.4: a): In-situ pressure evolution with cooling for initial pressures 1.05 GPa, 0.81 GPa, 0.53 GPa and 0.12 GPa, respectively. Arrows mark melting temperatures T_m. b): Temperature-pressure phase diagram of Daphne 7373. Inset: Pressure loss with cooling as a function of initial pressure at 300 K. Graphs are reproduced from Yokogawa *et al.* [157].

surface and does not expand or contract in the entire temperature-pressure region that is studied to keep pressure constant inside the pressure cell. Such an ideal pressure medium does not exist. Best hydrostaticity can be achieved by Helium. However, using Helium as a pressure medium necessitates continuous monitoring and re-adjustment of the pressure as Helium density is varying strongly with temperature. Using a pressure medium that is already a liquid at ambient conditions greatly simplifies the handling of high pressures since the contraction with cooling is not as dramatic as for Helium. In particular, Daphne oil 7373 is an industrial oil with properties that are very suitable for high-pressure measurements. At ambient temperature it remains liquid up to 2.2 GPa, so pressures up to this value can be applied in hydrostatic conditions, see Fig. 4.4. When cooled down, Daphne oil 7373 solidifies very gradually and especially at higher pressures the solidification is not followed by a significant loss of pressure [157].

Since high pressure already increases the packing of the oil's molecules at ambient temperature, the solidification of the oil below the melting temperature leads to ever smaller loss of pressure, the higher the initial pressure, as can be seen in the inset of Fig. 4.4 b). The linear decrease of the lost pressure $-\Delta\boldsymbol{P}$ is captured by the equation

$$-\Delta\boldsymbol{P} = -0.14\boldsymbol{P} + 0.27 \quad [\text{GPa}]\,,$$

so, around $\boldsymbol{P}$=1.9 GPa one expects no pressure loss at all as $-\Delta\boldsymbol{P}$ goes to 0. We have chosen to work at this pressure value. To do this, we first calibrated the pressure inside the pressure cell against the primary pressure of the hydraulic press. The calibration has been done by measuring the resistance of a 2 m long Manganin wire inside the pressure cell by a four-point measurement. Manganin's electrical resistance is known to increase linearly with hydrostatic pressure [160] and thus allows to calculate the

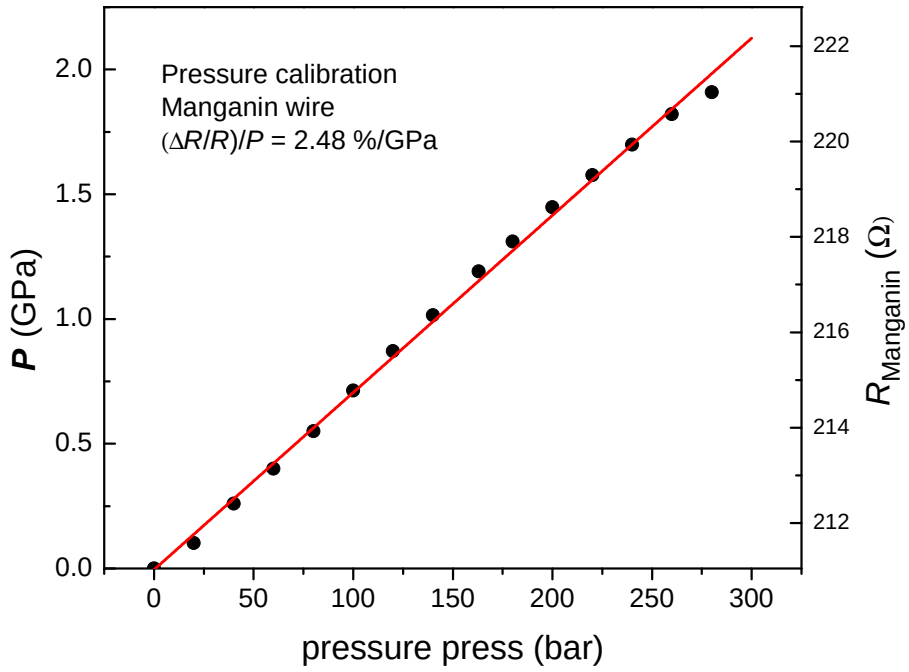

Figure 4.5: Right axis: Manganin wire resistance as a function of primary pressure of the hydraulic press. Left axis: Calculated secondary pressure inside the pressure cell. As expected, the secondary pressure increases linearly (fit) with the applied primary pressure.

absolute pressure from the relative increase of the Manganin's resistance

$$\frac{\Delta R}{R} \,/\, \boldsymbol{P} = 2.48\,[\%\,/\,\mathrm{GPa}]\,,$$

see Fig. 4.5.

4.3 Change of T_c

With this calibration done, we can apply 1.9 GPa by pressurising the BeCu pressure cell with 280 bar. We can verify that this pressure is indeed not lost when cooling down by measuring the change of T_c before and after applying pressure. This is done by tracking the NMR coil's resonance frequency as we cool through T_c. In the SC state susceptibility measurements are in principle surface sensitive because they probe the sample only within the London penetration depth $\lambda_L \approx 2000\,\text{Å}$. Thus, if the surface has a somewhat different doping than the bulk, it can strongly affect the resonance frequency, as can be seen in Fig. 4.6a in case of the O-II sample. An ac-susceptibility measurement, shown in Fig. 4.7 confirms the bulk T_c. The surface problem occurs only in ^{17}O-enriched samples: Additional oxygen is adsorbed at the sample's edges if the sample is not quenched fast enough after the isotope substitution procedure. The bulk properties probed with NMR are in excellent agreement with another particularly clean and homogeneous non-enriched sample of identical doping whose tuning frequency has a single sharp T_c, see ref. [148] for details.

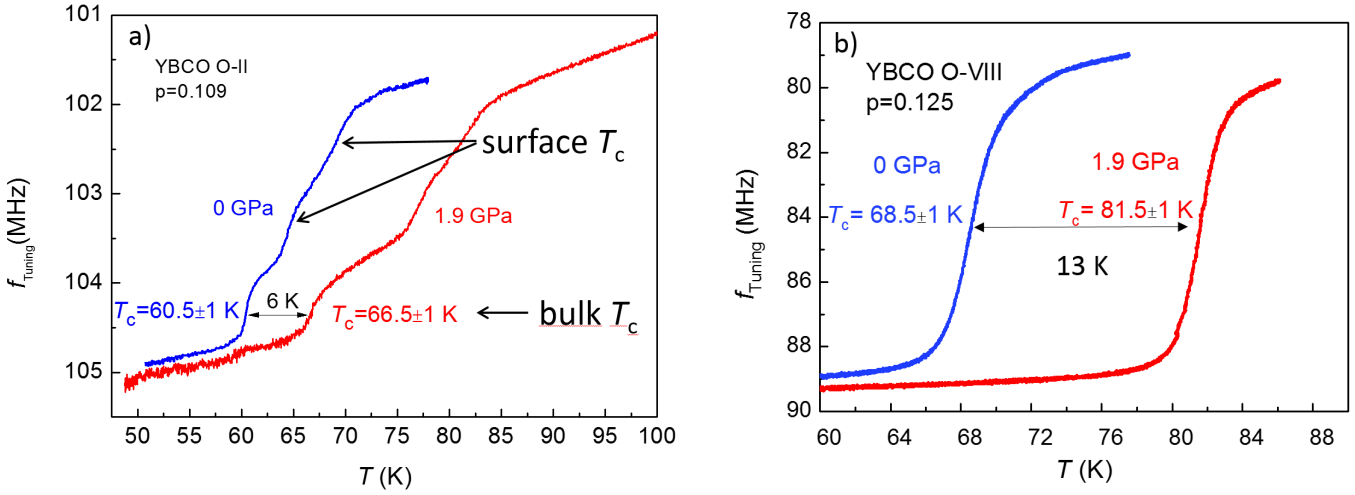

Figure 4.6: a): Tuning frequency of NMR tank circuit of O-II (p=0.109) sample. T_c is determined from the midpoint of lowest step that corresponds to the bulk T_c. b): Tuning frequency of O-VIII (p=0.125) sample.

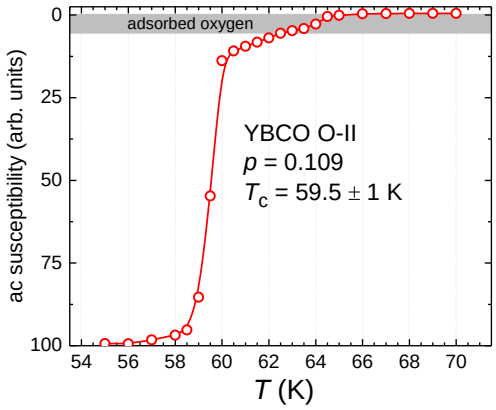

Figure 4.7: ac-susceptibility of the ^{17}O-enriched YBCO O-II sample shown in Fig. 4.6a. Adsorbed oxygen leads to a surface T_c of $\approx$ 64 K. The small decrease at the 64 K (marked in grey) implies that at most 5% of the sample within the London penetration depth λ_L is affected by oxygen adsorption. The line is a guide to the eye.

The T_c increases by about 6 K and 13 K for the O-II and O-VIII samples, respectively. These increases are consistent with the reported $\frac{dT_c}{dP}$ in Fig. 4.2b from ref. [2] for a pressure of 1.9 GPa. We can thus conclude that not more than 0.1 GPa of pressure has been lost at low temperature where the Daphne oil has solidified.

It should be mentioned that after applying the pressure at ambient temperature the pressure cell is mounted on the probe and has to be cooled rapidly below 200 K so oxygen mobility in the chain-layer is significantly reduced. This is important since hydrostatic pressure can affect the ordering of the CuO-chains. If left at ambient temperature for an extended duration this process can significantly increase T_c of underdoped samples with previously disordered chains [70]. The relaxation time into

the new chain-order amounts to multiple hours. Since we use detwinned and highly ordered samples and cool below 250 K within less than two hours after pressurisation, we believe that these effects are absent in our experiments.

4.3.1 Pressure-induced doping: Literature survey

Before discussing how charge order is affected by hydrostatic pressure it is important to assess the doping effect of pressure in a more quantitative way. This is important as the strength of charge order is known to be strongly doping-dependent, forming a dome centered around $p \approx 0.12$ [83, 86, 84]. Cyr-Choinière *et al.* have proposed a model to asses the pressure induced doping [2]. They made two assumptions: Firstly, pressure increases the doping by facilitating the charge transfer from CuO-chains to CuO_2-planes. To first approximation this effect is linear in the applied pressure $\boldsymbol{P}$. Secondly, the charge transfer must be stronger in a sample with a higher oxygen concentration in the chain layer, so the linear increase of hole doping is assumed to be proportional to the initial doping. Altogether, this gives

$$p(\boldsymbol{P}) = p_0 + b \cdot p_0 \cdot \boldsymbol{P} \tag{4.1}$$

Within this model there is only one parameter, b, that controls the pressure-induced doping effect of pressure. Using eq. 4.1 and the parabolic form of $T_c(p)$ [35], Cyr-Choinière *et al.* determined $b = 0.01\,\mathrm{GPa}^{-1}$ from the pressure dependence of T_c for the overdoped sample studied by Sadewasser *et al.* up to 11 GPa [70]. By repeating the same procedure using the high-pressure data by Alireza *et al.* we find a somewhat higher value, $b = 0.018\,\mathrm{GPa}^{-1}$, see Fig. 4.8. The application of 1 GPa changes the doping from p_0 to $p_0 \cdot (1 + b)$, so b is the percentage by which the doping increases per GPa ($b = 0.01 = 1\%$). Thus, within the model proposed by Cyr-Choinière *et al.* the pressure induced doping for either value of b is rather small and these values can be compared with those reported in the literature: Jorgensen *et al.* have estimated the induced doping to be 0.0065 holes/GPa for $YBa_2Cu_3O_{6.93}$ and 0.008 holes/GPa for $YBa_2Cu_3O_{6.60}$, so approximately a 4% and 7% increase of doping per GPa, respectively. These estimations are deduced from Bond-Valence-Sums based on structural data up to only 0.58 GPa [154]. Murayama *et al.* have measured strongly decreasing Hall numbers at $T > T_c$, decreasing by 8-10% per GPa in fully oxygenated YBCO. Assuming that the Hall number is inversely proportional to the carrier density, they inferred a 8-10% per GPa increase in the hole doping [161]. On the other hand, Gupta & Gupta did an electronic structure calculation that resulted in an increased doping of only 0.0017 holes/GPa $YBa_2Cu_3O_7$, *i.e.* roughly a 1% increase in hole doping per GPa [162], consistent with the estimation of Cyr-Choinière *et al.*. We cannot resolve the large discrepancy in the estimated pressure-induced hole doping from experiments and simulations but would like to point out that if the hole doping increased at the rate suggested by Jorgensen *et al.*,

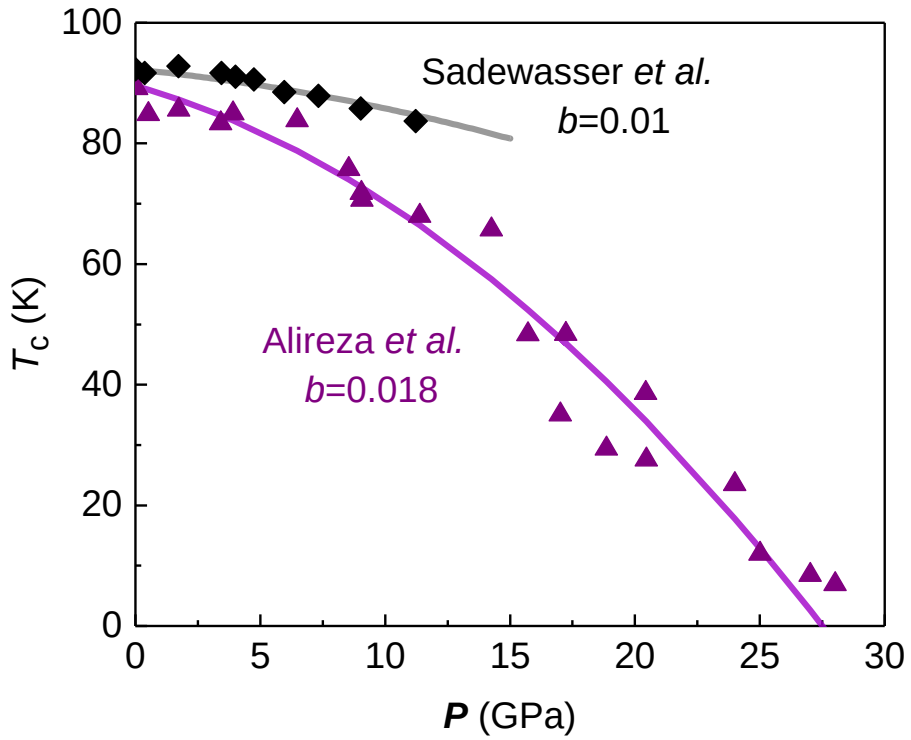

Figure 4.8: $T_c(\boldsymbol{P})$ for overdoped YBCO samples of Sadewasser *et al.* (black diamonds) with $p_0 \approx 0.175$ [70] and Alireza *et al.* (purple triangles) with $p_0 \approx 0.184$ [153]. We fit both the single crystal and polycrystalline samples simultaneously, as their pressure dependence is similar, see Fig. 4.1a. Lines describe $T_c(\boldsymbol{P})$ assuming the parabolic doping dependence of T_c (Tallon's law [35]) where the doping is changed through pressure $\boldsymbol{P}$ by eq. 4.1. Best fits to the data are found with $b = 0.01$ and $b = 0.018$, respectively.

then Alireza *et al.* would have been able to induce the necessary doping of $p \approx 0.27$ to suppress T_c in their fully oxygenated single crystal with less than 14 GPa, instead of 30 GPa. Form the estimation of Murayama *et al.* a pressure as little as 7 GPa would be sufficient.

4.3.2 Estimation of doping change from NMR

In YBCO the induced doping can also be estimated from resistivity or the Knight shift. The Knight shift increases with doping and its T-dependence, at least for $T > T_{CDW}$, is determined by the pseudogap [44]. The pseudogap turns out to have no intrinsic pressure effect: In LSCO, where the doping cannot change with pressure, for p=0.15 the upturn in resistivity due to the pseudogap is independent of pressure up to at least 2 GPa [163]. This implies that any change of the pseudogap in YBCO under pressure is exclusively due to the doping effect. Pressure-induced doping should diminish the pseudogap strength and T^* about linearly. In YBCO, resistivity curves appear to be largely pressure-insensitive across T^* and down to $T \approx T_{CDW}$ and start to differ appreciably only below T_{CDW} [2]. This implies that the pressure-induced doping must be small. This is confirmed by the small change of the Knight shift, with and without pressure, both for the O-II and the O-VIII sample, see Fig. 4.9.

From Fig. 4.9a it is visible that within the experimental precision the Knight shift is nearly identical at 0 GPa and 1.9 GPa for the O-II sample. There might, however, be a small increase of the Knight shift with pressure[2]. In Fig. 4.9b a similar comparison is made for the O-VIII sample at 0 GPa and 1.9 GPa. The Knight shift of the O-VIII sample with $p_0 = 0.125$ appears to have increased slightly at 1.9 GPa. For comparison an O-III sample with a little bit larger hole doping ($p_0 = 0.129 \pm 0.001$) is plotted in the same graph. We conclude that 1.9 GPa can have induced about half of the difference in doping between the samples, corresponding to about 0.002 holes. This gives a value of 0.001 holes/GPa and, given the initial doping $p_0 = 0.125$, we deduce $b = 0.008 \pm 0.008\,\mathrm{GPa}^{-1}$. This estimation of b lies slightly below the estimated values by Cyr-Choinière *et al.* ($b = 0.01\,\mathrm{GPa}^{-1}$) and our estimation from the pressure-dependence of T_c of Alireza *et al.* ($b = 0.018\,\mathrm{GPa}^{-1}$). The error bar is large with respect to the value itself but it poses a constraint on the b value for underdoped samples and is an important test for the assumed doping-independence of the b value. We can take the average value, $b = (0.01 + 0.018)/2 = 0.014$ from overdoped samples, as their b values are more accurate due to a larger pressure range. $b = 0.014$ is representable for both underdoped and overdoped samples. We can thus conclude that a pressure of 1.9 GPa changes the hole doping of the O-II sample from p_0=0.109 to p(1.9 GPa)=0.112, and find a change from p_0=0.125 to p(1.9 GPa)=0.128 for the O-VIII sample.

[2]Note that half of the uncertainty at high T is due to the field reference which is a ^{27}Al foil [164]. It is a systematic error and does not lead to scattering of the data points.

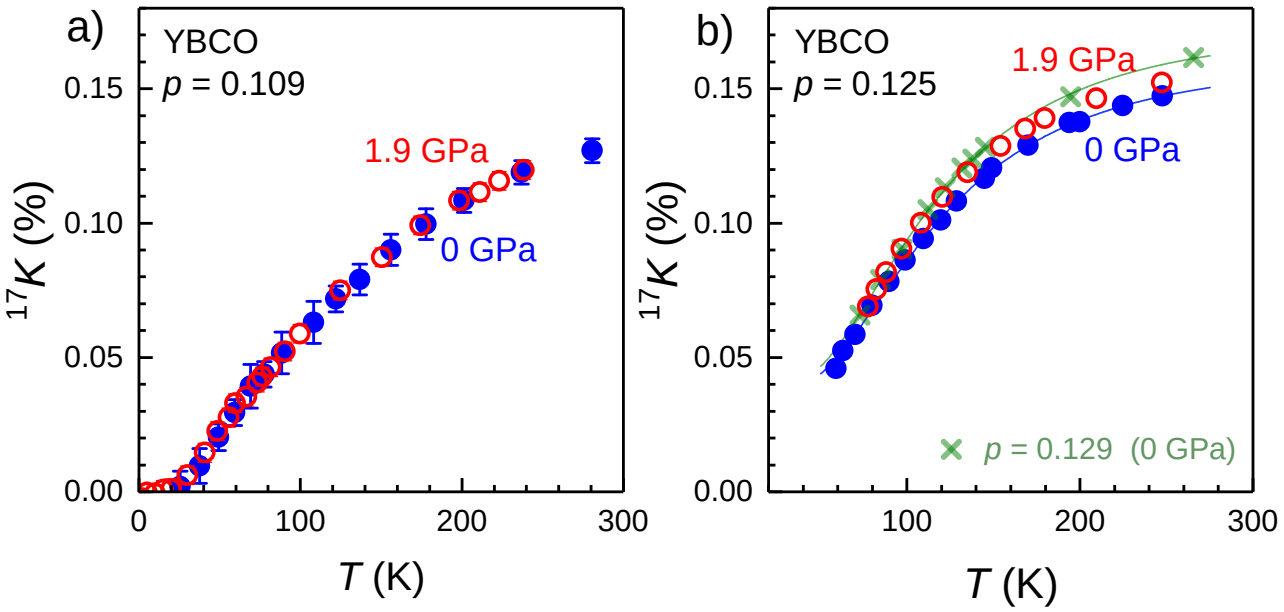

Figure 4.9: a): T-dependence of O(2) Knight shift for the O-II sample(p=0.109) at 0 GPa (blue circles) and 1.9 GPa (red circles) with B tilted 17° off the $\boldsymbol{c}$-axis. The orbital shift is negative in this field orientation ($K_{\rm orb} = -0.01218\%$), so the Knight shift becomes slightly negative at low T. b): T-dependence of O(2) Knight shift for O-VIII sample (p=0.125) at 0 GPa (blue circles) and 1.9 GPa (red circles) in comparison with the O(2) Knight for an O-III sample (p=0.129) at 0 GPa (green crosses)with $B \parallel \boldsymbol{b}$-axis for all measurements. Lines are guides to the eye. At high T the O-VIII sample at 1.9 GPa is in the middle between the O-VIII and O-III samples at 0 GPa.

4.4 NMR study of pressure effects on short-range CDW

In chapter 3 it has been shown that NMR is sensitive to the 2D CDW through the quadrupolar broadening of ^{17}O spectra of O-sites located in the CuO_2 planes. The broadening is T-dependent and increases with cooling as CDW correlations grow. At ambient pressure, this parameter shows the same T-dependence as the intensity of elastic scattering in XRD. Here, the quadrupole broadening has been measured for the O-II and O-VIII samples, with and without pressure.

O-II sample

In the measurements under hydrostatic pressure it is not possible to rotate the sample, so all measurements of the O-II sample were performed with a tilt of 18° towards the ***b***-axis. This allows to resolve all peaks and to study the long-range 3D CDW phase in high magnetic field. The quadrupole broadening of O(2) at ambient pressure has been measured previously by Wu *et al.* [87] with the field tilted by $\approx 16°$ towards the ***a***-axis. As it had not been realised before that the quadrupole broadenings with $\approx 16°$ towards the ***a***-axis and ***b***-axis differ, only a few ambient spectra have been measured in the pressure cell at 15 T to check the orientation before applying the pressure. To properly determine its change with pressure, the quadrupole broadening has been remeasured inside the pressure cell after releasing the pressure.

To improve the signal-to-noise ratio it is best to use high magnetic field but the field has to remain lower than the onset field of in-plane 3D CDW correlations that lead to a line splitting. Knowing that the onset field is 10 T at ambient pressure, spectra were acquired at 10 T. To check whether the ambient pressure data is the same before and after pressurisation it is necessary to account for the use of different magnetic fields. For this we rescale the magnetic broadening by a factor of (15 T/10 T =) 1.5. Then the rescaled magnetic broadenings and the field independent quadrupole broadening can be used to calculate the expected satellite widths at 15 T using eqs. 3.4a to 3.4e. In Fig. 4.10 it is shown that the measured satellite widths at 15 T, before the pressurisation, are consistent with the calculated Gaussian widths based on the more complete data set at 10 T, so there appears to be no irreversible change to the sample after the application of 1.9 GPa. Small differences at high T are explained by the Lorentzian character of the peaks.

Transport measurements by Putzke *et al.* have determined both the increase of T_c and the concomitant rise of the irreversibility field B_{irr} under hydrostatic pressure in an O-II sample of similar doping [7]. As B_{irr} is found to increase by about 3 T/GPa at low T (4 K), H_{c2} must increase at a similar rate. As H_{c2} sets the field scale for field induced phenomena, the onset field for long-ranged charge order should also increase [98]. Consequently, spectra that were acquired at 1.9 GPa and 15 T show no line splitting and the quadrupole broadening at low T is not affected by an unresolved splitting.

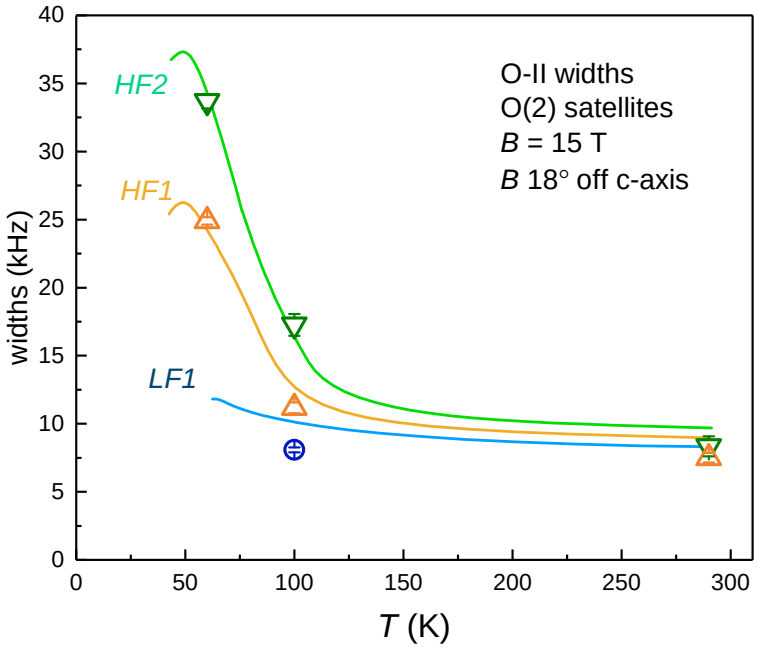

Figure 4.10: O(2) satellite widths at ambient pressure measured at 15 T before pressurisation to 1.9 GPa (empty symbols). Lines are ambient pressure widths calculated from broadening parameters that are determined from widths originally measured at 10 T after releasing the pressure. For the comparison the magnetic broadening of the 10 T data has been increased by a factor of 1.5 to account for the difference in fields.

Fig. 4.11 shows the quadrupole broadening of the O-II sample, divided by the effective quadrupole frequency, ν_{quad}=0.360 MHz.

From Fig. 4.11a, it can be seen that in the O-II sample there is no pressure-induced change in the dimensionless quadrupole broadening $\frac{\delta\nu_{\mathrm{quad}}}{\nu_{\mathrm{quad}}}$ within experimental precision for $T > T_{\mathrm{c}}$. Below T_{c} the two data sets differ since the balance of superconductivity and charge order has been changed in favour of superconductivity. If the quadrupole broadening at 1.9 GPa had been measured at the same field of 10 T as at ambient pressure, this difference would be even larger. The strength of the quadrupole broadening can be estimated by fitting it to a *Curie-Weiss* function of the form

$$\frac{\delta\nu_{\mathrm{quad}}}{\nu_{\mathrm{quad}}}(T) = \frac{A}{T-\Theta} + const. \tag{4.2}$$

where Θ is the *Weiss temperature* at which the quadrupole broadening would diverge and A is proportional to the CDW-amplitude and a pressure-independent constant accounts for non-zero quadrupole broadening at high T. This fitting has no particular physical motivation but it has the advantage that it allows to determine a parameter A which determines the quadrupole broadening in the entire T-range above T_{c}. The quadrupole broadening has also been measured at 12 T and 1.9 GPa. Since the quadrupole broadening is field-independent above T_{c} 12 T data has been fit together with data at 15 T by Curie-Weiss and is shown in Fig. 4.11b. All fitting results are summarised in table 4.1.

The fitting results confirm that the amplitude parameter A is very similar at 0 GPa and 1.9 GPa.

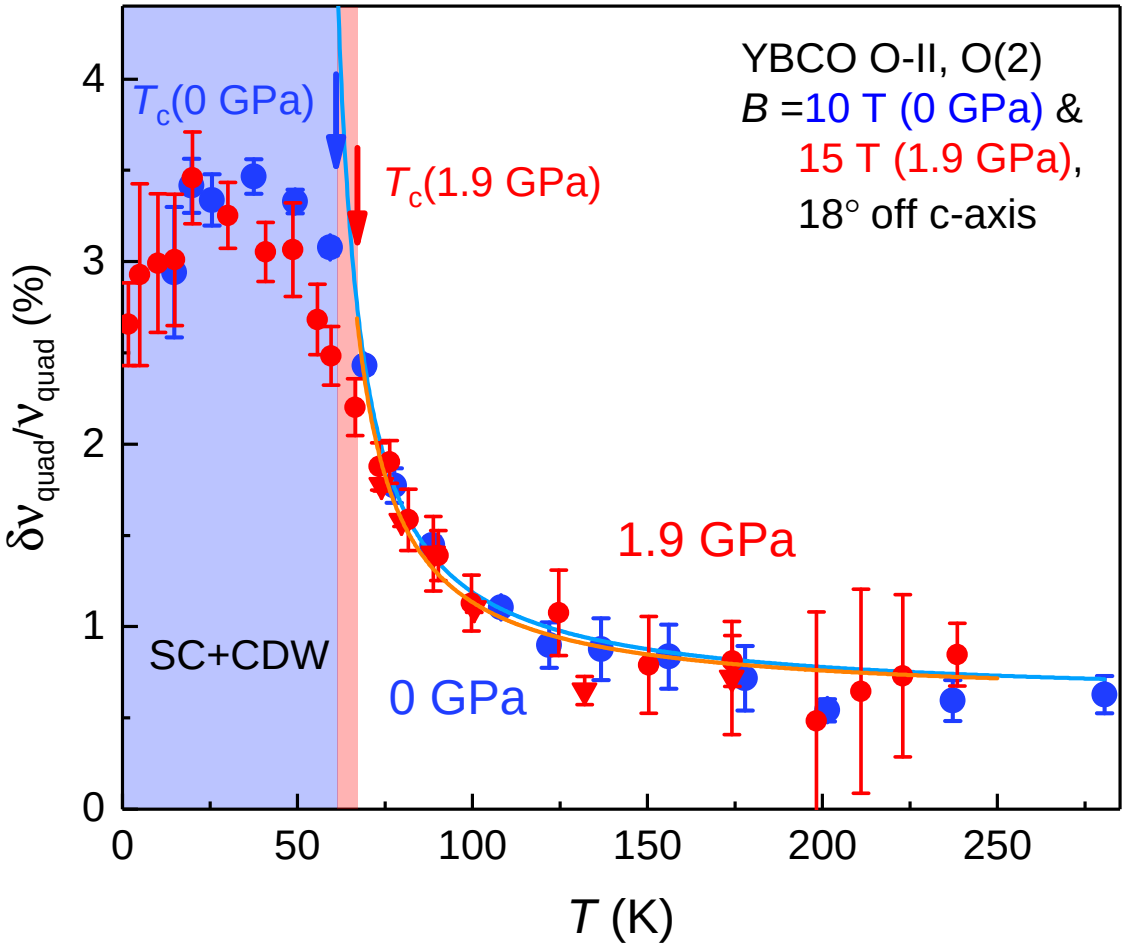

Figure 4.11: Comparison of T-dependence of dimensionless quadrupole broadening for O(2)-site at ambient pressure, measured at 10 T (blue circles) and at 1.9 GPa, measured at 15 T (red circles) & 12 T (red triangles). Measurements at 12 T are only shown for $T > T_c$ where the quadrupole broadening is field-independent. As H_{c2} is different for 0 GPa and 1.9 GPa and different fields were used, quantitative comparison below the respective T_cs is not possible. Lines are Curie-Weiss fits up to T_c. At 1.9 GPa, 12 T & 15 T data are fitted together. Curie-Weiss fits at 0 GPa & 1.9 GPa share the same background *const.*=0.6 % which is the average of all $\frac{\delta\nu_{quad}}{\nu_{quad}}$ for T >175 K.

P [GPa]	field [T]	A (amplitude)	Θ [K]
0	10	27.1±2.6	54.5±1.5
1.9	12 & 15	24.0±3.6	55.5±3.3

Table 4.1: Results from Curie-Weiss fitting of the dimensionless quadrupole broadening of the O-II sample. Since $\frac{\delta\nu_{quad}}{\nu_{quad}}$ is field-independent for $T > T_c$, data at 12 T & 15 T for the same pressure of 1.9 GPa has been fitted together to reduce the experimental uncertainty.

$\boldsymbol{P}$ [GPa]	field [T]	A (amplitude)	Θ [K]
0	15	58.5±9.2	48.7±5.1
1.9	15	43.8±2.2	54.3±1.7

Table 4.2: Results from Curie-Weiss fitting of the dimensionless quadrupole broadening of the O-VIII sample.

The conclusion is that the pressure of 1.9 GPa does not significantly change the strength of the short-ranged 2D CDW above T_c in this O-II sample. This does not mean that the quadrupole broadening is pressure-insensitive. As we expect a small pressure-induced doping that brings the O-II sample slightly closer towards $p \approx 0.12$, where charge order is strongest, we should expect the quadrupole broadening to increase. As an increase is not found[3], it is possible that positive doping and negative intrinsic effects of pressure compensate at this particular pressure of 1.9 GPa. This hypothesis is quite consistent with recent measurements by Putzke *at al.* on a O-II sample of very similar doping [7] and will be discussed more thoroughly in the next subsections.

4.4.1 O-VIII sample

The quadrupole broadening has also been studied with and without pressure for the O-VIII sample (y=6.68, p=0.125). For the O-VIII sample the doping and intrinsic effects of pressure combine differently, as $p = 0.125$ is at or near the peak of charge order. Consequently, an increase of doping can only decrease the CDW strength.

Fig. 4.12 compares the dimensionless quadrupole broadening of the O(3F) site at ambient pressure and at 1.9 GPa. A field of 15 T has been applied along the $\boldsymbol{b}$-axis for both pressures. The ambient pressure data has already been discussed in chapter 3. The Curie-Weiss fits of the quadrupole broadening are summarised in table 4.2.

The quadrupole broadening of the O-VIII sample at ambient pressure is slightly reduced. The amplitude parameter A decreases by 25±22%. The large uncertainty is mostly due to the fact that the ambient pressure data does not fit well with a Curie-Weiss dependence. We do not draw conclusions from the exact value of the suppression of A, but irrespective of the large uncertainty in the reduction of A, the similarity of the data with and without pressure lets us conclude that 1.9 GPa is not sufficient to completely suppress the CDW at this doping.

The doping dependence of the XRD intensity at ambient pressure, as estimated by Hücker *et al.* [86],

[3] Unfortunately, the quadrupole broadening has not been studied systematically as a function of doping with NMR, so it is difficult to predict how much the quadrupole broadening should have increased due to the estimated pressure-induced doping.

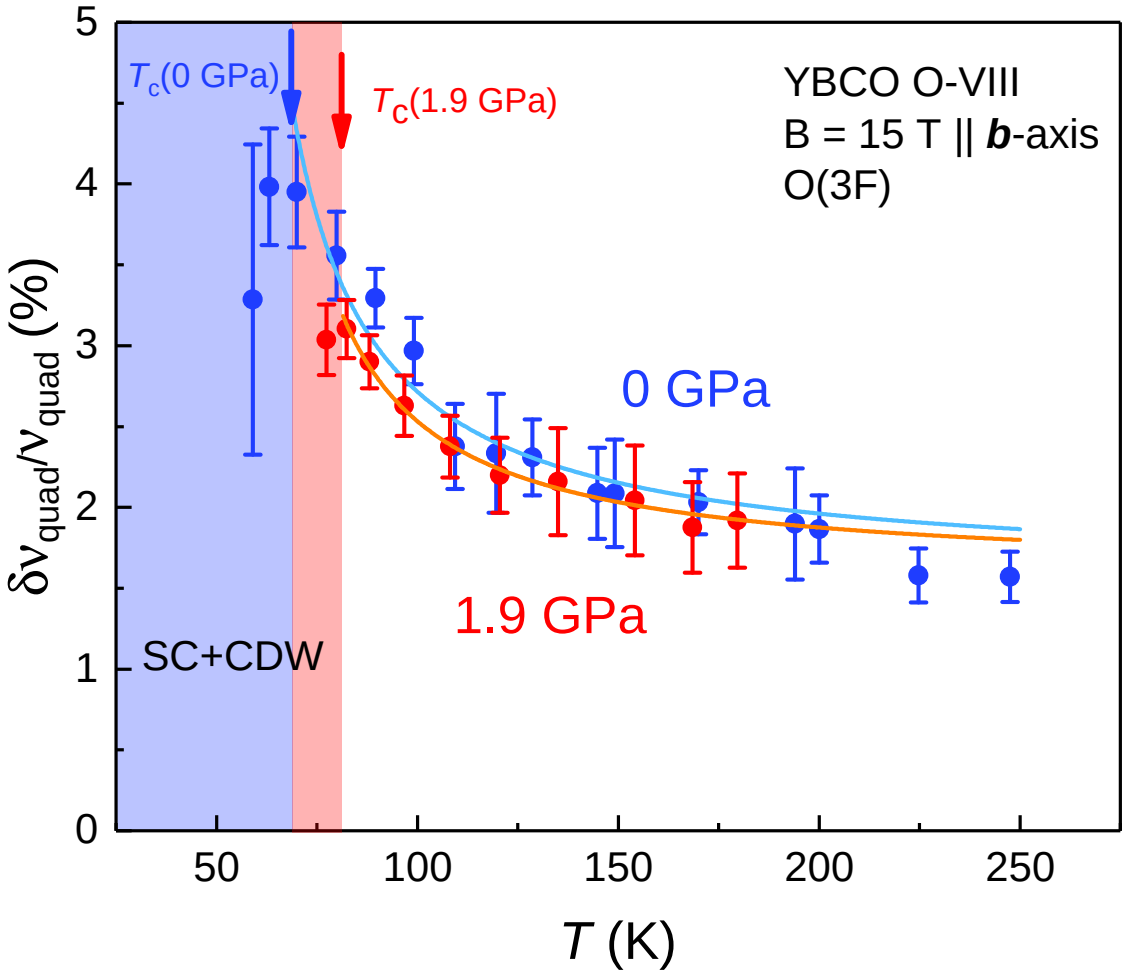

Figure 4.12: T-dependence of the dimensionless quadrupole broadening of O(3F) at ambient pressure (blue circles) and 1.9 GPa (red circles) measured with a field of 15 T along the ***b***-axis. In this orientation quadrupole frequencies are $\nu_{\rm quad}$(0 GPa)=947 kHz and $\nu_{\rm quad}$(1.9 GPa)=953 kHz. Lines are Curie-Weiss fits up to the respective T_cs with T-independent background, *const.*, fixed to 1.58%.

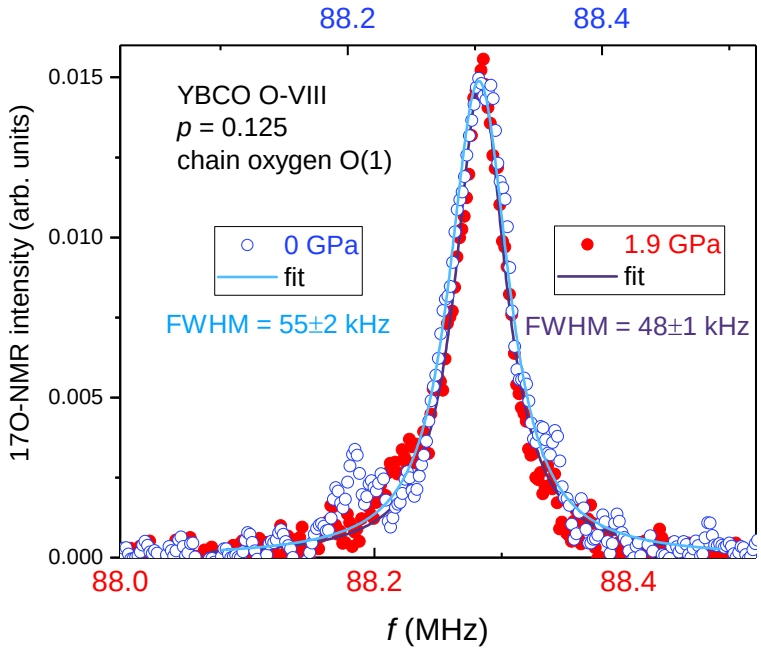

Figure 4.13: O(1) chain oxygen spectrum of the $HF1$ satellite at 168.5 K and $B = 15$ T. The horizontal scale has been adjusted that the peaks coincide but the intensity is plotted on the same absolute scale. Lines are fits to Voigt lineshapes and show that the FWHM reduces by ≈ 15 % at 1.9 GPa.

is too weak to result in a visible change of the CDW amplitude by a change of the hole doping from $p = 0.125$ to $p = 0.128$. Thus, the weakening of the quadrupole broadening is likely to be solely an intrisic effect of hydrostatic pressure.

We have also investigated the pressure-induced change in the degree of chain-oxygen ordering. We find that the FWHM of O(1) satellites is reduced, as shown in Fig 4.13. The reduced FWHM signals increased oxygen ordering and confirms work in O-III ordered YBCO under pressure by Huang *et al.* [155]. This implies that the T-independent background of the quadrupole broadening is expected to decrease with increasing pressure, so a part of the decrease of the total quadrupole broadening in Fig. 4.12 might be due to a reduced background. We have not done measurements at $T > 200$ K since chain oxygen mobility increases with temperature and leads to oxygen reordering [70].

4.5 Pressure effect on field-induced CDW

To study the effect of hydrostatic pressure on the 3D long-ranged CDW, the O-II sample has been subjected to high magnetic fields up to 28.5 T. For the high field measurements no changes have been done to the pressure cell after having studied the quadrupole broadening at low fields, so the orientation of the sample and the pressure in the cell have not changed from a tilt of 18° off the $\boldsymbol{c}$-axis towards the $\boldsymbol{b}$-axis and a pressure of 1.9 GPa inside the cell. In the period between the low field measurements

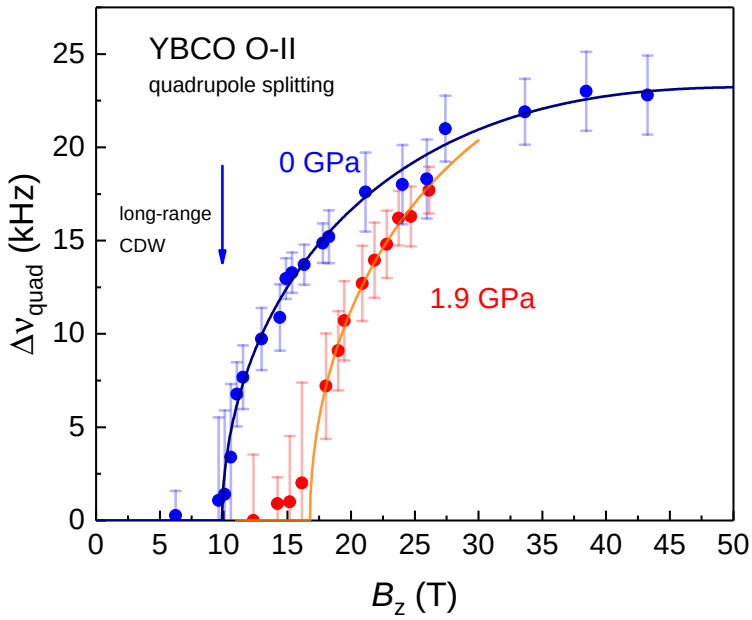

Figure 4.14: B_z-dependence of the quadrupole splitting of O(2) sites due to long-range charge order. Ambient pressure (blue circles) and 1.9 GPa (red circles) have been measured in very similar orientations (tilt of 16-18° off the ***c***-axis towards the ***b***-axis). $\Delta\nu_{\mathrm{quad}}$ is plotted as a function of B_z, the ***c***-axis component of the applied magnetic field. Ambient pressure data was published in ref. [73]. Lines are fits to a tanh-function, defined in chapter 3, to determine the onset field.

and the high field run the pressure cell was kept in liquid nitrogen to impede oxygen re-ordering in the CuO-chains.

As discussed in chapter 3, the key signature of the 3D CDW phase in NMR is a quadrupole splitting of the O(2) satellites. At 1.9 GPa, the ^{17}O-spectra are qualitatively very similar to high field spectra at ambient pressure, so the quadrupole splitting could be extracted by fitting the O(2) satellites with two peaks that have an intensity ratio of 2-to-1. The resulting quadrupole splitting is shown in Fig. 4.14. The essential difference between ambient and high pressure quadrupole splittings is a higher onset field at high pressure. The magnitude of the splitting at the highest accessible field is not found to be diminished in comparison to ambient pressure data. Since for 1.9 GPa the splitting is still increasing at $B_z \approx 27$ T, we cannot reliably determine at which value it will saturate. At the highest field the quadrupole splitting with and without pressure are of similar magnitude. This shows the amplitude of the quadrupole splitting, much like the quadrupole broadening, is weakly affected by a pressure of 1.9 GPa in case of the O-II sample.

With the application of pressure, the onset field has increased from 10 T to 17 T. This can be understood as an effect of strengthened SC. As mentioned before, from transport measurements by Putzke *et al.* [7] an increase of H_{c2} by ≈ 3 T/GPa is expected. H_{c2} determines the density of SC vortices at a given field. If, as proposed by Wu *et al.* [73], long-range CDW order is achieved once patches of charge order

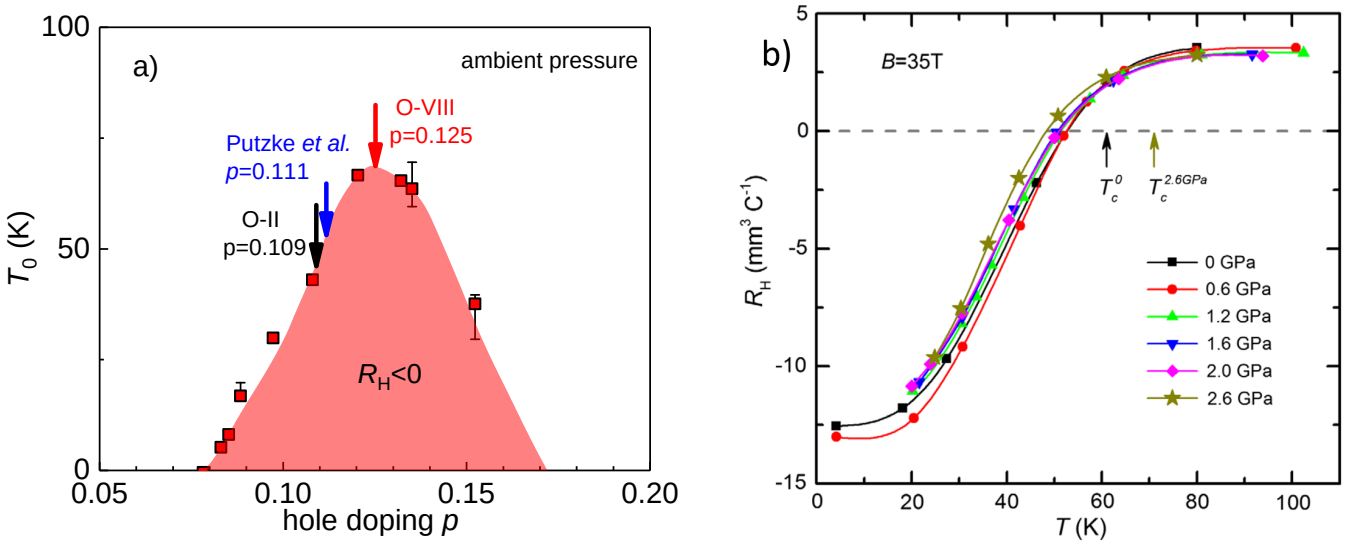

Figure 4.15: a): Doping-dependence of T_0 at ambient pressure. At T_0 the Hall number $R_{\rm H}(p)$ changes sign, reproduced from ref. [83]. Arrows indicate the dopings of the samples studied by NMR (black arrow for O-II & red arrow for O-VIII) and the $p \approx 0.11$ sample studied by Putzke *et al.* (blue arrow). We determine the samples doping to be $p = 0.111$ from the fact that it has $T_0(0\,\text{GPa})$=54 K. b): T-dependence of the Hall number $R_{\rm H}$ measured by Putzke *et al.* at $B = 35$ T for hydrostatic pressures from 0 GPa to 2.6 GPa. The Fig. is reproduced from ref. [7].

around vortices start to overlap, then an increased H_{c2} would lead to an increased onset field of long range charge order.

4.6 Comparison with electrical transport measurements

A negative Hall number [7, 2] and slow quantum oscillations [165, 156], both signs of the small electron pockets due to the reconstruction of the Fermi surface by charge order, have been measured up to 1-2 GPa, confirming that within the pressure range studied by NMR there is at most a partial suppression of the CDW. Measurements of T_0, the temperature at which the Hall number $R_{\rm H}$ changes sign are of particular interest, because the doping dependence of T_0 at ambient pressure is very well characterised [83, 98] and thus allows to determine the effect due to pressure-induced doping on T_0. Putzke *et al.* have studied the evolution of $T_0(\boldsymbol{P})$, *i.e.* as a function of hydrostatic pressure $\boldsymbol{P}$, up to 2.6 GPa for a sample with a nominal hole doping of $p \approx 0.11$ [7]. They found that $T_0(\boldsymbol{P})$ varies slowly as a function of pressure ($\frac{\mathrm{d}T_0}{\mathrm{d}\boldsymbol{P}}$=-1.1 K/GPa) and concluded from this that the rate of the suppression of charge order is too weak to explain the concomitant increase of the superconducting $T_{\rm c}(\boldsymbol{P})$ of $\frac{\mathrm{d}T_{\rm c}}{\mathrm{d}\boldsymbol{P}}$=+3.8 K/GPa. Here we show that considering the effect of the pressure-induced doping, which tends to increase T_0, one can reach a different conclusion.

Essentially, pressure-induced doping, although it is very small, can still affect the pressure-dependence

of $T_0(\boldsymbol{P})$ since the doping dependence of T_0 (at ambient pressure) is very strong (see Fig. 4.15a): From $p = 0.08$ to $p = 0.12$ T_0 increases by more than 65 K, giving a large slope of about 1640 K/hole. Consequently, multiplying this number by the small pressure induced doping of about 0.0015 holes/GPa as estimated previously, leads to a non-negligible increase of T_0, namely $\left(\frac{\mathrm{d}T_0}{\mathrm{d}\boldsymbol{P}}\right)_{\mathrm{dop.}}$=+2.5 K/GPa. The experimentally determined slope $\left(\frac{\mathrm{d}T_0}{\mathrm{d}\boldsymbol{P}}\right)_{\mathrm{tot.}}$= -1.1 K/GPa is thus the combined effect of a positive doping effect and a negative intrinsic pressure effect, as shown in eq. 4.3.

$$\begin{aligned}\left(\frac{\mathrm{d}T_0}{\mathrm{d}\boldsymbol{P}}\right)_{\mathrm{tot.}} &= \left(\frac{\mathrm{d}T_0}{\mathrm{d}\boldsymbol{P}}\right)_{\mathrm{dop.}} &&+ \left(\frac{\mathrm{d}T_0}{\mathrm{d}\boldsymbol{P}}\right)_{\mathrm{intr.}} \\ -1.1\,\mathrm{K/GPa} &= +2.5\,\mathrm{K/GPa} &&+ \left(\frac{\mathrm{d}T_0}{\mathrm{d}\boldsymbol{P}}\right)_{\mathrm{intr.}}\end{aligned} \tag{4.3}$$

From eq. 4.3 it follows that $\left(\frac{\mathrm{d}T_0}{\mathrm{d}\boldsymbol{P}}\right)_{\mathrm{intr.}}$=-3.6 K/GPa. Remarkably, this intrinsic suppression of T_0 is of nearly equal magnitude (but opposite sign) as the rate at which T_c increases ($\frac{\mathrm{d}T_\mathrm{c}}{\mathrm{d}\boldsymbol{P}}$=+3.8 K/GPa). If one assumes that the intrinsic rate of suppression $\left(\frac{\mathrm{d}T_0}{\mathrm{d}\boldsymbol{P}}\right)_{\mathrm{intr.}}$=-3.6 K/GPa is independent of pressure, one can predict $T_0(\boldsymbol{P})$ from eq. 4.4.

$$T_0(\boldsymbol{P}) = T_0(p_0 + b \cdot p_0 \cdot \boldsymbol{P})|_{0\,\mathrm{GPa}} + \left(\frac{\mathrm{d}T_0}{\mathrm{d}\boldsymbol{P}}\right)_{\mathrm{intr.}} \cdot \boldsymbol{P} \tag{4.4}$$

The first term in the equation accounts for the pressure-induced doping dependence and is given by the parabolic[4] ambient pressure doping dependence $T_0(p)|_{0\,\mathrm{GPa}}$, in which the doping changes due to pressure, following eq. 4.1.

We can plot eq. 4.4 for the sample studied by Putzke *et al.* using $p_0 = 0.111$. This is done in Fig. 4.16 where it is additionally shown how T_0 would change if there were no effect from induced doping.

Interestingly, the assumption that T_0 is reduced linearly at a rate of -3.6 K/GPa leads to complete suppression of T_0, and hence of charge order, near 15 GPa. The sample of Putzke *et al.* has not been studied up to such high pressures but measurements of Sadewasser *et al.* [70] have shown that T_c for a similar YBCO sample ($p \approx 0.117$) saturates at around 15 GPa. Thus we find that, once the effect of pressure-induced doping is taken into account, the data of Putzke *et al.* [7] actually support the proposal of Cyr-Choinière *et al.* that the suppression of the CDW goes hand in hand with the pressure-induced increase of T_c [2].

Furthermore, the interplay of doping and intrinsic pressure effects can help understanding our NMR data. As shown in Fig. 4.15a, the O-II sample studied with NMR and the sample of Putzke *et al.* are close in doping and both lie on the left side of the T_0 dome, where doping and intrinsic pressure-effects can cancel. Hence, it is possible that similar cancellation occurs for the quadrupole broadening. As the O-VIII sample lies at the top of the T_0 dome, there is no cancellation and we observe the intrinsic weakening of the quadrupole broadening under pressure.

[4] To produce Fig. 4.16, $T_0(p)|_{0\,\mathrm{GPa}}$, as shown in Fig. 4.15a, was fit by a 4$^{\mathrm{th}}$-order polynomial.

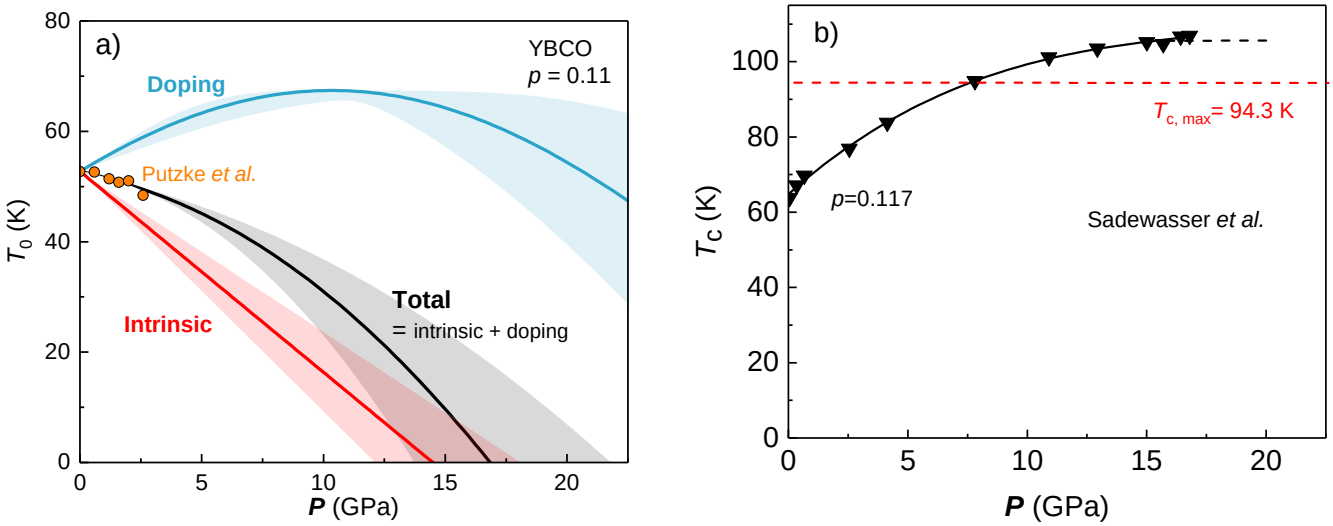

Figure 4.16: a): Pressure dependence of T_0 for the $p \approx 0.11$ YBCO sample studied by Putzke *et al.* [7] (orange circles). The black curve is calculated from eq. 4.4 using $b = 0.014$ and includes doping and intrinsic pressure effects on T_0. The shaded grey area corresponds to $0.01 \leq b \leq 0.018$.. The red line shows the intrinsic suppression of T_0. Here the doping effect due to pressure-induced doping is excluded. Again, shaded red area corresponds to $0.01 \leq b \leq 0.018$. The light blue line is the calculated pressure dependence due to the pressure-induced doping effect, excluding the intrinsic effect. b) Pressure dependence of T_c for the YBCO6.66 ($p \approx 0.117$) sample studied up to 17 GPa by Sadewasser *et al.* [70]. Data is reproduced from ref. [70].

4.7 Comparison with X-ray diffraction

To date, two X-ray studies of YBCO under hydrostatic pressure have been published. Both conclude that charge order disappears with the application of only 1 GPa [90, 155]. The two studies are briefly discussed in the following.

Huang *et al.* have performed elastic X-ray diffraction measurements of O-III ordered YBCO6.73 sample from 1 to 6 GPa, applied by a diamond-anvil cell (DAC) with Helium as the pressure medium [155]. They have verified the existence of a CDW superstructure peak at q_{CDW}=(3.31,0,1.4) using resonant soft X-ray diffraction (RSXS) at ambient pressure first and changed to the high pressure setup to investigate the pressure-evolution of the CDW peak thereafter. No signal was found at q_{CDW} at the lowest pressure of 1 GPa. Fig. 4.17 shows the absence of CDW-intensity at 1 GPa.

The authors found that the degree of the chain-oxygen ordering increases with pressure and thus deduced that the removal disorder is responsible for the disappearance of the CDW signal, because disorder can act as pinning centers for fluctuating CDWs [87]. However, the authors are not sure whether their sensitivity inside the DAC is sufficiently high to see the rather weak CDW signal. As no ambient pressure measurements have been performed inside DAC, it is not clear whether the additional background from the diamonds masks the CDW intensity. This is a crucial point, since the quadrupole broadening measured by NMR is proportional to the hard XRD intensity at ambient pressure and both

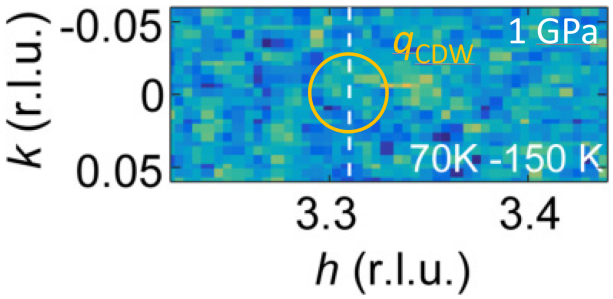

Figure 4.17: Hard X-ray intensity of the YBCO6.73 sample with O-III chain order measured at 1 GPa inside a diamond-anvil cell by Huang *et al.* [155]. Intensity at 150 K has been subtracted from the intensity at 70 K. Upon cooling no peak appears at q_{CDW} (encircled in yellow). The figure is reproduced from ref. [155].

are signatures of the same phenomenon. If sensitivity is not an issue and hard X-ray intensity should be visible inside the DAC at 0 GPa but not at 1 GPa, then it would imply that the XRD-intensity and the quadrupole broadening must have different origins. This would be very surprising. It would not only put into question how the quadrupole broadening and hard XRD-intensity are related. This would also be at odds with the close relation of the NMR line splitting and the XRD intensity and correlation length in the 3D CDW phase in high fields.

Consequently, it is very important to check if the CDW intensity is visible inside the DAC when no pressure is applied.

The second X-ray study by Souliou *et al.* [90] has utilised inelastic X-ray diffraction (IXS) in an O-VIII ordered YBCO6.60 sample to study the phonon dispersion and linewidth around q_{CDW}. It extends ambient pressure IXS measurements by Le Tacon *et al.* [89] into the regime of hydrostatic pressures up to 1.5 GPa, equally using a DAC and Helium as the pressure medium. Since the studied features are inelastic in nature, these measurements are not affected by the additional elastic background coming from the diamonds of the DAC.

At ambient pressure IXS finds two remarkable features: Below T_{c}, there is a sharp partial phonon softening appearing in a transverse acoustic phonon branch that is strongest around the CDW wave vector q_{CDW}=(0,0.31,6.5). The energy of the softened acoustic and its line width at ambient pressure are shown in Fig. 4.18. The linewidth of this phonon branch increases strongly below T_{CDW} ≈150 K and is sharply peaked in reciprocal space around q_{CDW}=(0,0.31,6.5), see Fig. 4.19. Since these phenomena appear at q_{CDW} they are clearly linked to charge order. Especially, the increase of the linewidth must be linked to the 2D short-range CDW since, firstly, the line broadening and the elastic intensity of the 2D CDW increase simultaneously below T_{CDW} ≈150 K and, secondly, since the line broadening is peaked at the half-integer L=6.5. CDW peaks at half-integer L are seen both along (H,0) as well as (0,K). The phonon softening has a different T-dependence. It appears below T_{c} and has been interpreted to be induced by superconductivity.

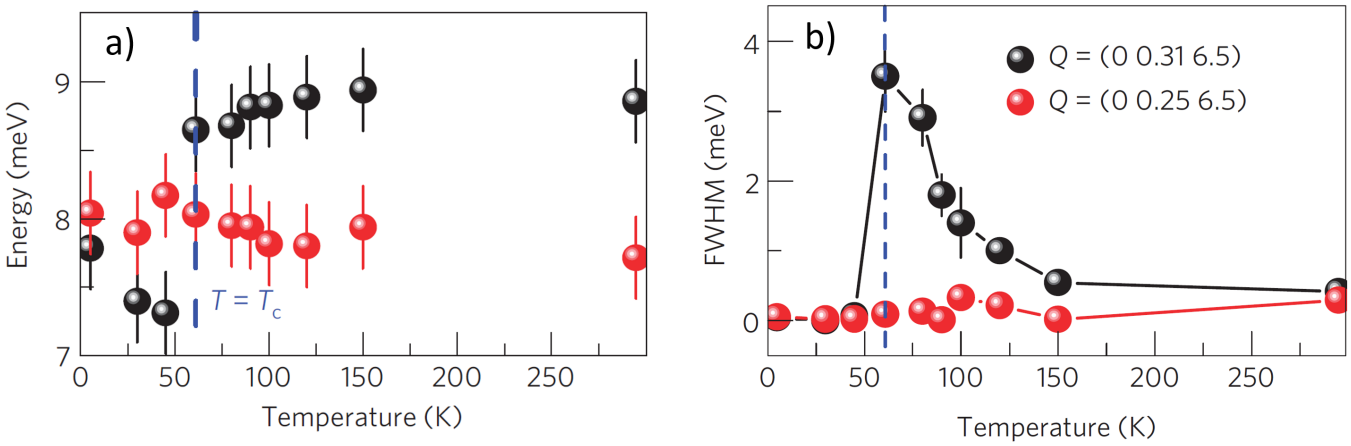

Figure 4.18: a): T-dependence of the acoustic phonon branch for YBCO6.6 at q_{CDW}=(0, 0.31, 6.5) (black circles) and at another wave vector q=(0, 0.25, 6.5) (red circles) where the anomaly is absent. The acoustic phonon's energy drops sharply below T_{c}. b): T-dependence of the acoustic phonon's line width (FWHM) which increases strongly below T_{CDW} ≈150 K, but drops below T_{c}. Figures are reproduced from ref. [89].

With the application of hydrostatic pressure both the line broadening at $T \approx T_{\mathrm{c}}$, as well as the phonon softening below T_{c} are suppressed at pressures between 0.8 GPa and 1.5 GPa (Fig. 4.20). The rapid suppression is unexpected. To be consistent with the NMR and transport measurements both anomalies should be only weakly reduced in this range of pressures.

When measurements give contradictory results there are two possible explanations. Either the measurement have been done in unequal conditions or the conclusions from at least one of the measurements have to be revised.

The first impulse is to assume that the conditions in which the measurements have been done are not equal. In case of measurements under hydrostatic pressure, generally, the degree of hydrostaticity can vary due to the use of different pressure media [166]. Non-hydrostatic conditions are usually the result of pressurisation beyond the point where the pressure medium solidifies, see ref. [167] for a discussion of non-hydrostatic effects in Fe-based SC. However, by applying 1.9 GPa at ambient T we do not reach the solidification of our pressure medium. At low temperatures all pressure media eventually solidify which leads to shear strain that might lead to inconsistent results. Both X-ray studies have been performed with Helium as pressure medium. Even when it solidifies (which is not yet the case at $T \approx T_{\mathrm{c}}$ for the line width measurements in Fig. 4.20a), it still remains one of the softest pressure media available [166]. The transport measurements of Putzke *et al.* [7], as well as the NMR measurements, presented in this chapter, used industrial oils whose hydrostaticity is worse than in case of Helium. Technically, it should be possible to repeat the IXS measurements with Daphne oil 7373, as its optical

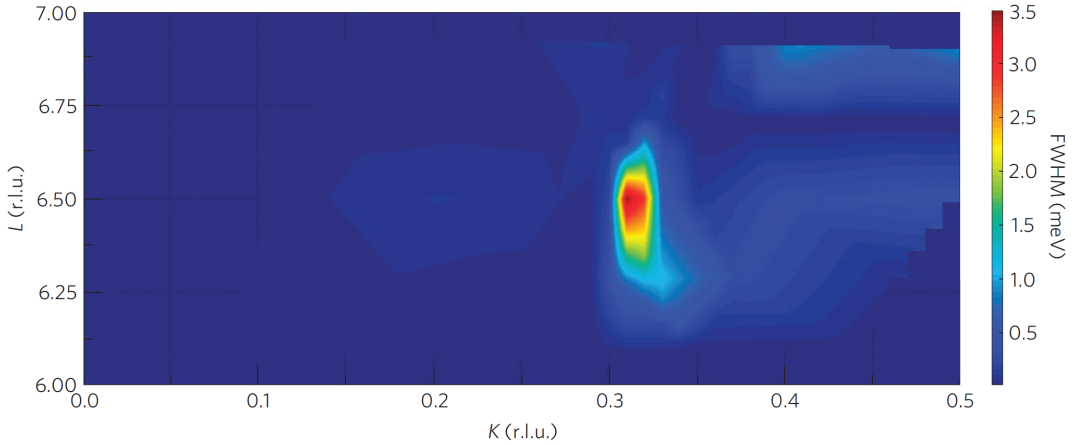

Figure 4.19: YBCO6.6 momentum dependence of the FWHM of the phonon broadening in the (K,L)-plane at $T = T_c$ and ambient pressure. The phonon broadening is peaked at q_{CDW}=(0,0.31,6.5). The figure is reproduced from ref. [89].

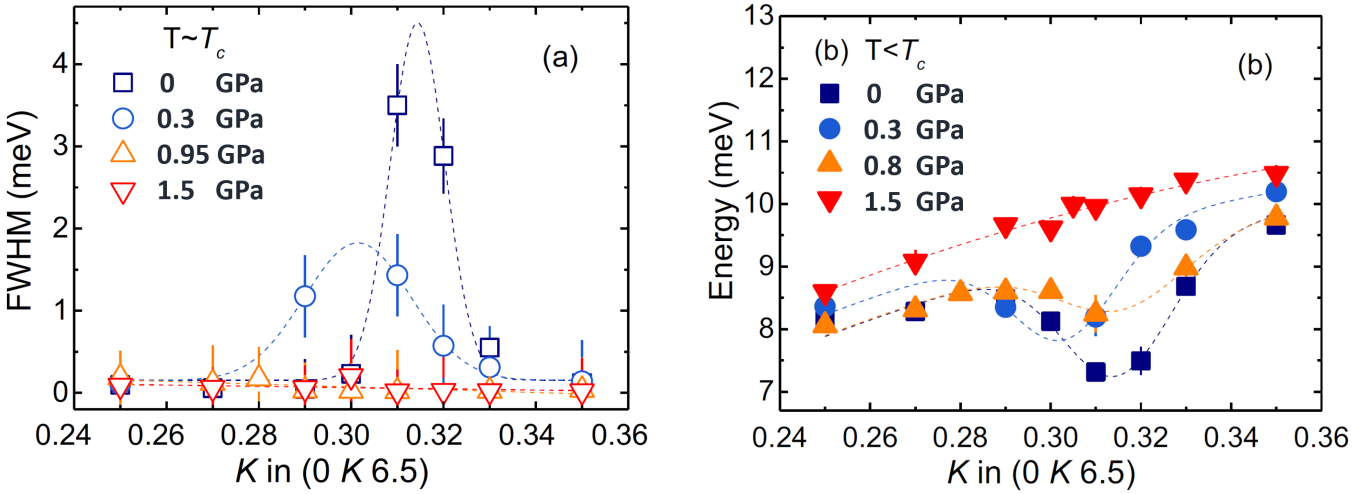

Figure 4.20: a): Suppression with hydrostatic pressure of the line broadening of the acoustic phonon branch around q_{CDW}=(0,0.31,6.5) at $T \approx T_c$. b): Suppression with hydrostatic pressure of the phonon softening at q_{CDW}=(0,0.31,6.5) below T_c. Figures are reproduced from ref. [90].

properties are favourable [168]. Hard X-ray diffraction in Daphne oil of another CDW system has been recently performed by Ivashko *et al.* [169]. However, the non-hydrostaticity hypothesis in the case of YBCO appears to be unlikely: Due to its relatively large bulk modulus of about 120 GPa [170], it is unlikely that small shear strains will dominate over high, largely isotropic pressures. Furthermore, if non-hydrostatic conditions could affect charge order, we expect that our measured change of T_c is inconsistent with respect to measurements in Helium. This is not the case, as can be seen from Fig. 4.2b, where most points for $0.1 < p < 0.13$ are from studies with Helium as the pressure medium.

4.7.1 Alternative interpretation of the phonon softening

A potentially more fruitful approach to the contradictory results might be to use them as a motivation to review what is the basis for the conclusions and to look for alternative interpretations of the data. A possible hypothesis that could be checked is whether the phonon softening is not produced by the 2D short-range CDW but is rather a signature of the 3D long-range CDW transition. The available data on the wave vector and the T-dependence are in principle consistent with an incomplete Kohn anomaly due to the uniaxial 3D CDW.

All IXS measurements of the acoustic phonon softening in YBCO have been constrained to q_{CDW} along (0,K) due to strong and broad elastic signal coming from chain-superstructures that dominate IXS spectra and obscure the intensity of the phonons for (H,0) [88, 89, 90]. XRD in high fields has shown that the 3D CDW modulation runs only along the (0,K)-direction [92, 143], consistent with the phonon softening measured along (0,K). If no softening exists along (H,0), it is unlikely to be due to the 2D CDW but could be interpreted as a more conventional Kohn anomaly belonging to the 3D CDW phase, similarly to the situation found in 1D metals with a uniaxial CDW. On the mean-field level, an incomplete phonon softening already exists for $T > T_{CDW}$, but complete softening down to zero energy is achieved only for $T \leq T_{CDW}$, as shown in Fig. 4.21 [171]. T_{CO}, the temperature at which the 3D CDW transition occurs, is well characterised by ultrasound measurements in high magnetic fields. For YBCO p=0.122 Laliberté *et al.* find T_{CO}=47 K, just below T_c [98]. Remarkably, at q_{CDW}=(0,0.31,6.5) in Fig. 4.18a, the energy is minimal at 45 K and is not yet decreased at T_c=61 K. If finer resolution in T were available, it would be interesting to see whether the phonon softening is strongest at T_{CO}. An implication of this would be that IXS (or INS) in magnetic fields should find an enhanced phonon softening, even in fields weaker than those applied in the ultrasound measurements of ref. [98]. Such an experiment could allow to distinguish between the 3D CDW scenario and the superconductivity-induced softening, as suggested by Le Tacon *et al.* and supported by a theoretical model of Liu *et al.* [172].

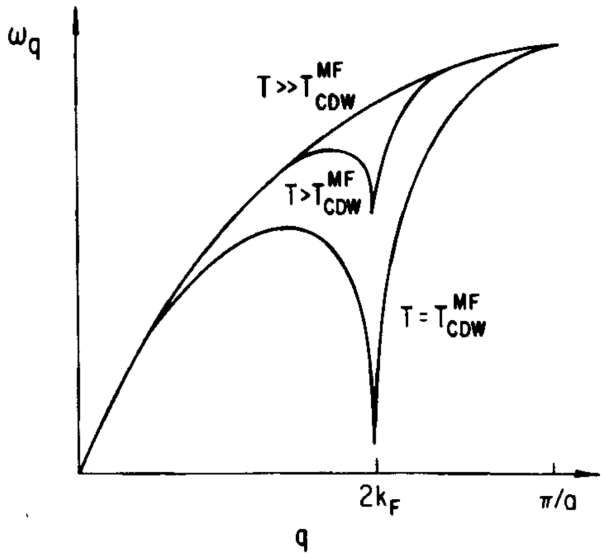

Figure 4.21: Phonon softening of an acoustic phonon branch in a 1D metal undergoing a CDW transition due to Fermi surface nesting at $T = T_{\mathrm{CDW}}$. At temperatures not too far above T_{CDW} a partial softening exists that becomes complete at $T = T_{\mathrm{CDW}}$. MF stands for "mean-field". The figure is reproduced from ref. [171].

The considerations made so far all concern the phonon softening and not the phonon line broadening. The broadening is peaked sharply at half integer L (Fig. 4.19), while the 3D CDW peak is found at integer L, so the broadening is unlikely to be related to the 3D CDW.

At present, we have no explanation as to how the broadening can disappear at a pressure as small as 1 GPa, without the disappearance of the 2D CDW. Nevertheless, we would like to point out one important aspect about the measurement of the broadening under pressure.

The broadening was measured close to T_{c}, where it is found to be maximal at ambient pressure. However, below T_{c}, it is rapidly diminished, so it is important not to fall below T_{c}. T_{c} was not measured during the IXS experiments and is estimated from a sample of similar oxygen concentration. Souliou *et al.* took care to measure the broadening at increasing T in order to match the T_{c} with increasing pressure. Still, there is some possibility that a part of the measurements was made at T slightly below T_{c}. This can be seen from Fig. 4.22a: For example, the measurement at 15 kbar=1.5 GPa (empty red triangle) is below the reference T_{c}. Normally, the $T_{\mathrm{c}}(\boldsymbol{P})$ from Sadewasser *et al.* given by the grey circles in Fig. 4.22a overestimates the T_{c} of Souliou *et al.*, since the sample is reported to have a $T_{\mathrm{c}} = 61$ K at ambient pressure, while the sample of Sadewasser *et al.* has $T_{\mathrm{c}} = 64$ K. However, the reported $T_{\mathrm{c}} = 61$ K is unexpectedly low for $p = 0.12$, especially, as the chains have O-VIII ordering. Typical O-VIII samples have $T_{\mathrm{c}} > 64.5$ K [24, 173]. Hence, it would be helpful if the phonon broadening were measured at $T > T_{\mathrm{c}}$, for example at 85 K.

We conclude that more XRD measurements are necessary to understand the contradictory results

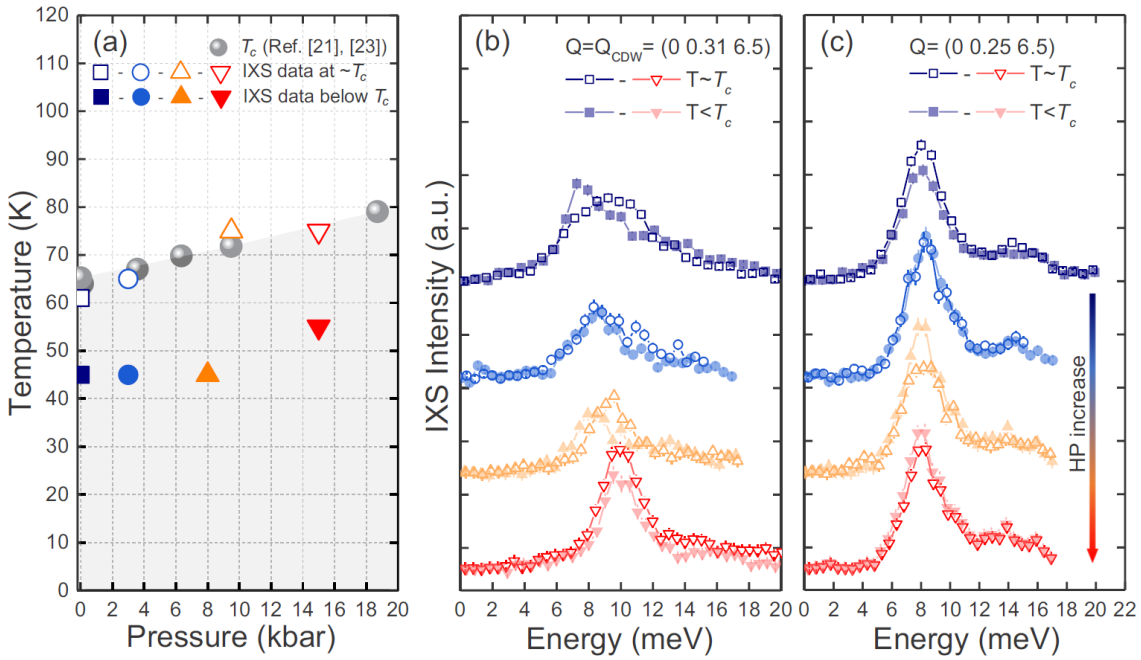

Figure 4.22: a): $\boldsymbol{P}$-T diagram showing at which T the IXS measurements were done. Open symbols correspond to $T \sim T_c$, filled symbols are at $T < T_c$. Grey circles indicate $T_c(\boldsymbol{P})$ and are taken from Sadewasser *et al.*. b) & c): IXS spectra at q_{CDW}=(0,0.31,6.5) and a different q=(0,0.25,6.5). Figures are reproduced from ref. [90].

between electrical transport & NMR on one hand, and elastic and inelastic XRD on the other hand. Firstly, it is important to verify whether the CDW peak can be seen in the DAC at ambient pressure. Then the phonon broadening should be measured at higher T.

To test the proposed scenario for the phonon softening due to the 3D CDW a finer resolution of the softening as a function of T is desirable. We suggest IXS (or INS) measurements in magnetic fields to clarify the effect of SC on the softening.

4.8 Summary

In this chapter we have investigated the effect of hydrostatic pressure on the field-independent and field-induced charge order in YBCO. We found that charge order is only weakly affected by the application of 1.9 GPa. The amplitude of field-independent charge order decreases by $\sim 20 \pm 10$ %. The field-induced charge order has a higher onset field, as expected for the increased H_{c2}, but above the onset field the amplitude at 1.9 GPa rises rapidly to value comparable to those found at ambient pressure. We study the effect of pressure-induced doping and find that it is small but relevant to understand the change of $T_0(\boldsymbol{P})$ in transport measurements of Putzke *et al.*. We find that NMR and transport measurements are consistent with the proposal by Cyr-Choinière *et al.* that the gradual suppression of charge order leads to an increase of T_c which saturates at $\boldsymbol{P} \sim 15$ GPa.

These conclusions are not consistent with the complete suppression of charge order at ≈ 1 GPa, as found in XRD measurements by Huang *et al.* and Souliou *et al.*. We suggest additional XRD experiments that whould help to test the contradictory conclusions and should lead to a better understanding of charge order in YBCO.

Chapter 5

Tuning magnetic order in $La_{2-x}Sr_xCuO_4$ with high magnetic fields

5.1 $La_{2-x}Sr_xCuO_4$ in high magnetic fields

Cuprate superconductors generally show a strong competition of different electronic phases. Magnetic field has been a useful tool to suppress superconductivity and reveal the competing phases [4]. Any magnetic phase is expected to be unfavourable to SC, since the pairing state is normally time-reversal-symmetric (singlet) and magnetic moments locally break time-reversal symmetry and lead to depairing. Whether the antiferromagnetism (AFM) in cuprates can be thought of as a competing phase to SC, is not answered easily. Since SC is achieved by hole doping, it is difficult to disentangle the effect of SC from the effect of the doping itself. In hole doped cuprates the 3D Néel state is strongly suppressed upon weak hole doping of the parent compound but does not necessarily vanish before SC sets in. Mukuda *et al.* have shown that p_c, the critical doping at which the 3D Néel state ends, increases with the number of CuO_2-layers per unit cell, n [36]. Single-layer ($n = 1$) LSCO has $p_c = 0.02$, bi-layer ($n = 2$) YBCO has $p_c = 0.055$. In compounds with $n = 5$, the 3D Néel state extends well into the SC state up to $p_c = 0.10$. Above p_c, in YBCO and LSCO, AFM extends in form of an anti-ferromagnetically correlated spin glass into the doping range where superconductivity appears [174, 175, 176]. Unlike in YBCO, the spin glass in LSCO does not vanish in the doping range where charge order is found, but instead is strongly enhanced around the characteristic $p \approx 0.12$ where charge order is maximal, as can be seen in Fig. 5.6. It is around $p = 0.12$ that the competition of SC with AFM becomes evident. SC can be easily weakened with moderate magnetic fields and the AF-correlation length grows as a function of field [71]. Neutron scattering and μSR studies [177, 9] show evidence of magnetic moments that become stronger with the application of magnetic field. NMR/NQR confirm the quasi-static nature of the magnetic moments [178, 179, 180, 181]. Khaykovich *et al.* [10] and Chang *et al.* [9] have shown

that the AFM order can even be induced at higher dopings of $p = 0.144$ and $p = 0.145$, respectively, while it appears to be completely absent in zero field.

In this chapter, we present evidence that the signatures of magnetic field-induced AFM order extend at least up to, but not far above the doping p^* where Cyr-Choinière *et al.* from Louis Taillefer's group recently localised the endpoint of the pseudogap [182].

5.2 Determination of doping

Holes can be continuously added to the parent compound La_2CuO_4 by replacing a La^{3+} ion with Sr^{2+}. Since all holes go into the CuO_2-plane there is a direct correspondence between the Sr-concentration x and the hole doping $p = x$. The Sr-concentration is a priori known from the chemical synthesis of the sample but experience has shown that it is essential to verify it by measuring the superconducting T_c or the transition temperature T_s from the high-temperature tetragonal (HTT) to the low-temperature orthorhombic (LTO) crystal structure.

A doping determination from T_c is possible in the range where superconductivity persists but two aspects make this difficult: Firstly, the superconducting dome is quite flat around optimal doping and T_c varies by only a few Kelvin over an extended doping range. Secondly, sample quality can strongly affect the T_c itself. On the other hand, the structural transition which occurs at $T_s = 520$ K in the parent compound is progressively suppressed upon Sr-doping and disappears around $x = p = 0.21$. Its monotonic dependence is shown in Fig. 5.1 and serves as a reliable reference to determine the Sr-concentration and hence the hole doping p for a given structural transition temperature T_s. The hole doping p is usually given as an absolute value or as a percentage (e.g. $p = 0.21 = 21\%$). In both cases it signifies the fraction of a hole per CuO_2-plane in a unit cell.

We have studied four LSCO samples of which three are close to optimal doping and one is clearly overdoped. We label these samples with the hole dopings 14.8%, 15.5%, 17.1% and 21% that we determined by a procedure that is described in the following pages.

We determine T_c in zero field by tracking the resonance frequency of the NMR tank-circuit. The resonance frequency increases strongly at T_c due to the sample surface's diamagnetic contribution to the circuit's inductance. This diamagnetic contribution is proportional to the ac susceptibility. In Fig. 5.2 scaled ac susceptibilities are reported for four LSCO samples.

T_s can be determined from anomalies in the ^{139}La-NMR spectra and $^{139}T_1$ spin-lattice relaxation times [188, 180]. The clearest anomaly at T_s is a peak in $\frac{1}{T_1T}$ due to quadrupolar fluctuations. These fluctuations come from fluctuating orientations of the CuO_6-octahedra. Below T_s the CuO_6-octahedra remain tilted, causing the LTO structure. $\frac{1}{T_1T}$ is shown in the top panel of figure 5.3. The bottom

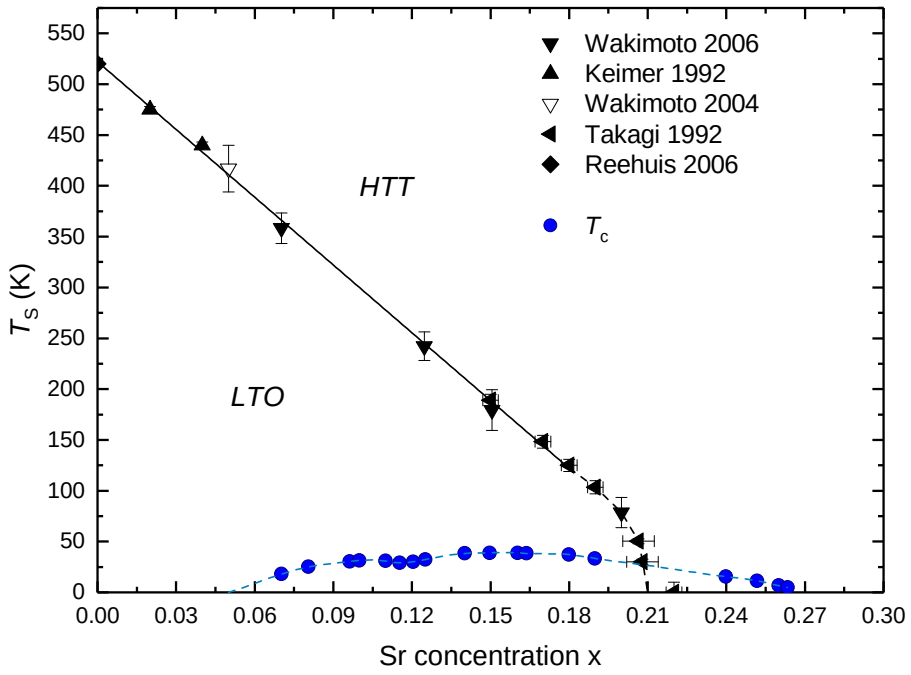

Figure 5.1: The *HTT* to *LTO* structural transition temperatures T_s are reproduced from [183, 184, 185, 186, 187]. The straight line is a linear fit of T_s for $0 \leq x \leq 0.18$. T_c is from Ido [67]. Dashed lines are guides to the eye.

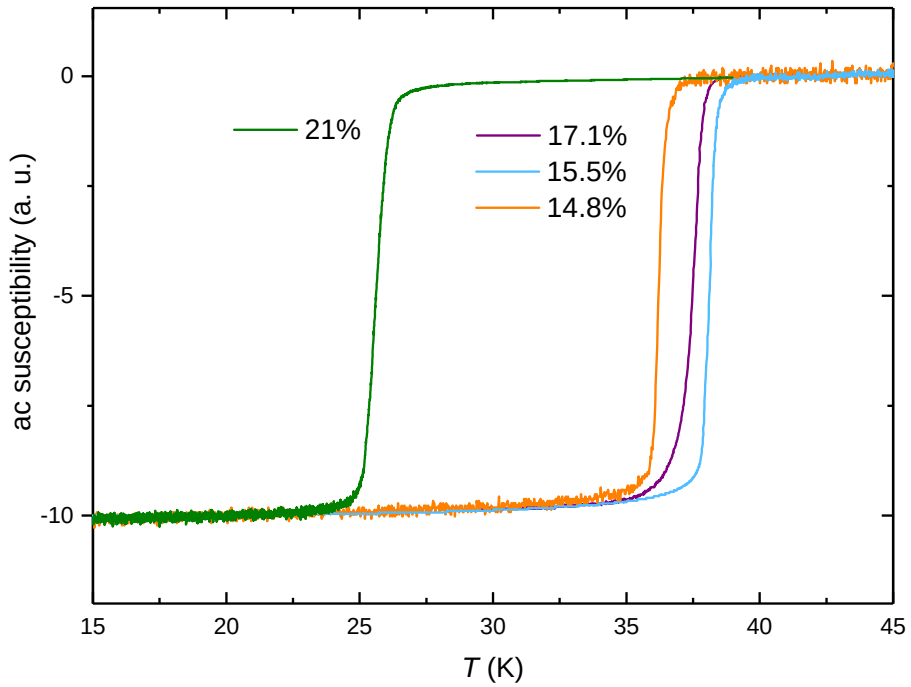

Figure 5.2: T-dependence of in situ ac susceptibility measured in the NMR circuit in zero field. T_c is definded from the midpoint of the drop in the ac susceptibility.

panel shows the corresponding stretching exponent of the T_1 relaxation, β. For purely magnetic and homogeneous relaxation one expects $\beta = 1$ because the data has been fit to the theoretical formula for magnetic relaxation, but due to the additional quadrupolar fluctuations β becomes smaller than 1. For 14.8%[1], 15.5% and 17.1% maxima in $\frac{1}{T_1T}$ coincide with minima in the stretching exponent β and T_s can be determined precisely. For 21% there is no such correspondence at first sight. $\frac{1}{T_1T}$ increases down to the lowest measured temperature without developing a peak although the stretching exponent β has a rather narrow minimum at 6 K. This is not due to superconductivity because it has been suppressed by applying a strong magnetic field. H_{c2} (at $T = 0$) is ≈ 45 T [189], see also Fig. 5.24a. A decreasing stretching exponent is expected with decreasing temperature if there is a distribution of relaxation rates, signaling growing electronic inhomogeneity upon cooling. It is not evident why such a putative inhomogeneity should increase when cooling until 6 K and suddenly decrease below 6 K. Hence, we conclude that the minimum of β is due to the structural transition, as for lower dopings, and that $T_s = 6\,\mathrm{K}$ for 21%. The absence of a peak in $\frac{1}{T_1T}$ must then be explained by some small additional relaxation mechanism that masks the decrease of the quadrupolar fluctuations below $T_s = 6\,\mathrm{K}$. This will be discussed in depth at the end of this chapter.

Fig. 5.4 summarises the sample information. The samples' dopings are determined by matching the measured T_s with the reference $T_s(p)$ provided in Fig. 5.1. Since $T_s(p)$ ends close to $p = 21\%$ our overdoped sample with $T_s = 6\,\mathrm{K}$ must have a doping close to 21%.

5.3 Bloembergen-Purcell-Pound Theory of Relaxation (BPP)

Before we advance to the principal results on the relaxation rate $\frac{1}{T_1}$ in LSCO in high magnetic fields a short introduction to the framework of relaxation due to freezing of fluctuations shall be given, which is known as Bloembergen-Purcell-Pound Theory, or BPP Theory for short [190]. BPP has been initially developed to describe the relaxation of liquids in the very first NMR experiments after World War II. Various liquids were studied close to ambient temperature, including water mixed with the more viscous glycerin. It was found that the relaxation rate $\frac{1}{T_1}$ increased over several orders of magnitude upon cooling or by increasing the viscosity η of the liquid, until $\frac{1}{T_1}$ reached a maximum. Decrease of the temperature T or increase of η both slow down the frequency of the molecules' Brownian motion and thus increase the correlation time $\tau_c \propto \frac{\eta}{T}$. Eventually, the corresponding fluctuation frequency $\frac{1}{\tau_c}$ becomes comparable to the nuclei's Lamor frequency ω_L. Since fluctuations at $\omega = \frac{1}{\tau_c} = \omega_L$ are most efficient in relaxing the nuclear spins, a peak in $\frac{1}{T_1}$ is observed. Upon further cooling or increasing η the relaxation becomes less efficient and $\frac{1}{T_1}$ decreases.

[1] in a previous neutron scattering and μSR study by Chang *et al.* [9] a sample from the same batch with very similar T_s and T_c has been determined as $p = 14.5\%$ due to a slightly different procedure to determine the doping.

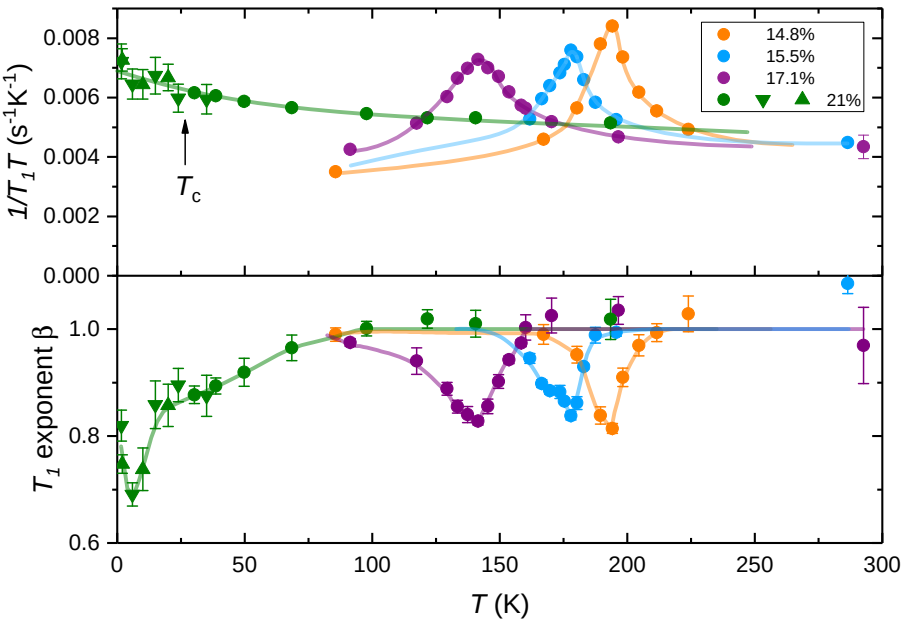

Figure 5.3: Top panel: T-dependence of $\frac{1}{T_1 T}$. Bottom panel: Corresponding T-dependence of T_1 stretching exponents β. Filled circles were measured at 15 T (19 T for lowest T of 14.8%). In 21% superconductivity has been suppressed below T_c by 40 T (▼) or 45 T (▲).

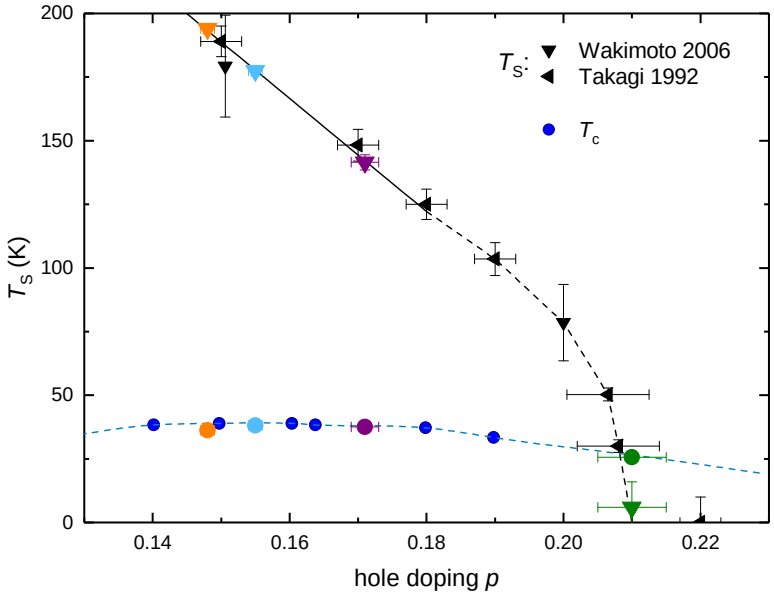

hole doping p	T_c (K)	T_s (K)
● 14.8±0.1 %	36.2±1	194±2
● 15.5±0.1%	38.1±1	177.5±2
● 17.1±0.2%	37.5±1	141.5±3
● 21.0±0.5%	25.6±1	6±10

Figure 5.4: Reduced range of fig. 5.1 including coloured triangles and circles for T_s and T_c, respectively, for all studied samples. The table on the right contains the full sample information.

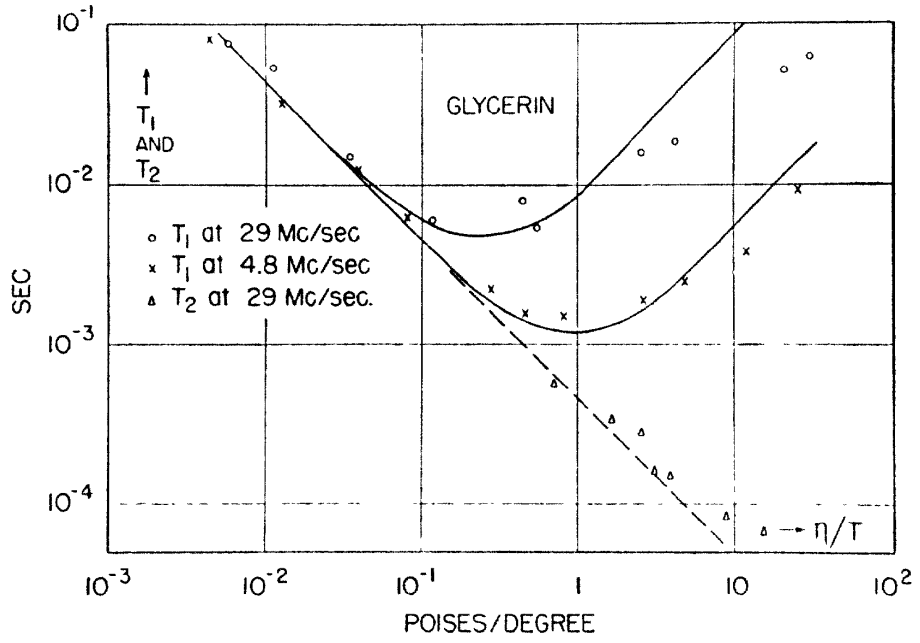

Figure 5.5: τ_c-dependence of T_1 and T_2 on a log-log scale at 29 MHz and 4.8 MHz (B = 0.68 T and 0.11 T in ^{1}H-NMR). The figure is reproduced from the original BPP publication [190].

Figure 5.5 shows the τ_c-dependence of T_2 and T_1 in Glycerin at two magnetic fields. Note that a *minimum* in T_1 corresponds to a *maximum* in $\frac{1}{T_1}$. One should also note that the T_1 minimum is shifted to larger $\frac{\eta}{T}$, *i.e.* longer τ_c, for lower frequency. In addition, the minimal T_1 is smaller for low frequency which means that $\frac{1}{T_1}_{max}$ *increases* for *decreasing* frequency.

Bloembergen, Purcell and Pound derived an expression for the relaxation rate $\frac{1}{T_1}$ that captures the discussed frequency dependence under the hypothesis of an auto-correlation function of the fluctuating field that decays exponentially:

$$\langle \boldsymbol{h}(t)\boldsymbol{h}(0)\rangle = \langle h^2\rangle e^{-\frac{t}{\tau_c}} \tag{5.1}$$

Fourier transformation of this expression leads to

$$\frac{1}{T_1} = \langle h_\perp^2\rangle \gamma_n^2 \frac{2\tau_c}{1+(\omega_L\tau_c)^2} \tag{5.2}$$

Here $2\langle h_\perp^2\rangle$ is the time-averaged squared transverse fluctuating field in the two transverse directions. There could be an additional prefactor of order 1, but we cannot determine it because we do not know the exact hyperfine coupling. For simplicity we use $\langle h_\perp^2\rangle = h_\perp^2$ with $h_\perp$ in [T][2], with γ_n as the nuclear gyromagnetic ratio in $\left[\frac{\text{MHz}}{\text{T}}\right]$ and the angular Larmor frequency $\omega_L = 2\pi f$. f is the actual resonance frequency in [MHz].

[2]If $h_\perp$ fluctuates randomly then $\langle h_\perp\rangle$ could be averaged out while $\langle h_\perp^2\rangle$ remains finite, so in general $\langle h_\perp\rangle^2 \neq \langle h_\perp^2\rangle$. For LSCO $p = 0.115$, Ohsugi estimated $\langle h_\perp\rangle$ directly from the low T NQR spectrum and found $\langle h_\perp\rangle$=0.042 T [191]. As we will see further, fits with a BPP model derived from eq. 5.2 give $\sqrt{\langle h_\perp^2\rangle} = h_\perp \approx 0.04$ T in LSCO $p = 0.12$ measured by Mitrović *et al.* [178] and $p = 0.115$ measured by Arsenault *et al.* [180].

It can be easily seen that

$$\frac{1}{T_1}_{max} = \frac{h_\perp^2 \gamma_n^2}{\omega_L} \text{ , when } \quad \omega_L = \frac{1}{\tau_c}. \tag{5.3}$$

In the case of liquids $h_\perp$ originates from dipolar fields from neighbouring molecules' nuclei. But in a system with magnetic ions $h_\perp$ should be proportional to the local field produced by electronic magnetic moments.

Different models have been used to describe the correlation time $\tau_c(T)$. Let us consider a correlation time of the form:

$$\tau_c(T) = \tau_\infty e^{\frac{E_0}{T}} . \tag{5.4}$$

It describes fluctuations that continuously slow down on cooling, eventually freezing at $T = 0$ (*i.e.* there is no phase transition at finite T). Here $k_\mathrm{B} = 1$, so energies have the units of Kelvin. τ_∞ is a short correlation time in the limit of infinite temperature ($T \gg T_\mathrm{p}$, where T_p is the peak temperature) and E_0 is some characteristic activation energy of the fluctuations. Other activated behaviour like *Vogel-Fulcher* with a modified exponential $\sim e^{\frac{E_0}{T-T_0}}$ has been used in the context of glasses [192] if $\tau_c(T)$ appears to diverge at a non-zero temperature T_0, but also power-law T-dependence of $\tau_c(T)$ has been invoked in some models. In the simple case of eq. 5.4 one can easily determine the BPP peak temperature T_p by inserting eq. 5.4 into the condition $\omega_L = \frac{1}{\tau_c}$ and solving for T_p to get:

$$T_\mathrm{p} = \frac{-E_0}{\ln(\omega_L \tau_\infty)} . \tag{5.5}$$

We shall now proceed to discuss the BPP theory in the context of LSCO.

5.4 BPP applied to LSCO

In superconducting LSCO, the magnetic order can be described as an anti-ferromagnetically correlated spin glass. This leads to a broad peak in the spin-lattice relaxation rate $\frac{1}{T_1}$ as a function of temperature. The temperature at which this peak appears in NMR, NQR and μSR can serve to define the so-called glassy transition temperature T_g. It is called glassy transition since close to and below T_g many properties are similar to prototypical spin-glasses like CuMn [193]. Such properties are, for example, a hysteretic T-dependence of the magnetisation [194, 22] and the aforementioned broad peak in $\frac{1}{T_1}$. One should add that a peak in $\frac{1}{T_1}$ is expected at any magnetic transition. The glassiness is reflected in an unusually wide T range over which fluctuations slow down and in combination with the heterogeneity of the freezing process this results in an unusually broad peak at T_g. The doping dependence of T_g is shown in Fig. 5.6.

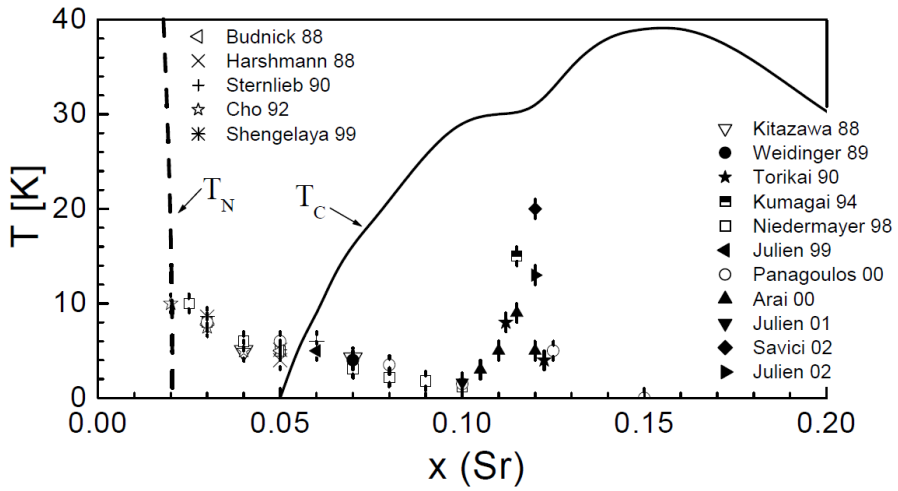

Figure 5.6: Sr-doping dependence of the glassy magnetic ordering temperature T_g as seen by low frequency probes like NQR/NMR and μSR. This figure is reproduced from [176].

From Figure 5.6 one can see that this magnetic order becomes stronger around $x = 0.12$ and appears to be dying away quickly for $x > 0.12$. We have investigated the doping range above $p = 0.12$ by measuring $\frac{1}{T_1}$ in high fields and find that relaxation rates are enhanced by fields and model them with the BPP theory including a distribution of correlation times to account for the inhomogeneous nature of the spin-glass.

5.5 LSCO $p = 0.12$

To demonstrate the modeling of the relaxation rate, we shall first see an example of $\frac{1}{T_1}$ for $p = 0.12$. Mitrović *et al.* have measured $\frac{1}{T_1}(T)$ at 14 T and found that the characteristic peak of the spin-glass T_g occurs at 14 K [178]. To observe the peak in the relaxation rate, ^{139}La-NMR is used since ^{63}Cu-NMR is hampered by the *wipe-out effect* [195]: the ^{63}Cu-NMR signal is lost due to fast spin-spin relaxation (T_2) [196, 197]. ^{139}La-NMR is not affected by this problem, since its hyperfine coupling to the moments on Cu is two orders of magnitude weaker [197].

Mitrović *et al.* found that the relaxation curves are stretched at low T which indicates that there is a broad distribution of relaxation times, see Fig. 5.7. Although there is a distribution of relaxation rates we can try to describe the relaxation process through a "typical" relaxation rate. The typical relaxation rate is best defined by the *median* of the distribution of $\frac{1}{T_1}$. It is the value which splits the cumulative probability into equal halves, see Fig. 5.8 for an example. To determine the median one needs to know the exact probability density function. This is not possible experimentally: As shown in Fig. 5.7a, the stretched relaxation curves can be fit by different types of distributions, *e. g.* a log-normal distribution, or the stretched exponential decay which has another underlying distribution.

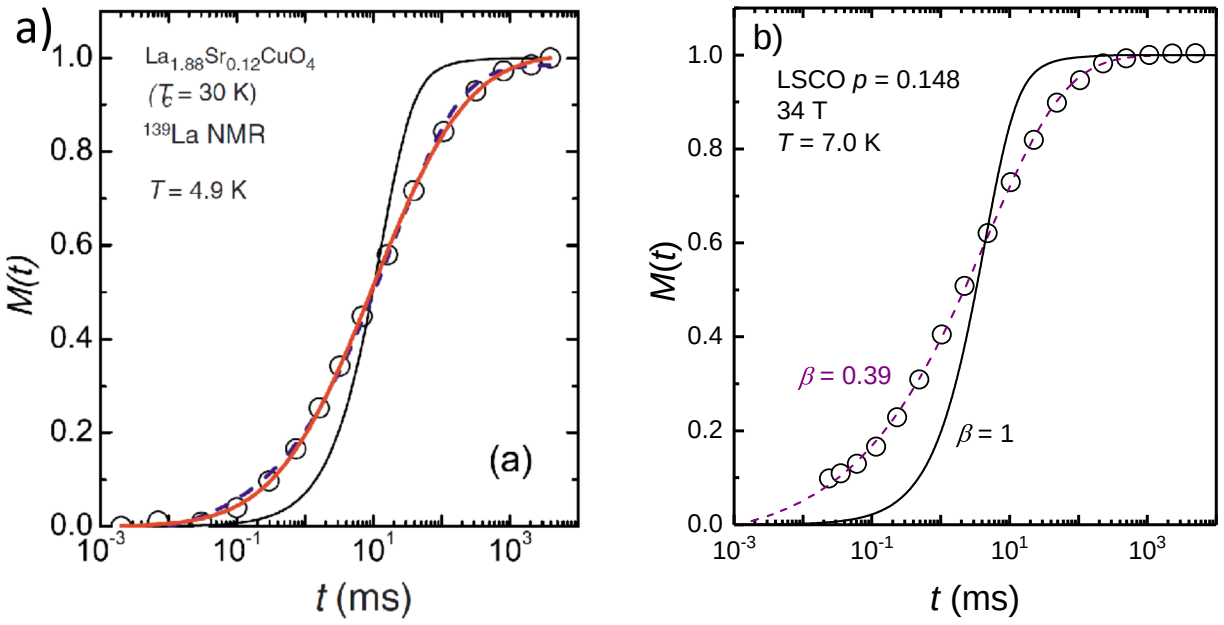

Figure 5.7: a): Relaxations curve $M(t)$ of LSCO 12% measured by saturation-recovery at 14 T and 4.9 K, reproduced from Mitrović *et al.* [178]. Data is fitted to a stretched exponential decay (dashed line) and a log-normal distribution of relaxation rates (orange line). The black line shows the relaxation curve for magnetic relaxation with a single T_1 (no distribution, $\beta = 1$). b): Similar relaxation curve $M(t)$ of LSCO 14.8% measured by saturation-recovery at 34 T and 7 K. The dashed line is a stretched relaxation decay with $\beta = 0.39$, the black line has $\beta = 1$.

However, the median relaxation rate turns out to be similar irrespective of the distribution [178]. The usual procedure to account for the stretched relaxation curve is to fit it with stretched exponential decay that is described by the parameter $\frac{1}{T_1}_{\text{stretch}}$ and the stretch exponent β. This ad-hoc approach is justified when $\beta \gtrsim 0.4$ because then $\frac{1}{T_1}_{\text{stretch}}$ corresponds to the median relaxation rate $\frac{1}{T_1}_{\text{median}}$ [119]. In the following, we use the stretched exponential decay to determine the "typical" relaxation rate.

5.5.1 BPP-fitting of $\frac{1}{T_1}$ with a distribution of correlation times

In Fig. 5.9a, the T-dependence of $\frac{1}{T_1}_{\text{stretch}}$ is reproduced for LSCO $p = 0.12$. In addition, a standard BPP peak (filled gray area) is shown whose parameters are chosen such that its peak temperature T_{p} coincides with the peak of the data at T_{g}. Assuming an exponentially activated correlation time τ_{c}, following eq. 5.5, T_{p} is fully determined by the measurement frequency ω_L and the parameters of τ_{c}: τ_∞ and E_0. τ_∞ is the correlation time at infinite temperature and should not depend on microscopic details. It has been found that $\tau_\infty \approx 0.02$ ps can be universally used to fit the peak in $\frac{1}{T_1}$ for a variety of La-based cuprates [196], so this value has been equally used for the standard BPP peak in Fig. 5.9a. Thus, the remaining parameter, $E_0 = 160$ K, fully determines the peak position. The peak height is determined independently by $h_\perp$. Clearly, the standard BPP peak does not account for the

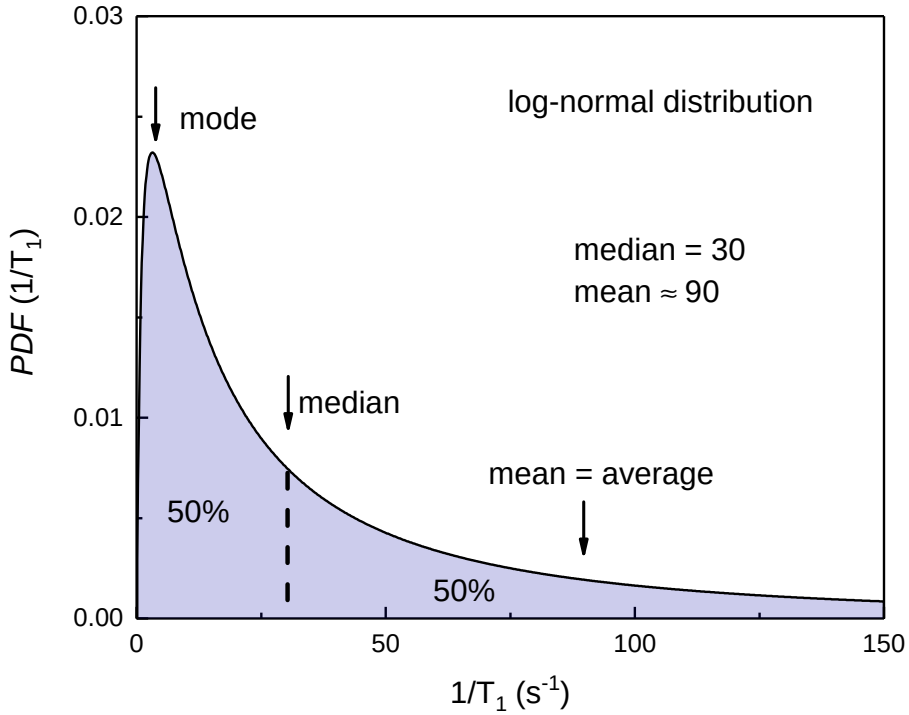

Figure 5.8: A log-normal distribution of relaxation rates $1/T_1$. Since this distribution is asymmetric the *mode*, the *median* and the *mean* (average) do not coincide: the probability density function $PDF(1/T_1)$ is maximal at the mode, the median splits the cumulative probability density into two equal halves. The mean relaxation rate is much higher due to the tail that continues to infinity (not shown).

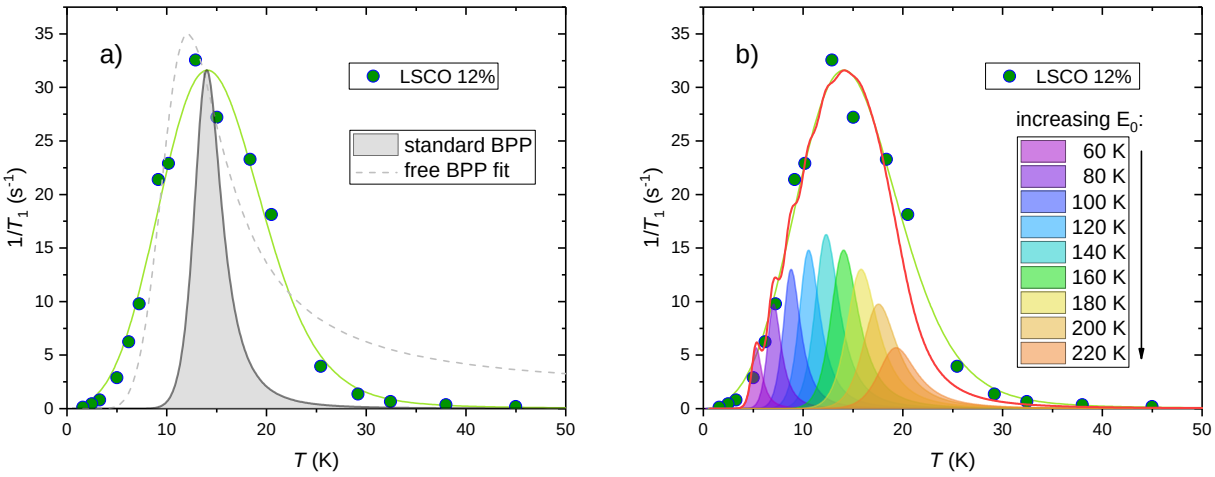

Figure 5.9: a):Green circles • are $\frac{1}{T_1}_{\text{stretch}}$ data of LSCO 12% reproduced from Mitrović *et al.* [178] where a T-linear contribution corresponding to constant $1/T_1T$ has been subtracted. The applied field is $B = 14$ T. Filled gray curve: Standard BPP peak with E_0=160 K. Dashed grey line: Standard BPP fit with completely free parameters. Light green line: Fit of E_0-distributed BPP model as explained in the text. b): Coloured peaks visualise the effect of a distribution of activation energies E_0. Each peak is a standard BPP peak with fixed activation energy E_0 in the range $60\,\text{K} \leq \text{E}_0 \leq 220\,\text{K}$. Peak heights vary like a Gaussian function centered around E_0=140 K such that the sum of all standard BPP peaks (red line) describes the data much better than the single gray BPP peak in a).

T-dependence of the data because it is much too narrow[3]. At low T the relaxation rate is many orders of magnitude too small.

To account for a broad peak in $\frac{1}{T_1}$ Suh *et al.* [198] and Curro *et al.* [196] have assumed that the activation energy is distributed around a most probable value E_0[4]. Through eq. 5.5 this directly leads to a distribution of $T_\mathrm{p}(E_0)$ and naturally gives a broadened peak in $\frac{1}{T_1}$. Fig. 5.9b visualises the effect of summing standard BPP peaks with varying E_0 in the range $60\,\mathrm{K} \leq \mathrm{E}_0 \leq 220\,\mathrm{K}$. The nine peaks shown in Fig. 5.9b add up to the red line which already follows the data more properly than a single BPP peak. In the continuous limit the sum turns into the integral

$$\begin{aligned} T^{-1}_{1,\,\text{distributed BPP}}(T) &= \frac{1}{\mathcal{N}} \int_0^\infty T^{-1}_{1,\mathrm{BPP}}(E_\mathrm{a}, T) \cdot e^{-\frac{(E_0-E_\mathrm{a})^2}{2\Delta E_0^2}} \,\mathrm{d}E_\mathrm{a} \\ &= \frac{1}{\mathcal{N}} \int_0^\infty h_\perp^2 \gamma_n^2 \frac{2\tau_c(E_\mathrm{a})}{1+(\omega_L \tau_c(E_\mathrm{a}))^2} \cdot e^{-\frac{(E_0-E_\mathrm{a})^2}{2\Delta E_0^2}} \,\mathrm{d}E_\mathrm{a} \\ &= \frac{1}{\mathcal{N}} \int_0^\infty h_\perp^2 \gamma_n^2 \frac{2\tau_\infty e^{\frac{E_a}{T}}}{1+(\omega_L \tau_\infty e^{\frac{E_a}{T}})^2} \cdot e^{-\frac{(E_0-E_\mathrm{a})^2}{2\Delta E_0^2}} \,\mathrm{d}E_\mathrm{a}\,. \end{aligned} \tag{5.6}$$

Here $\frac{1}{\mathcal{N}}$ ensures the normalisation by

$$\mathcal{N} = \int_0^\infty e^{-\frac{(E_0-E_\mathrm{a})^2}{2\Delta E_0^2}} \,\mathrm{d}E_\mathrm{a}$$

and ΔE_0 is the width of a Gaussian distribution of energies E_a centered around E_0. The light green line in Fig. 5.9 shows that using the integral, which convolutes $T^{-1}_{1,\mathrm{BPP}}(T)$ at each temperature T with the Gaussian distribution of activation energies, $T^{-1}_{\text{distributed, BPP}}(T)$ follows the data nicely. It should be emphasised that ΔE_0 and all other parameters are assumed to be T-independent. The correlation time comprises the full T-dependence. This implies that $h_\perp$ only determines the peak height but never changes the shape of $T^{-1}_{1,\,\text{distributed BPP}}(T)$. If one assumed an uncorrelated distribution of $h_\perp$, similarly as in case of the activation energy, $T^{-1}_{1,\,\text{distributed BPP}}(T)$ would only be sensitive to the average of this distribution because the integrals over $\mathrm{d}E_a$ and $\mathrm{d}h_\perp$ factorise.

We use this model to fit the experimentally determined $\frac{1}{T_1\,\text{stretch}}$. The light green line in Fig. 5.9 has been determined by a non-linear fitting procedure in *Mathematica*. It has been found that all parameters are cross-correlated with τ_∞, so a very large range of τ_∞ fits the data well. On the other hand, once τ_∞ is fixed, the other parameters $h_\perp$, E_0 and ΔE_0 can be determined reliably, as shown in Fig. 5.10. From Fig. 5.10b one can see that it is important to use the same value for τ_∞ if comparing $\frac{1}{T_1}(T)$ of two different samples or the same sample at two different fields, since the chosen τ_∞ value strongly affects the fluctuating field $h_\perp$. It is also interesting to notice that the ratio of the activation energy distribution's center to its width is nearly constant irrespective of τ_∞. It will be shown that

[3] Keeping all parameters free gives a qualitatively better fit at the expense of an artificially long τ_∞ which would overestimates the relaxation rate at high T, see grey dashed line in Fig. 5.9a.

[4] There are other ways to introduce distributions to describe relaxation data, see, *e.g.*, ref. [199].

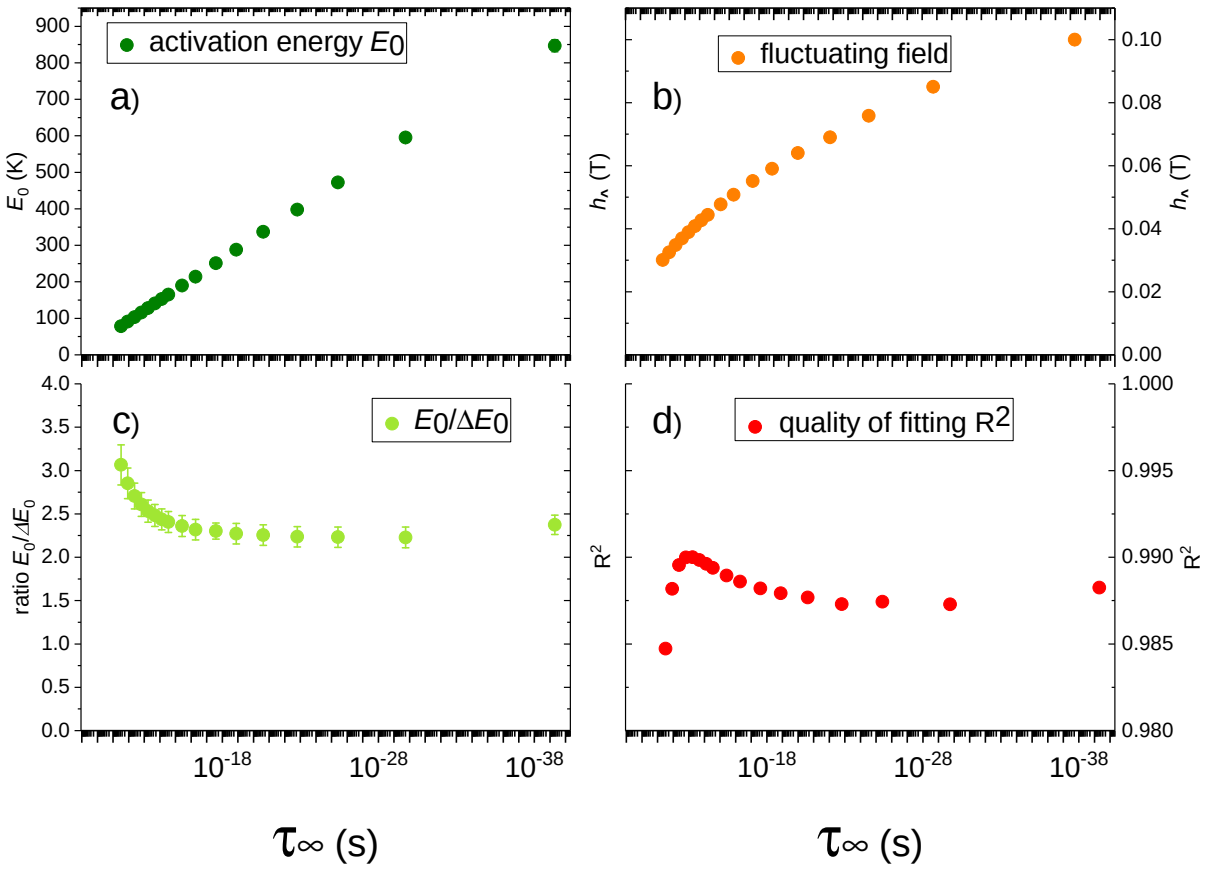

Figure 5.10: Linear-log plots of the convoluted BPP-fitting parameters'τ_∞-dependence over **30** orders of magnitude. a) Dark green circles show the center of activation energy distribution E_0 (K). b) Fluctuating field $h_\perp$ (T) as orange circles. c) Ratio of energy E_0 and the width of the distribution ΔE_0. E_0 and ΔE_0 both increase for shortening τ_∞, so the ratio is nearly constant $\frac{E_0}{\Delta E_0} \approx 2.3$. d) The quality of the fit measured by R^2 is optimal close to $\tau_\infty = 0.02$ ps but R^2 stays close to optimal for a very large range of τ_∞. The error bars are smaller than the symbol size for a) and b).

this ratio is also field-independent, so fixing the ratio can make the fitting at low fields more reliable.

When we fit $\frac{1}{T_1}_{\text{stretch}}(T)$ by $T^{-1}_{1,\,\text{distributed BPP}}(T)$ there is a technical issue that should be briefly explained here. Its full discussion is moved to the appendix.

The form in which $T^{-1}_{1,\,\text{distributed BPP}}(T)$ is constructed gives the mean $1/T_1$. This is because the convolution of some function $f(x)$ with a probability density function $PDF(x)$ (in our case we convolute $T^{-1}_{1,\text{BPP}}$ with a Gaussian where $x = E_a$, as stated in eq. 5.6) by construction gives the mean value of that function with respect to the probability density function:

$$f_{\text{mean}} = \int f(x) \cdot PDF(x)\, \mathrm{d}x\,.$$

On the other hand, $\frac{1}{T_1}_{\text{stretch}}$ corresponds to the median $1/T_1$ and, in general, the mean can be much larger than the median, as can be seen from Fig. 5.8. It is the long tail of the distribution that makes

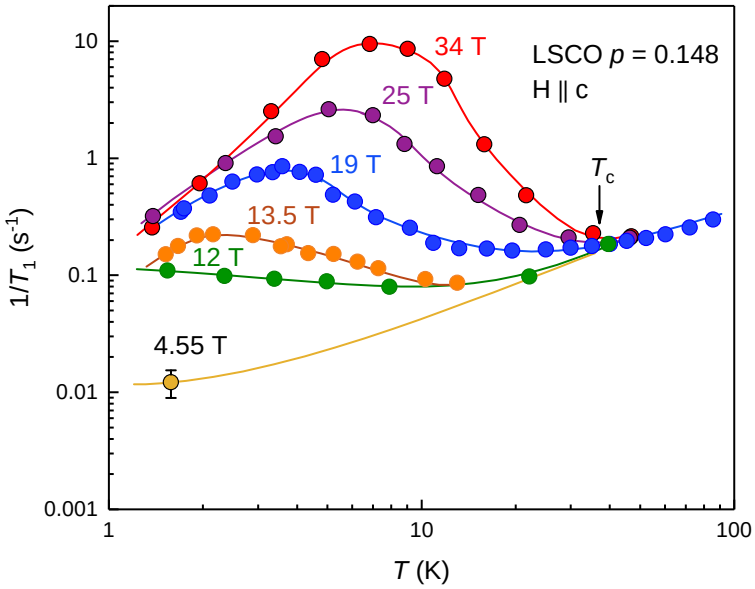

Figure 5.11: T dependence of $\frac{1}{T_1}$ at high fields. The data corresponds to $T_{1,\mathrm{stretch}}^{-1}$ from saturation-recovery relaxation measurements of the ^{139}La central peak. A peak appears above 12 T and grows in amplitude. The peak position shifts towards higher T. The field dependence sets in close to the superconducting T_c. Lines are guides to the eye.

the mean very large. Consequently, fitting a median relaxation rate by a mean relaxation rate is in general wrong. However, a realistic distribution of relaxation rates does not have a tail that extends to infinity. By considering the effect of truncation of the tail we can show that $\frac{1}{T_1}_{\mathrm{mean}} \approx \frac{1}{T_1}_{\mathrm{median}}$ and thus justify our model.

5.6 LSCO $p = 0.148$

After having discussed the T-dependence of $\frac{1}{T_1}$ for the $p = 0.12$ we can turn to a higher doped sample, LSCO $p = 0.148$. It is a sample from the same batch as the $p = 0.145$ sample in the neutron+μSR study by Chang *et al.* where field induced magnetic order was found above $\mu_0 H_c = 7$ T [9].

5.6.1 Relaxation rate $\frac{1}{T_1}$

We have studied $\frac{1}{T_1}(T)$ up to 34 T and find a broad peak with a strong field dependence: The peak height increases with field with no sign of saturation up to 34 T and T_p, the peak temperature, also increases with field, as shown in Fig. 5.11.

The recovery curves start to become stretched at all measured fields, already above T_c, see Fig. 5.12. We find no peak at pumped ^{4}He temperatures of ~ 1.7 K for $B \leq 12$ T, but as T_p is field dependent, we cannot exclude that a peak would become visible at $T < 1.7$ K.

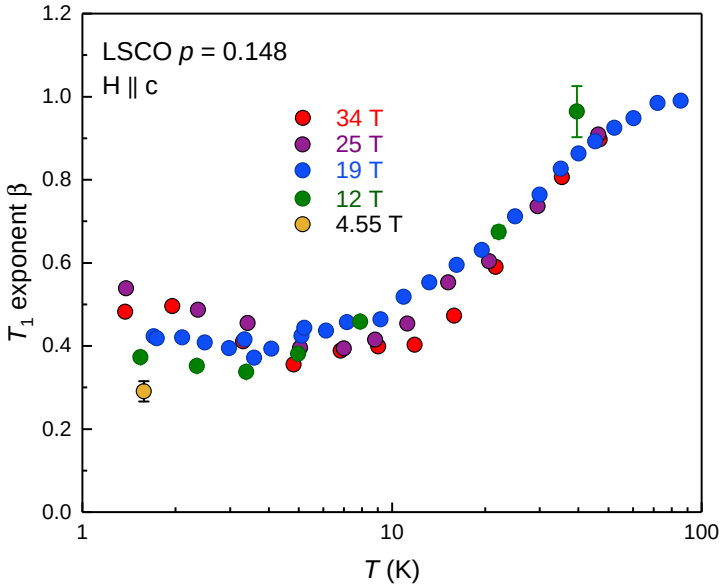

Figure 5.12: T dependence of T_1 stretch exponent β. $\beta < 1$ implies that T_1 is distributed. At the lowest $T \sim 1.7$ K β is decreasing for decreasing field which makes measurements very long to reach saturation.

Measurements at low T and low fields are difficult since the signal intensity is weak and the stretched relaxation curves require long waiting times to reach saturation.

The relaxation rates of $p = 0.148$ at high fields are qualitatively very similar to those found in $p = 0.12$, so we can conclude that in the high field limit $p = 0.148$ undergoes the same glassy magnetic ordering as $p = 0.12$ at zero or low field. However, it is not evident where exactly the enhancement of $\frac{1}{T_1}$ starts.

5.6.2 Background of the relaxation rate

In a number of LSCO samples there appears to be an extended range of temperatures $T_c \lesssim T \lesssim T_s$ where $\frac{1}{T_1T}$ is constant on ^{139}La, as pointed out by Baek *et al.* [188, 200, 179, 180]. It looks like constant $\frac{1}{T_1T}$ as expected for simple metals from the Korringa relation [201], but LSCO is not a simple metal and, in fact, if measured on ^{63}Cu or ^{17}O in the same T range, $\frac{1}{T_1T}$ is not constant [202, 203, 204]. It turns out that $^{63}(T_1T)^{-1}$ increases with cooling while $^{17}(T_1T)^{-1}$ decreases, so it is possible that $^{139}(T_1T)^{-1}$ is constant by accident. Below T_c, on the other hand, independently of the nuclear site $\frac{1}{T_1T}$ is expected to be gapped.

We assume that the approximately constant $^{139}(T_1T)^{-1}$ acts as a background on top of which the enhanced relaxation due to glassy magnetic ordering develops. This implies that both relaxation mechanisms are to some extent uncorrelated. We can model the B and T-dependence of the $\frac{1}{T_1T}$ background below T_c and subtract it. To do this correctly, we would need to know the full B & T-

dependences of the SC gap $\Delta(B,T)$. For our purpose, any function that mimics a gap and is gradually filled with increasing field is sufficient. A simple function to model the background below T_c is the following:

$$\frac{1}{T_1T}_{\text{backgr.}}(B,T) = c_0 + (c_1 - c_0)\exp\left(\frac{\Delta}{T_c}\right)\exp\left(-\frac{\Delta}{T}\right) \tag{5.7}$$

c_0 is the minimal relaxation rate and c_1 is the constant relaxation above T_c, so $(c_1 - c_0)$ is the magnitude of the decrease from c_1 down to $c_0(B)$. The second exp leads to an exponential decrease with lowering T and the first exp is necessary to make sure that the background is equal to c_1 at T_c. For a d-wave SC one expects a power-law decrease, not an exponential, but for our purpose an exponential decrease is an acceptable approximation. Δ and T_c both depend on B in a complicated way but we take the simplest possible expressions:

$$T_c(B) = T_{c,0}\sqrt{1 - \frac{B}{\mu_0 H_{c2}}} \qquad \text{mean-field approximation} \tag{5.7a}$$

$$\Delta(B) = 2.15\,T_c(B,T) \qquad \text{effective d-wave gap} \tag{5.7b}$$

$$c_0(B) = \frac{B}{\mu_0 H_{c2}} \qquad \text{linearly increasing minimal } \frac{1}{T_1T} \tag{5.7c}$$

Eq. 5.7b is based on the scaling between T_c and the SC gap for a d-wave BCS superconductor [205] and assumes that it holds for $B > 0$. Eq. 5.7c is consistent with measurements of Zheng *et al.* that show linearly increasing $\frac{1}{T_1T}$ with field at 4.2 K in Tl-1201 [206]. All that is needed to plot eq. 5.7 is the zero-field T_c and H_{c2}. We use data from ref. [189]. Above $T_c(B)$ the background is constant: $\frac{1}{T_1T}(T > T_c) = 0.0034\,\text{s}^{-1}\text{K}^{-1}$.

Fig. 5.13 shows the $\frac{1}{T_1T}$ with the calculated $\frac{1}{T_1T}_{\text{backgr.}}$ at the fields that correspond to the data. In addition $\frac{1}{T_1T}(B = 19\,\text{T})$, where the field has been applied in the plane is shown and scaled to the high T data with field applied along the $\boldsymbol{c}$-axis. The scaling factor $\frac{1}{T_1T}$ data between both field orientations is the same as for LSCO $p = 0.115$ of Arsenault *et al.* [180].

Interestingly, after scaling, $\frac{1}{T_1T}(B = 19\,\text{T})$ in both orientations starts to increase slowly already below ≈ 70 K. As H_{c2} for $H \perp \boldsymbol{c}$ is much higher than for $H \parallel \boldsymbol{c}$, SC strongly suppresses the enhancement of $\frac{1}{T_1T}$ for $H \perp \boldsymbol{c}$. Relative to this data and its corresponding calculated background for 4.55 T, even the data point at 4.55 T $\parallel \boldsymbol{c}$ appears to be enhanced by more than an order of magnitude. Thus, from NMR one would infer that even at $B = 4.55\,\text{T} < \mu_0 H_c = 7$ T there is some signature of field enhanced glassy magnetism.

5.6.3 BPP fits for LSCO $p = 0.148$

In this section the relaxation data is fit by the BPP model. Introducing a distribution of τ_∞ allows to accurately fit data at high fields and opens a route to extend the analysis to lower fields where no peak

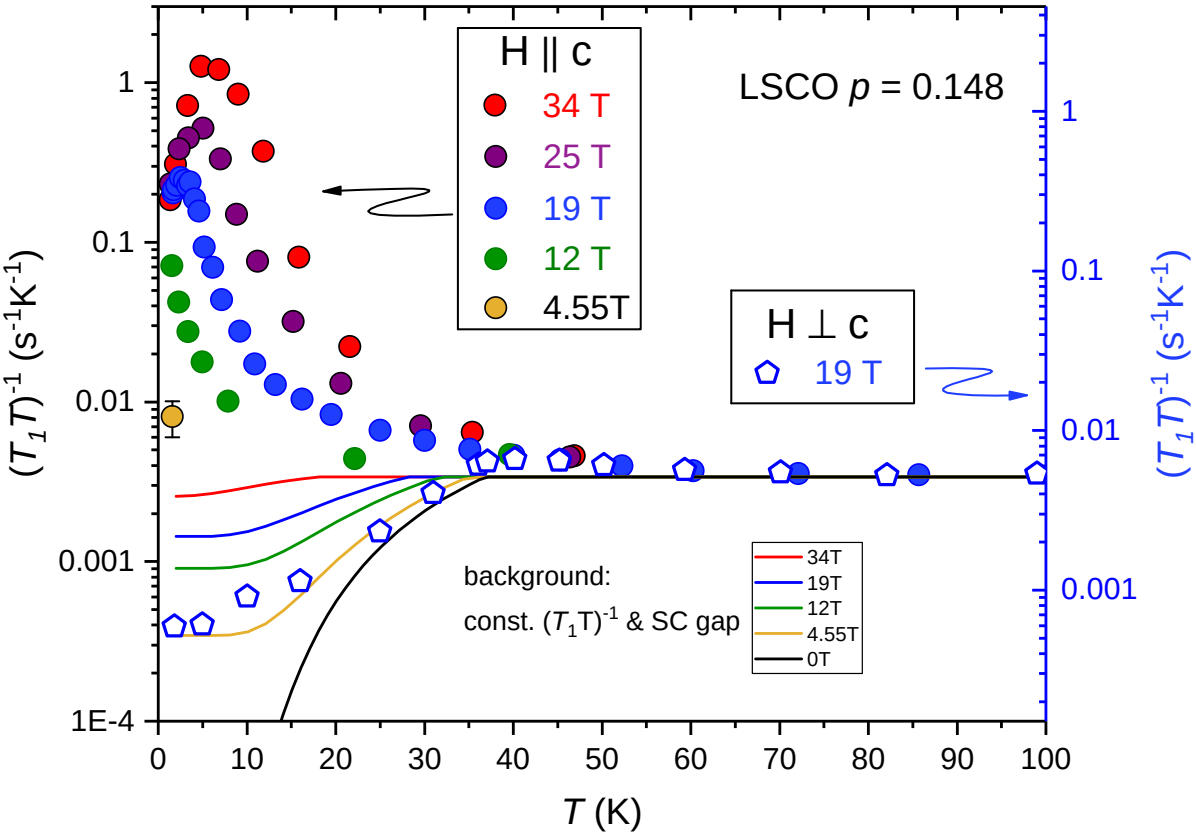

Figure 5.13: T dependence of $\frac{1}{T_1T}$ of the data presented in Fig. 5.11, together with $\frac{1}{T_1T}_{\text{backgr.}}$ calculated by eq. 5.7 using $T_c = 37$ K & $\mu_0 H_{c2} = 45$ T (coloured lines). $\frac{1}{T_1T}$ for an in-plane field of 19 T (empty blue pentagons) scaled at high T with the other data. The scaling factor is 1.5. While $\frac{1}{T_1T}$ for field along the ***c***-axis is enhanced at all fields, $\frac{1}{T_1T}$ with in-plane field is strongly suppressed below T_c.

can be identified. This allows to extract the fluctuating field $h_\perp$ in the entire measured field range, which can then be compared with ordered moments determined from neutron scattering.

As discussed for LSCO $p = 0.12$, we can fit the enhancement of $\frac{1}{T_1}$ with the BPP model by introducing a distribution of correlation times $\tau_c(T)$. Assuming that $\tau_c(T)$ follows eq. 5.4 we have shown that a Gaussian distribution of the activation energies E_a describes LSCO $p = 0.12$. However, there is no reason that τ_∞, the correlation time in the high T limit, is not distributed. We find that to fit LSCO $p = 0.148$ properly in the T-range above the peak a distribution of τ_∞ has to be added, but the center of the distribution is always kept at 0.02 ps.

Correlation times like 0.02 ps are small numbers. It is easier to work with $\ln \tau_\infty = a$ instead. $\tau_\infty = 0.02$ ps gives $a_0 = -31.5$. We center the Gaussian distribution of correlation times around a_0 and give it a width Δa. The full expression for the distributed BPP model becomes

$$\begin{aligned} T^{-1}_{1,\,\mathrm{BPP\,dist.}}(T) &= \frac{1}{\mathcal{N}} \int_0^\infty \int_{-\infty}^\infty T^{-1}_{1,\mathrm{BPP}}(E_\mathrm{a}, a, T) \cdot e^{-\frac{(E_0 - E_\mathrm{a})^2}{2\Delta E_0^2}} e^{-\frac{(a_0 - a)^2}{2\Delta a^2}} \mathrm{d}E_\mathrm{a} \mathrm{d}a \\ &= \frac{1}{\mathcal{N}} \int_0^\infty \int_{-\infty}^\infty h_\perp^2 \gamma_n^2 \frac{2\tau_c(E_\mathrm{a}, a)}{1 + (\omega_L \tau_c(E_\mathrm{a}, a))^2} \cdot e^{-\frac{(E_0 - E_\mathrm{a})^2}{2\Delta E_0^2}} e^{-\frac{(a_0 - a)^2}{2\Delta a^2}} \mathrm{d}E_\mathrm{a} \mathrm{d}a \qquad (5.8) \\ &= \frac{1}{\mathcal{N}} \int_0^\infty \int_{-\infty}^\infty h_\perp^2 \gamma_n^2 \frac{2e^{a + \frac{E_a}{T}}}{1 + (\omega_L e^{a + \frac{E_a}{T}})^2} \cdot e^{-\frac{(E_0 - E_\mathrm{a})^2}{2\Delta E_0^2}} e^{-\frac{(a_0 - a)^2}{2\Delta a^2}} \mathrm{d}E_\mathrm{a} \mathrm{d}a \,. \end{aligned}$$

The normalisation is now

$$\mathcal{N} = \int_0^\infty \int_{-\infty}^\infty e^{-\frac{(E_0 - E_\mathrm{a})^2}{2\Delta E_0^2}} e^{-\frac{(a_0 - a)^2}{2\Delta a^2}} \mathrm{d}E_\mathrm{a} \mathrm{d}a \,.$$

Integrating a over the full numerical range is computationally demanding, but limiting the integration range to $a_0 - 3\Delta a \leq a \leq a_0 + 3\Delta a$ leads to equivalent results when $\Delta a > 1$. When $\Delta a \leqq 1$, we keep a fixed Δa-independent integration range of ± 3.

One can convince oneself that introducing the distribution of τ_∞ improves the fit quality significantly at T above the peak. Fig. 5.14 compares fits with and without the distribution for data at 19 T.

We fit $T^{-1}_{1,\,\mathrm{stretch}}$ after subtracting the background given by eq. 5.7 (multiplied by T). It is important to remark that for $B > 12$ T the field dependence of the background makes a negligible difference but as we extend the analysis to $B \leq 12$ T in the following, we use eq. 5.7 at all fields for consistency. Fig. 5.15 shows $T^{-1}_{1,\,\mathrm{stretch}}$ before and after the background subtraction for all fields where we can identify a peak and where unconstrained fits to eq. 5.8 can be performed. Fig. 5.15 also includes fits for $B \leq 12$ T that have been made with the constraint that $E_0/\Delta E_0 = 2.37$.

Fig. 5.16 summarises the field dependence from all parameters of the BPP fits. Fig. 5.16c) shows that the ratio $E_0/\Delta E_0$ has no strong field dependence. The average value is 2.37 and is very similar to the ratio found for LSCO $p = 0.12$, as shown in Fig. 5.10c). This ratio captures the general shape of the peak in $T_1^{-1}(T)$ around $p = 0.12$. Constraining it, we can get a stable fit at $B = 12$ T, although

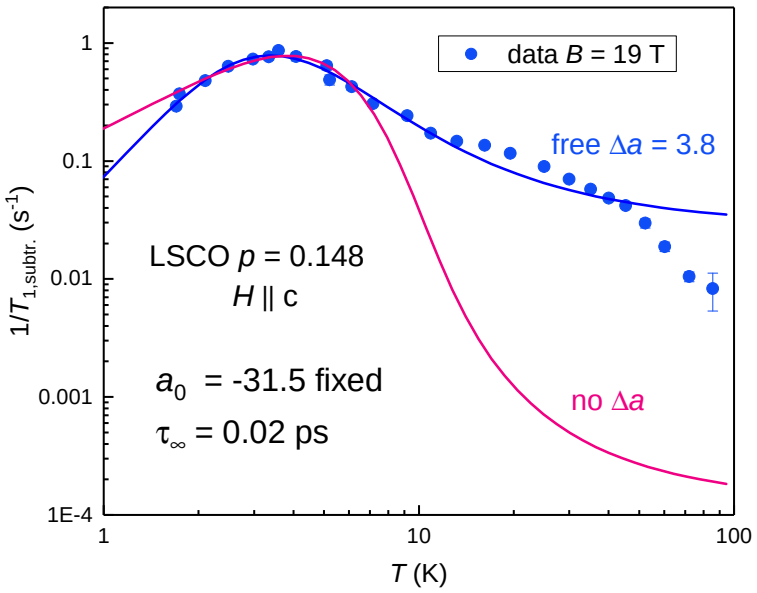

Figure 5.14: Distributed fits to background subtracted $T_{1,\,\mathrm{stretch}}^{-1}$ at $B = 19$ T. The blue line includes the τ_∞ distribution with $\Delta a = 3.8$ whereas τ_∞ is not distributed (no Δa) for the pink line. In both cases $a_0 = -31.5$ is fixed, corresponding to τ_∞=0.02 ps.

no peak can be identified by eye. For $B = 10$ T, $T_1^{-1}(T)$ could not be measured at intermediate $T \sim 10$ K, because the signal becomes very weak due to strong SC. However, it can be recovered at lower T since the nuclear magnetisation is proportional to $1/T$.

The field dependence of the BPP parameters reflects three characteristic behaviours of the peak in $T_1^{-1}(T)$ with decreasing field:

1) The fluctuating field $h_\perp$ decreases strongly, as shown in Fig. 5.16b). This is reflected in the decreased peak amplitude. According to eq. 5.3 a decreasing peak height necessarily implies a strongly decreasing fluctuating field, as $1/\omega_L \propto 1/B$.

2) E_0 decreases, as shown in panel a). This makes the peak move to lower T. However, a decreasing peak temperature T_p is expected even for constant E_0, according to eq. 5.5, as $-1/\ln(B)$ goes to zero at $B = 0$. We are unable to determine E_0 for $B < 12$ T, but if E_0 goes to zero at a non-zero field, T_p will likewise.

3) According to Fig. 5.16d) the distribution of τ_∞ increases rapidly at low fields. This leads to an increasingly broadened peak. Δa is a logarithmic quantity, so it gives an estimation over how many orders of magnitude τ_∞ is distributed. As a was defined using the natural logarithm through $\ln \tau_\infty$, an order of magnitude change of τ_∞ increases or decreases a by a factor $\ln 10^{\pm 1} = \pm 2.3$. The strong growth of Δa at 10 T implies that the parameter E_0 and with it, the peak temperature T_p, loose their meaning as in the limit of large Δa the relaxation rate becomes T independent.

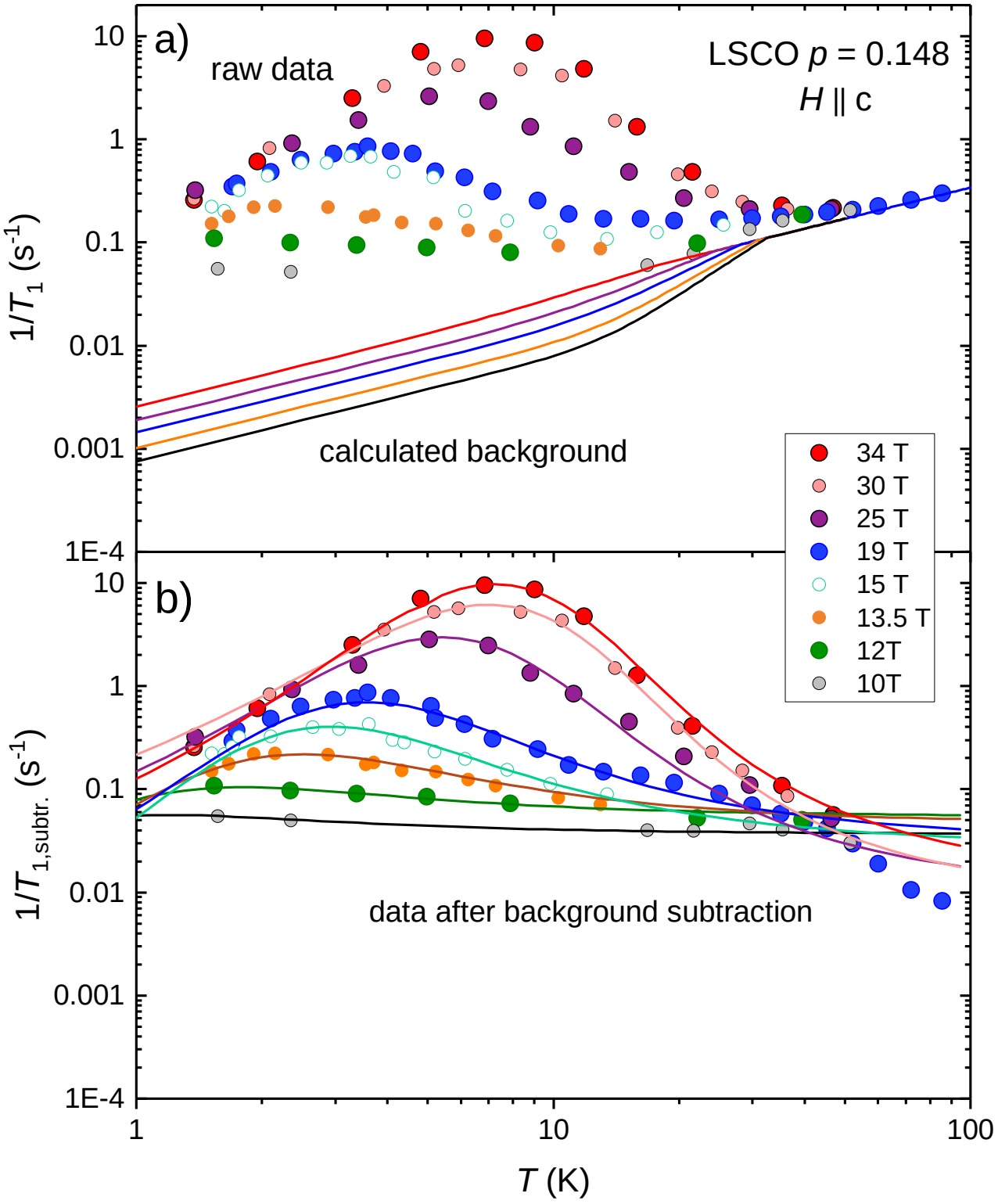

Figure 5.15: Top panel a): T dependence of $T_{1,\mathrm{stretch}}^{-1}$ for $10\,\mathrm{T} \leq B \leq 34\,\mathrm{T}$. Lines show the background described by eq. 5.7 for selected fields. Lower panel b): Data from a) after subtraction. The subtraction affects only the high T range. Lines are fits to the distributed BPP model given by eq. 5.8.

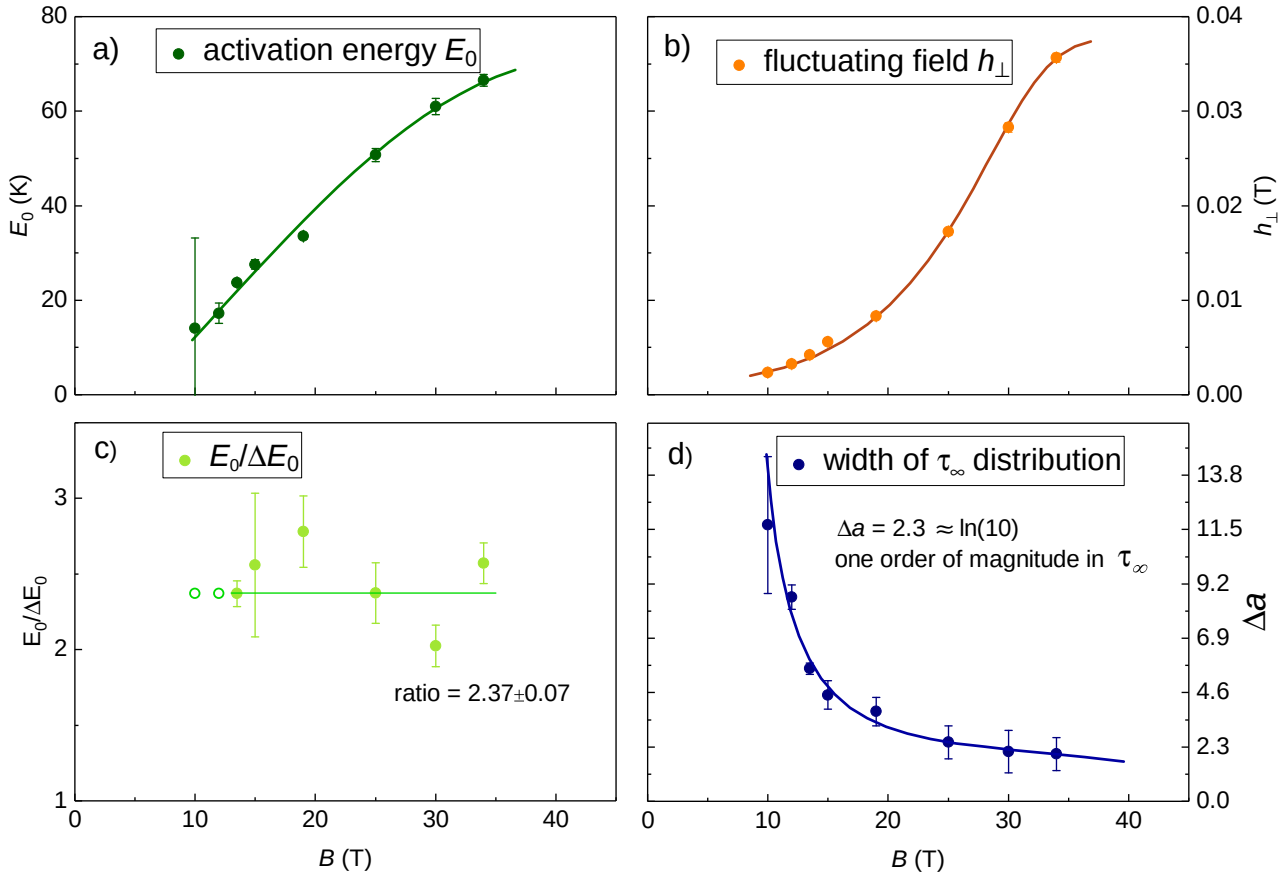

Figure 5.16: Field dependence of BPP fit-parameters to eq. 5.8. Fits for $B \geq 13.5$ are free, for $B \leq 12$ the constraint $E_0/\Delta E_0 = 2.37$ has been used. a): E_0 is the principal parameter to determine the peak temperature T_p. For $B = 10$ T $1/T_1(T)$ is flat, so T_p is ill-defined. This is reflected in the large error bar at 10 T. b): The fluctuating field increases rapidly with field. It fully determines the height of the peak. c): The ratio $E_0/\Delta E_0$ is nearly constant and can be fixed to 2.37 for low fields (empty symbols) as determined from the constant fit (green line). d): Rapidly increasing distribution of τ_∞ for decreasing B. The distribution increases by an order of magnitude as Δa increases by a factor of $2.3 \approx \ln 10$. At 10 T, τ_∞ is spread over 5 orders of magnitude. Lines in panels a), b) & d) are guides to the eye.

Discussion of the fitting results

After having shown that the BPP model with a distributed correlation time $\tau_c(T)$ can be used to model the experimental data, we discuss the meaning of the extracted parameters.

The difficulty in interpreting the field dependence of the fitting parameters comes from the fact that the classical BPP model has no intrinsic field dependence. The field only has an indirect effect through the frequency $\omega_L = \gamma B$. The T-dependence is fully captured by the slowing down of $\tau_c(T)$.

Applying BPP to a superconductor which is intrinsically field dependent can lead to field dependent parameters. This is especially the case if the spin-freezing feeds of the gradual suppression of the SC by the field. Then it is not solely the SC background that is B-dependent but the spin-freezing itself. However, SC is not only field but also temperature dependent. Thus, the parameters of the BPP model should also possess a T-dependence. Above T_c we expect no field dependence, so fitting with a B-dependent BPP model leads to the paradoxical result that, e.g. the fluctuating field is field dependent above T_c. To compensate this, all fitting parameters should have a T-dependence that makes them gradually field-independent as one approaches T_c from below. The reason that we can assume no T-dependence at fixed field is that $\tau_c(T) \propto e^{\frac{E_0}{T}}$ depends more dramatically on T than any other parameter and thus effectively masks their T-dependences. As abruptly as the contribution of $T_{1,\,\mathrm{BPP\,dist.}}^{-1}(T)$ to the total relaxation rate $T_1^{-1}(T)$ increases with cooling below T_c, it also falls off above T_c. The metallic background increases $T_1^{-1}(T)$ linearly with increasing T, so even if fluctuating fields still exist above T_c, they fluctuate so rapidly that they give no substantial contribution to the relaxation rate.

Thus, the T-independent BPP parameters can be seen as average quantities where the average is taken over the T range where glassy spin freezing contributes significantly to the total relaxation rate.

Interpretation of E_0 as spin stiffness

So far the parameter E_0 has been loosely called 'activation energy', in analogy to situations where E_0 corresponds to the energy barrier between a ground state with energy E_g and an excited state with energy $E_a = E_g + E_0$. Here the probability to be thermally excited is $p(a)/p(g) = e^{-\frac{E_0}{T}}$ and the transition rate $\tau_c^{-1} \propto e^{-\frac{E_0}{T}}$. From this perspective E_0 is the characteristic energy that is required to activate spin fluctuations.

Another way to arrive at an exponential correlation time is by comparing the BPP model with the predicted relaxation rate of the 2D Heisenberg AFM in the intermediate T regime, also called *renormalised classical*. Following Chakravarty and Orbach [207]:

$$\frac{1}{T_1} \propto \xi(T) \propto \exp(\frac{2\pi\rho_s}{T})\,, \tag{5.9}$$

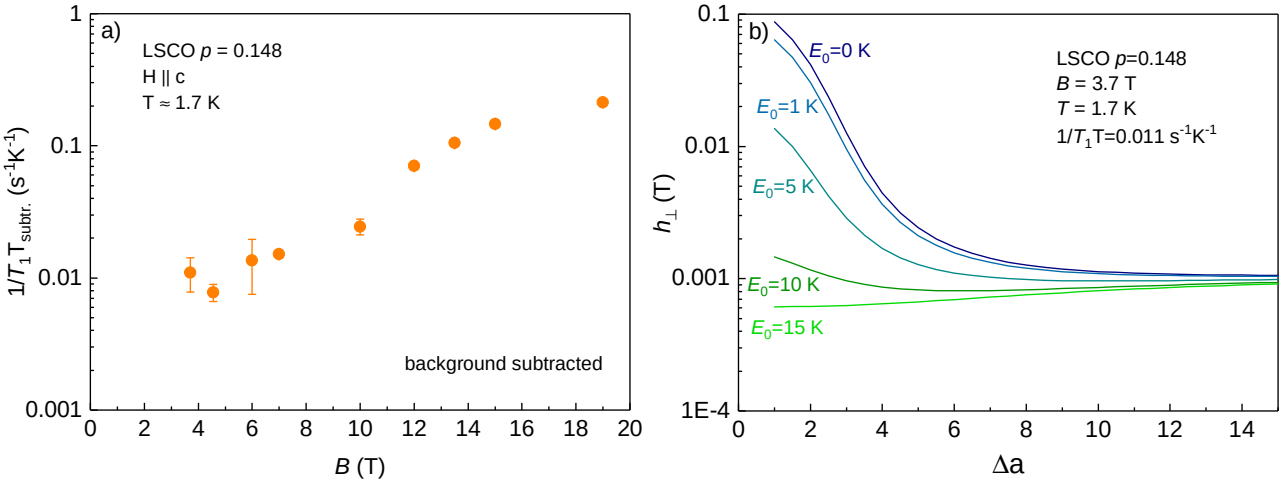

Figure 5.17: a): $1/T_1T$ of LSCO $p = 0.148$ after background subtraction at $T \approx 1.7$ K at low fields. b): Calculated $h_\perp$ for $1/T_1T = 0.011$ s^{-1}K^{-1} at 3.7 T for different E_0 as a function of Δa. In the limit of large Δa all curves merge, so $h_\perp(B)$ can be determined from a single relaxation time measurement.

where weaker T-dependences have been neglected. ρ_s is the spin stiffness and microscopically, ρ_s is proportional to the coupling J between neighbouring spins. $\xi(T) \propto \exp(\frac{2\pi\rho_s}{T})$ is found to describe the undoped parent compound LCO very accurately [208]. When T is large, as in the renormalised classical regime, then $\omega_L\tau_c \ll 1$ and the BPP model given by eq. 5.2 is simply proportional to $\tau_c = \tau_\infty \exp\frac{E_0}{T}$. Comparing this to eq. 5.9 allows to identify E_0 as $2\pi\rho_s$. With hole doping things become more complicated. The holes disrupt the AFM correlations and J is effectively reduced [209]. It is possible that similar but weaker correlations of a form as described by eq. 5.9 still exist for hole dopings of up to $p \sim 0.15$. Then E_0 is a measure of the planar coupling of neighbouring spins.
We interpret the increase of Δa, the width of the distribution of τ_∞, as a signature of the increasing inhomogeneity with decreasing field as strengthened SC takes the place of AFM correlations.

Scaling of fluctuating fields $h_\perp$ with ordered moments from neutron scattering

The energy at which magnetic fluctuations are probed by spin-lattice relaxation measurements in NMR, $\hbar\omega_L \sim \mu$eV, is much lower than the energy resolution of standard neutron scattering measurements (meV). Thus, the fluctuating fields $h_\perp$ that are determined from the BBP fits correspond to quasi-static ordered moments that would contribute to the elastic intensity in neutron scattering by $\boldsymbol{\mu}^2 \propto I_{NS}$.
Chang *et al.* have performed neutron scattering in their $p = 0.145$ sample up to only 13 T. At low fields, we do not have full T-dependences from which we could determine $h_\perp$ from BPP fits as at higher fields. Still, $h_\perp$ can be evaluated from the T_1-value at a single temperature because the large Δa leads to a very broad peak in $T_1^{-1}(T)$ that effectively becomes a T-independent constant. Fig. 5.17b shows indeed that the fluctuating field is independent of E_0 in the limit of large Δa.

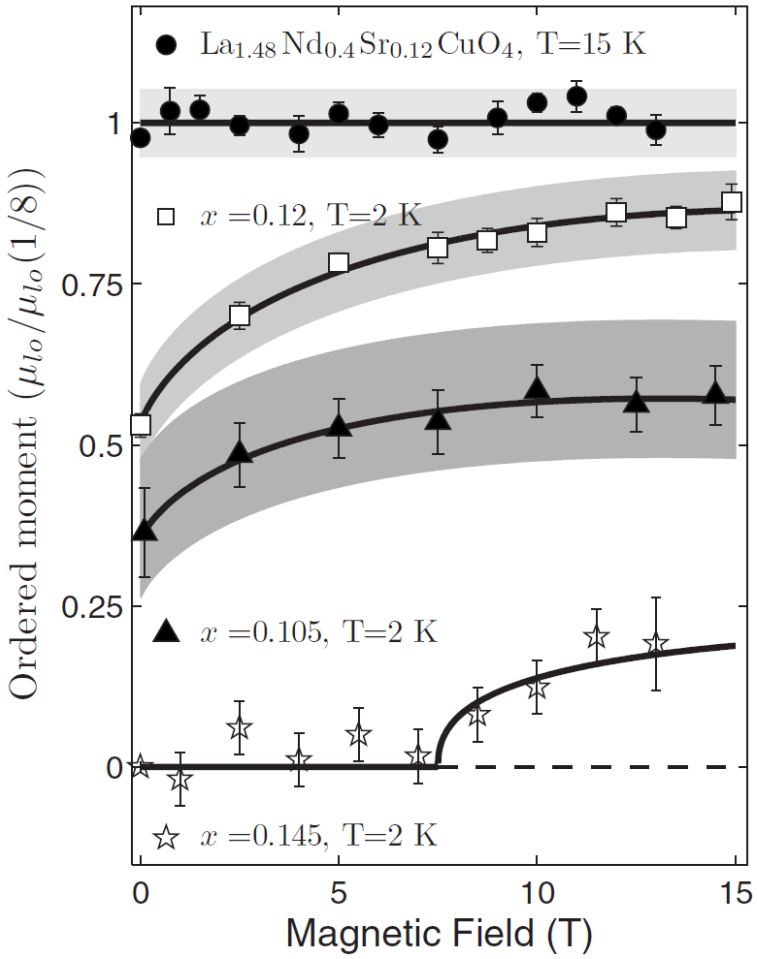

Figure 5.18: Field dependences of the ordered moment for LNSCO and three LSCO samples. The ordered moment $\boldsymbol{\mu} = \sqrt{I(H)}$ is determined from the scattering intensity $I(H)$ at Q_{IC}, the incommensurate AFM wave vector. The ordered moments at $x = 0.12$ and $x = 0.105$ are scaled by the moment of LNSCO ($\boldsymbol{\mu} = 0.36\,\mu_B$) and are fit to $\boldsymbol{\mu} \propto \sqrt{\frac{H}{H_c} \ln \frac{H_c}{H}}$. The data at $x = 0.145$ has no absolute scale. The line is a guide to the eye. This figure is reproduced from ref. [9].

From Fig. 5.16a) one can see that E_0 is continuously decreasing and $E_0 < 15$ K for $B < 12$ T. According to Fig. 5.16d all relaxation times for $B < 12$ T are in the large Δa limit.

We are able to compare the field dependence of fluctuating fields and ordered moments from NMR and neutron scattering over an extended range and find that they scale well, as shown in Fig. 5.19. As Chang *et al.* have also studied LSCO $p = 0.12$ as a function of field with neutron scattering and with μSR at zero field, they could determine the absolute value of the ordered moment. The neutron scattering data is reproduced in Fig. 5.18.

Using LSCO $p = 0.12$ data of Mitrovic *et al.* for which we find $h_\perp(14\,\mathrm{T}) = 0.040 \pm 0.001$ T we are able to assign a scale to the data for LSCO $p = 0.148$. We do not determine the ordered moment directly from the fluctuating field $h_\perp$ because the distributed BPP model is not be expected to be correct on a quantitative level, although it captures relative differences between samples or different

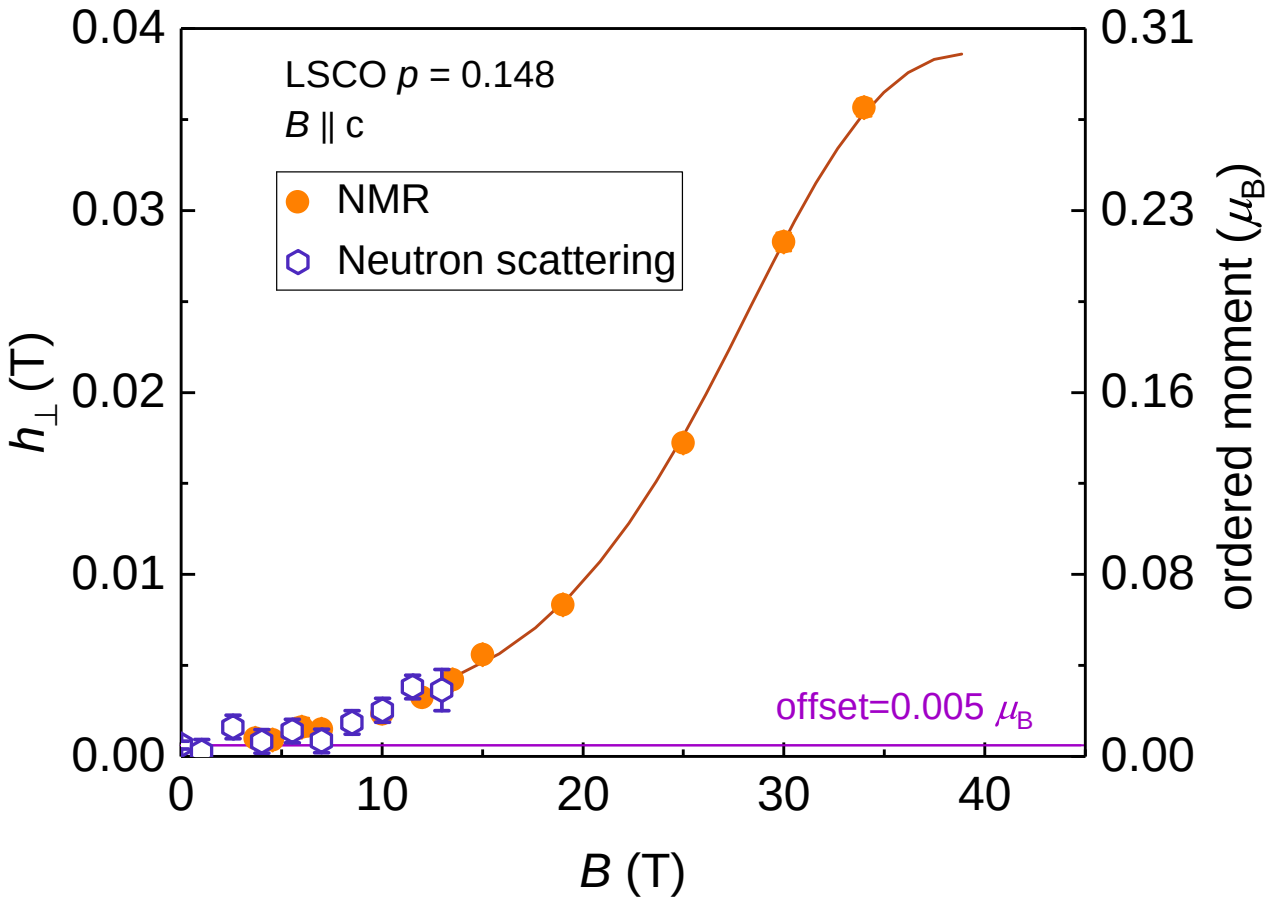

Figure 5.19: Comparison of the fluctuating field $h_\perp$ as determined by NMR with ordered moment determined by neutron scattering for LSCO $p = 0.148$. The right-hand scale of the ordered moment is determined from $h_\perp = 0.04$ T of LSCO $p = 0.12$ at 14 T which corresponds to 0.31 μ_B according to Chang *et al.*. Since they find that the ordered moment of $p = 0.12$ is nearly saturated at 14 T, we expect that the fluctuating field of the $p = 0.148$ sample cannot become higher than in the $p = 0.12$ sample, so our guide to the eye saturates at $h_\perp \sim 0.04$ T.

fields quite well. In addition, there is some uncertainty about the hyperfine coupling constant which is the proportionality factor between the local field and the moment.

The NMR data of Fig. 5.17a does not show an onset at $B = 7$ T. The fluctuating field is already non-zero at the lowest measured field, 3.7 T. In fact, from μSR Chang *et al.* could not exclude that the ordered moment at zero-field is as large as 0.005 μ_B, so we offset the neutron data by this value. The comparison in Fig. 5.19 suggests that there is a finite ordered moment in LSCO $p = 0.148$ in zero field. This is consistent with μSR data of Panagopoulos *et al.* [210]. For $p = 0.15$ an anomaly in the shape of the muon's relaxation time is still seen at very low temperatures which is ascribed to a glassy transition below 45 mK. In later work published in 2002 Panagopoulos *et al.* investigated this effect with Zn-doped LSCO and Y-doped Bi2212 and found that the muon relaxation is enhanced by Zn-doping up to $p \approx 0.19$ [211], so for an extended period of time there have been indications for magnetic

correlations at very low temperatures that persist up to the putative endpoint of the pseudogap [182]. Although the data suggests that $B = 7$ T does not correspond to a real onset field, both $h_\perp$ from NMR and the ordered moment from neutron scattering start to increase more rapidly in this field range. Consequently, we can identify $B \approx 7$ T as the field scale at which the signatures of AFM start to become apparent at $p = 0.148$. At 7 T we find $h_\perp = 0.0015$ T, so we define this value as the approximate detection limit of neutron scattering.

Summary LSCO $p = 0.148$

Using the BPP model with an exponential correlation time where both E_0 and τ_∞ are distributed we can fit the spin-lattice relaxation data at different fields. We extend the analysis to the lowest fields which allows to compare and scale the fluctuating field $h_\perp(B)$ with the ordered moment as determined from neutron scattering by Chang *et al.* [9].
The NMR data suggests that the ordered moment is increasing gradually as a function of field and that there might be already a small ordered moment in zero field at very low T. This result is consistent with μSR data of Panagopoulos *et al.* [210]. Thus, the sharp onset field of $\mu_0 H_c = 7$ T as determined from neutron scattering might be the result of an insufficient signal-to-noise ratio. Nevertheless, $B \approx 7$ T can identified as the field scale at which the signatures of AFM start to become most apparent.

5.7 LSCO $p = 0.155$

Gradually increasing the doping we turn to LSCO $p = 0.155$. Although the doping is only slightly higher, the relaxation rates at 19 T for $p = 0.155$ are an order of magnitude smaller than for the $p = 0.148$ at the same field. But still, the relaxation rate is clearly enhanced above the constant background. This sample has not yet been investigated in fields higher than 19 T. Still, we can extract the fluctuating fields from data up to 19 T.

Fig. 5.20a shows $T_1^{-1}(T)$ at 19 T down to 1.7 K. The BPP fit suggests that a peak would become visible either by decreasing the T or increasing the field. According to the fit, the peak is very flat. So, as for the low field regime of LSCO $p = 0.148$, we can extract the fluctuating field from the $1/T_1T$ data at the lowest accessible T of ≈ 1.7 K, shown in Fig. 5.20b. $1/T_1T$ has an upturn at low field. This effect is expected from the standard BPP model: As the fluctuating field becomes approximately constant at low field the relaxation rate increases at low fields because the peak scales with $1/\omega_L$. This effect is also visible in Fig. 5.17 for LSCO $p = 0.148$.
Fig. 5.22 compares the fluctuating fields for $p = 0.148$, $p = 0.155$ and $p = 0.171$. The fluctuating fields has a similar field dependence for $p = 0.148$ and $p = 0.155$, if shifted by 8.3 T, so the field scale has increased by this value. In analogy to $p = 0.148$, we expect that neutron scattering at low T of a

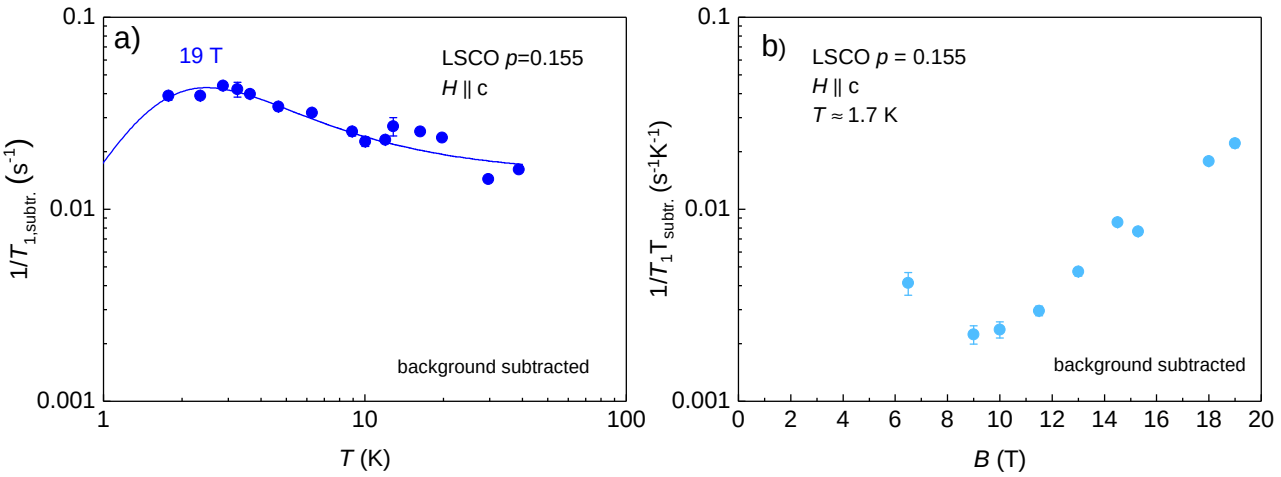

Figure 5.20: a): $1/T_1$ of LSCO $p = 0.155$ after subtraction of the calculated background given by eq. 5.7. The line is a distributed BPP fit with $E_0 = 23$ K & $\Delta a = 7$. b): $1/T_1T$ of LSCO $p = 0.148$ after background subtraction at $T \approx 1.7$ K at low fields.

$p = 0.155$ sample would detect an AFM signal at about 15.3 T.

5.8 LSCO $p = 0.171$

If the field scale increased by 8.3 T between $p = 0.148$ and $p = 0.155$, *i.e.* by about 12 T per percent of doping, then the field scale should increase by another 19 T when going to $p = 0.171$. For $p = 0.148$ we started to see a peak in $T_1^{-1}(T)$ above 12 T. The necessary field would thus lie above 39 T at $p = 0.171$. Static fields up to 45 T can be reached at NHMFL, so we went to Tallahassee to look for signatures of spin freezing in LSCO $p = 0.171$ with the help of Arneil Reyes and Sanath Kumar Rama Krishna.

Fig. 5.21a summarises raw $1/T_1T$ at different fields. Measurements up to 34 T have been performed in LNCMI Grenoble.

Although there is strong enhancement of the relaxation rate at 44.7 T, we do not see a peak down to 1.5 K. From the perspective of BPP, seeing a peak at high field becomes more difficult since the peak height is proportional to $1/\omega_L$. However, assuming that Δa is large, we can determine the fluctuating field responsible for the enhancement of the relaxation rate.

We find that the fluctuating field of LSCO $p = 0.171$ has a similar finite value of ≈ 0.6 mT in the low field limit, as for the other samples. This value corresponds to a moment of 0.005 μ_B in neutron scattering. The field dependence of all samples is similar, which suggests that the growth of the fluctuating field is determined by the same mechanism for all samples, with a field scale that increases approximately linearly with doping. This is consistent with the speculative phase diagram proposed by Chang *et al.* [9], reproduced in Fig. 5.23a.

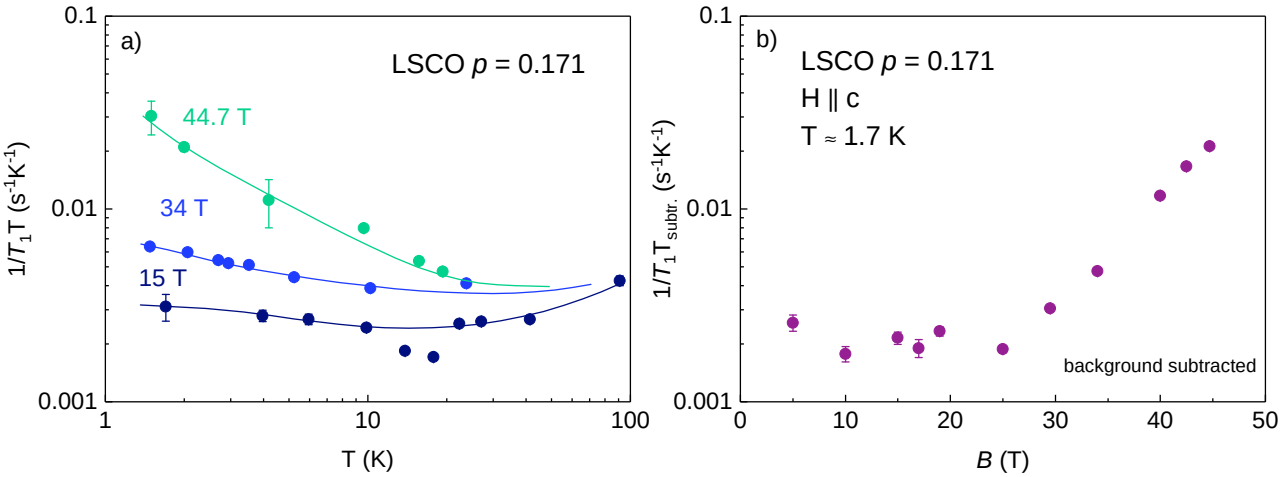

Figure 5.21: a): Unsubtracted raw $1/T_1T$ of LSCO $p = 0.171$. The lines are guides to the eye. The small dip around 20 K at 15 T could be due to the vortex melting transition. Large error bars at 44.7 T are due to problems with T-stabilisation. b): $1/T_1T$ of LSCO $p = 0.171$ after background subtraction at $T \approx 1.7$ K.

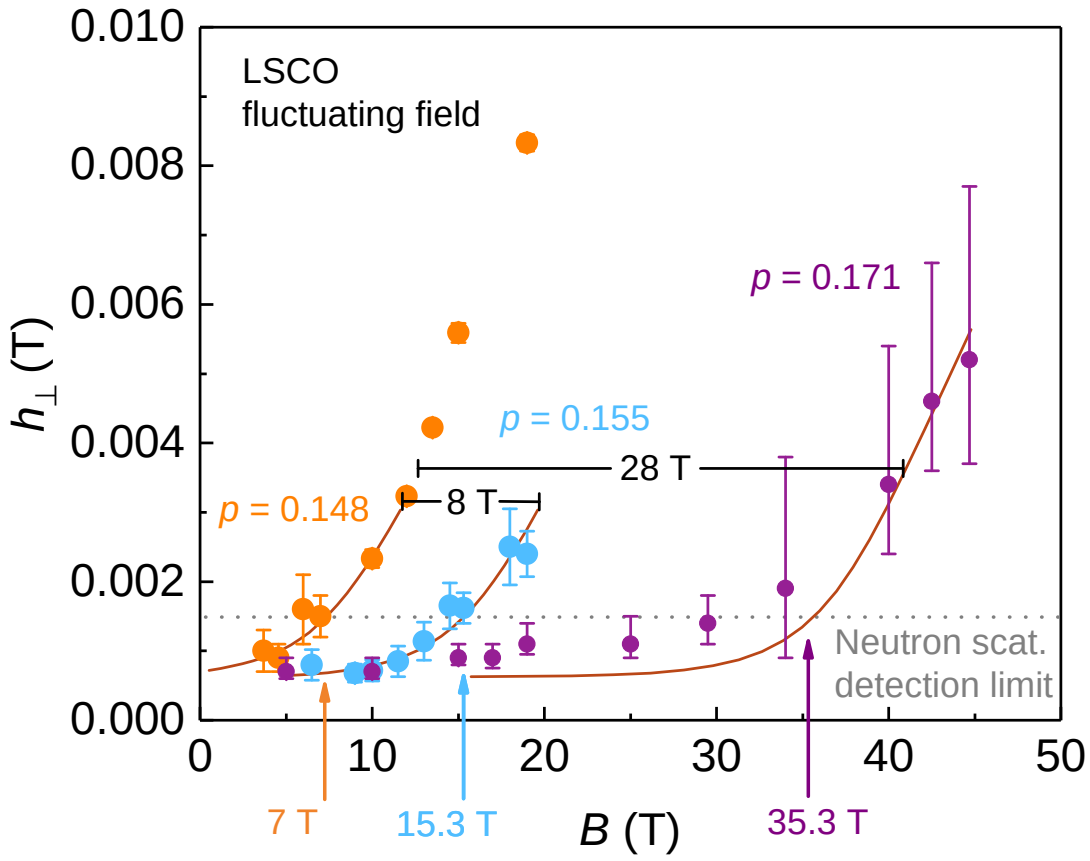

Figure 5.22: Comparison of fluctuating fields for LSCO $p = 0.148$, $p = 0.155$ & $p = 0.171$. Continuous lines are identical guides to the eye, horizontally offset by about 8 T and 28 T. From NMR there is no onset field for $h_\perp$ but in neutron scattering by Chang *et al.* in their $p = 0.145$ sample a moment is detected above 7 T. In $p = 0.148$, at 7 T we find $h_\perp = 0.0015$ T, so we use this value to define the corresponding field scale for $p = 0.155$ and $p = 0.171$. It is the point, marked by an arrow, where the guide to the eye crosses the dotted line.

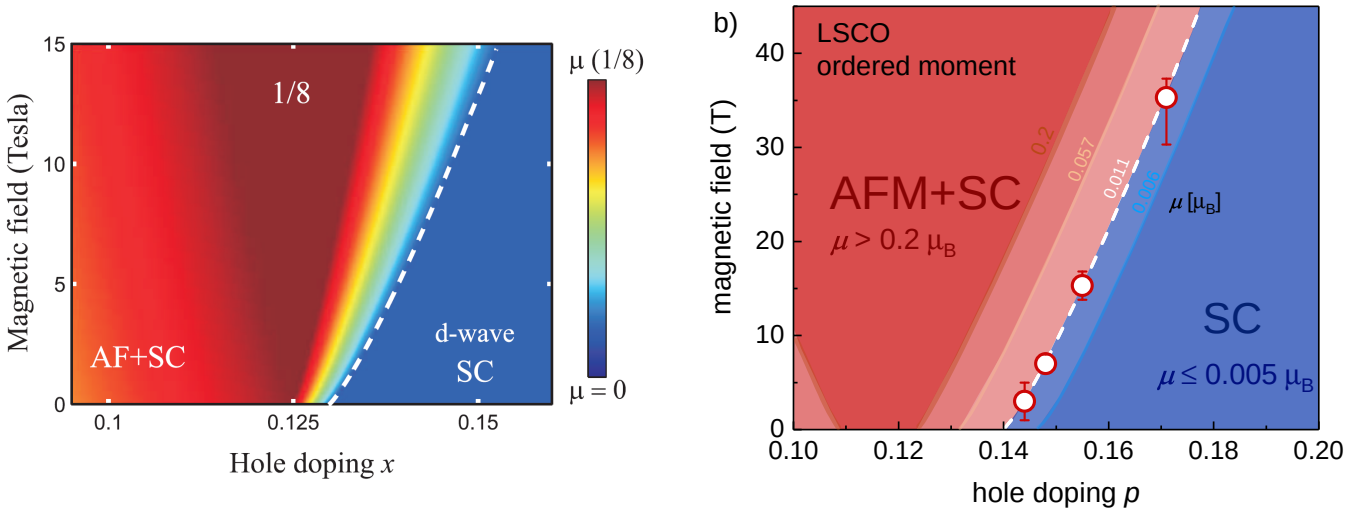

Figure 5.23: a): False colour plot of the ordered moment μ scaled by $\mu(1/8)$ of LNSCO $p = 0.125$ in the doping-field phase diagram reproduced from Chang *et al.* [9]. The white dashed line separates the AFM+SC phase where the ordered moment is large (red colour) and the d-wave SC phase, where there is no moment (blue colour). b): Doping-field phase diagram based on LSCO data only, summarised in the main text. White circles correspond to the onset field at 3 T at $p = 0.144$, as reported by Khaykovich *et al.*, and to the field scale where $h_\perp(B)$ increases above ≈1.5 mT in Fig. 5.22 (corresponding to ordered moment $\boldsymbol{\mu} > 0.011\,\mu_B$ in neutron scattering). Data points are connected by a white dashed line. In this doping range SC extends up to about 45 T. Dark red region corresponds to $h_\perp(B) > 0.026$ T (corresponding to $\boldsymbol{\mu} > 0.2\,\mu_B$). Light red colours correspond to smaller moments.

Inspired by this plot, in Fig. 5.23b we summarise the joint results in LSCO from the neutron scattering study of Khaykovich *et al.* [10] at $p = 0.144$, μSR + neutron scattering at $0.105 \leq p \leq 0.145$ of Chang *et al.* and $h_\perp$ from NMR for $0.148 \leq p \leq 0.171$ presented in this chapter, as well as $h_\perp$ determined from published NMR data of Julien *et al.* at $p = 0.10$ [197], Mitrović *et al.* at $p = 0.12$ [178] and Arsenault *et al.* at $p = 0.115$ [180]. From LSCO $p = 0.12$ at 14 T we found that the proportionality factor between $h_\perp$ and the ordered moment $\boldsymbol{\mu}$ from neutron scattering is $\frac{0.31}{0.04} = 7.75\,\mu_B/\mathrm{T}$. This allows us to convert $h_\perp$ into corresponding moments for direct comparison with ordered moments from neutron scattering. There are small differences between both plots: In LSCO, the ordered moment is strongest at $p = 0.115$, not at $p = 1/8$. This is consistent with the depression in T_c being most pronounced at $p = 0.115$, as well as T_g being largest at $0.115 \leq p \leq 0.12$, see Fig. 5.6. Thus, the dashed line is not identical in both plots, but it has a similar almost linear doping dependence.

5.9 LSCO $p = 0.21$

We have studied the relaxation rate in a sample with $p = 0.21$. The analysis of the relaxation rate is more complicated for this sample since the structural transition occurs at $T_s = 6 \pm 10$ K. Thus, the

relaxation rate can potentially have three different contributions: Some non-freezing background that is gapped by SC, quadrupolar relaxation due to the structural transition and potentially a contribution from glassy magnetism. In the following we argue that the possible contribution from glassy magnetism most be very small. Measurements in fields above 15 T have been performed at NHMFL by Rui Zhou.

Fig. 5.24 shows the field and temperature dependence of $1/T_1T$. The field dependence of $p = 0.21$ differs from other samples since $1/T_1T$ saturates at about 40 T, which suggests that SC has been suppressed. $\mu_0 H_{c2}(T = 0)$ is estimated to be 45 T [189]. A field-independent relaxation rate is not expected from BPP. Most likely, the growth of $1/T_1T$ is due to the growth of the gapped background as SC is gradually removed.

The T-dependence in Fig. 5.24c shows that $1/T_1T$ is always increasing with cooling, already far above T_s, so we do not find a well defined constant background. However, for $T > 100$ K it is not clear which other mechanism could contribute to the relaxation, so we estimate $\frac{1}{T_1T}_{\text{backgr.}} = 0.005 \pm 0.001$ s^{-1}K^{-1}. The T_1 exponent starts to decrease below 100 K, which is consistent with a gradual onset of quadrupolar fluctuations, so the increase of $1/T_1T$ by 0.002 ± 0.001 s^{-1}K^{-1} can be essentially explained by quadrupolar fluctuations due to the structural transition. There are two arguments for this:

Firstly, the structural transition is not driven by SC. It occurs at much higher T than T_c at lower dopings. Thus, we expect that the quadrupolar fluctuations are unaffected by SC and are not gapped. Fig. 5.24b shows, that by subtracting the calculated background at 15 T using eq. 5.7 one reveals a remaining contribution that is largest close to T_s, which we identified by the minimum of the T_1 exponent β. This contribution is likely to come from quadrupole fluctuations, although it could include some glassy magnetic relaxation. The uncertainty about the size of the quadrupolar contribution is large since eq. 5.7 is based on a very simple model.

Secondly, the low T stretch exponent is nearly identical at 15 T in the SC state and at 40 T and above, where SC has been suppressed. This means that the minimum of the stretch exponent must be determined by a relaxation process that is field independent.

However, $1/T_1T$ appears to increase by about 0.001 s^{-1}K^{-1} below T_s. This change is close to the limit of our experimental precision, but instead of neglecting it we can estimate how large the fluctuating field would be, provided this increase is due to glassy magnetic relaxation. Assuming that Δa is large, we find $h_\perp = 0.7$ mT. This value is below the threshold of field-induced magnetism that we defined at lower doping. So within our model, we can exclude that there is any significant ordered moment in LSCO $p = 0.21$, even when SC is completely removed.

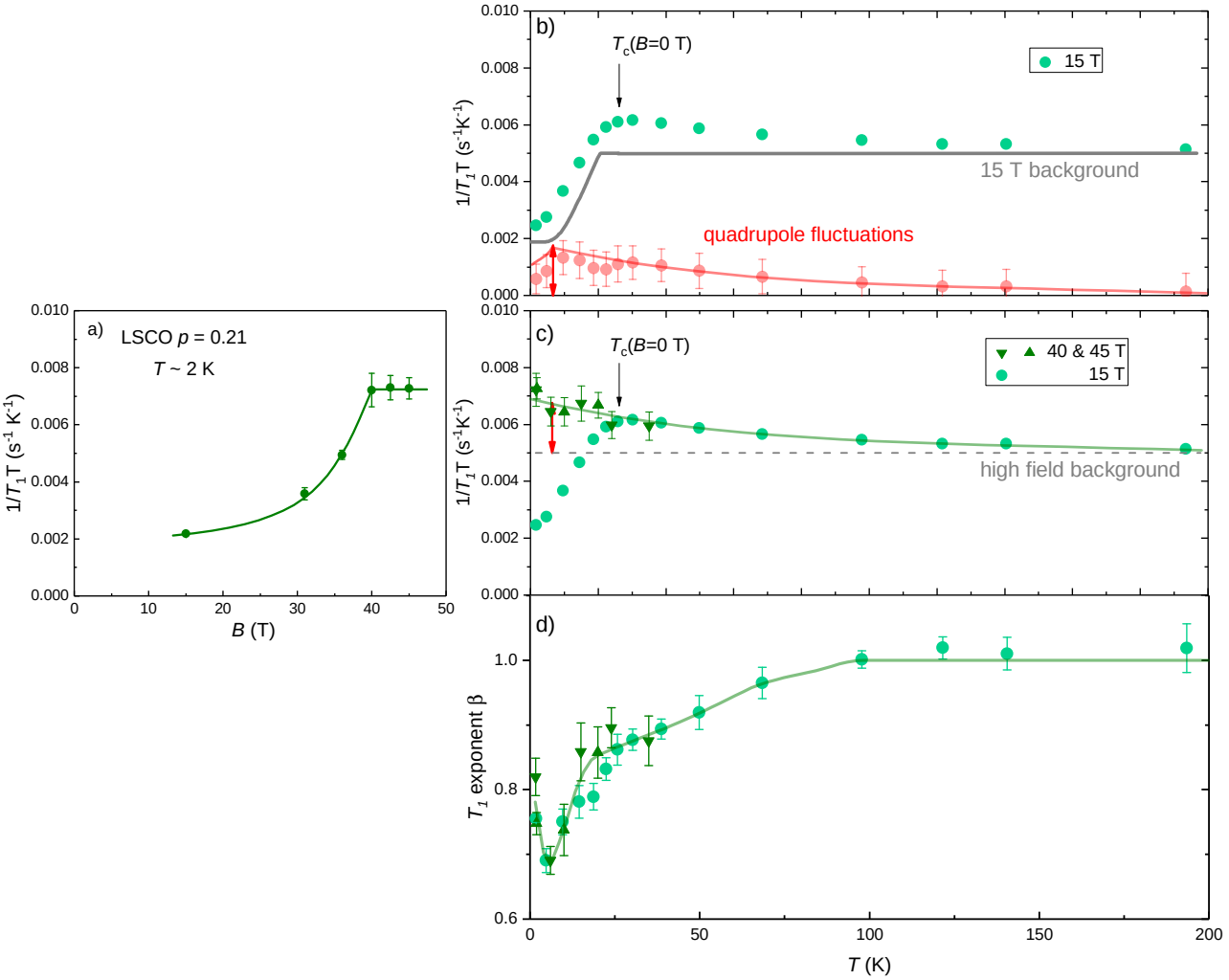

Figure 5.24: a): Field dependence of $1/T_1T$ of LSCO $p = 0.21$ at ≈ 2 K. The line is a guide to the eye. b): T dependence of $1/T_1T$ of $p = 0.21$ at 15 T (green circles). The continuous grey line is the calculated background at 15 T. This background is subtracted from $1/T_1T$ at 15 T to reveal the quadrupole fluctuations (red circles) that peak close to $T_s = 6$ K which is determined from the minimum of the stretch exponent in d). The red arrow marks the amplitude of the quadrupole fluctuations at T_s. c) & d): Green symbols: T dependence of $1/T_1T$ of $p = 0.21$ at 15 T and in 40 & 45 T at low T to suppress SC and their corresponding stretch exponents in panel c). The green lines are guides to the eye, the dashed grey line is the constant metallic background. Same red arrows as in b) shows that the amplitude of the quadrupole fluctuations is of the same order as the increase of $1/T_1T$ at low T.

5.10 Discussion

Width and T_2

In this chapter the focus has been on measurements of the spin-lattice relaxation rate of LSCO in the doping range from $p = 12$ to $p = 0.21$ which has allowed to determine the AFM ordered moment. Neither peak widths nor spin-spin relaxation rates ($1/T_2$) have been mentioned, although both are in principle sensitive to the presence of an ordered moment and could serve to corroborate the spin-lattice relaxation results. In practice, both quantities are not very sensitive to AFM ordering since the ordered moments are oriented in the plane. Thus the peak width and $1/T_2$ couple to the ordered moment only through off-diagonal elements of the hyperfine coupling tensor when the external field is applied along the $\boldsymbol{c}$-axis. However, we cannot study the same physics with the field in the CuO_2-plane because this does not suppress SC sufficiently to enhance the AFM ordering.

However, in LSCO $p = 0.115$ ordered moments exist in zero field, so measurements with $H \perp c$ are possible. Arsenault *et al.* have studied the linewidth in detail an found that while $H \parallel c$ leads to a subtle broadening with cooling, $H \perp c$ leads to a small splitting of the central peak at low T [180]. Strong broadening of the NQR peaks in zero field has also been observed by Ohsugi around $p = 0.115$ [181]. Since our relaxation rate data at $p = 0.148$ in high field is qualitatively very similar to data of Arsenault *et al.* at $p = 0.115$[5], it is highly probable that moments in the field-induced ordered are also aligned in the CuO_2-planes. We only determine the average size of $h_\perp$. Thus, our measurements are consistent with any commensurate or incommensurate modulations of the spin density, as well as the broad hyperfine field distribution that has been inferred from the low T ^{63}Cu-NQR spectrum of LBCO $p = 0.125$ by Hunt *et al.* [212].

To gain insight into the form of the distribution of $h_\perp$ we need to fit the full relaxation curves, not only the median $1/T_1$. This would allow to extract information that is encoded in the stretch exponent β. This procedure has been attempted but not concluded at the stage of writing this manuscript.

Field-induced or field-enhanced?

From neutron scattering and μSR of LSCO $p = 0.145$ Chang *et al.* concluded that there is field-induced AFM order above an onset field of $\mu_0 H_c = 7$ T [9]. The fluctuating field from NMR shows no onset field at 7 T. Instead, there is a gradual enhancement of the fluctuating field. However, 7 T can be identified as the field scale where the fluctuating field starts to increase rapidly with field. Thus, the principal conclusions of Chang *et al.* are confirmed by NMR up to higher fields and higher dopings, as

[5] Fitting $p = 0.115$ with $\mu_0 H \perp c$ of 9 T with the distributed BPP model gives $h_\perp = 0.041$ T (0.036 T), $E_0 = 90.5$ K (66.5 K) and $\Delta E_0 = 54$ K (26 K), where values in parentheses ( ) correspond to $p = 0.148$ at 34 T.

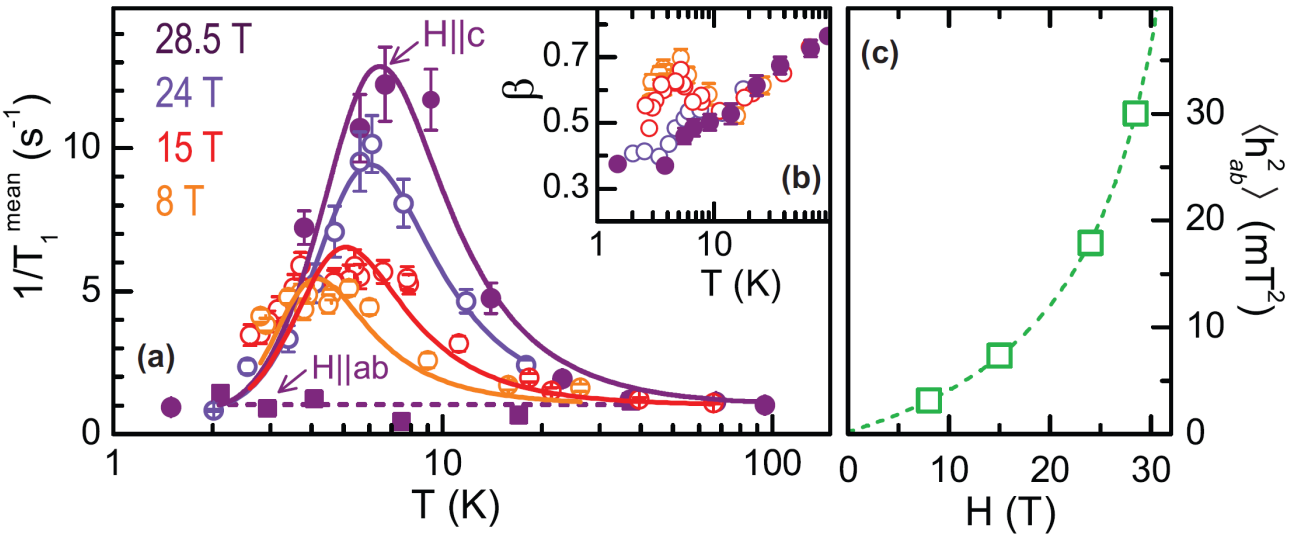

Figure 5.25: a): Peak in ^{63}Cu $1/T_1$ of YBCO 6.45 $p = 0.08$ at different fields. Lines are simple BPP fits with identical correlation times $\tau_c(T)$. Note that $H \parallel$ ab gives no visible peak. Inset b): Stretch exponent β at different fields signaling a distributed relaxation rate. c): Field dependence of the fluctuating field $h_{ab} = h_\perp$. The line is a guide to the eye. This figure has been reproduced from ref. [213].

summarised in Fig. 5.23b.

Comparison to other cuprates

It has been mentioned before that Panagopoulos *et al.* have performed μSR measurements in Bi-2201 and Zn-doped YBCO where they find very similar spin freezing as in LSCO with a similar doping dependence at low T [211].

Field enhanced magnetism is also found in YBCO: Haug *et al.* have performed neutron scattering in magnetic fields with YBCO6.35 and YBCO6.45 and found that particularly for YBCO6.45 the scattering intensity at the AFM wave vector is enhanced with increasing magnetic field. Wu *et al.* have shown that the field enhanced magnetism found in YBCO6.45 (p=0.08) is glassy [213]. They studied the field dependence of ^{63}Cu spin-lattice relaxation rate and showed that a broad peak grows with field, with an increasing peak temperature that follows the frequency dependence as expected from a simple BPP model.

This work is important, because it was able to disentangle the effects of field and frequency: While the increased peak height signals that the glassy magnetism is intrinsically enhanced by the field, the increase of the peak temperature is a result of the shorter time-scale ω_L^{-1}. This showed that it is the shorter time-scale of neutron scattering that is responsible for systematically higher onset temperatures for glassy magnetic ordering in neutron scattering compared to low-frequency probes like μSR, NQR & NMR.

A puzzling question concerning the glassy magnetism in YBCO is why it happens to end so abruptly

at $p = 0.08$ [214], the doping where charge order appears. Field-induced magnetic order has been excluded by Wu *et al.* around $p = 0.12$ down to 1.5 K and fields that surpass H_{c2} [13]. Magnetic ordering could occur at $T < 1.5$ K but the principal question, why magnetic order is so much stronger in LSCO, would still need an answer.

p^* and the pseudogap

In this chapter, we have shown that magnetic fields are able to induce a frozen, or nearly frozen, magnetic state in $La_{2-x}Sr_xCuO_4$ at doping levels much higher than hitherto believed: for fields of the order of the upper critical field H_{c2}, field-dependent spin fluctuations can be detected up to the doping level that marks the pseudogap boundary at $p \approx 0.18$ but not, or not far, beyond.

The immediate implication of this result is that great care should be taken when interpreting data from measurements performed in high fields. Among these, recent transport measurements in LSCO have been interpreted in terms of a sharp change in the number of carriers across the critical doping for the pseudogap phase located at $p^* = 0.18$ [3]. Given that the frozen state is not a spin-glass with randomly oriented moments but rather a (disordered) incommensurate antiferromagnet, it is likely that the Fermi surface is reconstructed into small pockets in high fields, thus translating into a small number of effective carriers. Indeed, calculations based on such an antiferromagnetic scenario appear able to explain the transport data [215, 216]. It should also be pointed out that the Fermi surface might already undergo reconstruction as soon as magnetic moments appear to be static on the time scale of the period of quasiparticle Fermi-surface orbits in high fields, typically $\frac{2\pi}{\omega_c} \sim 10^{-12}$ s, where ω_c is the cyclotron frequency [217]. Therefore, moments need not to be strictly frozen at the NMR timescale to provide a sensible explanation.

Evidence for a change in carrier density is not restricted to LSCO. Similar transport results have been obtained in YBCO [4], but again in very high fields, so it cannot be excluded that, there also, glassy freezing can be induced by fields of the order of H_{c2} on approaching p^*. If we take as a criterion the typical field at which moments appear static in a standard neutron scattering experiment (7 T for $p = 0.148$ in LSCO), we see from Fig. 5.23b that this should be ∼35 T for our $p = 0.171$ sample, which is about $0.7\,\mu_0 H_{c2}$ for this concentration. This suggests that close to p^*, clearly detecting field-induced spin freezing requires fields which are a significant fraction of H_{c2}. With $\mu_0 H_{c2} \sim 150$ T near $p^* = 0.19$ in YBCO, fields in excess of 100 T would be needed to have an experimental signature of slow spin fluctuations. Quite a challenge for NMR!

The last piece of evidence for a change in carrier density comes from transport measurements in Nd-doped LSCO [218, 219]. There, however, because the stripe instability is much stronger than in LSCO, glassy spin freezing is present up to $p^* = 0.23$ already in zero-field. Therefore, even if the field can

enhance moments in Nd-LSCO, translational symmetry is already broken in zero-field and transport results are likely to become quite insensitive to the field strength. So, these results are not inconsistent with the possibility that the change of carrier density is due to magnetic order and that it is field-induced when not present in zero-field.

These considerations bring us to two important questions: firstly, if spin freezing is field-induced does this mean that these results tell us nothing about the ground state of the pseudogap phase in zero-field? It is difficult to answer this question. Certainly, the putative pseudogap quantum critical point inferred from effective mass enhancement seen in quantum oscillations [95] and specific heat measurements [220] cannot be a standard antiferromagnetic quantum critical point as found in heavy fermions [221] or in the pnictides [222] because T^* does not correspond to T_N in cuprates. As recently discussed by Tranquada and coworkers, the neutron scattering data in zero-field are not consistent with quantum critical behavior of the low-energy spin fluctuations [223], which is actually consistent with the smooth evolution of $1/T_1$ on Cu across p^* [202, 179]. However, we believe that one cannot exclude the possibility that the slowing down of spin fluctuations is already present in zero field but actually starting at temperatures below those used in neutron scattering or NMR experiments, so far (typically 4 K to 1.5 K). As mentioned above, Panagopoulos *et al.* claim that magnetic order onsets at 45 mK for LSCO $p = 0.15$ in zero field [210]. So, it is possible that the field only *resurrects* the spin freezing that was hidden at very low temperatures. That we see a gradual enhancement of low-energy spin fluctuations with increasing field and no sharp transition may actually be consistent with such a viewpoint. Therefore, it is conceivable that the pseudogap state corresponds to peculiar spin correlations that ultimately freeze out at low temperatures. Our results thus urge for experimental investigations of spin dynamics at mK temperatures.

Charge order

The second important question raised by our results is whether the glassy magnetic order is the primary competitor of superconductivity or whether the primary order is a charge-density wave that subsequently triggers magnetic freezing. This second option would comply with the widely accepted view that glassy freezing near $p = 0.12$ is a consequence of charge-stripe order in La-based cuprates. Until recently, there was only evidence for CDW correlations in LSCO for $0.11 \leq p \leq 0.13$ in zero field [66] but very recent experiments by Wen *et al.* at SLAC in Stanford have finally been able to detect them up to $p = 0.16$ [6]. Because the CDW correlations discovered by Wen *et al.* at $p = 0.144$ and $p = 0.16$ are partially quenched by the onset of superconductivity [6], they are likely to be enhanced by a magnetic field applied along the $\boldsymbol{c}$-axis. Therefore, it possible that the spin-frozen

ground state is, in turn, a consequence of the presence of CDW correlations. However, in the absence of direct experimental evidence of field-enhanced CDW correlations in slightly overdoped LSCO we cannot exclude the first option above in which spin-freezing would be an independent phenomenon. Our results evidently urge for X-ray scattering investigations in high magnetic fields.

5.11 Summary

This chapter was focused on the spin-lattice relaxation rate $1/T_1$ of LSCO in the doping range for $p \geq 0.10$. Measurements of $1/T_1$ in high magnetic fields for $0.148 \leq p \leq 0.21$ show that magnetic fields are able to induce a frozen, or nearly frozen, magnetic state up to unexpectedly high doping levels. The data is analysed using the Bloembergen-Purcell-Pound (BPP) model with distributed correlation times. An important parameter of this model is the fluctuating field $h_\perp$ which is proportional to the strength of anti-ferromagnetic (AFM) order. The model describes the data on a qualitative level but the field and doping dependence of the fluctuating fields can be compared on a semi-quantitative level to ordered moments as determined from μSR and neutron scattering.

Magnetic field is found to enhance $h_\perp$. While being very small in zero field, $h_\perp$ of $p = 0.148$ grows dramatically in high fields where it attains the same order of magnitude as in LSCO $p = 0.12$. The enhancement of $h_\perp$ is found in dopings up to $p = 0.171$. At $p = 0.21$ no evidence of significant AFM order is found. This result has implications for transport measurements in high fields that localise the endpoint of the pseudogap at $p^* = 0.18$. It suggests that slow spin fluctuations might lead to a reconstruction of the Fermi surface. However, an important question that remains is whether magnetic field reveals a property of the normal state that might be hidden at low T or whether the spin order close to p^* is absent in zero field down to low T and is a phenomenon purely induced by magnetic field.

Conclusion and outlook

Since the summaries of each chapter already contain conclusions and the principal results, here a more general conclusion shall be made which allows a wider scope for the outlook.

One conclusion from high field studies of cuprates is the following: Looking back, it has occurred repeatedly that the application of high field allowed to discover a phenomenon that would later be confirmed to be a zero-field property. An example of this has been presented in case of STM in magnetic field by Hoffman *et al.* [11] which revealed a periodic modulation of the LDOS in $Bi_2Sr_2CaCu_2O_{8+\delta}$. The same modulation was shortly thereafter confirmed in zero field by Howald *et al.* [12]. Similarly, the initial discovery of the field-induced long-ranged CDW in YBCO by Wu *et al.* [13] has preceded the finding of short-range charge order in zero field using XRD [14, 15]. In these examples the field-induced vortex halos metaphorically act as magnifying glasses of short-ranged orderings that can be easily overlooked otherwise. Whether this is also the case for spin order in LSCO close to the endpoint of the pseudogap remains to be seen. From existing neutron scattering data, *e.g.* by Lake *et al.* [8] at $p = 0.163$, it is difficult to exclude that static order of small amplitude exists in zero field, potentially at lower T than investigated so far. Whether the order could be sufficiently strong to reconstruct the Fermi-surface is another question.

The order found in high fields is also interesting in its own right since having a longer correlation length and a larger amplitude it will be less sensitive to effects like disorder that could mask behaviour of the pure system which is more easily studied theoretically or in numerical simulations.

The complementarity of zero field and high field studies can be extended in both directions. The extension towards pulsed fields up to 100 T is evident, as pulsed fields have been essential in discovering the Fermi-surface reconstruction in YBCO [16]. Since higher fields lead to longer correlation lengths, the opposite direction would be towards shorter correlation lengths. Shorter correlation lengths are expected for fluctuating spin or charge correlations which are also important as AFM fluctuations are thought to lead to Cooper pairing in cuprates.

Appendix A

Justification for the distributed BPP model

After having introduced the distributed BPP model it has been mentioned that fitting the experimental $\frac{1}{T_1}_{\text{stretch}}(T)$ by eq. 5.6 could be wrong since the way in which $T^{-1}_{1,\,\text{distributed BPP}}(T)$ is constructed, is a mean relaxation rate, while $\frac{1}{T_1}_{\text{stretch}}(T)$ corresponds to the median relaxation rate. Where lies the problem?

Experimentally we find that the relaxation rate is distributed at any T where $\beta < 1$. However we do not know the underlying experimental distribution. What we are looking for is a set of parameters (E_0, ΔE_0, $h_\perp$, τ_∞ & Δa) from which we can calculate a model distribution which describes the experimental distribution of relaxation rates sufficiently well that we can reproduce the T-dependence of $\frac{1}{T_1}_{\text{stretch}}(T)$ at any T. The experimental distribution changes with T: Its form changes such that the median relaxation rate eventually develops a peak with cooling and also β has a non-monotonic T-dependence. To model this we need the median, but calculating the median of a model distribution is complicated: For this a histogram of the model distribution of relaxation rates has to be constructed whose median is evaluated numerically. This process has to be embedded in an automated fitting routine which finds the best set of model parameters. Computationally, this is a difficult task that we do not know how to solve efficiently.

However, we know how to calculate the mean relaxation rate because it is only an integral, as shown in eq. 5.6 and eq. 5.8 and it is easily implemented in a fitting routine in *Mathematica*. As mentioned, the mean relaxation rate calculated from the model distribution depends only on the average fluctuating field, so an advantage of the mean relaxation rate is that we do not need to assume a specific distribution of fluctuating fields. This would be necessary if we wanted to calculate the histogram of the model distribution of relaxation rates.

Thus, what we have are two distributions whose exact form we do not know: First, the experimental

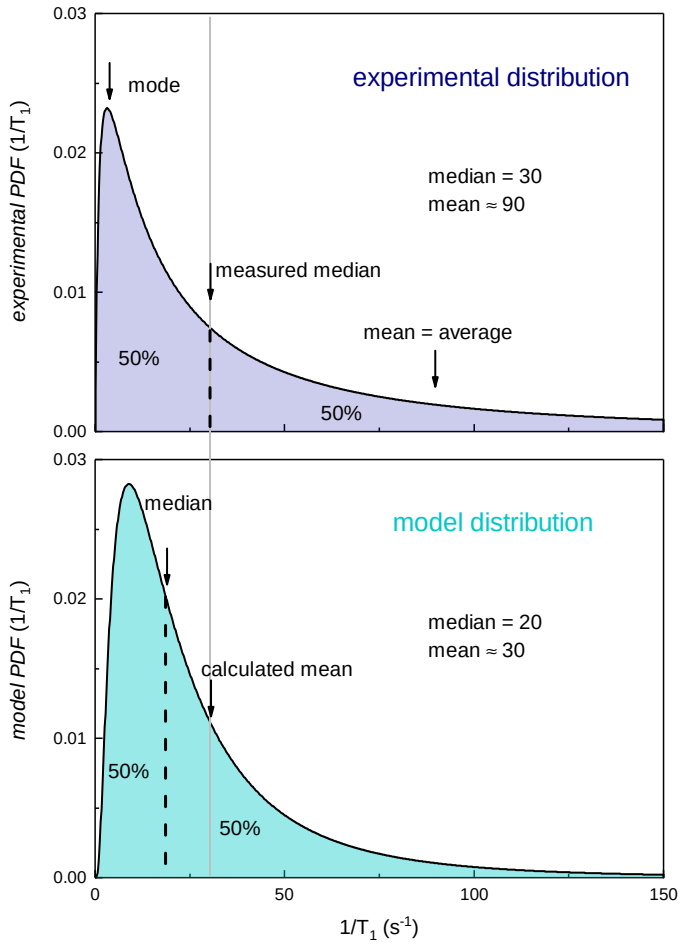

Figure A.1: Situation where the model distribution of relaxation rates has a smaller asymmetry than the experimental distribution such that $\frac{1}{T_1}_{\text{mean, model}}(T) = \frac{1}{T_1}_{\text{median, experimental}}(T)$, as indicated by the grey vertical line. The model distribution is wrong since its median relaxation rate differs from the experimental median.

distribution is unknown but its median relaxation rate can be estimated from $\frac{1}{T_1}_{\text{stretch}}$ and second, as we make no assumption about the fluctuating field, the model distribution is unknown but we can calculate its mean. Both distributions are not necessarily equal: Mitrović *et al.* have shown that the distribution of relaxation rates can be described by a log-normal distribution, which is asymmetric and for which generally $f_{\text{mean}}(T) > f_{\text{median}}(T)$ holds [178]. So, when we fit $\frac{1}{T_1}_{\text{stretch}}(T)$ to eq. 5.6 we are at risk to find a wrong model distribution whose calculated mean fulfills the equality

$$\frac{1}{T_1}_{\text{mean, model}}(T) = \frac{1}{T_1}_{\text{median, experimental}}(T)\,.$$

As a consequence the median of the fitted wrong distribution will be systematically too small:

$$\frac{1}{T_1}_{\text{median, model}}(T) < \frac{1}{T_1}_{\text{median, experimental}}(T)\,.$$

This situation is visualised in Fig. A.1.

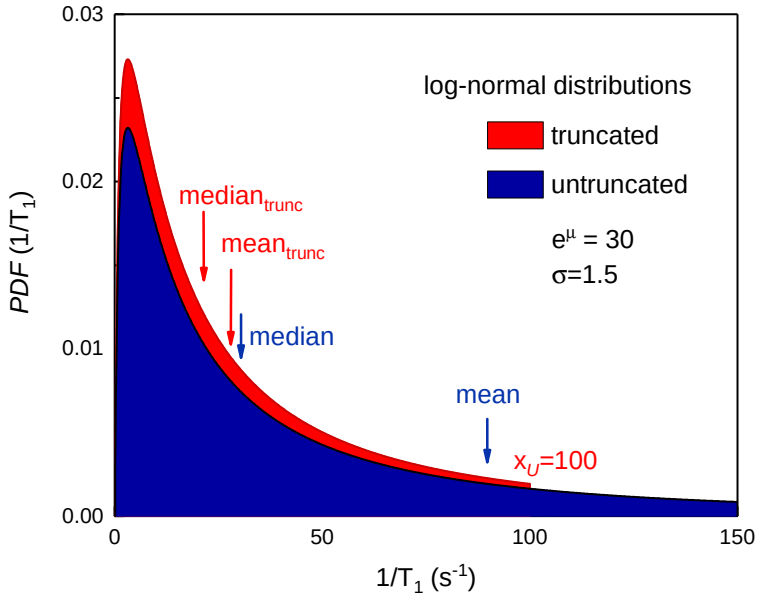

Figure A.2: Regular (untruncated) and truncated log-normal probability distribution functions of the relaxation rate $\frac{1}{T_1}$. The regular log-normal distribution has a median $\exp(\mu) = 30$, $\sigma = 1.5$. The mean is much larger. For the truncated distribution ($x_U = 100$) the mean decreases strongly, so one finds meadian $\sim$ mean$_{\text{trunc}}$. After truncation the distribution is normalised again, so the integrated area is conserved.

However, in a realistic situation the mean relaxation rate does not differ greatly from the median because the distribution of relaxation rates cannot extend to infinity. In BPP $\frac{1}{T_1}_{max} = \frac{h_\perp^2 \gamma_n^2}{\omega_L}$, so an infinite relaxation rate would imply an infinite fluctuating moment.

Thus, to justify the fitting by eq. 5.6 we show that the mean and median relaxation rates are similar, although the distribution of relaxation rates is asymmetric. Fortunately, for the log-normal distribution there are analytical expressions for the relation of the mean and the median with which one can verify the effect of the truncation. Unfortunately this requires a bit of mathematics.

A.1 Untruncated Log-normal distribution

It is instructive to see the difference of the median and the mean for an untruncated log-normal distribution first, and then add the effect of truncation.

Conventionally, the log-normal distribution of the relaxation rate $\frac{1}{T_1} = R_1$ is parametrised by two parameters, μ, the center of the Gaussian, and σ, the standard deviation of the Gaussian:

$$PDF_{\log-\text{normal, base } e}(R_1) = (\sqrt{2\pi}\sigma R_1)^{-1}\, e^{-(\ln R_1 - \mu)^2/2\sigma^2} \tag{A.1}$$

The corresponding median and mean relaxation rates are

$$T_{1,\,\mathrm{median}}^{-1} = e^{\mu} \tag{A.1a}$$

$$T_{1,\,\mathrm{mean}}^{-1} = e^{\mu+\sigma^2/2} = T_{1,\,\mathrm{median}}^{-1}\, e^{\sigma^2/2} \tag{A.1b}$$

From Eq. (A.1b) one can directly see that mean and median are proportional and that the scaling factor is very sensitive to σ. As Mitrović *et al.* have determined μ and σ for the full T-range one can calculate the scaling factor $\exp(\frac{\sigma^2}{2})$ for LSCO $p = 0.12$.

Fig. A.3a compares $\frac{1}{T_1}_{\mathrm{stretch}}$, $T_{1,\,\mathrm{median}}^{-1}$ and $T_{1,\,\mathrm{mean}}^{-1}$. As already stated by Mitrović *et al.*, $T_{1,\,\mathrm{stretch}}^{-1}$ and $T_{1,\,\mathrm{median}}^{-1}$ are very similar. $T_{1,\,\mathrm{mean}}^{-1}$ is much larger. At low T, where $\sigma(T)$ is increasing strongly, the temperature dependence of the mean relaxation rate deviates strongly from the median. The scaling factor which is the ratio of the mean and median relaxation rate grows very quickly with decreasing T. Evidently, fitting $T_{1,\,\mathrm{stretch}}^{-1}(T)$ by the mean relaxation rate determined from Eq. (5.6) would not seem to be a reasonable procedure if the distribution of $\frac{1}{T_1}$ were described by an untruncated log-normal distribution.

A.2 Truncated Log-normal distribution

In case of the truncated log-normal distribution an explicit expression for mean is available from Zaninetti [224]. The scaling factor changes by a multiplicative factor that depends on the left and right cut-offs:

$$T_{1,\,\mathrm{mean,\,truncated}}^{-1} = T_{1,\,\mathrm{median}}^{-1}\, e^{\sigma^2/2} \cdot \frac{\mathrm{erf}(a_1) + \mathrm{erf}(a_2)}{\mathrm{erf}(a_3) + \mathrm{erf}(a_4)} \tag{A.2}$$

Here $\mathrm{erf}(x) = \frac{2}{\sqrt{\pi}} \int_0^x \exp(-t^2)\mathrm{d}t$ is the error function. The parameters a_1 to a_4 depend on the lower and upper cut-offs, x_L & x_U:

$$a_1 = \frac{1}{2} \frac{\sqrt{2}(-\sigma^2 + \ln(x_L) - \ln(T_{1,\,\mathrm{median}}^{-1}))}{\sigma} \tag{A.2a}$$

$$a_2 = \frac{1}{2} \frac{\sqrt{2}(\sigma^2 + \ln(T_{1,\,\mathrm{median}}^{-1}) - \ln(x_U))}{\sigma} \tag{A.2b}$$

$$a_3 = \frac{1}{2} \frac{\sqrt{2}(\ln(x_L) - \ln(T_{1,\,\mathrm{median}}^{-1}))}{\sigma} \tag{A.2c}$$

$$a_4 = \frac{1}{2} \frac{\sqrt{2}(-\ln(x_U) - \ln(T_{1,\,\mathrm{median}}^{-1}))}{\sigma} \tag{A.2d}$$

Equation A.2 looks complicated but it is very similar to eq. A.1b, because the $T_{1,\,\mathrm{mean,\,truncated}}^{-1}$ remains proportional to $T_{1,\,\mathrm{median}}^{-1}$. We can thus plot the scaling factor for the truncated log-normal distribution. It will change depending on cut-offs x_U & x_L if these are within the same order of magnitude as $T_{1,\,\mathrm{median}}^{-1}$.

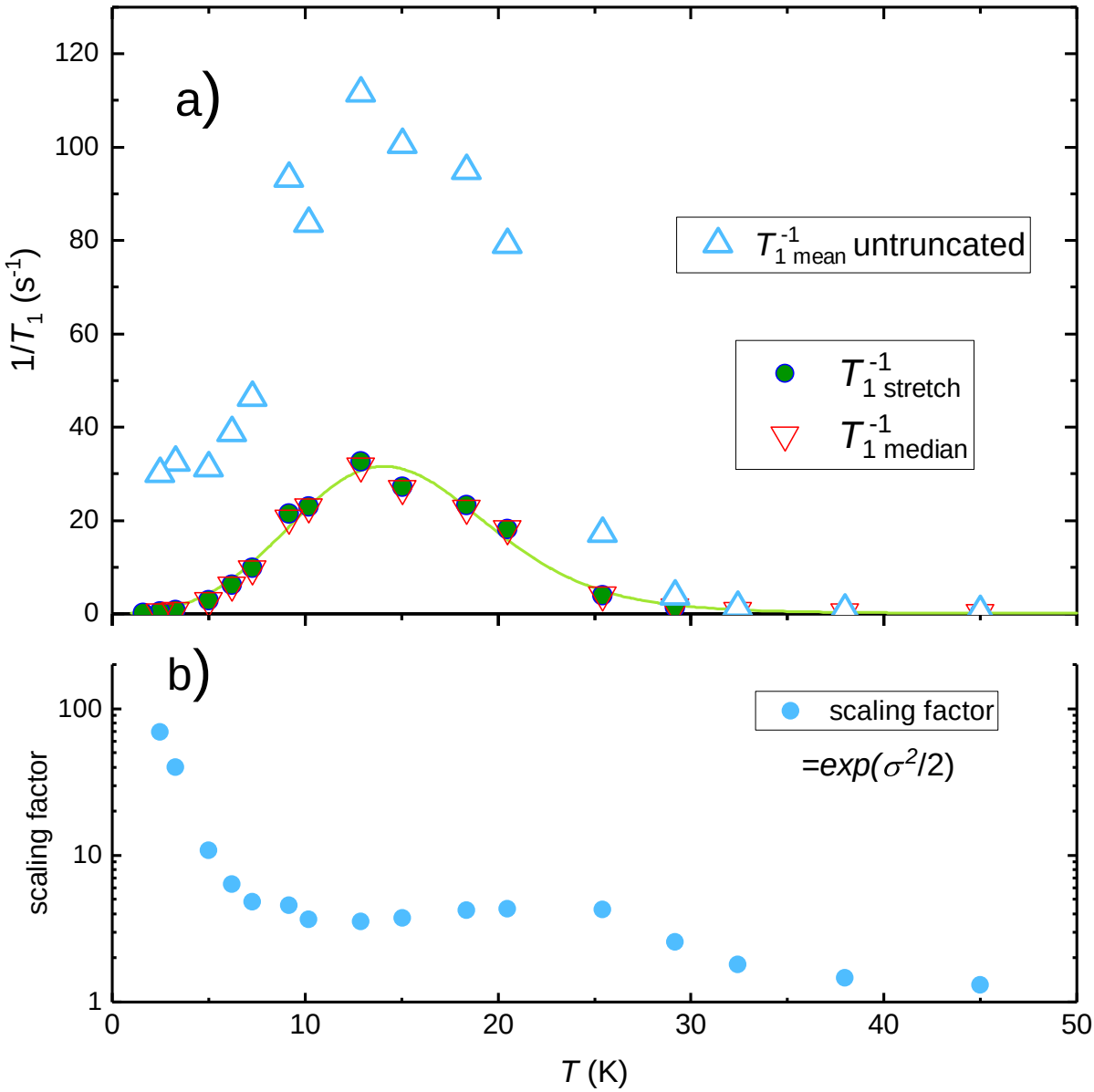

Figure A.3: a): T-dependence of LSCO 12% for $T_{1,\,\mathrm{stretch}}^{-1}$ and $T_{1,\,\mathrm{median}}^{-1}$, as well as $T_{1,\,\mathrm{mean}}^{-1}$. While $T_{1,\,\mathrm{stretch}}^{-1}$ and $T_{1,\,\mathrm{median}}^{-1}$ are always nearly identical, $T_{1,\,\mathrm{mean}}^{-1}$ is much larger than the median. b) T-dependence of the scaling factor between the mean and the median relaxation rate calculated from widths $\sigma(T)$ of the log-normal distributions.

x_L is not zero, but it is much smaller than $T^{-1}_{1,\,\mathrm{median}}$. As long as $H < H_{c2}$ there is some SC and there is in principle no lower bound on the relaxation rate. So x_L has no effect on $T^{-1}_{1,\,\mathrm{mean,\,truncated}}$. On the other hand, x_U cannot become very large, because the fluctuating field $h_\perp$ is of finite size.

From ^{139}La-NQR spectra of LSCO $p = 0.115$ Ohsugi deduced a local field $h_\perp \approx 0.042$ T [191]. With this estimation of $h_\perp$ we can calculate the maximal relaxation rate that one would expect based on the BPP mechanism. For $\omega_L = 2\pi\gamma_n B$, where $B = 14$ T is the applied field, we find:

$$\frac{1}{T_1}_{max} = \frac{h_\perp^2 \gamma_n^2}{\omega_L} \approx 100\,\mathrm{s}^{-1}$$

This value is about three times larger than the experimentally determined maximal relaxation rate of LSCO $p = 0.12$ at the peak, see Fig. 5.9a. Using it as an upper cut-off x_U for the truncated log-normal distribution, we calculate the scaling factor using eq. A.2 and find that the scaling factor is substantially reduced and that the mean and median relaxation times become similar, as shown in Fig. A.4. In principle, x_U does not need to be T-independent. It is possible that it follows $T^{-1}_{1,\,\mathrm{median}}$. In that case the scaling factor would be small at all temperatures.

A.3 Concluding remarks about the fitting procedure

The preceding paragraph does not intend to prove that the median and the mean relaxation rates are equal. The aim was to show that the introduction of an upper cut-off can make these quantities similar. To be able to determine the mean relaxation rate we would have to know the true distribution of relaxation rates, which is impossible from the measured relaxation curves alone.

The conclusion is that it is reasonable to fit $T^{-1}_{1,\,\mathrm{stretch}}$ by $T^{-1}_{\mathrm{distributed\,BPP}}(T)$ and the parameters E_0, ΔE_0,τ_∞, Δa and $h_\perp$ that produce the mean relaxation rate $T^{-1}_{\mathrm{distributed\,BPP}}(T)$ are similar to the set of parameters that characterise the distribution that is responsible for the measured stretched relaxation curves.

Nevertheless, the BPP model should not be treated as a quantitative model. On a semi-quantitative level we find that it can describe the main features of the NMR data.

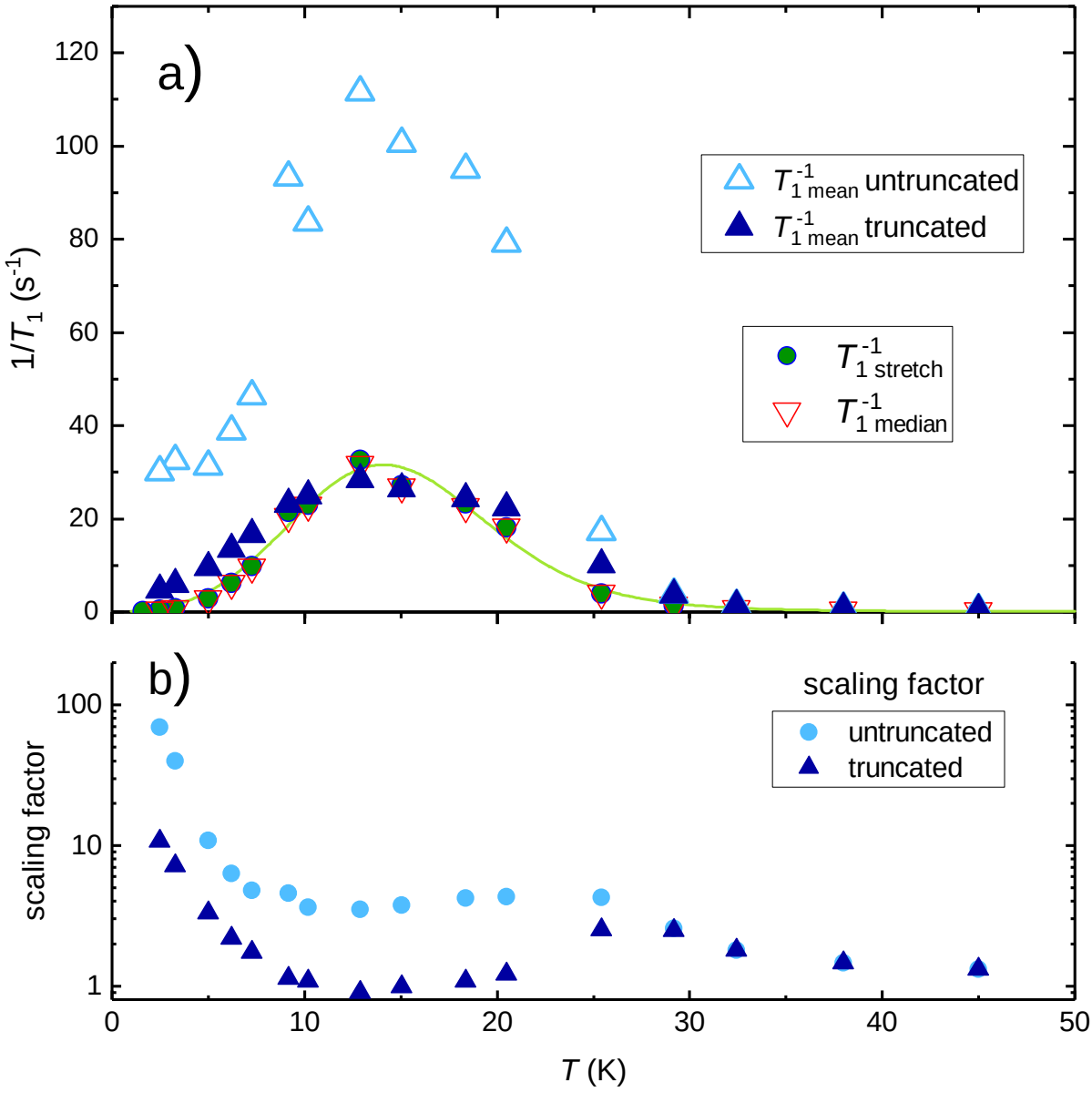

Figure A.4: a)T-dependence of LSCO 12% for $T_{1,\,\mathrm{stretch}}^{-1}$ and $T_{1,\,\mathrm{median}}^{-1}$, , as in Fig. A.3 with the difference that $T_{1,\,\mathrm{mean}}^{-1}$ is calculated for the truncated log-normal distribution with $x_U = 100\,\mathrm{s}^{-1}$. $T_{1,\,\mathrm{mean,truncated}}^{-1}$ (dark blue triangles) is similar to $T_{1,\,\mathrm{median}}^{-1}$. b) T-dependence of the scaling factor between the mean and the median relaxation rate calculated from widths $\sigma(T)$ of the untruncated and truncated log-normal distributions. The truncated scaling factor is substantially smaller.

Acknowledgements

I would like to thank Prof. Pietro Carretta and Prof. Matthieu Le Tacon for having accepted to be reporters of the PhD manuscript as well as Dr. Simone Fratini and Prof. Antony Carrington for being examiners at the PhD defense and for giving valuable comments, suggestions and asking pertinent questions.

My deepest gratitude goes to Dr. Marc-Henri Julien for mentoring me throughout the past four and a half years, living up to what it means to do sincere and honest science on a day to day basis. He not only introduced me to the physics of cuprates and charge order through daily discussions, a rare privilege for a PhD student, but also opened to me the world of skitouring, the beauty of the mountains that surround us, taught me how to do a 'conversion' and never denied but rather encouraged opportunities to go skiing. An anecdote to visualise this: Before coming to LNCMI, during our first skype conversation, I asked whether gloves need to be worn during experimental work, a fear since I easily get sweaty palms. His answer was: "Gloves? No, we only wear gloves for skiing!"

Dr. Hadrien Mayaffre extraordinarily impersonates a combination of scientific excellence in any imaginable respect with an unpretentiousness and humbleness that can maybe only be matched by a Japanese, namely Dr. Yo Tokunaga. Hadrien's scientific expertise lays the foundation of all the work done during the PhD. I am especially grateful for all help linked to teaching Mechanics at the University of Grenoble including being responsible for me for the 'label RES'. His joyfulness and serenity make it a pleasure to be around him.

Dr. Steffen Krämer and Dr. Mladen Horvatić have supported me when I encountered experimental and theoretical problems in quite different ways: While Steffen is cool and rather casual in discussing such problems Mladen goes to the core of the problem and solves it - without exception - in a systematic and thorough way. I thank both for innumerable helpful discussions! I had valuable but rare opportunities to talk to Prof. Claude Berthier due to his sickness while I was at LNCMI. His sudden death on 27th June 2018 was a huge blow to our group and the NMR community.

Two postdocs have helped me make my first experimental steps in NMR: Dr. Michihiro Hirata and Dr. Rui Zhou. Michi shared his simulations of NMR spectra for different CDW patterns with me and his guidance for proper preparation and utilisation of the pressure cell was essential for the success of the project on hydrostatic pressure. Working with Rui has been the most memorable aspect of the PhD. While being a mature scientist that I look up to, with a work load and work ethic that is unmatched, he was never shy of a good joke. His ruigorous work has contributed immensely to the results summarised in this manuscript.

It has been a pleasure, both on a personal and professional level, to work together with Mehdi Frachet, PhD student of Dr. David Le Boeuf. His generosity, help with organisational and administrative issues at the university, friendship and openness to discussions have been highly appreciated, especially during the cumbrous process of writing the mansuscript. I hope this thesis will be of help for your own writing, Mehdi. It is a pleasure to share the office with you and I happily look back at our stay in Cargese in August 2017.
David Le Boeuf and Mehdi, together with Dr. Cyril Proust at LNCMI Toulouse, initiated the project on LSCO and were very kind to orient, cut and share high quality LSCO samples that they received from Prof. Johan Chang and Dr. Masafumi Horio at the University of Zurich, grown at Hokkaido University by Dr. Tohru Nakano and Prof. Naoki Momono. Working and exchanging with the ultrasound group has been of utmost importance to get an understanding of the properties of LSCO in high fields.

I want to thank the administative team of LNCMI: Natacha Hubert, Dominique Vitiello, especially La Grave's finest, Amélie Pic, and Alexandra Gasparini who has solved any administrative problem I had. I strongly believe that she would also solve the cuprate problem if only asked for. I would also like to thank the directors of LNCMI, Dr. Geert Rikken and Prof. Francoise Hippert and more recently Dr. Charles Simon, for supporting me during the PhD and prolonging the financial support for three months after the end of the LANEF PhD grant, as well as keeping me after the end of the PhD. I thank Robert Pankow, as well as Claude Mollard and Jean-Marc Tudela of the workshop. I thank Dr. Ghenadie Novitchi and Dr. Fatima Rida from the chemistry lab.

I have profited from an enlightening discussions with Dr. Andrej Mesaros in which he has explained the effect of discommensurations on CDWs and showed how to use polar plots to visualise the effect of the phase and the wavelength of commensurate modulations which subsequently entered into the manuscript such as multiple discussions of inelastic X-ray diffraction on YBCO with Dr. Michaela

Souliou. In this context I would also like to thank our room mate Dr. Shangfei Wu for his curiosity and multiple helpful discussion about IXS data in YBCO which have helped to develop a scenario in which the phonon softening is an effect of the long-range CDW.

I am happy to belong to the Ukrainian-Russian gang at LNCMI who have become my friends: Artur, Leonid, Inna, Vladimir and Anna Orlova. I thank Dr. Anna Orlova for suggesting to use the asymmetric Pseudo-Voigt function to fit NMR spectra in high fields. I also thank other colleagues, staff and fellow students for making LNCMI a pleasant work place.

Most importantly, I thank my family, my aunt, my brother and my parents for their support over the past years.

Bibliography

[1] H. Gretarsson, S. M. Souliou, S. Jeong, J. Porras, T. Loew, M. Bluschke, M. Minola, B. Keimer, and M. Le Tacon. Light-induced metastable state in charge-ordered $YBa_2Cu_3O_{6+x}$. *Phys. Rev. B*, 98:075134, 2018.

[2] O. Cyr-Choinière, D. LeBoeuf, S. Badoux, S. Dufour-Beauséjour, D. A. Bonn, W. N. Hardy, R. Liang, D. Graf, N. Doiron-Leyraud, and Louis Taillefer. Sensitivity of T_c to pressure and magnetic field in the cuprate superconductor $YBa_2Cu_3O_y$: Evidence of charge-order suppression by pressure. *Phys. Rev. B*, 98:064513, 2018.

[3] F. Laliberté, W. Tabis, S. Badoux, B. Vignolle, D. Destraz, N. Momono, T. Kurosawa, K. Yamada, H. Takagi, N. Doiron-Leyraud, C. Proust, and L. Taillefer. Origin of the metal-to-insulator crossover in cuprate superconductors. *arXiv preprint arXiv:1606.04491*, 2016.

[4] S. Badoux, W. Tabis, F. Laliberté, G. Grissonnanche, B. Vignolle, D. Vignolles, J. Béard, D. A. Bonn, W. N. Hardy, R. Liang, N. Doiron-Leyraud, L. Taillefer, and C. Proust. Change of carrier density at the pseudogap critical point of a cuprate superconductor. *Nature*, 531(7593):210, 2016.

[5] R. Comin and A. Damascelli. Resonant X-Ray Scattering Studies of Charge Order in Cuprates. *Annual Review of Condensed Matter Physics*, 7(1):369–405, 2016.

[6] J.-J. Wen, H. Huang, S.-J. Lee, H. Jang, J. Knight, Y.-S. Lee, M. Fujita, K. M. Suzuki, S. Asano, S. A. Kivelson, C.-C. Kao, and J.-S. Lee. Observation of intertwined density-wave orders and superconductivity in $La_{2-x}Sr_xCuO_4$. *arXiv preprint arXiv:1810.10600*, 2018.

[7] C. Putzke, J. Ayres, J. Buhot, S. Licciardello, N. E. Hussey, S. Friedemann, and A. Carrington. Charge Order and Superconductivity in Underdoped $YBa_2Cu_3O_{7-\delta}$ under Pressure. *Phys. Rev. Lett.*, 120:117002, 2018.

[8] B. Lake, G. Aeppli, K. N. Clausen, D. F. McMorrow, K. Lefmann, N. E. Hussey, N. Mangkorntong, M. Nohara, H. Takagi, T. E. Mason, and A. Schröder. Spins in the vortices of a high-temperature superconductor. *Science*, 291(5509):1759–1762, 2001.

[9] J. Chang, Ch. Niedermayer, R. Gilardi, N. B. Christensen, H. M. Rønnow, D. F. McMorrow, M. Ay, J. Stahn, O. Sobolev, A. Hiess, S. Pailhes, C. Baines, N. Momono, M. Oda, M. Ido, and J. Mesot. Tuning competing orders in $La_{2-x}Sr_xCuO_4$ cuprate superconductors by the application of an external magnetic field. *Phys. Rev. B*, 78:104525, 2008.

[10] B. Khaykovich, S. Wakimoto, R. J. Birgeneau, M. A. Kastner, Y. S. Lee, P. Smeibidl, P. Vorderwisch, and K. Yamada. Field-induced transition between magnetically disordered and ordered phases in underdoped $La_{2-x}Sr_xCuO_4$. *Phys. Rev. B*, 71:220508, 2005.

[11] J. E. Hoffman, E. W. Hudson, K. M. Lang, V. Madhavan, H. Eisaki, S. Uchida, and J. C. Davis. A four unit cell periodic pattern of quasi-particle states surrounding vortex cores in $Bi_2Sr_2CaCu_2O_{8+\delta}$. *Science*, 295(5554):466–469, 2002.

[12] C. Howald, H. Eisaki, N. Kaneko, M. Greven, and A. Kapitulnik. Periodic density-of-states modulations in superconducting $Bi_2Sr_2CaCu_2O_{8+\delta}$. *Phys. Rev. B*, 67:014533, 2003.

[13] T. Wu, H. Mayaffre, S. Krämer, M. Horvatić, C. Berthier, W. N. Hardy, R. Liang, D. A. Bonn, and M.-H. Julien. Magnetic-field-induced charge-stripe order in the high-temperature superconductor $YBa_2Cu_3O_y$. *Nature*, 477(7363):191, 2011.

[14] G. Ghiringhelli, M. Le Tacon, M. Minola, S. Blanco-Canosa, C. Mazzoli, N. B. Brookes, G. M. De Luca, A. Frano, D. G. Hawthorn, F. He, T. Loew, M. Moretti Sala, D. C. Peets, M. Salluzzo, E. Schierle, R. Sutarto, G. A. Sawatzky, E. Weschke, B. Keimer, and L. Braicovich. Long-range incommensurate charge fluctuations in $(Y,Nd)Ba_2Cu_3O_{6+x}$. *Science*, 337(6096):821–825, 2012.

[15] J. Chang, E. Blackburn, A. T. Holmes, N. B. Christensen, J. Larsen, J. Mesot, R. Liang, D. A. Bonn, W. N. Hardy, A. Watenphul, M. v. Zimmermann, E. M. Forgan, and S. M. Hayden. Direct observation of competition between superconductivity and charge density wave order in $YBa_2Cu_3O_{6.67}$. *Nature Physics*, 8(12):871, 2012.

[16] N. Doiron-Leyraud, C. Proust, D. LeBoeuf, J. Levallois, J.-B. Bonnemaison, R. Liang, D. A. Bonn, W. N. Hardy, and L. Taillefer. Quantum oscillations and the Fermi surface in an underdoped high-Tc superconductor. *Nature*, 447(7144):565, 2007.

[17] S. W. Jang, H. Sakakibara, H. Kino, T. Kotani, K. Kuroki, and M. J. Han. Direct theoretical evidence for weaker correlations in electron-doped and Hg-based hole-doped cuprates. *Scientific reports*, 6:33397, 2016.

[18] A. Frano. The Cuprates: A Charge Density Wave. In *Spin Spirals and Charge Textures in Transition-Metal-Oxide Heterostructures*, pages 91–138. Springer, 2014.

[19] Patrick A. Lee, N. Nagaosa, and X.-G. Wen. Doping a Mott insulator: Physics of high-temperature superconductivity. *Rev. Mod. Phys.*, 78:17–85, 2006.

[20] R. Coldea, S. M. Hayden, G. Aeppli, T. G. Perring, C. D. Frost, T. E. Mason, S.-W. Cheong, and Z. Fisk. Spin Waves and Electronic Interactions in La_2CuO_4. *Phys. Rev. Lett.*, 86:5377–5380, 2001.

[21] Avinash Singh. Quantum corrections in an antiferromagnet: A systematic diagrammatical treatment of the Hubbard model. *Phys. Rev. B*, 43:3617–3625, 1991.

[22] D. C. Johnston, F Borsa, P. Carretta, J. H. Cho, F. C. Chou, M. Corti, R. J. Gooding, E Lai, A Lascialfari, and L. L. *et al.* Miller. Magnetic Properties of Single-Layer Cuprates. In *High-Tc Superconductivity 1996: Ten Years after the Discovery*, pages 311–348. Springer, 1997.

[23] S. Uchida, T. Ido, H. Takagi, T. Arima, Y. Tokura, and S. Tajima. Optical spectra of $La_{2-x}Sr_xCuO_4$: Effect of carrier doping on the electronic structure of the CuO_2 plane. *Phys. Rev. B*, 43:7942–7954, 1991.

[24] N. H. Andersen, M. von Zimmermann, T. Frello, M. Käll, D. Mønster, P.-A. Lindgård, J. Madsen, T. Niemöller, H. F. Poulsen, O. Schmidt, J. R. Schneider, T. Wolf, P. Dosanjh, R. Liang, and W. N. Hardy. Superstructure formation and the structural phase diagram of $YBa_2Cu_3O_{6+x}$. *Physica C: Superconductivity*, 317:259–269, 1999.

[25] Ruixing Liang, D. A. Bonn, and W. N. Hardy. Evaluation of CuO_2 plane hole doping in $YBa_2Cu_3O_{6+x}$ single crystals. *Phys. Rev. B*, 73:180505, 2006.

[26] K. Segawa and Y. Ando. Transport Anomalies and the Role of Pseudogap in the 60-K Phase of $YBa_2Cu_3O_{7-\delta}$. *Phys. Rev. Lett.*, 86:4907–4910, 2001.

[27] D. J. Derro, E. W. Hudson, K. M. Lang, S. H. Pan, J. C. Davis, J. T. Markert, and A. L. de Lozanne. Nanoscale One-Dimensional Scattering Resonances in the CuO Chains of $YBa_2Cu_3O_{6+x}$. *Phys. Rev. Lett.*, 88:097002, 2002.

[28] Z. Yamani, B. W. Statt, W. A. MacFarlane, Ruixing Liang, D. A. Bonn, and W. N. Hardy. NMR evidence for Friedel-like oscillations in the CuO chains of ortho-II $YBa_2Cu_3O_{6.5}$. *Phys. Rev. B*, 73:212506, 2006.

[29] M. Bluschke, A. Frano, E. Schierle, D. Putzky, F. Ghorbani, R. Ortiz, H. Suzuki, G. Christiani, G. Logvenov, E. Weschke, R. J. Birgeneau, E. H. da Silva Neto, S. Minola, M.and Blanco-Canosa, and B. Keimer. Stabilization of three-dimensional charge order in $YBa_2Cu_3O_{6+x}$ via epitaxial growth. *Nature communications*, 9(1):2978, 2018.

[30] N. P. Armitage, P. Fournier, and R. L. Greene. Progress and perspectives on electron-doped cuprates. *Rev. Mod. Phys.*, 82:2421–2487, 2010.

[31] C. Proust, E. Boaknin, R. W. Hill, L. Taillefer, and A. P. Mackenzie. Heat Transport in a Strongly Overdoped Cuprate: Fermi Liquid and a Pure d-Wave BCS Superconductor. *Phys. Rev. Lett.*, 89:147003, 2002.

[32] N. E. Hussey, M. Abdel-Jawad, A. Carrington, A. P. Mackenzie, and L. Balicas. A coherent three-dimensional Fermi surface in a high-transition-temperature superconductor. *Nature*, 425(6960):814, 2003.

[33] B. Vignolle, A. Carrington, R. A. Cooper, M. M. J. French, A. P. Mackenzie, C. Jaudet, D. Vignolles, C. Proust, and N. E. Hussey. Quantum oscillations in an overdoped high-Tc superconductor. *Nature*, 455(7215):952, 2008.

[34] M. Platé, J. D. F. Mottershead, I. S. Elfimov, D. C. Peets, Ruixing Liang, D. A. Bonn, W. N. Hardy, S. Chiuzbaian, M. Falub, M. Shi, L. Patthey, and A. Damascelli. Fermi Surface and Quasiparticle Excitations of Overdoped $Tl_2Ba_2CuO_{6+\delta}$. *Phys. Rev. Lett.*, 95:077001, Aug 2005.

[35] J. L. Tallon, C. Bernhard, H. Shaked, R. L. Hitterman, and J. D. Jorgensen. Generic superconducting phase behavior in high-T_c cuprates: T_c variation with hole concentration in $YBa_2Cu_3O_{7-\delta}$. *Phys. Rev. B*, 51:12911–12914, 1995.

[36] H. Mukuda, S. Shimizu, A. Iyo, and Y. Kitaoka. High-tc superconductivity and antiferromagnetism in multilayered copper oxides - a new paradigm of superconducting mechanism -. *Journal of the Physical Society of Japan*, 81(1):011008, 2011.

[37] Y. Ando and K. Segawa. Magnetoresistance of Untwinned $YBa_2Cu_3O_y$ Single Crystals in a Wide Range of Doping: Anomalous Hole-Doping Dependence of the Coherence Length. *Phys. Rev. Lett.*, 88:167005, 2002.

[38] G. Grissonnanche, O. Cyr-Choiniere, F. Laliberté, S. R. De Cotret, A. Juneau-Fecteau, S. Dufour-Beauséjour, M.-E. Delage, D. LeBoeuf, J. Chang, B. J. Ramshaw, D. A. Bonn, W. N. Hardy, R. Liang, S. Adachi, N. E. Hussey, C. Vignolle, B. Proust, M. Sutherland, S. Krämer, J.-H. Park, D. Graf, N. Doiron-Leyraud, and L. Taillefer. Direct measurement of the upper critical field in cuprate superconductors. *Nature communications*, 5:3280, 2014.

[39] C. C. Tsuei, J. R. Kirtley, G. Hammerl, J. Mannhart, H. Raffy, and Z. Z. Li. Robust $d_{x^2-y^2}$ Pairing Symmetry in Hole-Doped Cuprate Superconductors. *Phys. Rev. Lett.*, 93:187004, 2004.

[40] G. Kotliar and J. Liu. Superexchange mechanism and d-wave superconductivity. *Phys. Rev. B*, 38:5142–5145, 1988.

[41] P. Monthoux and D. J. Scalapino. Self-consistent $d_{x^2-y^2}$ pairing in a two-dimensional Hubbard model. *Phys. Rev. Lett.*, 72:1874–1877, 1994.

[42] T. Imai, T. Shimizu, H. Yasuoka, Y. Ueda, and K. Kosuge. Anomalous Temperature Dependence of Cu Nuclear Spin-Lattice Relaxation in $YBa_2Cu_3O_{6.91}$. *Journal of the Physical Society of Japan*, 57(7):2280–2283, 1988.

[43] W. Warren, R. E. Walstedt, G. F. Brennert, R. J. Cava, R. Tycko, R. F. Bell, and G. Dabbagh. Cu spin dynamics and superconducting precursor effects in planes above T_c in $YBa_2Cu_3O_{6.7}$. *Phys. Rev. Lett.*, 62:1193–1196, 1989.

[44] H. Alloul, T. Ohno, and P. Mendels. ^{89}Y NMR evidence for a fermi-liquid behavior in $YBa_2Cu_3O_{6+x}$. *Phys. Rev. Lett.*, 63:1700–1703, 1989.

[45] J. W. Loram, J. L. Luo, J. R. Cooper, W. Y. Liang, and J. L. Tallon. The condensation energy and pseudogap energy scale of Bi: 2212 from the electronic specific heat. *Physica C: Superconductivity*, 341:831–834, 2000.

[46] D. S. Marshall, D. S. Dessau, A. G. Loeser, C-H. Park, A. Y. Matsuura, J. N. Eckstein, I. Bozovic, P. Fournier, A. Kapitulnik, W. E. Spicer, and Z.-X. Shen. Unconventional Electronic Structure Evolution with Hole Doping in $Bi_2Sr_2CaCu_2O_{8+\delta}$: Angle-Resolved Photoemission Results. *Phys. Rev. Lett.*, 76:4841–4844, 1996.

[47] H. Ding, T. Yokoya, J. C. Campuzano, T. Takahashi, M. Randeria, M. R. Norman, T. Mochiku, K. Kadowaki, and J. Giapintzakis. Spectroscopic evidence for a pseudogap in the normal state of underdoped high-Tc superconductors. *Nature*, 382(6586):51, 1996.

[48] A. G. Loeser, Z.-X. Shen, D. S. Dessau, D. S. Marshall, C. H. Park, P. Fournier, and A. Kapitulnik. Excitation gap in the normal state of underdoped $Bi_2Sr_2CaCu_2O_{8+\delta}$. *Science*, 273(5273):325–329, 1996.

[49] L. Zhao, C. A. Belvin, R. Liang, D. A. Bonn, W. N. Hardy, N. P. Armitage, and D. Hsieh. A global inversion-symmetry-broken phase inside the pseudogap region of $YBa_2Cu_3O_y$. *Nature Physics*, 13(3):250, 2017.

[50] Y. Sato, S. Kasahara, H. Murayama, Y. Kasahara, E.-G. Moon, T. Nishizaki, T. Loew, J. Porras, B. Keimer, T. Shibauchi, and Y. Matsuda. Thermodynamic evidence for a nematic phase transition at the onset of the pseudogap in $YBa_2Cu_3O_y$. *Nature Physics*, 13(11):1074, 2017.

[51] J. Xia, E. Schemm, G. Deutscher, S. A. Kivelson, D. A. Bonn, W. N. Hardy, R. Liang, W. Siemons, G. Koster, M. M. Fejer, and A. Kapitulnik. Polar Kerr-Effect Measurements of the High-Temperature $YBa_2Cu_3O_{6+x}$ Superconductor: Evidence for Broken Symmetry near the Pseudogap Temperature. *Phys. Rev. Lett.*, 100:127002, Mar 2008.

[52] B. Fauqué, Y. Sidis, V. Hinkov, S. Pailhès, C. T. Lin, X. Chaud, and P. Bourges. Magnetic Order in the Pseudogap Phase of High-T_C Superconductors. *Phys. Rev. Lett.*, 96:197001, 2006.

[53] R. Daou, J. Chang, D. LeBoeuf, O. Cyr-Choiniere, F. Laliberté, N. Doiron-Leyraud, B. J. Ramshaw, R. Liang, D. A. Bonn, W. N. Hardy, and L. Taillefer. Broken rotational symmetry in the pseudogap phase of a high-Tc superconductor. *Nature*, 463(7280):519, 2010.

[54] Hovnatan Karapetyan, Jing Xia, M. Hücker, G. D. Gu, J. M. Tranquada, M. M. Fejer, and A. Kapitulnik. Evidence of Chiral Order in the Charge-Ordered Phase of Superconducting $La_{1.875}Ba_{0.125}Cuo_4$ Single Crystals Using Polar Kerr-Effect Measurements. *Phys. Rev. Lett.*, 112:047003, 2014.

[55] T. Ito, K. Takenaka, and S. Uchida. Systematic deviation from T-linear behavior in the in-plane resistivity of $YBa_2Cu_3O_{7-y}$: Evidence for dominant spin scattering. *Phys. Rev. Lett.*, 70:3995–3998, 1993.

[56] T. Nakano, M. Oda, C. Manabe, N. Momono, Y. Miura, and M. Ido. Magnetic properties and electronic conduction of superconducting $La_{2-x}Sr_xCuO_4$. *Phys. Rev. B*, 49:16000–16008, 1994.

[57] R. Zhou, M. Hirata, T. Wu, I. Vinograd, H. Mayaffre, S. Krämer, A. P Reyes, P. L. Kuhns, R. Liang, W. N. Hardy, D. A. Bonn, and M.-H. Julien. Spin susceptibility of charge-ordered $YBa_2Cu_3O_y$ across the upper critical field. *Proceedings of the National Academy of Sciences*, 114(50):13148–13153, 2017.

[58] Jan Zaanen and Olle Gunnarsson. Charged magnetic domain lines and the magnetism of high-T_c oxides. *Phys. Rev. B*, 40:7391–7394, 1989.

[59] D. Poilblanc and T. M. Rice. Charged solitons in the Hartree-Fock approximation to the large-U Hubbard model. *Phys. Rev. B*, 39:9749–9752, 1989.

[60] C. H. Chen, S-W. Cheong, and A. S. Cooper. Charge modulations in $La_{2-x}Sr_xNiO_{4+y}$: Ordering of polarons. *Phys. Rev. Lett.*, 71:2461–2464, 1993.

[61] J. M. Tranquada, D. J. Buttrey, V. Sachan, and J. E. Lorenzo. Simultaneous Ordering of Holes and Spins in $La_2NiO_{4.125}$. *Phys. Rev. Lett.*, 73:1003–1006, 1994.

[62] J. M. Tranquada, B. J. Sternlieb, J. D. Axe, Y. Nakamura, and S. Uchida. Evidence for stripe correlations of spins and holes in copper oxide superconductors. *nature*, 375(6532):561, 1995.

[63] M. v. Zimmermann, A. Vigliante, T. Niemöller, N. Ichikawa, T. Frello, J. Madsen, P. Wochner, S. Uchida, N. H. Andersen, J. M. Tranquada, D. Gibbs, and J. R. Schneider. Hard-X-ray diffraction study of charge stripe order in $La_{1.48}Nd_{0.4}Sr_{0.12}CuO_4$. *EPL (Europhysics Letters)*, 41(6):629, 1998.

[64] R. J. Birgeneau, Y. Endoh, K. Kakurai, Y. Hidaka, T. Murakami, M. A. Kastner, T. R. Thurston, G. Shirane, and K. Yamada. Static and dynamic spin fluctuations in superconducting $La_{2-x}Sr_xCuO_4$. *Phys. Rev. B*, 39:2868–2871, 1989.

[65] K. Yamada, C. H. Lee, K. Kurahashi, J. Wada, S. Wakimoto, S. Ueki, H. Kimura, Y. Endoh, S. Hosoya, G. Shirane, R. J. Birgeneau, M. Greven, M. A. Kastner, and Y. J. Kim. Doping dependence of the spatially modulated dynamical spin correlations and the superconducting-transition temperature in $La_{2-x}Sr_xCuO_4$. *Phys. Rev. B*, 57:6165–6172, 1998.

[66] T. P. Croft, C. Lester, M. S. Senn, A. Bombardi, and S. M. Hayden. Charge density wave fluctuations in $La_{2-x}Sr_xCuO_4$ and their competition with superconductivity. *Phys. Rev. B*, 89:224513, 2014.

[67] M. Ido, N. Momono, and M. Oda. Correlation between Superconducting Gap and Pseudogap in High-Tc Cuprates. *J. Low Temp. Phys.*, 117:329, 1999.

[68] M. Hücker, M. v. Zimmermann, G. D. Gu, Z. J. Xu, J. S. Wen, Guangyong Xu, H. J. Kang, A. Zheludev, and J. M. Tranquada. Stripe order in superconducting $La_{2-x}Ba_xCuO_4$ ($0.095 \leqslant x \leqslant 0.155$). *Phys. Rev. B*, 83:104506, 2011.

[69] M. Hücker, M. v. Zimmermann, M. Debessai, J. S. Schilling, J. M. Tranquada, and G. D. Gu. Spontaneous Symmetry Breaking by Charge Stripes in the High Pressure Phase of Superconducting $La_{1.875}Ba_{0.125}CuO_4$. *Phys. Rev. Lett.*, 104:057004, 2010.

[70] S. Sadewasser, J. S. Schilling, A. P. Paulikas, and B. W. Veal. Pressure dependence of T_c to 17 GPa with and without relaxation effects in superconducting $YBa_2Cu_3O_x$. *Phys. Rev. B*, 61:741–749, 2000.

[71] B. Lake, H. M. Rønnow, N. B. Christensen, G. Aeppli, K. Lefmann, D. F. McMorrow, P. Vorderwisch, P. Smeibidl, N. Mangkorntong, T. Sasagawa, M. Nohara, and T. E. Takagi, H.and Mason. Antiferromagnetic order induced by an applied magnetic field in a high-temperature superconductor. *Nature*, 415(6869):299, 2002.

[72] V. F. Mitrović, E. E. Sigmund, W. P. Halperin, A. P. Reyes, P. Kuhns, and W. G. Moulton. Antiferromagnetism in the vortex cores of $YBa_2Cu_3O_{7-\delta}$. *Phys. Rev. B*, 67:220503, 2003.

[73] T. Wu, H. Mayaffre, S. Krämer, M. Horvatić, C. Berthier, P. L. Kuhns, A. P. Reyes, R. Liang, W. N. Hardy, D. A. Bonn, and M.-H. Julien. Emergence of charge order from the vortex state of a high-temperature superconductor. *Nature communications*, 4:2113, 2013.

[74] C. Howald, H. Eisaki, N. Kaneko, and A. Kapitulnik. Coexistence of periodic modulation of quasiparticle states and superconductivity in $Bi_2Sr_2CaCu_2O_{8+\delta}$. *Proceedings of the National Academy of Sciences*, 100(17):9705–9709, 2003.

[75] M. Vershinin, S. Misra, S. Ono, Y. Abe, Y. Ando, and A. Yazdani. Local ordering in the pseudogap state of the high-Tc superconductor $Bi_2Sr_2CaCu_2O_{8+\delta}$. *Science*, 303(5666):1995–1998, 2004.

[76] J. E. Hoffman, K. McElroy, D.-H. Lee, K. M. Lang, H. Eisaki, S. Uchida, and J. C. Davis. Imaging quasiparticle interference in $Bi_2Sr_2CaCu_2O_{8+\delta}$. *Science*, 297(5584):1148–1151, 2002.

[77] A. Yazdani, E. H. da Silva Neto, and P. Aynajian. Spectroscopic imaging of strongly correlated electronic states. *Annual Review of Condensed Matter Physics*, 7:11–33, 2016.

[78] Ø. Fischer, M. Kugler, I. Maggio-Aprile, C. Berthod, and C. Renner. Scanning tunneling spectroscopy of high-temperature superconductors. *Rev. Mod. Phys.*, 79:353–419, 2007.

[79] K. Fujita, A. R. Schmidt, E.-A. Kim, M. J. Lawler, D. H. Lee, J. C. Davis, H. Eisaki, and S. Uchida. Spectroscopic imaging scanning tunneling microscopy studies of electronic structure in the superconducting and pseudogap phases of cuprate high-T c superconductors. *Journal of the Physical Society of Japan*, 81(1):011005, 2011.

[80] W. D. Wise, M. C. Boyer, K. Chatterjee, T. Kondo, T. Takeuchi, H. Ikuta, Y. Wang, and E. W. Hudson. Charge-density-wave origin of cuprate checkerboard visualized by scanning tunnelling microscopy. *Nature Physics*, 4(9):696, 2008.

[81] T. Hanaguri, C. Lupien, Y. Kohsaka, D.-H. Lee, M. Azuma, M. Takano, H. Takagi, and J. C. Davis. A 'checkerboard'electronic crystal state in lightly hole-doped $Ca_{2-x}Na_xCuO_2Cl_2$. *Nature*, 430(7003):1001, 2004.

[82] C. V. Parker, P. Aynajian, E. H. da Silva Neto, A. Pushp, S. Ono, J. Wen, Z. Xu, G. Gu, and A. Yazdani. Fluctuating stripes at the onset of the pseudogap in the high-Tc superconductor $Bi_2Sr_2CaCu_2O_{8+x}$. *Nature*, 468(7324):677, 2010.

[83] D. LeBoeuf, N. Doiron-Leyraud, B. Vignolle, M. Sutherland, B. J. Ramshaw, J. Levallois, R. Daou, F. Laliberté, O. Cyr-Choinière, J. Chang, Y. J. Jo, L. Balicas, R. Liang, D. A. Bonn, W. N. Hardy, C. Proust, and L. Taillefer. Lifshitz critical point in the cuprate superconductor $YBa_2Cu_3O_y$ from high-field Hall effect measurements. *Phys. Rev. B*, 83:054506, 2011.

[84] S. Blanco-Canosa, A. Frano, E. Schierle, J. Porras, T. Loew, M. Minola, M. Bluschke, E. Weschke, B. Keimer, and M. Le Tacon. Resonant x-ray scattering study of charge-density wave correlations in $YBa_2Cu_3O_{6+x}$. *Phys. Rev. B*, 90:054513, 2014.

[85] R. Comin, A. Frano, M. M. Yee, Y. Yoshida, H. Eisaki, E. Schierle, E. Weschke, R. Sutarto, F. He, A. Soumyanarayanan, M. Le Tacon, I. S. Elfimov, J. E. Hoffman, G. A. Sawatzky, B. Keimer, and A. Damascelli. Charge order driven by Fermi-arc instability in $Bi_2Sr_{2-x}La_xCuO_{6+\delta}$. *Science*, 343(6169):390–392, 2014.

[86] M. Hücker, N. B. Christensen, A. T. Holmes, E. Blackburn, E. M. Forgan, R. Liang, D. A. Bonn, W. N. Hardy, O. Gutowski, M. v. Zimmermann, S. M. Hayden, and J. Chang. Competing charge, spin, and superconducting orders in underdoped $YBa_2Cu_3O_y$. *Phys. Rev. B*, 90:054514, 2014.

[87] T. Wu, Hadrien Mayaffre, S. Krämer, M. Horvatić, C. Berthier, W.N. Hardy, R. Liang, D. A. Bonn, and M.-H. Julien. Incipient charge order observed by NMR in the normal state of $YBa_2Cu_3O_y$. *Nature communications*, 6:6438, 2015.

[88] E. Blackburn, J. Chang, A. H. Said, B. M. Leu, R. Liang, D. A. Bonn, W. N. Hardy, E. M. Forgan, and S. M. Hayden. Inelastic x-ray study of phonon broadening and charge-density wave formation in ortho-II-ordered $YBa_2Cu_3O_{6.54}$. *Phys. Rev. B*, 88:054506, 2013.

[89] M. Le Tacon, A. Bosak, S. M. Souliou, G. Dellea, T. Loew, R. Heid, K. P. Bohnen, G. Ghiringhelli, M. Krisch, and B. Keimer. Inelastic X-ray scattering in $YBa_2Cu_3O_{6.6}$ reveals giant phonon anomalies and elastic central peak due to charge-density-wave formation. *Nature Physics*, 10(1):52, 2014.

[90] S. M. Souliou, H. Gretarsson, G. Garbarino, A. Bosak, J. Porras, T. Loew, B. Keimer, and M. Le Tacon. Rapid suppression of the charge density wave in $YBa_2Cu_3O_{6.6}$ under hydrostatic pressure. *Phys. Rev. B*, 97:020503, 2018.

[91] S. Gerber, H. Jang, H. Nojiri, S. Matsuzawa, H. Yasumura, D. A. Bonn, R. Liang, W. N. Hardy, Z. Islam, A. Mehta, S. Song, M. Sikorski, D. Stefanescu, Y. Feng, S. A. Kivelson, T. P. Devereaux, Z.-X. Shen, C.-C. Kao, W.-S. Lee, D. Zhu, and J.-S. Lee. Three-dimensional charge density wave order in $YBa_2Cu_3O_{6.67}$ at high magnetic fields. *Science*, 350(6263):949–952, 2015.

[92] J. Chang, E. Blackburn, O. Ivashko, A. T. Holmes, N. B. Christensen, M. Hücker, R. Liang, D. A. Bonn, W. N. Hardy, U. Rütt, M. v. Zimmermann, E. M. Forgan, and S. M. Hayden. Magnetic field controlled charge density wave coupling in underdoped $YBa_2Cu_3O_{6+x}$. *Nature communications*, 7:11494, 2016.

[93] D. LeBoeuf, S. Krämer, W. N. Hardy, R. Liang, D. A. Bonn, and C. Proust. Thermodynamic phase diagram of static charge order in underdoped $YBa_2Cu_3O_y$. *Nature Physics*, 9(2):79, 2013.

[94] Marc-Henri Julien. Magnetic fields make waves in cuprates. *Science*, 350(6263):914–915, 2015.

[95] B. J. Ramshaw, S. E. Sebastian, R. D. McDonald, J. Day, B. S. Tan, Z. Zhu, J. B. Betts, R. Liang, D. A. Bonn, W. N. Hardy, and N. Harrison. Quasiparticle mass enhancement approaching optimal doping in a high-Tc superconductor. *Science*, 348(6232):317–320, 2015.

[96] H. Yao, D.-H. Lee, and S. Kivelson. Fermi-surface reconstruction in a smectic phase of a high-temperature superconductor. *Phys. Rev. B*, 84:012507, 2011.

[97] N. Harrison and S. E. Sebastian. Protected Nodal Electron Pocket from Multiple-**Q** Ordering in Underdoped High Temperature Superconductors. *Phys. Rev. Lett.*, 106:226402, 2011.

[98] F. Laliberté, M. Frachet, S. Benhabib, B. Borgnic, T. Loew, J. Porras, M. Tacon, B. Keimer, S. Wiedmann, C. Proust, and D. LeBoeuf. High field charge order across the phase diagram of $YBa_2Cu_3O_y$. *npj Quantum Materials*, 3(1):11, 2018.

[99] E. H. da Silva Neto, P. Aynajian, A. Frano, R. Comin, E. Schierle, E. Weschke, A. Gyenis, J. Wen, J. Schneeloch, Z. Xu, S. Ono, G. Gu, M. Le Tacon, and A. Yazdani. Ubiquitous interplay between charge ordering and high-temperature superconductivity in cuprates. *Science*, 343(6169):393–396, 2014.

[100] W. Tabis, Y. Li, M. Le Tacon, L. Braicovich, A. Kreyssig, M. Minola, G. Dellea, E. Weschke, M. J. Veit, M. Ramazanoglu, A. I. Goldman, T. Schmitt, G. Ghiringhelli, N. Barišić, M. K. Chan, C. J. Dorow, X. Yu, G.and Zhao, B. Keimer, and M. Greven. Charge order and its connection with Fermi-liquid charge transport in a pristine high-Tc cuprate. *Nature communications*, 5:5875, 2014.

[101] N. Barišić, S. Badoux, M. K. Chan, C. Dorow, W. Tabis, B. Vignolle, G. Yu, J. Béard, X. Zhao, C. Proust, and M. Greven. Universal quantum oscillations in the underdoped cuprate superconductors. *Nature Physics*, 9(12):761, 2013.

[102] E. H. da Silva Neto, R. Comin, F. He, R. Sutarto, Y. Jiang, R. L. Greene, G. A. Sawatzky, and A. Damascelli. Charge ordering in the electron-doped superconductor $Nd_{2-x}Ce_xCuO_4$. *Science*, 347(6219):282–285, 2015.

[103] S. Kawasaki, Z. Li, M. Kitahashi, C. T. Lin, P. L. Kuhns, A. P. Reyes, and G.-q. Zheng. Charge-density-wave order takes over antiferromagnetism in $Bi_2Sr_{2-x}La_xCuO_6$ superconductors. *Nature communications*, 8(1):1267, 2017.

[104] A. Abragam. *The principles of nuclear magnetism*. Oxford university press, 1961.

[105] C. P. Slichter. *Principles of magnetic resonance*, volume 1. Springer Science & Business Media, 2013.

[106] F. Hammerath. *Magnetism and Superconductivity in Iron-based Superconductors as Probed by Nuclear Magnetic Resonance*. Springer Science & Business Media, 2012.

[107] M.-H. Julien. *Des supraconducteurs à Haute Température Critique aux Echelles de Spins: une Etude par Résonance Magnétique Nucléaire*. PhD thesis, Université Joseph Fourier (Grenoble), 1997.

[108] C. De Vaulx. *Etude par Resonance Magnétique de Cobaltates* Na_xCoO_2. PhD thesis, Université Joseph-Fourier-Grenoble I, 2007.

[109] R. Zhou. *Nuclear Magnetic Resonance Study on Iron-Based Superconductor* $Ba_{1-x}K_xFe_2As_2$, $BaFe_{2-x}Ni_xAs_2$ *and* LiFeAs. PhD thesis, The University of the Chinese Academy of Sciences, 2014.

[110] A. Rigamonti, F. Borsa, and P. Carretta. Basic aspects and main results of NMR-NQR spectroscopies in high-temperature superconductors. *Reports on Progress in Physics*, 61(10):1367, 1998.

[111] Russell E. Walstedt. *The NMR probe of high-Tc materials*, volume 228. Springer, 2008.

[112] D. I. Hoult and N. S. Ginsberg. The quantum origins of the free induction decay signal and spin noise. *Journal of Magnetic Resonance*, 148(1):182–199, 2001.

[113] G. C. Carter, L. H. Bennett, and D. J. Kahan. *Metallic shifts in NMR: a review of the theory and comprehensive critical data compilation of metallic materials*. Pergamon, 1977.

[114] Tôru Moriya. The effect of electron-electron interaction on the nuclear spin relaxation in metals. *Journal of the Physical Society of Japan*, 18(4):516–520, 1963.

[115] B. S. Shastry. t-J model and nuclear magnetic relaxation in high-T_c materials. *Phys. Rev. Lett.*, 63:1288–1291, 1989.

[116] P. C. Hammel, M. Takigawa, R. H. Heffner, Z. Fisk, and K. C. Ott. Spin dynamics at oxygen sites in $YBa_2Cu_3O_7$. *Phys. Rev. Lett.*, 63:1992–1995, 1989.

[117] M. Horvatic. Magnetic nuclear spin-lattice relaxation in nmr of orthorhombic crystals in the presence of strong quadrupole coupling. *Journal of Physics: Condensed Matter*, 4(26):5811, 1992.

[118] A. Suter, M. Mali, J. Roos, and D. Brinkmann. Mixed magnetic and quadrupolar relaxation in the presence of a dominant static zeeman hamiltonian. *Journal of Physics: Condensed Matter*, 10(26):5977, 1998.

[119] D. C. Johnston. Stretched exponential relaxation arising from a continuous sum of exponential decays. *Phys. Rev. B*, 74:184430, 2006.

[120] J. J. Olivero and R.L. Longbothum. Empirical fits to the Voigt line width: A brief review. *Journal of Quantitative Spectroscopy and Radiative Transfer*, 17(2):233–236, 1977.

[121] Peter Nagel. *Thermodynamik und Kinetik der Sauerstoffordnung in* $YBa_2Cu_3O_x$. FZKA, 2001.

[122] P. Nagel, V. Pasler, C. Meingast, A. I. Rykov, and S. Tajima. Anomalously Large Oxygen-Ordering Contribution to the Thermal Expansion of Untwinned $YBa_2Cu_3O_{6.95}$ Single Crystals: A Glasslike Transition near Room Temperature. *Phys. Rev. Lett.*, 85:2376–2379, 2000.

[123] S. Ouazi, J. Bobroff, H. Alloul, M. Le Tacon, N. Blanchard, G. Collin, M. H. Julien, M. Horvatić, and C. Berthier. Impurity-Induced Local Magnetism and Density of States in the Superconducting State of $YBa_2Cu_3O_7$. *Phys. Rev. Lett.*, 96:127005, 2006.

[124] Ernst Helmut Brandt. Properties of the ideal Ginzburg-Landau vortex lattice. *Phys. Rev. B*, 68:054506, 2003.

[125] M.-H. Julien, T. Fehér, M. Horvatić, C. Berthier, O. N. Bakharev, P. Ségransan, G. Collin, and J.-F. Marucco. ^{63}Cu NMR Evidence for Enhanced Antiferromagnetic Correlations around Zn Impurities in $YBa_2Cu_3O_{6.7}$. *Phys. Rev. Lett.*, 84:3422–3425, 2000.

[126] W. A. Atkinson, S. Ufkes, and A. P. Kampf. Structure of the charge density wave in cuprate superconductors: Lessons from NMR. *Phys. Rev. B*, 97:125147, 2018.

[127] J. Haase, C. P. Slichter, R. Stern, C. T. Milling, and D. G. Hinks. NMR evidence for spatial modulations in the cuprates. *Journal of Superconductivity*, 13(5):723–726, 2000.

[128] J. A Lee, Y. Xin, W. P. Halperin, A. P. Reyes, P. L. Kuhns, and M. K. Chan. Coherent charge and spin density waves in underdoped $HgBa_2CuO_{4+\delta}$. *New Journal of Physics*, 19(3):033024, 2017.

[129] M. Jurkutat. *NMR of Electron-Doped High-Temperature Superconductor* $Pr_{2-x}Ce_xCuO_4$. PhD thesis, Universität Leipzig, 2014.

[130] G.-q. Zheng, Y. Kitaoka, K. Ishida, and K. Asayama. Local hole distribution in the CuO2 plane of high-Tc Cu-oxides studied by Cu and oxygen NQR/NMR. *Journal of the Physical Society of Japan*, 64(7):2524–2532, 1995.

[131] J. Haase, O. P. Sushkov, P. Horsch, and G. V. M. Williams. Planar Cu and O hole densities in high-T_c cuprates determined with NMR. *Phys. Rev. B*, 69:094504, 2004.

[132] M. Jurkutat, J. Kohlrautz, S. Reichardt, A. Erb, G. V. M. Williams, and J. Haase. NMR of Cuprate Superconductors: Recent Developments. In *High-Tc Copper Oxide Superconductors and Related Novel Materials*, pages 77–97. Springer, 2017.

[133] R. Ofer and A. Keren. Nutation versus angular-dependent NQR spectroscopy and impact of underdoping on charge inhomogeneities in $YBa_2Cu_3O_y$. *Phys. Rev. B*, 80:224521, 2009.

[134] R. Blinc. Magnetic resonance and relaxation in structurally incommensurate systems. *Physics Reports*, 79(5):331–398, 1981.

[135] Y. A. Kharkov and O. P. Sushkov. The amplitudes and the structure of the charge density wave in YBCO. *Scientific reports*, 6:34551, 2016.

[136] A. Mesaros, K. Fujita, S. D. Edkins, M. H. Hamidian, H. Eisaki, S. Uchida, J. C. S. Davis, M. J. Lawler, and E.-A. Kim. Commensurate $4a_0$-period charge density modulations throughout the $Bi_2Sr_2CaCu_2O_{8+x}$ pseudogap regime. *Proceedings of the National Academy of Sciences*, 113(45):12661–12666, 2016.

[137] E. Blackburn, J. Chang, M. Hücker, A. T. Holmes, N. B. Christensen, Ruixing Liang, D. A. Bonn, W. N. Hardy, U. Rütt, O. Gutowski, M. v. Zimmermann, E. M. Forgan, and S. M. Hayden. X-Ray Diffraction Observations of a Charge-Density-Wave Order in Superconducting Ortho-II $YBa_2Cu_3O_{6.54}$ Single Crystals in Zero Magnetic Field. *Phys. Rev. Lett.*, 110:137004, 2013.

[138] W. L. McMillan. Theory of discommensurations and the commensurate-incommensurate charge-density-wave phase transition. *Phys. Rev. B*, 14:1496–1502, 1976.

[139] R. M. Fleming, D. E. Moncton, J. D. Axe, and G. S. Brown. High-Q-resolution scattering using synchrotron x radiation: $2H$-$TaSe_2$ and $NbSe_3$. *Phys. Rev. B*, 30:1877–1883, 1984.

[140] Ph. Leininger, D. Chernyshov, A. Bosak, H. Berger, and D. S. Inosov. Competing charge density waves and temperature-dependent nesting in $2H$-$TaSe_2$. *Phys. Rev. B*, 83:233101, 2011.

[141] B. H. Suits, S. Couturié, and C. P. Slichter. NMR test of McMillan's concept of discommensurations in $2H - TaSe_2$. *Phys. Rev. B*, 23:5142–5151, 1981.

[142] A. Soumyanarayanan, M. M. Yee, Y. He, J. van Wezel, D. J. Rahn, K. Rossnagel, E. W. Hudson, M. R. Norman, and J. E. Hoffman. Quantum phase transition from triangular to stripe charge order in $NbSe_2$. *Proceedings of the National Academy of Sciences*, 110(5):1623–1627, 2013.

[143] H. Jang, W.-S. Lee, H. Nojiri, S. Matsuzawa, H. Yasumura, L. Nie, A. V. Maharaj, S. Gerber, Y.-J. Liu, A. Mehta, D. A. Bonn, R. Liang, W. N. Hardy, C. A. Burns, Z. Islam, S. Song, J. Hastings, T. P. Devereaux, Z.-X. Shen, S. A. Kivelson, C.-C. Kao, D. Zhu, and J.-S. Lee. Ideal charge-density-wave order in the high-field state of superconducting YBCO. *Proceedings of the National Academy of Sciences*, 113(51):14645–14650, 2016.

[144] S. Blanco-Canosa, A. Frano, T. Loew, Y. Lu, J. Porras, G. Ghiringhelli, M. Minola, C. Mazzoli, L. Braicovich, E. Schierle, E. Weschke, M. Le Tacon, and B. Keimer. Momentum-Dependent Charge Correlations in $YBa_2Cu_3O_{6+\delta}$ Superconductors Probed by Resonant X-Ray Scattering: Evidence for Three Competing Phases. *Phys. Rev. Lett.*, 110:187001, 2013.

[145] R. Zhou, M. Hirata, T. Wu, I. Vinograd, H. Mayaffre, S. Krämer, M. Horvatić, C. Berthier, A. P. Reyes, P. L. Kuhns, R. Liang, W. N. Hardy, D. A. Bonn, and M.-H. Julien. Quasiparticle Scattering off Defects and Possible Bound States in Charge-Ordered $YBa_2Cu_3O_y$. *Phys. Rev. Lett.*, 118:017001, 2017.

[146] N. D. Mermin and H. Wagner. Absence of Ferromagnetism or Antiferromagnetism in One- or Two-Dimensional Isotropic Heisenberg Models. *Phys. Rev. Lett.*, 17:1133–1136, 1966.

[147] A. L. Stancik and E. B. Brauns. A simple asymmetric lineshape for fitting infrared absorption spectra. *Vibrational Spectroscopy*, 47(1):66–69, 2008.

[148] T. Wu, R. Zhou, M. Hirata, I. Vinograd, H. Mayaffre, R. Liang, W. N. Hardy, D. A. Bonn, T. Loew, J. Porras, D. Haug, C. T. Lin, V. Hinkov, B. Keimer, and M.-H. Julien. ^{63}Cu-NMR study of oxygen disorder in ortho-II $YBa_2Cu_3O_y$. *Phys. Rev. B*, 93:134518, 2016.

[149] Michael Tinkham. *Introduction to superconductivity*. Courier Corporation, 2004.

[150] H. Jang, W.-S. Lee, S. Song, H. Nojiri, S. Matsuzawa, H. Yasumura, H. Huang, Y.-J. Liu, J. Porras, M. Minola, B. Keimer, J. Hastings, D. Zhu, T. P. Devereaux, Z.-X. Shen, C.-C. Kao, and J.-S. Lee. Coincident onset of charge-density-wave order at a quantum critical point in underdoped $YBa_2Cu_3O_x$. *Phys. Rev. B*, 97:224513, 2018.

[151] C. W. Chu, P. H. Hor, R. L. Meng, L. Gao, Z. J. Huang, and Y. Q. Wang. Evidence for superconductivity above 40 K in the La-Ba-Cu-O compound system. *Phys. Rev. Lett.*, 58:405–407, 1987.

[152] P. H. Hor, L. Gao, R. L. Meng, Z. J. Huang, Y. Q. Wang, K. Forster, J. Vassilious, C. W. Chu, M. K. Wu, J. R. Ashburn, and C. J. Torng. High-pressure study of the new Y-Ba-Cu-O superconducting compound system. *Phys. Rev. Lett.*, 58:911–912, 1987.

[153] P. L. Alireza, G. H. Zhang, W. Guo, J. Porras, T. Loew, Y.-T. Hsu, G. G. Lonzarich, M. Le Tacon, B. Keimer, and Suchitra E. Sebastian. Accessing the entire overdoped regime in pristine $YBa_2Cu_3O_{6+x}$ by application of pressure. *Phys. Rev. B*, 95:100505, 2017.

[154] J. D. Jorgensen, S. Pei, P. Lightfoot, D. G. Hinks, B. W. Veal, B. Dabrowski, A. P. Paulikas, R. Kleb, and I. D. Brown. Pressure-induced charge transfer and dTc/dP in $YBa_2Cu_3O_{7-x}$. *Physica C: Superconductivity*, 171(1-2):93–102, 1990.

[155] H. Huang, H. Jang, M. Fujita, T. Nishizaki, Y. Lin, J. Wang, J. Ying, J. S. Smith, C. Kenney-Benson, G. Shen, W. L. Mao, C.-C. Kao, Y.-J. Liu, and J.-S. Lee. Modification of structural disorder by hydrostatic pressure in the superconducting cuprate $YBa_2Cu_3O_{6.73}$. *Phys. Rev. B*, 97:174508, 2018.

[156] C. Putzke, L. Malone, S. Badoux, B. Vignolle, D. Vignolles, W. Tabis, P. Walmsley, M. Bird, N. E. Hussey, C. Proust, and A. Carrington. Inverse correlation between quasiparticle mass and Tc in a cuprate high-Tc superconductor. *Science Advances*, 2(3), 2016.

[157] K. Yokogawa, K. Murata, H. Yoshino, and S. Aoyama. Solidification of high-pressure medium Daphne 7373. *Japanese journal of applied physics*, 46(6R):3636, 2007.

[158] M. Hirata, K. Ishikawa, K. Miyagawa, M. Tamura, C. Berthier, D. Basko, A. Kobayashi, G. Matsuno, and K. Kanoda. Observation of an anisotropic Dirac cone reshaping and ferrimagnetic spin polarization in an organic conductor. *Nature communications*, 7:12666, 2016.

[159] P. S. Wang, S. S. Sun, Y. Cui, W. H. Song, T. R. Li, R. Yu, H. Lei, and W. Yu. Pressure Induced Stripe-Order Antiferromagnetism and First-Order Phase Transition in FeSe. *Phys. Rev. Lett.*, 117:237001, 2016.

[160] Y. Atanov and E. Ivanova. Manganin Resistance gages as accurate instruments for high-pressure measurements. In E. C. Lloyd, editor, *Accurate Characterization of the High-pressure Environment: Proceedings*, pages 49–51. US National Bureau of Standards, 1971.

[161] C. Murayama, Y. Iye, T. Enomoto, N. Mori, Y. Yamada, T. Matsumoto, Y. Kubo, Y. Shimakawa, and T. Manako. Correlation between the pressure-induced changes in the Hall coefficient and Tc in superconducting cuprates. *Physica C: Superconductivity*, 183(4-6):277–285, 1991.

[162] R. P. Gupta and M. Gupta. Absence of pressure-induced charge transfer in superconducting $YBa_2Cu_3O_7$. *Physica C: Superconductivity*, 178(4-6):414–420, 1991.

[163] N. Doiron-Leyraud, O. Cyr-Choinière, S. Badoux, A. Ataei, C. Collignon, A. Gourgout, S. Dufour-Beauséjour, F. F. Tafti, F. Laliberté, M.-E. Boulanger, M. Matusiak, D. Graf, M. Kim, J.-S. Zhou, N. Momono, T. Kurosawa, H. Takagi, and L. Taillefer. Pseudogap phase of cuprate superconductors confined by Fermi surface topology. *Nature communications*, 8(1):2044, 2017.

[164] T. Meissner, S.e K. Goh, J. Haase, M. Richter, K. Koepernik, and H. Eschrig. Nuclear magnetic resonance at up to 10.1 GPa pressure detects an electronic topological transition in aluminum metal. *Journal of Physics: Condensed Matter*, 26(1):015501, 2013.

[165] S. Badoux. *Propriétés de l'état normal des cuprates sous-dopés sous champ magnétique intense.* PhD thesis, Université de Toulouse, Université Toulouse III-Paul Sabatier, 2014.

[166] S. Klotz, J. C. Chervin, P. Munsch, and G. Le Marchand. Hydrostatic limits of 11 pressure transmitting media. *Journal of Physics D: Applied Physics*, 42(7):075413, 2009.

[167] J. Schilling, N. Hillier, and N. Foroozani. What have we learned from high-pressure experiments on Cu-oxide and Fe-based superconductors? In *Journal of Physics: Conference Series*, volume 449, page 012021. IOP Publishing, 2013.

[168] K. Murata, K. Yokogawa, H. Yoshino, S. Klotz, P. Munsch, A. Irizawa, M. Nishiyama, K. Iizuka, T. Nanba, T. Okada, Y. Shiraga, and S. Aoyama. Pressure transmitting medium Daphne 7474 solidifying at 3.7 GPa at room temperature. *Review of Scientific Instruments*, 79(8):085101, 2008.

[169] O. Ivashko, L. Yang, D. Destraz, E. Martino, Y. Chen, C. Y. Guo, H. Q. Yuan, A. Pisoni, P. Matus, S. Pyon, K. Kudo, M. Nohara, L. Forro, H. M. Ronnow, M. Hücker, M. v. Zimmermann, and J. Chang. Charge-Stripe Order and Superconductivity in $Ir_{1-x}Pt_xTe_2$. *Scientific reports*, 7(1):17157, 2017.

[170] M. Lei, J. L. Sarrao, W. M. Visscher, T. M. Bell, J. D. Thompson, A. Migliori, U. W. Welp, and B. W. Veal. Elastic constants of a monocrystal of superconducting $YBa_2Cu_3O_{7-\delta}$. *Phys. Rev. B*, 47:6154–6156, 1993.

[171] George Gruner. *Density waves in solids*. CRC Press, 2018.

[172] Y.-H. Liu, R. M. Konik, T. M. Rice, and F.-C. Zhang. Giant phonon anomaly associated with superconducting fluctuations in the pseudogap phase of cuprates. *Nature communications*, 7:10378, 2016.

[173] A. J. Achkar, X. Mao, C. McMahon, R. Sutarto, F. He, R. Liang, D. A. Bonn, W. N. Hardy, and D. G. Hawthorn. Impact of Quenched Oxygen Disorder on Charge Density Wave Order in $YBa_2Cu_3O_{6+x}$. *Phys. Rev. Lett.*, 113:107002, 2014.

[174] J. H. Cho, F. Borsa, D. C. Johnston, and D. R. Torgeson. Spin dynamics in $La_{2-x}Sr_xCuO_4$ ($0.02 \leq x \leq 0.08$) from ^{139}La NQR relaxation: Fluctuations in a finite-length-scale system. *Phys. Rev. B*, 46:3179–3182, 1992.

[175] M.-H. Julien, F. Borsa, P. Carretta, M. Horvatić, C. Berthier, and C. T. Lin. Charge Segregation, Cluster Spin Glass, and Superconductivity in $La_{1.94}Sr_{0.06}CuO_4$. *Phys. Rev. Lett.*, 83:604–607, 1999.

[176] M.-H. Julien. Magnetic order and superconductivity in $La_{2-x}Sr_xCuO_4$: a review. *Physica B: Condensed Matter*, 329-333:693–696, 2003.

[177] A. T. Savici, A. Fukaya, I. M. Gat-Malureanu, T. Ito, P. L. Russo, Y. J. Uemura, C. R. Wiebe, P. P. Kyriakou, G. J. MacDougall, M. T. Rovers, G. M. Luke, K. M. Kojima, M. Goto, S. Uchida, R. Kadono, K. Yamada, S. Tajima, T. Masui, H. Eisaki, N. Kaneko, M. Greven, and G. D. Gu. Muon Spin Relaxation Studies of Magnetic-Field-Induced Effects in High-T_c Superconductors. *Phys. Rev. Lett.*, 95:157001, 2005.

[178] V. F. Mitrović, M.-H. Julien, C. de Vaulx, M. Horvatić, C. Berthier, T. Suzuki, and K. Yamada. Similar glassy features in the ^{139}La NMR response of pure and disordered $La_{1.88}Sr_{0.12}CuO_4$. *Phys. Rev. B*, 78:014504, 2008.

[179] S.-H. Baek, A. Erb, and B. Büchner. Low-energy spin dynamics and critical hole concentrations in $La_{2-x}Sr_xCuO_4$ ($0.07 \leq x \leq 0.2$) revealed by ^{139}La and ^{63}Cu nuclear magnetic resonance. *Phys. Rev. B*, 96:094519, 2017.

[180] A. Arsenault, S. K. Takahashi, T. Imai, W. He, Y. S. Lee, and M. Fujita. ^{139}La NMR investigation of the charge and spin order in a $La_{1.885}Sr_{0.115}CuO_4$ single crystal. *Phys. Rev. B*, 97:064511, 2018.

[181] Shigeki Ohsugi. Doping Dependence of the Electric Field Gradient at La Site in $La_{2-x}M_xCuO_4$ (M= Sr, Ba)—La-NQR Study—. *Journal of the Physical Society of Japan*, 64(10):3656–3659, 1995.

[182] O. Cyr-Choinière, R. Daou, F. Laliberté, C. Collignon, S. Badoux, D. LeBoeuf, J. Chang, B. J. Ramshaw, D. A. Bonn, W. N. Hardy, R. Liang, J.-Q. Yan, J.-G. Cheng, J.-S. Zhou, J. B. Goodenough, S. Pyon, T. Takayama, H. Takagi, N. Doiron-Leyraud, and L. Taillefer. Pseudogap temperature T^* of cuprate superconductors from the nernst effect. *Phys. Rev. B*, 97:064502, 2018.

[183] S. Wakimoto, H. Kimura, M. Fujita, K. Yamada, Y. Noda, G. Shirane, G. Gu, H. Kim, and R. J. Birgeneau. Incommensurate lattice distortion in the high temperature tetragonal phase of $La_{2-x}(Sr,Ba)_xCuO_4$. *J. Phys. Soc. Jpn.*, 75(7):074714–074714, 2006.

[184] B. Keimer, N. Belk, R. J. Birgeneau, A. Cassanho, C. Y. Chen, M. Greven, M. A. Kastner, A. Aharony, Y. Endoh, R. W. Erwin, and G. Shirane. Magnetic excitations in pure, lightly doped, and weakly metallic La_2CuO_4. *Phys. Rev. B*, 46:14034–14053, 1992.

[185] S. Wakimoto, S. Lee, P. M. Gehring, R. J. Birgeneau, and G. Shirane. Neutron scattering study of soft phonons and diffuse scattering in insulating La1. 95Sr0. 05CuO4. *J. Phys. Soc. Jpn.*, 73(12):3413–3417, 2004.

[186] H. Takagi, R. J. Cava, M. Marezio, B. Batlogg, J. J. Krajewski, W. F. Peck, P. Bordet, and D. E. Cox. Disappearance of superconductivity in overdoped $La_{2-x}Sr_xCuO_4$ at a structural phase boundary. *Phys. Rev. Lett.*, 68:3777–3780, 1992.

[187] M. Reehuis, C. Ulrich, K. Prokeš, A. Gozar, G. Blumberg, Seiki Komiya, Yoichi Ando, P. Pattison, and B. Keimer. Crystal structure and high-field magnetism of La_2CuO_4. *Phys. Rev. B*, 73:144513, 2006.

[188] S.-H. Baek, A. Erb, B. Büchner, and H.-J. Grafe. ^{139}La NMR investigation in underdoped $La_{1.93}Sr_{0.07}CuO_4$. *Phys. Rev. B*, 85:184508, 2012.

[189] V. Noiseux. *Variation de $H_{c2}(T \to 0)$ avec le dopage dans les cuprates $La_{2-x}Sr_xCuO_4$ et $Nd_{0.4}La_{1.6-x}Sr_xCuO_4$*. Master's project, Université de Sherbrooke, 2016. Online version: https://tinyurl.com/y8cv52u3.

[190] N. Bloembergen, E. M. Purcell, and R. V. Pound. Relaxation Effects in Nuclear Magnetic Resonance Absorption. *Phys. Rev.*, 73:679–712, 1948.

[191] Shigeki Ohsugi. La-NQR study of $La_{2-x}M_xCuO_4$ (M= Sr and Ba) around x 1/8. *Czechoslovak Journal of Physics*, 46(5):2669–2670, 1996.

[192] H. Vogel. Das Temperaturabhängigkeitsgesetz der Viskosität von Flüssigkeiten. *Phys. Zeitschr.*, 22:645–646, 1921.

[193] Y. J. Uemura, T. Yamazaki, D. R. Harshman, M. Senba, and E. J. Ansaldo. Muon-spin relaxation in AuFe and CuMn spin glasses. *Phys. Rev. B*, 31:546–563, 1985.

[194] F. C. Chou, N. R. Belk, M. A. Kastner, R. J. Birgeneau, and Amnon Aharony. Spin-Glass Behavior in $La_{1.96}Sr_{0.04}CuO_4$. *Phys. Rev. Lett.*, 75:2204–2207, 1995.

[195] A. W. Hunt, P. M. Singer, K. R. Thurber, and T. Imai. ^{63}Cu NQR Measurement of Stripe Order Parameter in $La_{2-x}Sr_xCuO_4$. *Phys. Rev. Lett.*, 82:4300–4303, 1999.

[196] N. J. Curro, P. C. Hammel, B. J. Suh, M. Hücker, B. Büchner, U. Ammerahl, and A. Revcolevschi. Inhomogeneous Low Frequency Spin Dynamics in $La_{1.65}Eu_{0.2}Sr_{0.15}CuO_4$. *Phys. Rev. Lett.*, 85:642–645, 2000.

[197] M.-H. Julien, A. Campana, A. Rigamonti, P. Carretta, F. Borsa, P. Kuhns, A. P. Reyes, W. G. Moulton, M. Horvatić, C. Berthier, A. Vietkin, and A. Revcolevschi. Glassy spin freezing and NMR wipeout effect in the high-T_c superconductor $La_{1.90}Sr_{0.10}CuO_4$: Critical discussion of the role of stripes. *Phys. Rev. B*, 63:144508, 2001.

[198] B. J. Suh, P. C. Hammel, M. Hücker, B. Büchner, U. Ammerahl, and A. Revcolevschi. Spin dynamics in the low-temperature tetragonal phase of $\cong \frac{1}{8}$ doped single crystal $La_{1.67}Eu_{0.2}Sr_{0.13}CuO_4$. *Phys. Rev. B*, 61:R9265–R9268, 2000.

[199] P. Carretta, A. Lascialfari, A. Rigamonti, P. Tedesco, F. Tedoldi, and I. A. Larionov. ^{89}Y nuclear magnetic resonance study of Ca-doped $Y_{1-x}Ca_xBa_2Cu_3O_y$ from the underdoped to the overdoped superconducting regime. *Phys. Rev. B*, 69:104512, 2004.

[200] S.-H. Baek, M. Hücker, A. Erb, G. D. Gu, B. Büchner, and H.-J. Grafe. Inhomogeneous slowing down of spin fluctuations induced by charge stripe order in 1/8-doped lanthanum cuprates. *arXiv preprint arXiv:1402.3077*, 2014.

[201] J. Korringa. Nuclear magnetic relaxation and resonnance line shift in metals. *Physica*, 16(7-8):601–610, 1950.

[202] S. Ohsugi, Y. Kitaoka, K. Ishida, G.-q. Zheng, and K. Asayama. Cu NMR and NQR Studies of High-T c Superconductor $La_{2-x}Sr_xCuO_4$. *Journal of the Physical Society of Japan*, 63(2):700–715, 1994.

[203] R. E. Walstedt, B. S. Shastry, and S-W. Cheong. NMR, neutron scattering, and the one-band model of $La_{2-x}Sr_xCuO_4$. *Phys. Rev. Lett.*, 72:3610–3613, 1994.

[204] P. M. Singer, T. Imai, F. C. Chou, K. Hirota, M. Takaba, T. Kakeshita, H. Eisaki, and S. Uchida. ^{17}O NMR study of the inhomogeneous electronic state in $La_{2-x}Sr_xCuO_4$ crystals. *Phys. Rev. B*, 72:014537, 2005.

[205] Hyekyung Won and Kazumi Maki. d-wave superconductor as a model of high-T_c superconductors. *Phys. Rev. B*, 49:1397–1402, 1994.

[206] G.-q. Zheng, H. Ozaki, Y. Kitaoka, P. Kuhns, A. P. Reyes, and W. G. Moulton. Delocalized Quasiparticles in the Vortex State of an Overdoped High- T_c Superconductor Probed by ^{63}Cu NMR. *Phys. Rev. Lett.*, 88:077003, 2002.

[207] S. Chakravarty and R. Orbach. Electron and nuclear magnetic relaxation in La_2CuO_4 and related cuprates. *Phys. Rev. Lett.*, 64:224–227, 1990.

[208] R. J. Birgeneau, A. Aharony, N. R. Belk, F. C. Chou, Y. Endoh, M. Greven, S. Hosoya, M. A. Kastner, C. H. Lee, Y. S. Lee, G. Shirane, S. Wakimoto, B. O. Wells, and K. Yamada. Magnetism and magnetic fluctuations in $La_{2-x}Sr_xCuO_4$ for x=0 (2D antiferromagnet), x=0.04 (3D spin glass) and x= 0.15 (superconductor). *Journal of Physics and Chemistry of Solids*, 56(12):1913–1920, 1995.

[209] N. Hasselmann, A. H. Castro Neto, and C. Morais Smith. Spin-glass phase of cuprates. *Phys. Rev. B*, 69:014424, 2004.

[210] C. Panagopoulos, B. D. Rainford, J. R. Cooper, and C. A. Scott. Antiferromagnetic correlations versus superfluid density in $La_{2-x}Sr_xCuO_4$. *Physica C: Superconductivity*, 341:843–846, 2000.

[211] C. Panagopoulos, J. L. Tallon, B. D. Rainford, T. Xiang, J. R. Cooper, and C. A. Scott. Evidence for a generic quantum transition in high-T_c cuprates. *Phys. Rev. B*, 66:064501, 2002.

[212] A. W. Hunt, P. M. Singer, A. F. Cederström, and T. Imai. Glassy slowing of stripe modulation in $(La, Eu, Nd)_{2-x}(Sr, Ba)_xCuO_4$: A^{63}Cu and ^{139}La NQR study down to 350 mK. *Phys. Rev. B*, 64:134525, 2001.

[213] T. Wu, H. Mayaffre, S. Krämer, M. Horvatić, C. Berthier, C. T. Lin, D. Haug, T. Loew, V. Hinkov, B. Keimer, and M.-H. Julien. Magnetic-field-enhanced spin freezing on the verge of charge ordering in $YBa_2Cu_3O_{6.45}$. *Phys. Rev. B*, 88:014511, 2013.

[214] S. Sanna, G. Allodi, G. Concas, A. D. Hillier, and R. De Renzi. Nanoscopic Coexistence of Magnetism and Superconductivity in $YBa_2Cu_3O_{6+x}$ Detected by Muon Spin Rotation. *Phys. Rev. Lett.*, 93:207001, 2004.

[215] J. G. Storey. Hall effect and Fermi surface reconstruction via electron pockets in the high-Tc cuprates. *EPL (Europhysics Letters)*, 113(2):27003, 2016.

[216] J. Mitscherling and W. Metzner. Longitudinal conductivity and Hall coefficient in two-dimensional metals with spiral magnetic order. *arXiv preprint arXiv:1807.10252*, 2018.

[217] N. Harrison, R. D. McDonald, and J. Singleton. Cuprate Fermi Orbits and Fermi Arcs: The Effect of Short-Range Antiferromagnetic Order. *Phys. Rev. Lett.*, 99:206406, 2007.

[218] C. Collignon, S. Badoux, S. A. A. Afshar, B. Michon, F. Laliberté, O. Cyr-Choinière, J.-S. Zhou, S. Licciardello, S. Wiedmann, N. Doiron-Leyraud, and Louis Taillefer. Fermi-surface transformation across the pseudogap critical point of the cuprate superconductor $La_{1.6-x}Nd_{0.4}Sr_xCuO_4$. *Phys. Rev. B*, 95:224517, 2017.

[219] B. Michon, A. Ataei, P. Bourgeois-Hope, C. Collignon, S. Y. Li, S. Badoux, A. Gourgout, F. Laliberté, J.-S. Zhou, Nicolas Doiron-Leyraud, and Louis Taillefer. Wiedemann-Franz Law and Abrupt Change in Conductivity across the Pseudogap Critical Point of a Cuprate Superconductor. *Phys. Rev. X*, 8:041010, 2018.

[220] B. Michon, C. Girod, S. Badoux, J. Kačmarčík, Q. Ma, M. Dragomir, H. A. Dabkowska, B. D. Gaulin, J.-S. Zhou, S. Pyon, T. Takayama, H. Takagi, S. Verret, N. Doiron-Leyraud, C. Marcenat, L. Taillefer, and T. Klein. Thermodynamic signatures of quantum criticality in cuprates. *arXiv preprint arXiv:1804.08502*, 2018.

[221] S. Kawasaki, M. Yashima, Y. Kitaoka, K. Takeda, K. Shimizu, Y. Oishi, M. Takata, T. C. Kobayashi, H. Harima, S. Araki, H. Shishido, R. Settai, and Y. Ōnuki. Pressure-induced unconventional superconductivity in the heavy-fermion antiferromagnet $cein_3$: An ^{115}In-nqr study under pressure. *Phys. Rev. B*, 77:064508, 2008.

[222] T. Shibauchi, A. Carrington, and Y. Matsuda. A Quantum Critical Point Lying Beneath the Superconducting Dome in Iron Pnictides. *Annual Review of Condensed Matter Physics*, 5(1):113–135, 2014.

[223] Y. Li, R. Zhong, M. B. Stone, A. I. Kolesnikov, G. D. Gu, I. A. Zaliznyak, and J. M. Tranquada. Low-energy antiferromagnetic spin fluctuations limit the coherent superconducting gap in cuprates. *arXiv preprint arXiv:1806.10633*, 2018.

[224] L. Zaninetti. A Left and Right Truncated Lognormal Distribution for the Stars. *Advances in Astrophysics*, 08 2017.

Abstract

Cuprates are materials that can be tuned from an anti-ferromagnetic insulator to a normal metal by increasing the carrier density through chemical doping. At intermediate doping, a rich variety of electronic phases emerges alongside, or intertwined, with the superconducting phase. The aim of this thesis was to characterise various aspects of the competition between superconductivity and charge or spin order, using nuclear magnetic resonance (NMR). A first part of the work consisted in improving the modelling of ^{17}O NMR spectra in the two charge-density wave (CDW) phases present in $YBa_2Cu_3O_y$: the short-range order and the (magnetic-field induced) long-range order. Besides providing a much more accurate analysis framework for NMR data as a function of field, doping and pressure (see hereafter), the results indicate that the CDW in high-fields is uniaxial (*i.e.* single wave vector q) and commensurate with the lattice, with a period of three unit cells ($q = 1/3$).

The second aspect of phase competition addressed in this work is the (controversial) effect of hydrostatic pressure. Our measurements show that a pressure of 1.9 GPa weakens the short-range CDW in the normal state and the long-range CDW observed in high fields only slightly. The results support the proposal that the continuous rise in T_c upon increasing pressure up to $\sim$15 GPa arises almost entirely from a gradual decrease of the CDW strength. This establishes hydrostatic pressure as a tuning parameter of the competition between CDW order and superconductivity in the cuprates. In the third part of the thesis, ^{139}La spin-lattice relaxation rate ($1/T_1$) measurements were used to study the effect of a magnetic field on glassy spin ordering in $La_{2-x}Sr_xCuO_4$. Using high fields up to 45 T, we reveal that the field is able to induce a frozen, or nearly so, phase at doping levels much higher than previously assumed, namely up to the putative endpoint of the pseudogap boundary, but not, or not far, beyond that point. This result has important implications for interpreting the pseudogap phase and its associated quantum criticality.